

Journal of Electrochemical Science and Engineering

J. Electrochem. Sci. Eng. 15(2) 2025





Open Access :: ISSN 1847-9286 www.jESE-online.org

Original scientific paper

High-performance supercapattery with nanotube-TiO₂/carbon nano tubes anode and coconut-shell-derived activated carbon cathode

Thi Thu Trang Nguyen^{1,⊠}, Thi Nhu Nguyet Pham^{2,3}, Hoang Anh Nguyen^{2,3}, Thi Nhu Quynh Nguyen^{2,3}, Nguyen Thanh Le Huynh^{2,3,™}, Van Viet Pham⁴, Hoang Nguyen^{2,3}, Viet Hai Le^{2,3}, Thi Thu Trang Nguyen⁵, Thi Thom Nguyen¹, Thi Nam Pham¹, Dai Lam Tran^{1,6}, Trong Lu Le¹

Corresponding authors: [™]ntttrang@itt.vast.edu; [™]hltnguyen@hcmus.edu.vn

Received: August 5, 2024; Accepted: December 23, 2024; Published: February 23, 2025

Abstract

This paper aims to present the fabrication of a Li-ion supercapattery by an anode designed for a lithium-ion battery (nanotube TiO_2 (NT- TiO_2) and carbon nanotubes (CNTs), namely as NT-TiO₂/CNTs) with a cathode designed for an electrochemical double-layer capacitor (derived activated carbon), resulting in high energy and densities of power. The hydrothermal route formed the composite NT-TiO₂/CNTs. DFT calculations provide the Li absorbed inside and outside isolated CNTs and NT-TiO₂/CNTs. The lithium diffusion energy barrier results show that Li is preferred energetically inside CNT. The energy barrier of Li diffusion for isolated CNTs is 1.21 eV, whereas that of NT-TiO₂/CNTs is computed at 0.69 eV. It demonstrated that the functionalized NT-TiO₂ improves the performance and the rate of Li diffusion of the isolated CNTs system, which agrees with the experiment. The results illustrate that the synergistic effect of high conductive CNT networks and welldispersed NT-TiO₂ structure can enhance hybrid capacitors' power and energy density through the brief diffusion routes for Li-ions and rapid transference of electrons. A Li-ion supercapattery battery, NT-TiO₂/CNTs-1||activated carbon (AC), achieved an energy density of 48.9 Wh kg⁻¹, surpassing supercapacitors, and a power density of 1667 W kg⁻¹ at a current rate of 1 A g^{-1} , exceeding that of Li-ion batteries.

¹Institute for Tropical Technology, Vietnam Academy of Science and Technology, Hanoi, Vietnam

²Vietnam National University Ho Chi Minh City, Vietnam

³University of Science, Ho Chi Minh City, Vietnam

⁴HUTECH University, Ho Chi Minh City, Vietnam

⁵University of Education, Ho Chi Minh City, Vietnam

⁶Graduate University of Science and Technology, Vietnam Academy of Science and Technology, Hanoi, Vietnam

Keywords

TiO₂/carbon nanotubes composite; hybrid Li-ion capacitor; density functional theory calculations; energy density; power density

Introduction

Storing energy by utilizing Li-ion batteries (LIBs) or supercapacitors does not yet meet hybrid and all-electric vehicles power and energy demands, primarily due to Faradaic reactions from the intercalation of Li-ions into the electrodes, LIBs can deliver a high energy density of approximately 150 Wh kg⁻¹[1-3]. Nonetheless, such energy storage systems have limitations, including short cycling lifetimes and low power densities caused by the resulting volumetric strain and inherently sluggish diffusion of solid-state lithium in bulk. Meanwhile, electrochemical double layer capacitors (EDLCs) offer prolonged electrochemical stability (roughly 10,000 cycles) and high capacity of power (2 to 5 kW kg⁻¹); nevertheless, these systems have minimal energy density (3 to 6 Wh kg⁻¹) for EDLCs due to limited charge accumulation [4,5]. Therefore, the invention of a hybrid Li-ion capacitor (LIC) that merges the merits of both aforementioned technologies can be considered a potential candidate for a revolutionary energy storage system. Hybrid Li-ion capacitors, or supercapatteries, typically feature supercapacitor electrodes (made of carbonaceous materials forming electric double layers) on one side and Li-ion intercalating electrodes on the other [6,7]. With this setup, the device stores charge *via* reversible anion adsorption/desorption on the cathode surface and reversible lithiumion insertion/extraction in the anode material [8].

Titanium dioxide (TiO₂) has drawn considerable attention as a battery electrode material. Due to its high chemical stability, affordability, abundant availability, and multiple oxidation states (III to V), it is applied in various fields, such as storing energy, photocatalysis, and dye degradation [5,9-11]. Nonetheless, a significant challenge for battery-type TiO₂ electrodes that limits their energy-storage performance is the insufficient cycling stability and electronic conductivity. This inadequacy, particularly during cycling, can lead to a loss of electrochemical sites [12]. Employing a LiPF₆-EC/DMC/DEC electrolyte with a concentration of 1 M, a cathode of carbon nanotube, and an anode of TiO₂-B nanowire, the hybrid Li-ion capacitor achieves a high energy density, which was 12.5 Wh kg⁻¹ [13]. Other studies have also reported on LICs using the compound of titanium anode electrodes. While these devices show a slight increase in energy density, their power capability remains constrained by the slow intercalation electrode reaction in LICs. Research suggests that growing an ordered array architecture directly on conductive substrates can address the limitations of mixing with polymer binders or conductive carbon while providing efficient transport pathways for ions and electrons [7,14].

Activated carbon (AC) is used widely for the cathode electrode in a hybrid Li-ion capacitor because of its excellent contact area and electrical conductivity [15-17]. Nonetheless, this is attributed to the limited ion transport through small tunnels due to the restricted ion transportation, which reduces electrochemical surface accessibility. Thus, finding alternative carbon materials that offer better power density and energy in an organic electrolyte is crucial. A coconut-shell-derived AC is one of the popular biomass-derived ACs that has received enormous attention in the electrochemical capacitor industry [18,19]. The supercapattery based on nanotube-TiO₂/carbon nanotubes||activated carbon (NT-TiO₂/CNTs||AC) offers high energy density, fast charge-discharge cycles, and a long lifespan. These features make them ideal for key applications, such as stabilizing renewable energy systems (like solar and wind), enhancing energy efficiency in electric vehicles by capturing regenerative braking energy, and providing fast-charging solutions in portable electronics. Their ability to manage energy fluctuations makes them valuable in smart grid systems.



Herein, we have developed a hybrid Li-ion capacitor constructed with synthesized NT-TiO $_2$ /CNTs and coconut-shell-derived AC. The hydrothermal structure is used to prepare the composites of the nanotube structure of TiO $_2$ and CNTs.

Experimental

Preparation of NT-TiO₂/CNTs nanocomposite

All chemicals were of high purity grade and were used without purifying. The NT-TiO₂/CNTs nanocomposites were prepared *via* a hydrothermal route. Initially, 1.13 g of TiO₂ was dispersed in 103.8 mL of NaOH with a concentration of 10 M and was magnetically stirred for one hour. After that, this mixture was transferred to a Teflon-lined autoclave before heating for 18 hours at 180 °C. This was followed by the step that the carbon nanotubes were added with distinct weight present, including 1, 3, and 5 wt.% of CNTs; the samples were marked as NT-TiO₂/CNTs-1, NT-TiO₂/CNTs-3, NT-TiO₂/CNTs-5, respectively. Next, 5 mL of deionized water was added to the solution, which was stirred for 1 hour until homogeneous. The resulting powder was then calcined at 500 °C for 2 hours at a heating rate of 5 °C min⁻¹. The residue was washed with deionized water and dried at 100 °C for 24 hours. For comparison, the same procedure was applied to prepare the pristine TiO₂ without CNTs, referred to as pristine NT-TiO₂.

Structural and morphological characterization of nanocomposite NT-TiO₂/CNTs

The nanocomposites NT-TiO₂/CNTs were analyzed using X-ray diffraction (XRD) on a D8 Advance diffractometer (Bruker) equipped with a LYNXEYE detector, with a Cu anode ($\lambda_{K\alpha}$ = 0.15689 nm) in the scan range of 20 to70° (0.02°/step). Raman scattering spectra were measured using an XPLORA spectrometer (HORIBA) with an excitation laser wavelength of 532 nm, and a measurement range from 50 to 2000 cm⁻¹. The pore volume distribution and specific surface area were determined by the Brunauer-Emmett-Teller (BET) method on a TriStar II-3000 (Micromeritics, USA). The morphology and particle size characteristics of composites were also examined by transmission electron microscopy (TEM) using a FEI Tecnai G2 F20 (USA).

Electrochemical characterization

The synthesized powders were combined in a porcelain mortar and pestle with acetylene black and polyvinylidene fluoride (PVDF) in a weight ratio of 80:15:5, respectively. The mixture was then coated onto the base (aluminum foil) to a 0.1 mm thickness, dried at 100 °C for 12 hours, and pressed to a final thickness of 200 μ m; the mass density of the electrode was controlled around 10 mg cm⁻². The electrode preparation was detailed in the Supplementary material. The cell was assembled with the prepared anodes and lithium metal as the counter electrode. The electrolyte LiPF₆ 1 M in a 1:1 EC:DMC (v/v) was used at 150 μ L, with three Whatman glass fibers as the separator. The full cell NT-TiO₂/CNTs-1|AC was assembled using coin-cell CR2032 type, the anode was the NT-TiO₂/CNTs composite electrode, and the cathode was the coconut-shell-derived AC electrode. The details of AC cathode preparation process are described in the Supplementary material. The LANHE CT2001A apparatus (China) was utilized at various current rates within a 0.o to 3.0 V voltage range to test the galvanostatic charge/discharge performance. The capacitance from GCD curves was calculated by Equation (1). The Ragone plot is constructed by plotting specific energy, E/Wh kg⁻¹, against specific power, E/W kg⁻¹, using the data from GCD curves, Equations (2) and (3):

$$C_{\rm sp} = \frac{I \, \Delta t}{m \, V} \tag{1}$$

$$E = \frac{1}{2 \times 3.6} C_{\rm sp} V^2 \tag{2}$$

$$P = \frac{3600E}{\Delta t} \tag{3}$$

where $C_{\rm sp}$ / F g⁻¹ is the specific (gravimetric) capacitance of the cell, I / A is the applied current, Δt /s is the discharge time, m / g is the mass of both electrodes, V / V is the potential window, and the given numerical factors are time/mass conversion factors.

Computational details

This research used calculations based on the first principles of density functional theory (DFT) from the Vienna *ab Initio* Simulation Package (VASP) [20,21]. Core regions were treated using the projector augmented wave (PAW) pseudopotentials [22,23]. The combination of generalized gradient approximation (GGA) [24,25] and the Perdew-Burke-Ernzerhof (PBE) [26,27] scheme was used to describe the exchange and correlation potentials. The GGA-PBE function has been reported with well-reasonably described carbon-based systems [28-37]. In all calculations, Grimme's DFT-D3 was employed to describe van der Waals interactions between carbon atoms [38], with an energy cutoff of 600 eV. All atomic positions were optimized using the conjugate gradient method, with self-consistent field (SCF) force values and conversion energy set to 10^{-6} eV and 0.002 eV nm⁻¹, respectively. DFT calculations were conducted with a Monkhorst–Pack [39]. $2 \times 2 \times 1$ k-point with the involvement of the DFT+U approach [40] because of the 3d electrons of Ti. Hubbard parameters with J set to 0.5 eV and U set to 0.0 eV were used to treat these electrons [41,42] along with Grimme's D3 dispersion corrections to account for van der Waals interactions [43]. The lithium diffusion paths were employed, utilizing the nudged elastic band (NEB) method [44] within six transition images.

Results and discussion

Structure and morphology of NT-TiO₂/CNTs

Figure 1a illustrates the XRD patterns of the pristine $NT-TiO_2$ and the composite $NT-TiO_2/CNTs$ samples. All peaks align well with the anatase phase (JCPDF-01-078-2486), exhibiting tetragonal symmetry with the point space group I41/amd [45,46]. The CNT content does not significantly change the anatase structure. The central peak (101) is observed at 25.3°, showing significant dependence on the synthesis. Under the assumption that the Debye-Scherrer equation is valid for spherical particles, the crystallite size was calculated using Equation (4):

$$D = \frac{K\lambda}{\beta \cos \theta} \tag{4}$$

where D is the average crystallite size (nm), β the full width at half maximum (FWHM), θ the Bragg diffraction angle, K is the Scherer constant number (0.89), and λ the wavelength of X-ray (0.154 nm). The lattice parameters and average crystallite size are presented in Table 1.

Table 1. Lattice parameters and average crystallite size of pristine NT-TiO₂ and NT-TiO₂/CNTs composites

	a = b / nm	<i>c</i> / nm	V / nm³	<i>D</i> / nm
NT-TiO ₂	0.37889	0.95537	0.13715	19.05
NT-TiO ₂ /CNTs-1	0.37879	0.95209	0.13661	14.57
NT-TiO ₂ /CNTs-3	0.37957	0.95552	0.13766	22.18
NTTiO ₂ /CNTs-5	0.37889	0.95537	0.13715	19.05

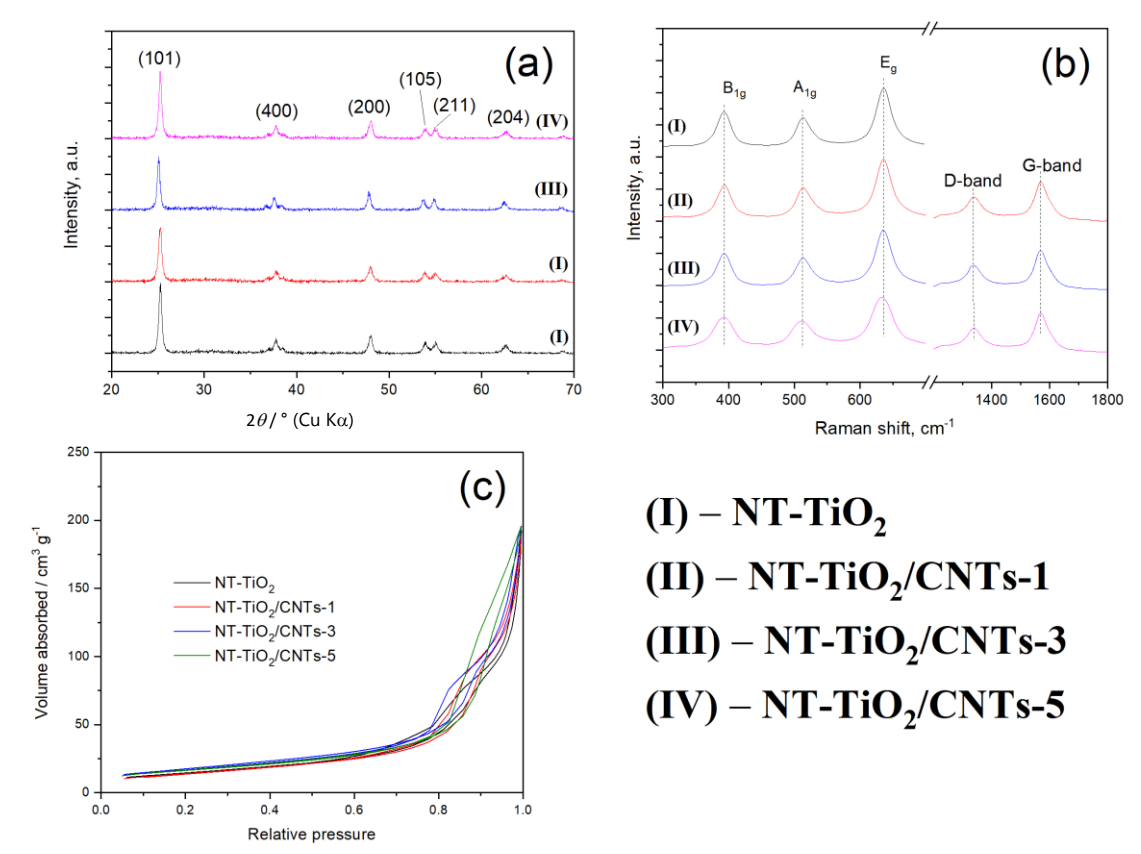


Figure 1. (a) XRD diagrams, (b) Raman spectra and (c) nitrogen adsorption/desorption isotherm of pristine $NT-TiO_2$ and $NT-TiO_2$ /CNTs composites

Raman spectra (Figure 1b) show three features of the anatase phase NT-TiO₂ and the D-/G-bands of carbon. The characteristic bands in the low-frequency region (200 to 800 cm⁻¹) at 400, 515, and 639 cm⁻¹ correspond to the anatase phase's B1g, A1g + B1g, and Eg modes. The B1g mode at 400 cm⁻¹ is associated with Ti–O stretching vibrations. All the samples exhibit the anatase phase, the three active modes of TiO₂, corresponding to 397 (A_{1g}) and 639 (E_g) cm⁻¹ [47,48]. Moreover, Raman spectroscopy is extensively employed to analyze the electronic structure of carbon-based materials. In the high-frequency region, the carbon Raman spectrum exhibits two distinct peaks: the D-band (1320 cm⁻¹) and the G-band (1571 cm⁻¹) [49,50].

Figure 1c compares the nitrogen adsorption/desorption isotherms at 77 K and the distribution in size. The multipoint BET method, based on adsorption data within the relative pressure (P/P_0) range of 0.05 to 0.30, was utilized to calculate the specific surface area, whereas the Barrett-Joyner-Halenda (BJH) desorption analysis was used to obtain the pore volume and average pore diameter. As a result, the isotherms display type IV behavior, characteristic of mesoporous materials, with hysteresis loops resembling type H3, indicating plate-like particle aggregates with slit-shaped pores. CNT loading notably affects the porous volume, with the maximum volume observed at a 0.05 ratio reaching approximately 162 m² g⁻¹, higher than the sample without CNTs. Although the BET surface area remains relatively unaffected by CNT loading, the BJH desorption analysis shows a correlation between porous volume and pore diameter. Pore sizes initially measured at 8.3 nm increase to 8.7 to 9.8 nm with CNT addition. The active surface area and average pore size are provided in Table 1.

Figure 2 illustrates TEM micrographs of NT-TiO $_2$ /CNTs composites, revealing the interconnection of nanotubes. The morphology of NT-TiO $_2$ (Figure 2a) and NT-TiO $_2$ /CNTs composites (Figure 2b to 2d) is uniform. The size of the nanotube is around 4-5 nm for the inner diameter and around 13-15 nm for

the outer diameter. The length of NT-TiO $_2$ can be found in the range of 100 to 150 nm. Moreover, fiber with a small diameter can be attributed to the CNT fiber. With a matrix interconnection, the NT-TiO $_2$ /CNTs can promote electron transfer and Li-transportation in the electrochemical performance.

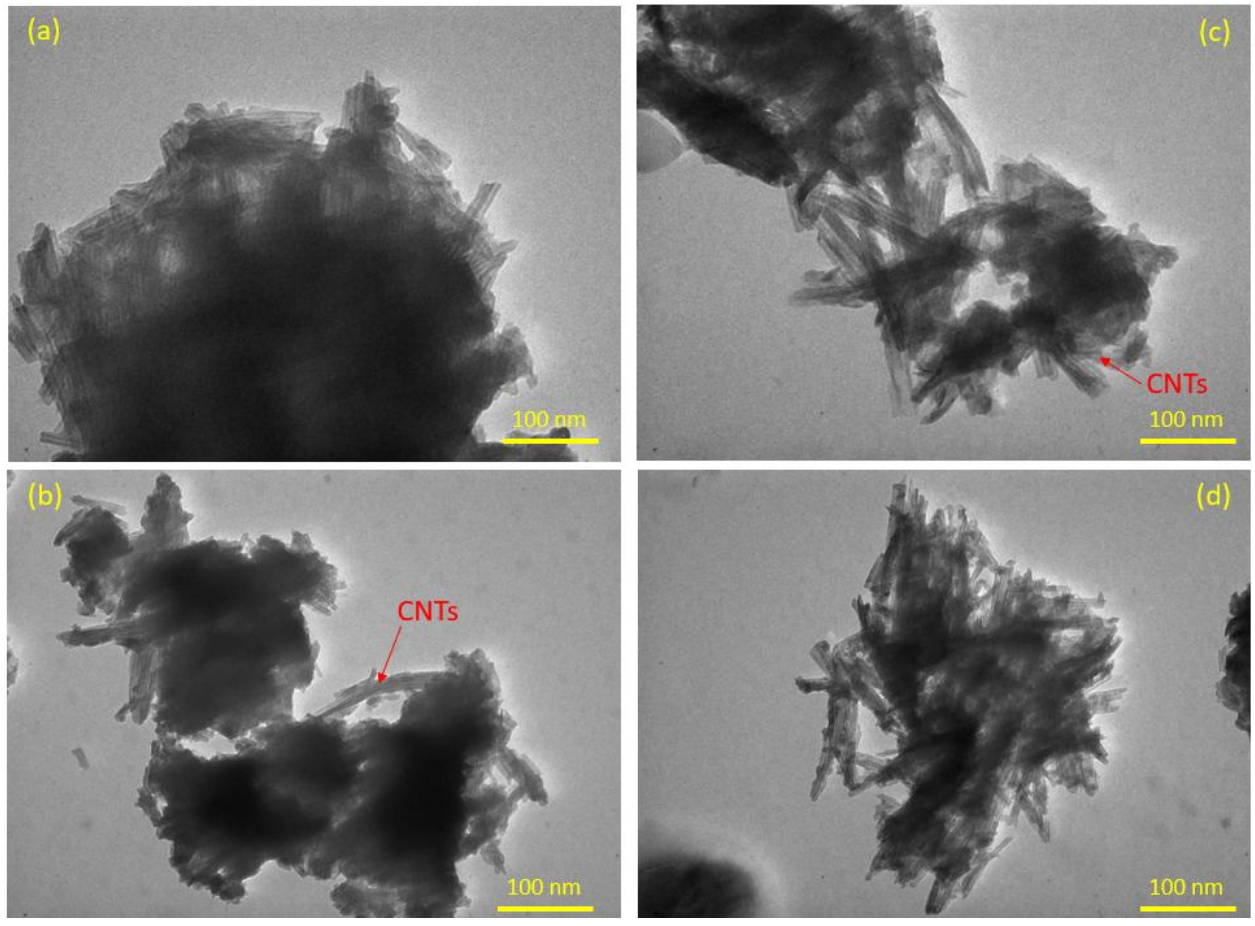


Figure 2. TEM images of (a) pristine NT-TiO₂; (b) NT-TiO₂/CNTs-1; (c) NT-TiO₂/CNTs-3; (d) NT-TiO₂/CNTs-5 composites

The survey XPS spectrum (Figure 3) reveals the presence of carbon, oxygen, and titanium, which validates the successful synthesis of the composite. In the high-resolution C1s spectrum, multiple carbon states are observed. The peak at 283.4 eV corresponds to sp² hybridized carbon, confirming the presence of intact carbon nanotubes. The C–O bonds at 284.8 eV may arise from functional groups on the CNTs or contaminants. Notably, the Ti–O–C interaction peak at 287.1 eV implies a robust interface between NT-TiO2 and CNTs, which can enhance charge transfer in applications such as photocatalysis or energy storage. The O 1s spectrum exhibits two oxygen environments. The lattice oxygen in TiO2 is shown at 528.4 eV, whereas the higher energy peak at 529.7 eV indicates surface-adsorbed oxygen species. The Ti 2p spectrum displays the expected spin-orbit splitting for Ti $2p_{3/2}$ and $2p_{1/2}$, confirming the presence of Ti⁴⁺ ions in the NT-TiO2 crystal structure. The absence of lower binding energy peaks suggests that Ti is primarily in the +4-oxidation state without significant reduction to Ti³⁺, which is favorable for maintaining the material's electronic properties. These XPS results confirm the successful fabrication of the NT-TiO2/CNTs composite with a robust interfacial interaction. For supercapattery, the NT-TiO2/CNTs interface could facilitate rapid electron transfer, improving charge/discharge rates and overall performance.

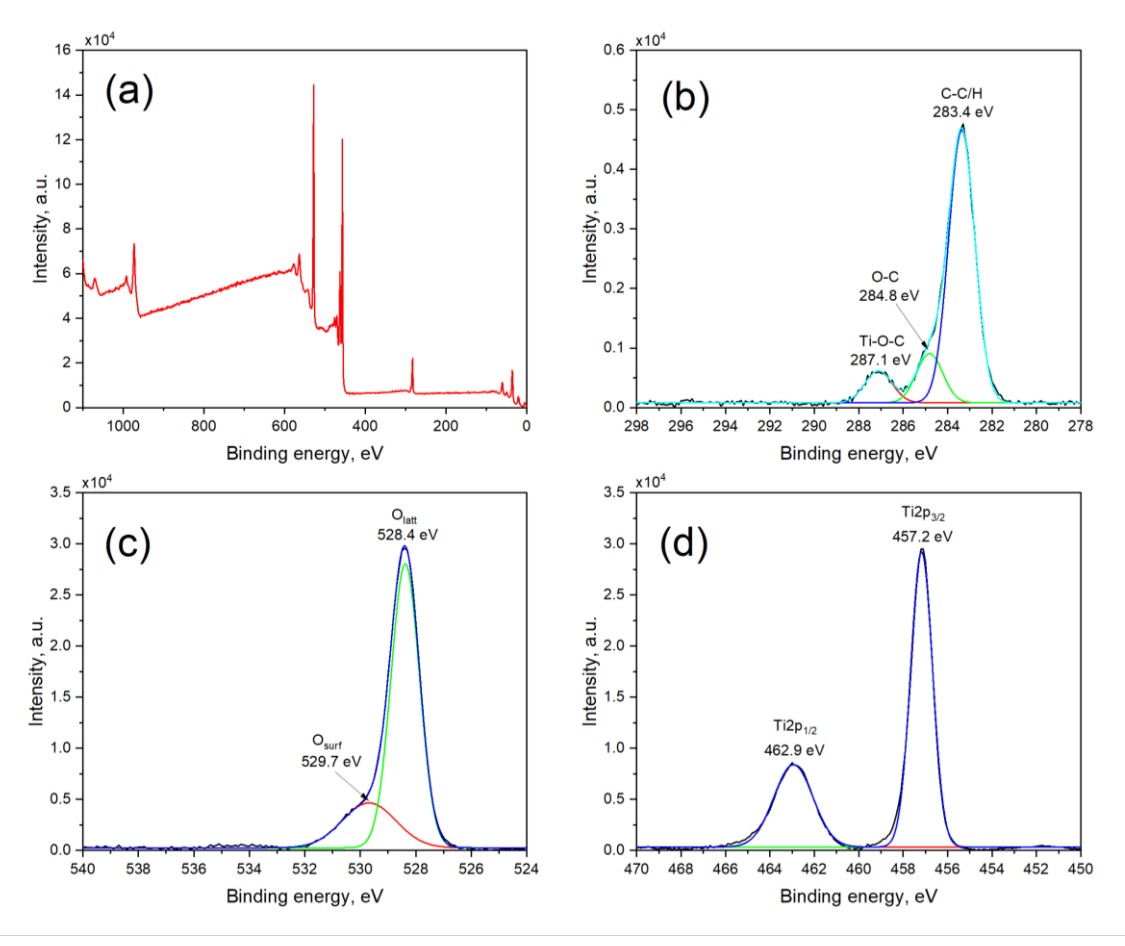


Figure 3. XPS spectrum of NT-TiO₂/CNTs-1: (a) full-scan profile, and narrow profiles (b) carbon, (c) oxygen, and (d) titanium

Electrochemical performance

Cyclic voltammetry (CV) studies were performed on the prepared samples within a voltage range of 1.5 to 2.5 V (vs. Li⁺/Li) to investigate the lithiation and delithiation behavior. The CV curves of pristine NT-TiO₂ and NT-TiO₂/CNTs electrodes are shown in Figure 4a-d and carried out at many scan rates (from 0.01 to 0.4 mV s⁻¹). The cycles show a characteristic cathodic/anodic peak at 1.6 V and 2.0 V due to the insertion/de-insertion of Li⁺ ions in the TiO₂ host. The area of CV curves indicates the total Li⁺ storage capacity, which generally comprises two parts: (i) Faradaic contributions with the Li⁺ diffusion-controlled redox reactions and (ii) non-Faradaic contributions from the double-layer capacitive effect. The cyclic voltammetry data were analyzed at different sweep rates using the following Equation (5):

$$I = av^b (5)$$

The scan rate v influences the measured current I following a power law relationship, with a and b as adjustable parameters. The b-value is determined from the slope of the log I versus log v plot. A b-value of 1.0 indicates a capacitive surface process, whereas a b-value of 0.5 suggests a diffusion-controlled process corresponding to the Ti^{4+}/Ti^{3+} redox reaction. Figure 4e shows that plotting log I versus log v results in a linear relationship with slopes of b = 0.55 for the anodic process in NT-TiO₂ and b = 0.62 for the NT-TiO₂/CNTs-1 electrode. A b-value of 0.55 is close to 0.50, which suggests that charge storage within the scan rate range of 0.01 to 0.4 mV s⁻¹ and a voltage window of 1.5 to 2.5 V is predominantly governed by diffusion-controlled insertion processes. Using Equation (6), the proportion of each contribution type is determined from the total charge storage at a given scan rate.

$$I = k_1 v + k_2 v^{1/2} (6)$$

Equation (6) can be altered to the Equation (7):

$$I/v^{1/2} = k_1 v^{1/2} + k_2 \tag{7}$$

In Equation 6, the first term (k_1v) represents the capacitive contribution to the current response, while the second term $(k_2v^{1/2})$ reflects diffusion-controlled process contribution. The coefficients k_1 and k_2 are obtained from the linear fit as the slope and y-intercept of linear relation defined by Equation (7). The total current response is separated into individual contributions by utilizing these values, which are then used in Equation (6).

Figure S1 to Figure S4 in the Supplementary material exhibit the charge contributions determined from CV curves at different potential scan rates. By comparing the total area to the shaded area at a scan rate of 0.40 mV s⁻¹, the capacitive contributions are found to be 73.8, 78.2, 74.1 and 72.3 % of the total charge for the pristine NT-TiO₂ and NT-TiO₂/CNTs electrodes. A Ti⁴⁺/Ti³⁺ redox reaction controls the diffusion-controlled charge at a given peak potential. Using the same approach, the contributions of the two charge storage processes at different scan rates are assessed and depicted in Figure 4f as a bar graph at a scan rate of 0.4 mV s⁻¹. With increasing scan rates, the capacitive contribution becomes the main factor determining the total charge stored in the cell. This increased capacitive effect at higher scan rates results from enhanced electron transfer due to a shorter Li⁺ diffusion path, which supports rapid charge storage and better long-term cyclability. Moreover, the diffusion-controlled process at the electrode surface and throughout the electrode contributes to faster Li⁺ kinetics, improved rate performance, and longer cycle life.

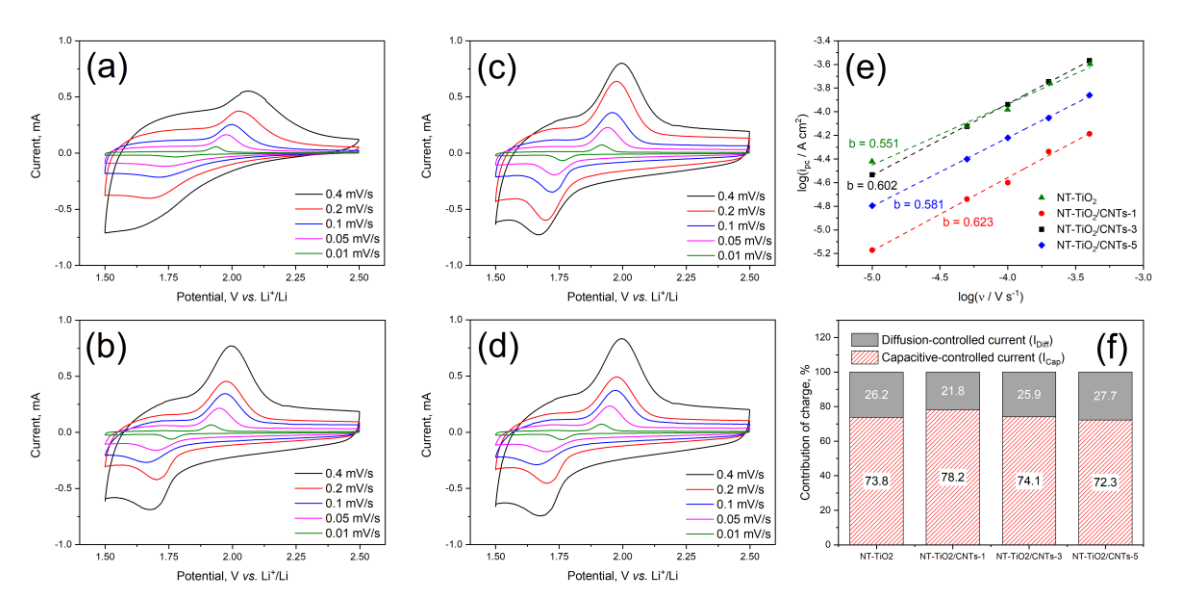


Figure 4. Cyclic voltammetry curves of (a) pristine NT-TiO₂, (b) NT-TiO₂/CNTs-1, (c) NT-TiO₂/CNTs-3 and (d) NT-TiO₂/CNTs-5 electrodes at various sweep rates from 0.01 to 0.4 mV s⁻¹; (e) log I vs. log v and (f) charge contributions for electrodes at 0.4 mV s⁻¹

The first charge-discharge curves at rate C/10 of NT-TiO₂ and NT-TiO₂/CNTs electrodes in 1.0 to 3.5 V in lithium half-cells are presented in Figure 5a-b, respectively. It has a notable reversible discharge capacity of 270 mAh g⁻¹ and a Coulombic efficiency of 100 % for NT-TiO₂/CNTs-1 electrode. The capacities for other electrodes are found to be 207 mAh g⁻¹ for pristine NT-TiO₂, 235 mAh g⁻¹ for NT-TiO₂/CNTs-3 and 214 mAh g⁻¹ for NT-TiO₂/CNTs-5. Long-term cycle performance is shown in Figure 5b. The NT-TiO₂/CNT-1 electrode delivers excellent cycle stability, maintaining 90 % capacity retention after 160 cycles. Moreover, the rate performance of the NT-TiO₂/CNTs-1 electrode is also measured

and presented in Figures 5c to 5d. It exhibits significantly outstanding rate capability, particularly at high C rates. It achieves capacities of 270, 235, 213, 193, 168, and 147 mAh g^{-1} at numerous current rates, including 0.1C, 0.2C, 0.5C, 1C, 2C, and 5C. These findings demonstrate that the NT-TiO₂/CNTs-1 electrode delivers a high reversible capacity, cycle stability, and outstanding rate performance.

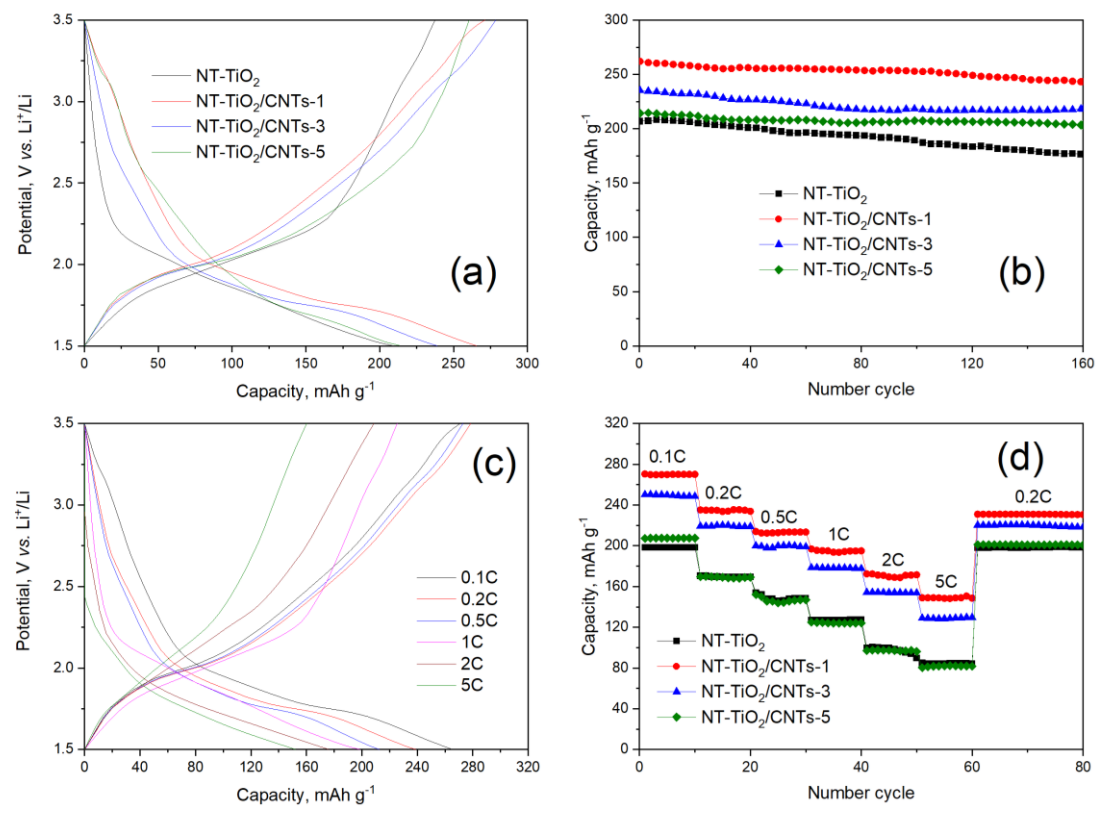


Figure 5. (a) Charge/discharge curves and (b) cycling behavior of pristine NT-TiO₂ and NT-TiO₂/CNTs electrodes at rate 0.1C; (c) typical charge/discharge curves and (d) cycling behavior at various rates from 0.1C to 5C of pristine NT-TiO₂ and NT-TiO₂/CNTs electrodes

Figure 6a displays the charge/discharge curves in the voltage window from 0-3 V of hybrid Li-ion capacitor in asymmetric configuration NT-TiO₂/CNTs||AC at different charge-discharge current rates and the long-term cycling stability at 10 A g-1 is shown in Figure 6c. As the current density discharge increases (0.2 to 10 A g⁻¹), the specific capacitances of the NT-TiO₂/CNTs | AC cells decrease because of the polarization effects and surface adsorption processes (Figure 6b). The specific capacitance is found to be 4.5 F g⁻¹ for pristine NT-TiO₂ | AC cell, 28.8 F g⁻¹ for NT-TiO₂/CNTs-1 | AC cell, 20.5 F g⁻¹ for NT-TiO₂/CNTs-3||AC cell, and 15.1 F g⁻¹ for NT-TiO₂/CNTs-5||AC cell at current rate 10 A g⁻¹. At high current densities, ions are near the surface of the electrode material due to the charge storage on the surface (non-Faraday mechanism), leading to a reduced capacitance value. The NT-TiO₂/CNTs-1||AC cell shows a suitable capacitance of 28.8 F g⁻¹ at a current density of 10 A g⁻¹, and the capacitance retention is nearly 85 % upon 5000 cycles. Figure 6d illustrates the Ragone plot of asymmetric cells NT-TiO₂/CNTs||AC (AC: coconut-shell derived activated carbon). At the current density of 1 A g⁻¹, TiO₂/CNTs-1||AC asymmetry cell displays superior performance, exhibiting an energy density of 48.9 Wh kg⁻¹ and a power density of 1677 W kg⁻¹. When the power density increases, the energy density of these electrodes decreases. Proportionally, NT-TiO₂/CNTs display a competitive performance compared with other hybrid supercapacitors [51-54].

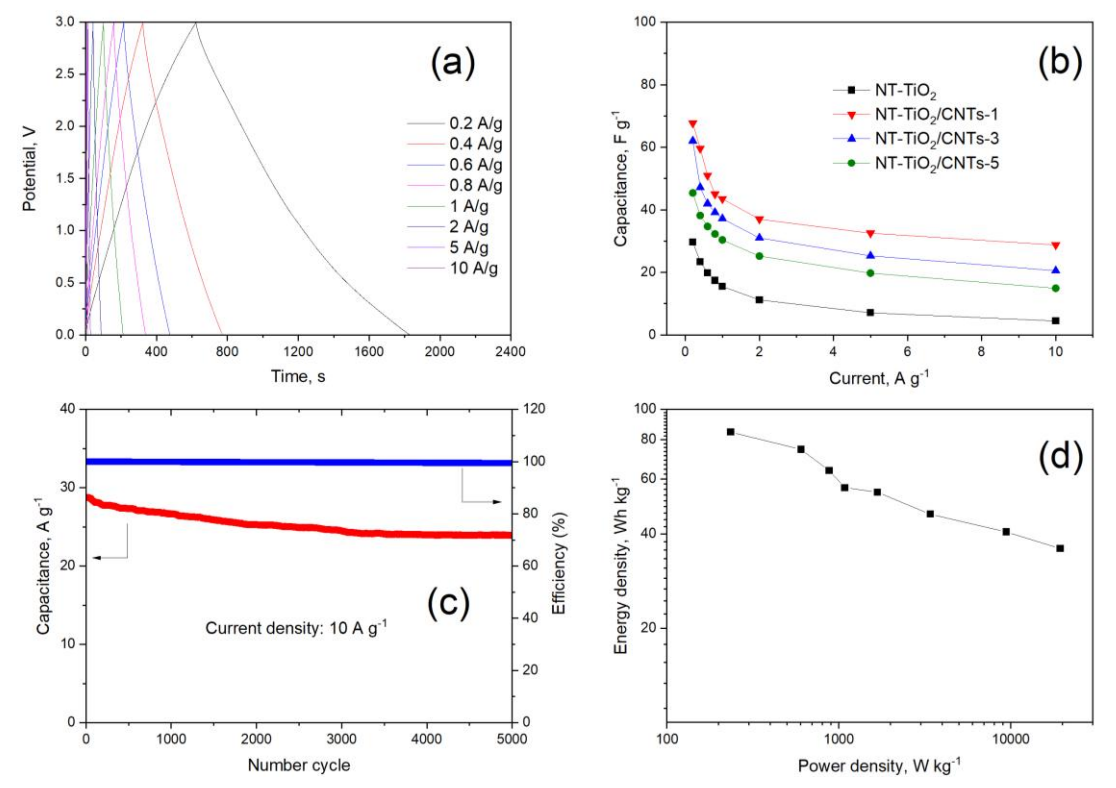


Figure 6. (a) Charge/discharge curves of NT-TiO₂/CNTs-1||AC cells at various rates from 0.2 to 10 A g^{-1} ; (b) specific capacitance vs. rate of NT-TiO₂/CNTs||AC cells; (c) cycling behavior of NT-TiO₂/CNTs-1||AC cell upon 5000 cycles at rate 10 A g^{-1} and (d) Ragone plot of NT-TiO₂/CNTs-1||AC

Computational part

The equilibrium structures

The NT-TiO₂ was constructed via three layers of (101) anatase surface (55). The NT-TiO₂/CNTs system was built as the (101) TiO₂ anatase functionalized 4 ×4 armchair carbon nanotube (CNTs), as shown in Figure 7. The interlayer-connected distances between the top layer of TiO₂ and the surface of CNTs were most stable at 0.236 and 0.224 nm. The average C–C bond lengths of pristine CNTs and NT-TiO₂/CNTs were computed as 0.143 and 0.143 nm, respectively. These parameters are consistent with the previous study of CNTs25 and prove that our methodology is reasonable for further calculations.

The adsorption energies (E_{ads}) of lithium on pristine CNT and the system of TiO₂/CNT were computed as $E_{ads} = E_{Li+sys} - E_{Li} - E_{sys}$, where E_{Li+sys} , E_{Li} and E_{sys} are defined as the DFT-total energy of Li adsorbed on systems, the isolated Li atom at the most stable position, and the pristine CNT and TiO₂/CNT, respectively.

Table 2 reported that in both systems of CNT with and without the functionalized TiO₂, the value of Li adsorption energies suggests Li can adsorb at the inside and outside surface of CNT. The functionalization of nanotube TiO₂ improved the lithium adsorption behavior corresponding with the negatively higher Li adsorption energies than the system of isolated CNTs in interior and exterior Li adsorption. The higher negative value of the adsorption energy proves that the Li atom slightly prefers to adsorb at the exterior side of armchair CNTs, and the CNTs system with the functionalized TiO₂ agrees well with the precious study [56] and our experiment. These points are also consistent with the closer Li-CNTs distance with Li adsorbed inside and outside surface of CNT in NT-TiO₂/CNTs compared to an isolated CNTs system. The mobility of Li in the electrodes significantly influences the charge/discharge rate of the LIBs. The Li diffusion paths of CNTs and NT-TiO₂/CNTs were investigated through the NEB method, in which Li moves along different possible reaction paths.



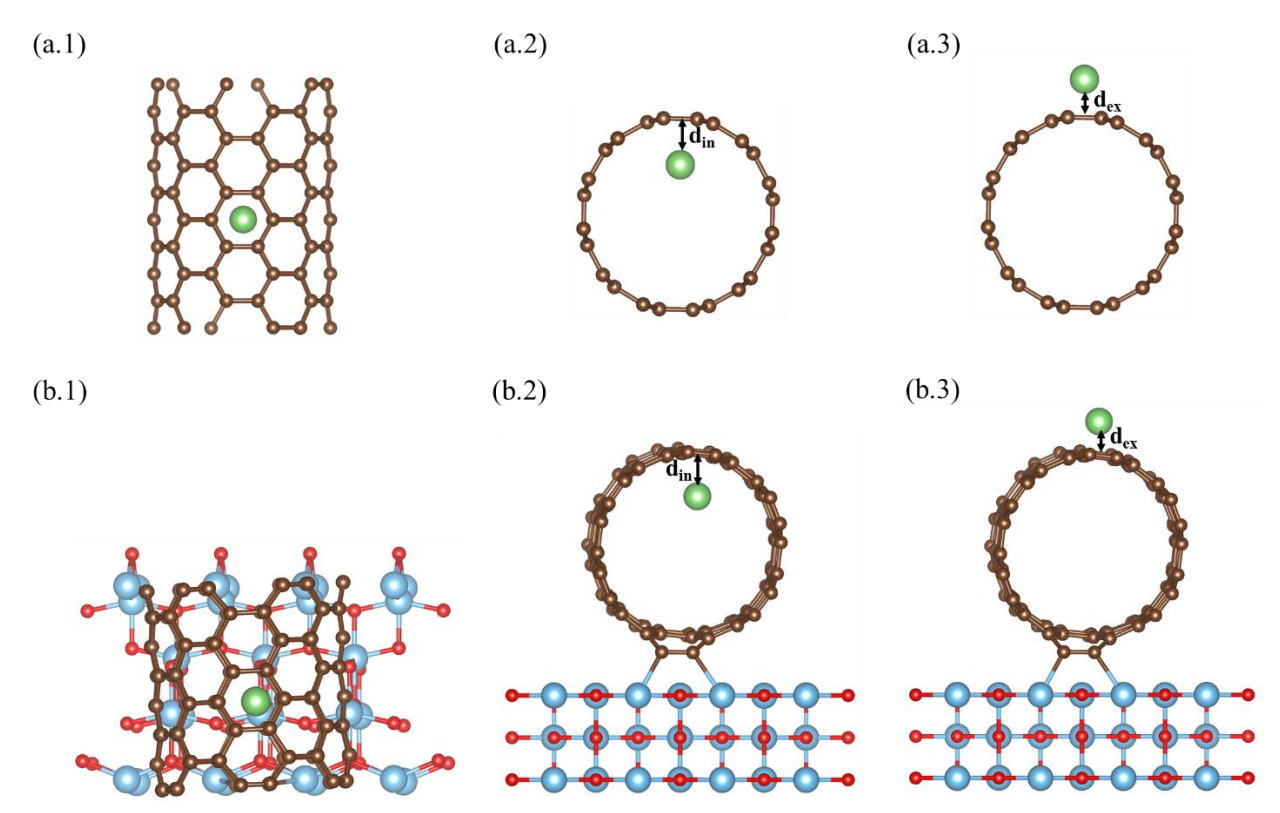


Figure 7. The most stable configurations of (a.1) armchair 4×4 Carbon nanotube (CNTs) and (b.1) NT-TiO₂/CNT. They are absorbed by a lithium atom (green atom) and stable lithium interior (a.2) or exterior (a.3) of the CNTs. The adsorbed Li inside and outside NT-TiO₂/CNT were shown in (b.2) and (b.3), respectively. The brown, red, blue, and green spheres represent carbon (C), oxygen (O), titanium (Ti), and lithium (Li) atoms, respectively

We studied the Li diffusion route by moving a lithium atom along the axis of the tube. The systems with Li atoms around the tube ends have much higher total energy than those on the inner or outer surface of the tube. This suggests that Li prefers to move across the CNTs wall and toward the direction of the open ends of CNT in both isolated 4×4 CNTs and NT-TiO₂/CNTs systems, as shown in Figure 8a-b. Figure 8c shows the energy diffusion barriers of isolated CNTs are 1.21 and 1.82 eV for the Li-interior and exterior surfaces of CNTs, respectively. In the case of NT-TiO₂/CNTs, the energy barrier of Li-CNTs interior is 0.69 eV, while lithium diffusing above the outer of CNTs should overcome a slightly higher energy barrier of 0.90 eV. The energy barrier for Li inside CNTs is lower than the CNTs out sites, matching well with the other theoretical study [57]. NT-TiO₂/CNTs in interior and exterior Li adsorption sites have lower energy barriers than the isolated system of CNTs. It demonstrated that the functionalization of NT-TiO₂ can enhance the performance and the rate of electron transfer of Li diffusion, which agrees with our experiment.

Table 2. Summary of the Li-CNTs distance in pristine CNTs and NT-TiO $_2$ /CNTs system. d_{in} and d_{ex} are described for the distance between Li adsorbed position inside (Li-interior) and outside (Li-exterior) surface of CNTs and the centroid of the nearest corresponding hexagonal ring of CNTs, respectively

	Li-in	terior	Li-exterior		
	d _{in} / nm	E _{ads} / eV	d _{in} / nm	E_{ads} / eV	
CNTs	0.0179	-1.42	0.0174	-1.67	
NT-TiO ₂ /CNTs	0.0176	-1.66	0.0174	-1.74	

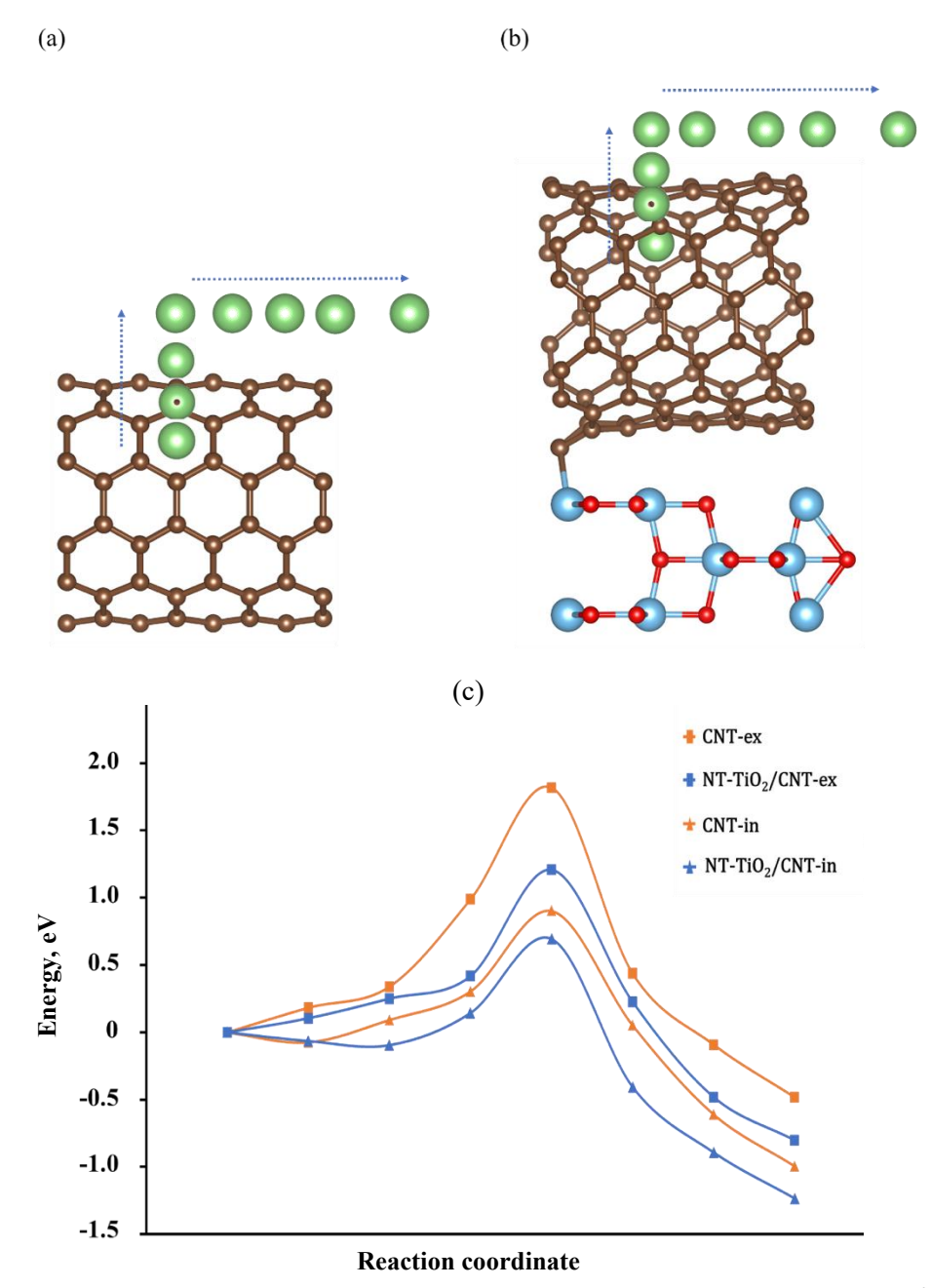


Figure 8. The most stable diffusion paths of Li via 6 transition steps for (a) CNT, (b) NT-TiO₂/CNTs. (c) The profile energy barrier of Li diffusion for CNTs and NT-TiO₂/CNTs with the interior and exterior Li adsorption

Conclusions

In conclusion, we have successfully designed the composites of nanotube structure TiO₂ with CNTs *via* a hydrothermal route. A high-performance supercapattery was developed and tested, featuring an NT-TiO₂/CNTs anode and a coconut-shell-derived AC cathode. The results indicate that the synergistic effect of well-dispersed NT-TiO₂ structure and high conductive CNTs network can improve hybrid capacitors' energy and power density through the short Li-ion diffusion paths and the quick electron transfer. The NT-TiO₂/CNTs-1||AC asymmetric cell displayed high energy density versus power density (48.9 *vs.* 1667 W kg⁻¹) at current rate 1 A g⁻¹ and superior cycle stability at 10 A g⁻¹ with capacitance retention of nearly 85 % after 5000 cycles. The DFT calculations provide two possible interior and exterior Li absorbed on CNTs and NT-TiO₂/CNTs. The energy diffusion barrier of Li at the inside and outside surfaces of isolated CNTs are computed at 1.21 and 1.82 eV, respectively. Besides that, the NT-TiO₂/CNTs also proved that the Li-interior diffusion energetically

is more favorable than that of Li-exterior, with a lower energy barrier of 0.21 eV. The Li diffusion energy barrier of Li located on the inside surface of isolated CNTs and NT-TiO $_2$ /CNTs are 1.21 and 0.69 eV, respectively. Our experiment and theoretical results demonstrated that NT-TiO $_2$ is promising to enhance the electron transfer rate and Li diffusion of isolated CNTs.

Supplementary material: Additional data are available electronically on article page of the journal's website: https://pub.iapchem.org/ojs/index.php/JESE/article/view/2451, or from the corresponding author upon request.

Data availability: The data supporting the findings of this study can be obtained from the corresponding author upon request.

Declaration of competing Interest: The authors have stated that they have no financial interests or personal connections that might have impacted the results presented in this paper.

Acknowledgments: This work was financially supported by the Vietnam Academy of Science and Technology (VAST) under the grant number VAST07.01/23-24.

Tang T.T. Nguyen, Nguyet N.T. Pham and Nam T. Pha have contributed equally

References

- [1] M. Armand, J.-M. Tarascon, Building better batteries, *Nature* **451** (2008) 652-657. http://dx.doi.org/10.1038/451652a
- [2] J.-M. Tarascon, M. Armand, Issues and challenges facing rechargeable lithium batteries, *Nature* **414** (2001) 359-367. https://doi.org/10.1038/35104644
- [3] V. Etacheri, R. Marom, R. Elazari, G. Salitra, D. Aurbach, Challenges in the development of advanced Li-ion batteries: a review, *Energy & Environmental Science* **4(9)** (2011) 3243-3262. https://doi.org/10.1039/C1EE01598B
- [4] A. Borenstein, O. Hanna, R. Attias, S. Luski, T. Brousse, D. Aurbach, Carbon-based composite materials for supercapacitor electrodes: a review, *Journal of Materials Chemistry A* **5(25)** (2017) 12653-12672. https://doi.org/10.1039/C7TA00863E
- [5] C. C. Raj, R. Prasanth, Advent of TiO₂ Nanotubes as Supercapacitor Electrode, *Journal of The Electrochemical Society* **165(9)** (2018) E345-E358. https://doi.org/10.1149/2.0561809jes
- [6] G. Z. Chen, Supercapacitor and supercapattery as emerging electrochemical energy stores. International Materials Reviews 62(4) (2017) 173-202. https://doi.org/10.1080/09506608.2016.1240914
- [7] T. M. David, T. Mathews, Recent Advances in Hybrid Supercapacitors, *In Metal, Metal-Oxides and Metal Sulfides for Batteries, Fuel Cells, Solar Cells, Photocatalysis and Health Sensors* **62** (2021) 75-113. https://doi.org/10.1007/978-3-030-63791-0_3
- [8] P. Lamba, P. Singh, P. Singh, P. Singh, Bharti; A. Kumar, M. Gupta, Y. Kumar, Recent advancements in supercapacitors based on different electrode materials: Classifications, synthesis methods and comparative performance, *Journal of Energy Storage* **48** (2022) 103871. https://doi.org/10.1016/j.est.2021.103871
- [9] X. Lu, G. Wang, T. Zhai, M. Yu, J. Gan, Y. Tong, Y. Li, Hydrogenated TiO2 Nanotube Arrays for Supercapacitors, *Nano Letters* **12(3)** (2012) 1690-1696. https://doi.org/10.1021/nl300173j
- [10] Poonam, K. Sharma, A. Arora, S. K. Tripathi, Review of supercapacitors: Materials and devices, *Journal of Energy Storage* 21 (2019) 801-825.
 https://doi.org/10.1016/j.est.2019.01.010
- [11] F. Shi, L. Li, X. L. Wang, C. D. Gu, J. P. Tu, Metal oxide-hydroxide based materials for supercapacitor, RSC Advances 4 (79) (2014) 41910-41921. https://doi.org/10.1039/C4RA06136E

- [12] F. Naeem, S. Naeem, Y. Zhao, D. Wang, J. Zhang, Y. Mei, G. Huang, TiO2 Nanomembranes Fabricated by Atomic Layer Deposition for Supercapacitor Electrode with Enhanced Capacitance, *Nanoscale Research Letters* **14(1)** (2019) 92. https://doi.org/10.1186/s11671-019-2912-3
- [13] Q. Wang, Z. H. Wen, J. H. Li, A Hybrid Supercapacitor Fabricated with a Carbon Nanotube Cathode and a TiO2–B Nanowire Anode, *Advanced Functional Materials* **16(16)** (2006) 2141-2146. https://doi.org/10.1002/adfm.200500937
- [14] I. Heng, F. W. Low, C. W. Lai, J. C. Juan, N. Amin, S. K. Tiong, High performance supercapattery with rGO/TiO2 nanocomposites anode and activated carbon cathode, *Journal of Alloys and Compounds* **796** (2019) 13-24. https://doi.org/10.1016/j.jallcom.2019.04.347
- [15] S. M. Benoy, M. Pandey, D. Bhattacharjya, B. K. Saikia, Recent trends in supercapacitor-battery hybrid energy storage devices based on carbon materials, *Journal of Energy Storage* **52** (2022) 104938. https://doi.org/10.1016/j.est.2022.104938
- [16] S. Saini, P. Chand, A. Joshi, Biomass derived carbon for supercapacitor applications: Review, *Journal of Energy Storage* **39** (2021) 102646. https://doi.org/10.1016/j.est.2021.102646
- [17] L. T. N. Huynh, T. N. Pham, T. H. Nguyen, V. H. Le, T. T. Nguyen, T. D. K. Nguyen, T. N. Tran, P. A. V. Ho, T. T. Co, T. T. T. Nguyen, T. K. A. Vo, T. H. Nguyen, T. T. Vu, V. M. Luong, H. Uyama, G. V. Pham, T. Hoang, D. L. Tran, Coconut shell-derived activated carbon and carbon nanotubes composite: a promising candidate for capacitive deionization electrode, *Synthetic Metals* 265 (2020) 116415. https://doi.org/10.1016/j.synthmet.2020.116415
- [18] F. Barzegar, A. A. Khaleed, F. U. Ugbo, K. O. Oyeniran, D. Y. Momodu, A. Bello, J. K. Dangbegnon, N. Manyala, Cycling and floating performance of symmetric supercapacitor derived from coconut shell biomass, *AIP Advances* **6(11)** (2016) 115306. https://doi.org/10.1063/1.4967348
- [19] J. Mi, X. R. Wang, R. J. Fan, W. H. Qu, W. C. Li, Coconut-Shell-Based Porous Carbons with a Tunable Micro/Mesopore Ratio for High-Performance Supercapacitors, *Energy & Fuels* **26(8)** (2012) 5321-5329. https://doi.org/10.1021/ef3009234
- [20] G. Kresse, J. Furthmüller, Efficiency of ab-initio total energy calculations for metals and semiconductors using a plane-wave basis set, *Computational Materials Science* **6(1)** (1996) 15-50. https://doi.org/10.1016/0927-0256(96)00008-0
- [21] G. Kresse, J. Furthmüller, Efficient iterative schemes for ab initio total-energy calculations using a plane-wave basis set, *Physical Review B* **54(16)** (1996) 11169. https://doi.org/10.1103/PhysRevB.54.11169
- [22] P. E. Blöchl, Projector augmented-wave method, *Physical Review B* **50** (1994) 17953. https://doi.org/10.1103/PhysRevB.50.17953
- [23] G. Kresse, D. Joubert, From ultrasoft pseudopotentials to the projector augmented-wave method, *Physical review B* **59(3)** (1999) 1758. https://doi.org/10.1103/PhysRevB.59.1758
- [24] J. P. Perdew, K. Burke, M. Ernzerhof, Generalized gradient approximation made simple, *Physical Review Letters* **77(18)** (1996) 3865. https://doi.org/10.1103/PhysRevLett.77.3865
- [25] J. P. Perdew, J. A. Chevary, S. H. Vosko, K. A. Jackson, M. R. Pederson, D. J. Singh, C. Fiolhais, Atoms, molecules, solids, and surfaces: Applications of the generalized gradient approximation for exchange and correlation, *Physical Review B* 46(11) (1992) 6671. https://doi.org/10.1103/PhysRevB.46.6671
- [26] B. Hammer, L. B. Hansen, J. K. Nørskov, Improved adsorption energetics within density-functional theory using revised Perdew-Burke-Ernzerhof functionals, *Physical Review B* **59(11)** (1999) 7413. https://doi.org/10.1103/PhysRevB.59.7413
- [27] M. Ernzerhof, G. E. Scuseria, Assessment of the Perdew–Burke–Ernzerhof exchange-correlation functional, *The Journal of Chemical Physics* 110(11) (1999) 5029-5036. https://doi.org/10.1063/1.478401



- [28] N. N. Pham, K. H. Kim, B. Han, S. G. Lee, Theoretical Investigation of the Active Sites in N-Doped Graphene Bilayer for the Oxygen Reduction Reaction in Alkaline Media in PEMFCs, *The Journal of Physical Chemistry C* **126(11)** (2022) 5863-5872. https://doi.org/10.1021/acs.jpcc.1c09657
- [29] N. N. Pham, S. G. Kang, Y. A. Son, S. Y. Lee, H. J. Kim, S. G. Lee, Electrochemical Oxygen-Reduction Activity and Carbon Monoxide Tolerance of Iron Phthalocyanine Functionalized with Graphene Quantum Dots: A Density Functional Theory Approach, *The Journal of Physical Chemistry C* **123(45)** (2019) 27483-27491. https://doi.org/10.1021/acs.jpcc.9b06750
- [30] T. V. Tam, S. G. Kang, M. H. Kim, S. G. Lee, S. H. Hur, J. S. Chung, W. M. Choi, Novel graphene hydrogel/B-doped graphene quantum dots composites as trifunctional electrocatalysts for Zn– air batteries and overall water splitting, *Advanced Energy Materials* **9(26)** (2019) 1900945. https://doi.org/10.1002/aenm.201900945
- [31] J. H. Lee, S. H. Kwon, S. Kwon, M. Cho, K. H. Kim, T. H. Han, S. G. Lee, Tunable electronic properties of nitrogen and sulfur doped graphene: Density functional theory approach, *Nanomaterials* **9(2)** (2019) 268. https://doi.org/10.3390/nano9020268
- [32] N. N. Pham, J. S. Park, H. T. Kim, H. J. Kim, Y. A. Son, S. G. Kang, S. G. Lee, Catalytic performance of graphene quantum dot supported manganese phthalocyanine for efficient oxygen reduction: density functional theory approach, *New Journal of Chemistry* **43(1)** (2019) 348-355. https://doi.org/10.1039/C8NJ05093G
- [33] H. J. Kwon, Y. Kwon, T. Kim, Y. Jung, S. Lee, M. Cho, S. Kwon, Enhanced competitive adsorption of CO₂ and H₂ on graphyne: A density functional theory study, *AIP Advances* **7(12)** (2017) 125013. https://doi.org/10.1063/1.5006839
- [34] H. W. Lee, H. S. Moon, J. Hur, I. T. Kim, M. S. Park, J. M. Yun, K. H. Kim, S. G. Lee, Mechanism of sodium adsorption on N-doped graphene nanoribbons for sodium ion battery applications: A density functional theory approach, *Carbon* **119** (2017) 492-501. https://doi.org/10.1016/j.carbon.2017.04.033
- [35] N. N. Pham, Nitrogen doping effects on the physical and chemical properties of bilayer graphdiyne: A density functional theory approach, *Applied Surface Science Advances* **11** (2022) 100301. https://doi.org/10.1016/j.apsadv.2022.100301
- [36] O. L. Li, N. N. Pham, J. Kim, H. Choi, D. H. Lee, Y. Yang, W. Yao, Y. R. Cho, S. G. Lee, Insights on boosting oxygen evolution reaction performance via boron incorporation into nitrogendoped carbon electrocatalysts, *Applied Surface Science* **528** (2020) 146979. https://doi.org/10.1016/j.apsusc.2020.146979
- [37] N. N. Pham, H. Guo, S. G. Lee, Influence of phosphorus-doped bilayer graphene configuration on the oxygen reduction reaction in acidic solution, *Carbon* **220** (2023) 118012. https://doi.org/10.1016/j.carbon.2023.118012
- [38] S. Grimme, J. Antony, S. Ehrlich, H. Krieg, A consistent and accurate ab initio parametrization of density functional dispersion correction (DFT-D) for the 94 elements H-Pu, *The Journal of Chemical Physics* **132(15)** (2010) 154104. https://doi.org/10.1063/1.3382344
- [39] H. J. Monkhorst, J. D. Pack, Special points for Brillouin-zone integrations, *Physical Review B* 13(12) (1976) 5188. https://doi.org/10.1103/PhysRevB.13.5188
- [40] S. L. Dudarev, G. A. Botton, S. Y. Savrasov, C. Humphreys, A. P. Sutton, Electron-energy-loss spectra and the structural stability of nickel oxide: An LSDA+U study, *Physical Review B* **57(3)** (1998) 1505. https://doi.org/10.1103/PhysRevB.57.1505
- [41] R. Long, N. J. English, O. V. Prezhdo, Photo-induced charge separation across the graphene— TiO2 interface is faster than energy losses: a time-domain ab initio analysis, *Journal of the American Chemical Society* **134(34)** (2012) 14238-14248. https://doi.org/10.1021/ja3063953
- [42] A. Du, Y. H. Ng, N. J. Bell, Z. Zhu, R. Amal, S. C. Smith, Hybrid graphene/titania nanocomposite: interface charge transfer, hole doping, and sensitization for visible light

- response, *The Journal of Physical Chemistry Letters* **2(8)** (2011) 894-899. https://doi.org/10.1021/jz2002698
- [43] S. Grimme, Semiempirical GGA-type density functional constructed with a long-range dispersion correction, *Journal of Computational Chemistry* **27(15)** (2006) 1787-1799. https://doi.org/10.1002/jcc.20495
- [44] H. Jónsson, G. Mills, K. W. Jacobsen, Nudged elastic band method for finding minimum energy paths of transitions. In Classical and quantum dynamics in condensed phase simulations, *World Scientific* (1998) 385-404. https://doi.org/10.1142/9789812839664 0016
- [45] J. Xu, C. Jia, B. Cao, W. F. Zhang, Electrochemical properties of anatase TiO2 nanotubes as an anode material for lithium-ion batteries, *Electrochimica Acta* **52(28)** (2007) 8044-8047. https://doi.org/10.1016/j.electacta.2007.06.077
- [46] L. F. Que, F. D. Yu, Z. B. Wang, D. M. Gu, Pseudocapacitance of TiO_{2-x}/CNT Anodes for High-Performance Quasi-Solid-State Li-Ion and Na-Ion Capacitors, *Small* **14(17)** (2018) 1704508. https://doi.org/10.1002/smll.201704508
- [47] A. Moya, A. Cherevan, S. Marchesan, P. Gebhardt, M. Prato, D. Eder, J. J. Vilatela, Oxygen vacancies and interfaces enhancing photocatalytic hydrogen production in mesoporous CNT/TiO2 hybrids, *Applied Catalysis B: Environmental* **179** (2015) 574-582. https://doi.org/10.1016/j.apcatb.2015.05.052
- [48] T. Ohsaka, F. Izumi, Y. Fujiki, Raman spectrum of anatase, TiO₂, *Journal of Raman Spectroscopy* **7(6)** (1978) 321-324. https://doi.org/10.1002/jrs.1250070606
- [49] A. V. Abega, H. M. Ngomo, I. Nongwe, H. E. Mukaya, P. M. A. Kouoh Sone, X. Yangkou Mbianda, Easy and convenient synthesis of CNT/TiO₂ nanohybrid by in-surface oxidation of Ti³⁺ ions and application in the photocatalytic degradation of organic contaminants in water, *Synthetic Metals* **251** (2019) 1-14. https://doi.org/10.1016/j.synthmet.2019.03.012
- [50] L. T. N. Huynh, H. H. A. Nguyen, T. T. D. Tran, T. T. T. Nguyen, T. M. A. Nguyen, T. H. La, V. M. Tran, M. L. P. Le, Electrode Composite LiFePO₄@Carbon: Structure and Electrochemical Performances, *Journal of Nanomaterials* 2019 (2019) 464920 https://doi.org/10.1155/2019/2464920
- [51] V. H. Pham, T. D. Nguyen-Phan, X. Tong, B. Rajagopalan, J. S. Chung, J. H. Dickerson, Hydrogenated TiO2@reduced graphene oxide sandwich-like nanosheets for high voltage supercapacitor applications, *Carbon* **126** (2018) 135-144. https://doi.org/10.1016/j.carbon.2017.10.026
- [52] A. Elmouwahidi, E. Bailón-García, J. Castelo-Quibén, A. F. Pérez-Cadenas, F. J. Maldonado-Hódar, F. Carrasco-Marín, Carbon—TiO2 composites as high-performance supercapacitor electrodes: synergistic effect between carbon and metal oxide phases, *Journal of Materials Chemistry A* **6(2)** (2018) 633-644. https://doi.org/10.1039/C7TA08023A
- [53] J. H. Kim, H. J. Choi, H. K. Kim, S. H. Lee, Y. H. Lee, A hybrid supercapacitor fabricated with an activated carbon as cathode and an urchin-like TiO₂ as anode, *International Journal of Hydrogen Energy* **41(31)** (2016) 13549-13556. https://doi.org/10.1016/j.ijhydene.2016.06.018
- [54] S. Yang, Y. Li, J. Sun, B. Cao, Laser induced oxygen-deficient TiO2/graphene hybrid for high-performance supercapacitor, *Journal of Power Sources* **431** (2019) 220-225. https://doi.org/10.1016/j.jpowsour.2019.05.016
- [55] S. Dargouthi, C. Minot, B. Tangour, Structural study of TiO2 nanotube based to the (101) anatase surface, *Superlattices and Microstructures* **102** (2017) 307-313. https://doi.org/10.1016/j.spmi.2016.12.058
- [56] G. Ramos-Sanchez, G. Chen, A. Harutyunyan, P. Balbuena, Theoretical and experimental investigations of the Li storage capacity in single-walled carbon nanotube bundles, RSC Advances 6(33) (2016) 27260-27266. https://doi.org/10.1039/C5RA27225D



[57] G. Qi, T. Rabczuk, Ab-initio investigation of lithium adsorption on short carbon nanotubes considering effects of the tube length, *Carbon* 155 (2019) 727-733. https://doi.org/10.1016/j.carbon.2019.08.027

©2024 by the authors; licensee IAPC, Zagreb, Croatia. This article is an open-access article distributed under the terms and conditions of the Creative Commons Attribution license (https://creativecommons.org/licenses/by/4.0/)



Open Access :: ISSN 1847-9286 www.jESE-online.org

Original scientific paper

Comparative voltammetric determination of ascorbic acid at three different carbon electrodes: application of carbon screenprinted electrode for citrus fruits analysis

Talytha Rodrigues Gaspari Paina¹, Izabel Cristina Eleotério¹, Nelson Ramos Stradiotto² and Marcelo Firmino de Oliveira¹,⊠

¹Grupo de Eletroquímica, Eletroanalítica e Química Forense (GEEQFor), Departamento de Química, Faculdade de Filosofia, Ciências e Letras de Ribeirão Preto, Universidade de São Paulo (DQ/FFCLRP/USP), Avenida Bandeirantes, 3900, Bairro Monte Alegre, Ribeirão Preto, SP, CEP 14040-901, Brazi

²Instituto de Química - Universidade Estadual Paulista (IQ-UNESP). Av. Prof. Francisco Degni, 55 - Jardim Quitandinha, Araraquara, SP, CEP 14800-900, Brazil

Corresponding author: [™] marcelex@usp.br

Received: January 29, 2024; Accepted: February 22, 2025; Published: March 3, 2025

Abstract

Determining the vitamin C (ascorbic acid) content in citrus fruits is crucial for dietary and nutritional considerations. Traditional analytical methods for ascorbic acid analysis often involve expensive and less portable electrodes, limiting their practicality in food analysis. This study focuses on the quantification of ascorbic acid in citrus fruits using a cost-effective and portable carbon screen-printed electrode. The efficiency of these electrodes was assessed using cyclic voltammetry and linear sweep voltammetry due to the irreversible oxidation behavior of ascorbic acid. A comparative analysis was performed with glassy carbon, carbon paste, and commercial carbon screen-printed electrodes, focusing on sensitivity variations based on analyte concentration and scanning rate. The carbon screenprinted electrode demonstrated superior sensitivity to the other electrodes tested, establishing it as a practical alternative for ascorbic acid analysis in citrus fruits. This study employed the standard addition method in conjunction with linear sweep voltammetry to accurately determine ascorbic acid concentrations in pear-orange, Tahiti lemon, and Ponkan tangerine samples. The obtained values were cross-referenced with existing literature data, enhancing our understanding of vitamin C content in these citrus fruits. Overall, this research highlights the potential of the carbon screen-printed electrode as a valuable tool for vitamin C analysis, offering new insights into food science and nutrition.

Keywords

Vitamin C; carbon electrodes; voltammetry techniques; standard addition method; juice samples

Introduction

Vitamin C, also known as ascorbic acid (AA), is a water-soluble essential nutrient with profound physiological significance. It assumes the form of the biologically active L-enantiomer, L-ascorbic acid, featuring a γ -lactone structure. Under physiological conditions, ascorbic acid exhibits a hexanoic sugar acid structure and maintains its ionic state as the ascorbate anion due to the presence of two dissociable protons, characterized by pKa values of 4.17 and 11.57 [1].

L-ascorbic acid readily oxidizes, forming the basis for its electrochemical detection. It establishes an irreversible redox pair with dehydroascorbic acid [1]. The acidity of AA is influenced by the conjugation of the carbonyl on carbon 1, notably enhancing the acidity of the hydroxyl on carbon 3 (p $K_a = 4.17$), while the hydroxyl on carbon 2, as part of an enol, exhibits equivalent acidity with a pKa of 11.57 [2-4]

Vitamin C has diverse properties, including its redox capabilities, which play a crucial role in electrochemical, biochemical, and pharmacological systems. It serves as a potent antioxidant, combating diseases caused by free radicals, such as heart disease [1]. Additionally, it contributes to iron absorption, collagen synthesis for cell growth and regeneration, immune response activation, wound healing, osteogenesis, and the maintenance of capillaries, bones, and teeth. Notably, humans, along with certain primates and guinea pigs, rely on dietary intake due to a genetic mutation that prevents the synthesis of ascorbate (the anionic portion of AA).

Given the paramount importance of vitamin C, various methods are employed to detect and quantify it, including spectroscopy, chromatography, and electrochemistry. In electrochemistry, carbon materials are highly exploited as electrode surfaces. This is due to the fact that, in addition to being chemically inert and low-cost compared to other materials, carbon materials also have a low background current and a wide potential window.

The glassy carbon electrode (GCE), sometimes referred to as a "conventional" electrode, has large overpotentials for oxygen and hydrogen evolution and is chemically stable. Compared to the carbon paste electrode (CPE), for example, it has, according to studies, much higher currents, even though both electrodes have the same surface área [1]. However, the CPE has a significantly lower background current, which makes it superior to glassy carbon from the point of view of background signal characteristics. In addition, it offers few beneficial properties, including repeatability, stability, and surface renewability, and has been explored by several authors [5,6], who have proven its effectiveness in both bare and modified forms.

However, while traditional electrochemical techniques with GCE and CPE offer high sensitivity, commercial carbon screen-printed electrodes (C-SPEs) have emerged as a more practical, easy-to-use, cost-effective, and efficient alternative. Recent studies, including [7], have demonstrated superior current responses C-SPEs compared to unmodified GCE, as well as its practicality, saving the effort, time and materials spent preparing a good carbon paste to be used as a CPE. Furthermore, the versatility of screen-printed electrodes has led to their increased application in analyzing a wide range of samples, simplifying the detection process by requiring only a solubilized matrix drop, such as powder or tablet [7].

Therefore, this study aims to compare the oxidation behavior of ascorbic acid using three carbon electrodes shown in Figure 1, *i.e.* GCE, CPE and C-SPE, highlighting their respective advantages and disadvantages. Citrus fruits, including pear-orange, Tahiti lemon, and Ponkan tangerine, served as the sample matrix, and the analysis employed cyclic voltammetry (CV) and linear sweep voltammetry (LSV) techniques, using C-SPE as the working electrode after proving its efficiency compared to other carbon electrodes.

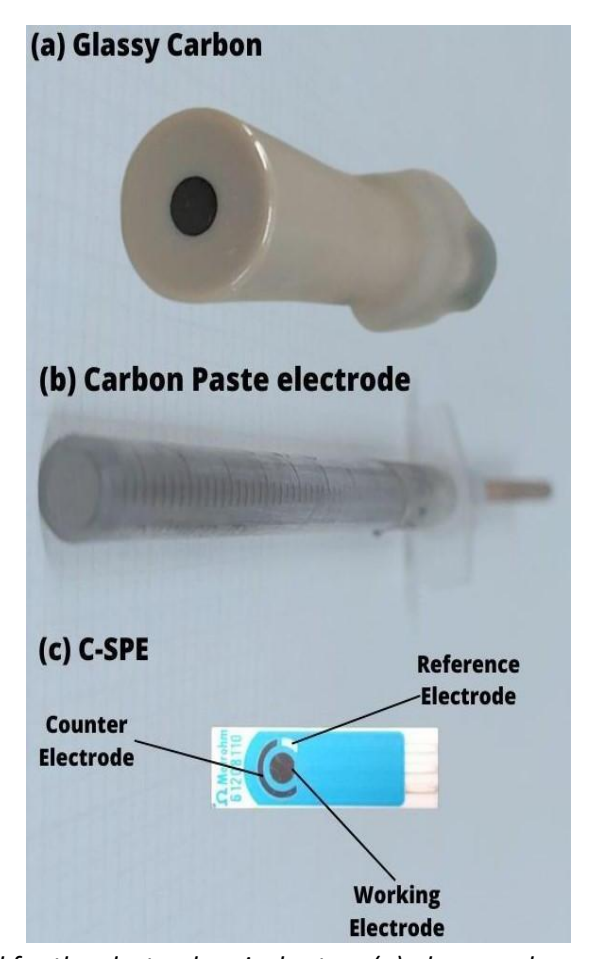


Figure 1. Electrodes used for the electrochemical setup: (a) glassy carbon electrode; (b) carbon paste electrode; (c) carbon screen-printed electrode wire as working electrode, reference electrode and auxiliary electrode

Experimental

Electrochemical setup

The experiments employed a glass cell equipped with three electrodes, a Metrohm® saturated Ag/AgCl/KCl, 3 mol L⁻¹ reference electrode, a platinum wire auxiliary electrode, and GCE, CPE, and C-SPE as working electrodes, each with a physical area of 0.0707 cm². The electrolyte solution, prepared in-house using Sigma Aldrich products, consisted of a 0.1 mol L⁻¹ buffer solution of potassium phosphate monobasic (99 % purity) and sodium phosphate dibasic heptahydrate (99 % purity), adjusted to pH 5.5 using a Mettler Toledo digital bench pH-meter, which has been used in other studies that have proven its effectiveness, due to the presence of ionizable hydrogens in the structure of the ascorbic acid molecule [2]. The active surface area of GCE, CPE, and C-SPE was calculated using the Randles-Ševčik equation [8] with 5 mmol L⁻¹ K₃[Fe(CN)₆] in 0.5 mol L⁻¹ KCl, at scan rates ranging from 5 to 200 mV s⁻¹, resulting in areas of 0.027, 0.044 and 0.063 cm², respectively.

Carbon paste electrode preparation

The CPE was created by blending 0.35 g of graphite powder (Fisher Scientific, 99.9 % purity) with 0.15 g of paraffin (Sigma Aldrich) at a 7:3 weight ratio. The mixture was heated in a mortar over a heating mantle at approximately 100 °C until it formed a paste, which took about 10 minutes. This paste was then packed into a cylindrical plastic tube resembling a syringe and compressed using a copper rod. Finally, the electrode surface was polished using abrasive paper, resulting in a 3 mm diameter electrode.

Standard ascorbic acid preparation

The chemical structure of AA is drawn in Figure 2a. For the analysis of AA oxidation profiles using carbon working electrodes, a 0.1 mol L⁻¹ AA standard solution was prepared by dissolving 0.4403 g of standard AA (100 % purity) from Sigma-Aldrich in 25 mL of deionized water using a 25 mL flask.

Analysis of standard ascorbic acid with glassy carbon electrode

For standard AA analyses, 100 μ L aliquots of the 0.1 mol L⁻¹ AA solution were sequentially added to 10 mL of 0.1 mol L⁻¹ phosphate buffer (pH 5.5), serving as the electrolyte in an electrochemical cell. The glassy carbon electrode, 3 mm diameter, from Metrohm®, was employed as the working electrode. Cyclic voltammograms were recorded after each 100 μ L AA addition to confirm the irreversibility of the oxidation process. This was done by varying AA concentration at the constant scan rate, and subsequently, the scan rate varied at a constant AA concentration. Experimental conditions for cyclic voltammetry included scanning rates of 50 mV s⁻¹ for concentration analysis (ranging from 0.99 to 4.76 mmol L⁻¹) and 5, 10, 25, 50 and 100 mV s⁻¹ for scan rate analysis, maintaining a fixed final AA concentration of 4.76 mmol L⁻¹. The potential range was set from -0.4 to +0.9 V, with a current scale of 5 mA.

Analysis of standard ascorbic acid with carbon paste electrode

At this stage, five 100 μ L aliquots of the 0.1 mol L⁻¹ AA standard solution were added to 10 mL of 0.1 mol L⁻¹ phosphate buffer, pH 5.5, which acted as the electrolyte in the electrochemical cell, using the CPE as the working electrode. Linear voltammograms were then generated for the addition of 100, 200, 300, 400 and 500 μ L of AA solution. The experimental conditions for the linear sweep voltammetry were a scanning rate of 50 mV s⁻¹ in the concentration variation analysis, which ranged from 0.99 to 4.76 mmol L⁻¹. As for GCE, potential scan rates of 5, 10, 25, 50 and 100 mV s⁻¹ were applied in the rate variation analysis with a fixed final concentration of 4.76 mmol L⁻¹ of the AA standard. The potential range was between -0.2 and +1.5 V, with a current scale of 5 mA.

Analysis of standard ascorbic acid with carbon screen-printed electrode

A 3 mm diameter carbon screen-printed electrode with Metrohm spatented carbon ink was used as a working electrode. To enhance peak quality, larger volumes (ranging from 11 to 15 μ L) of the 0.1 mol L⁻¹AA standard solution were added to a fixed volume of 0.1 mol L⁻¹ phosphate buffer, pH 5.5, to increase the sample concentration in the analysis. Experimental conditions for LSV included potential scanning rates of 50 mV s⁻¹ for concentration analysis (ranging from 23.9 to 30 mmol L⁻¹) and 5, 10, 25, 50 and 100 mV s⁻¹ for the scan rate analysis, maintaining a constant final AA concentration of 30 mmol L⁻¹. The potential range was set between -0.4 and +1.1 V, with a current scale of 5 mA.

Comparison of standard ascorbic acid analysis using three electrodes

First, to carry out the standard ascorbic acid analyses, five 0.5 μ L aliquots of the 0.1 mol L⁻¹ ascorbic acid standard solution were added to a fixed volume of 0.1 mol L⁻¹ phosphate buffer, pH 5.5, which acted as the electrolyte in the electrochemical cell, using C-SPE as the working electrode again. Linear voltammograms were generated with the same concentrations previously calculated for GCE and CPE. Experimental conditions for linear sweep voltammetry included potential scanning rates of 50 mV s⁻¹ for concentration analysis (ranging from 0.99 to 4.76 mmol L⁻¹). The potential range was set between -0.4 and +1.1 V, with a current scale of 5 mA.

Next, to compare the signals obtained from the three electrodes, all with 3 mm diameter, the same AA concentration was utilized for each. Experimental conditions for LSV included fixed AA

concentration (4.76 mmol L^{-1}) for all three electrodes, scan rates of 50 mV s⁻¹, potential range from 0.0 to +1.0 V, and a current scale of 5 mA.

Cyclic voltammetry and linear sweep voltammetry

Cyclic voltammetry and linear sweep voltammetry techniques were chosen to study the oxidation of ascorbic acid in standard solutions and citrus fruits due to the simplicity of these two techniques, which were sufficient for the qualitative and quantitative analysis of the analyte. Metrohm® AUTOLAB 128N potentiostat coupled to a computer was used for data acquisition.

Preparation and analysis of ascorbic acid in citrus fruits

Fruit juice was extracted using a manual juicer, filtered, and then combined with phosphate buffer solution pH 5.5 (0.1 mol L^{-1}). An 18 μ L aliquot of the mixture was added to the working electrode region of the C-SPE for AA determination using the standard addition method. Different standard AA solutions (0.05 mol L^{-1} for pear-orange, 0.1 mol L^{-1} for Tahiti lemon, and 0.05 mol L^{-1} for Ponkan tangerine) were employed. LSV was conducted with a potential range from -0.4 to +1.2 V, a scan rate of 50 mV s⁻¹, and a current scale of 5 mA.

Results and discussion

Analysis of standard ascorbic acid using GCE

The AA oxidation profile at GCE was analyzed as the concentration varied. Figure 2b shows that in higher sample concentrations, the anodic current at +0.6 V rises proportionally to electrolyte concentration, which is in line with theoretical expectations [9]. The potential shift observed corresponds to concentration changes, affirming the irreversible nature of the AA oxidation process. This data was used to construct a concentration-current graph.

In this study, the graph depicts a linear relationship between current and AA concentration, which aligns with the expected irreversibility of the reaction [10]. The linear fit equation, y = a + bx, provides the angular ($b = 8.72 \,\mu\text{A}$ mmol L⁻¹) and linear ($a = 6.27 \,\mu\text{A}$) coefficients. AA signal increased with concentration, resulting in one well-defined linear range, as displayed in Figure 2c.

The high Pearson correlation coefficient (r = 0.953) signifies a strong positive correlation between analyte concentration and current intensity, indicating their direct proportionality. Finally, the limit of detection (LoD), representing the minimum detectable concentration, can be calculated using the equation proposed by [9]. The limit of detection is calculated using the equation LoD = 3s/m, where 3 is the confidence factor, s represents the standard deviation of the blank, and m stands for the angular coefficient of the analytical curve. By substituting the given values into the equation, the LoD is determined by Equation (1):

LoD =
$$3s/m = (3 \times 5.1 \,\mu\text{A})/(35 \,\mu\text{A}/(4.76 - 0.99) \,\text{mmol L}^{-1}) = 1.64 \,\text{mmol L}^{-1}$$
 (1)

The determined limit of detection (LoD) at GCE of 1.64 mmol L⁻¹ is higher than the initial addition of AA at 0.99 mmol L⁻¹, which indicates that the chosen analyte quantities did not significantly differ from the blank (phosphate buffer solution at pH 5.5). The LoD represents the lowest concentration distinguishable from the electrolyte with a high level of confidence. Consequently, concentrations below the detection limit should be considered less reliable. Specifically at GCE, only the concentration of 0.99 mmol L⁻¹ cannot be readily distinguished from the blank, while concentrations ranging from 1.96 to 4.76 mmol L⁻¹ surpass LoD and are considered valid.

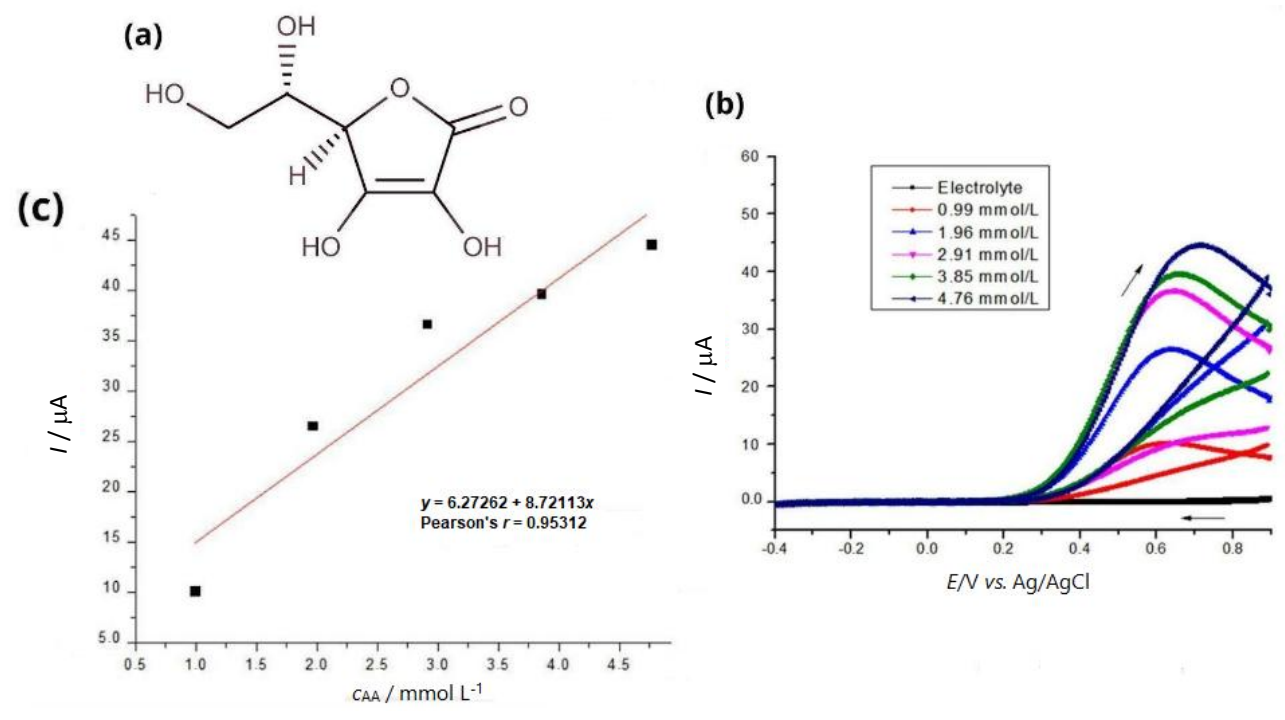


Figure 2. (a) Chemical structure of AA; (b) cyclic voltammograms at 50 mV s⁻¹ of GCE in 0.1 mol L⁻¹ phosphate buffer, pH 5.5, and varying the final AA concentration from 0.99 to 4.76 mmol L⁻¹; (c) linear correlation between peak current and AA concentration

Following this, the oxidation behavior of AA was examined with varying potential scan rates (Figure 3a). The oxidation potential in these voltammograms shifts towards more positive values, surpass-sing +0.6 V (potential associated with the occurrence of anodic current peaks)—as both the scan rate and concentration rise. Additionally, it is evident that the intensity of the anodic peak current escalates with a higher scan rate. Using this data, a relationship between the peak current (i_p) and the square root of the scan rate ($v^{1/2}$) is illustrated in Figure 3b. A closer examination of the variation of peak current with the scan rate shows a linear correlation between the peak current and the square root of the scan rate (r = 0.99). This indicates that the oxidation process occurring on the electrode surface is primarily diffusion-controlled rather than adsorption-controlled—the latter being the alternative possibility. This finding aligns with previous studies [2] that have similarly drawn this conclusion.

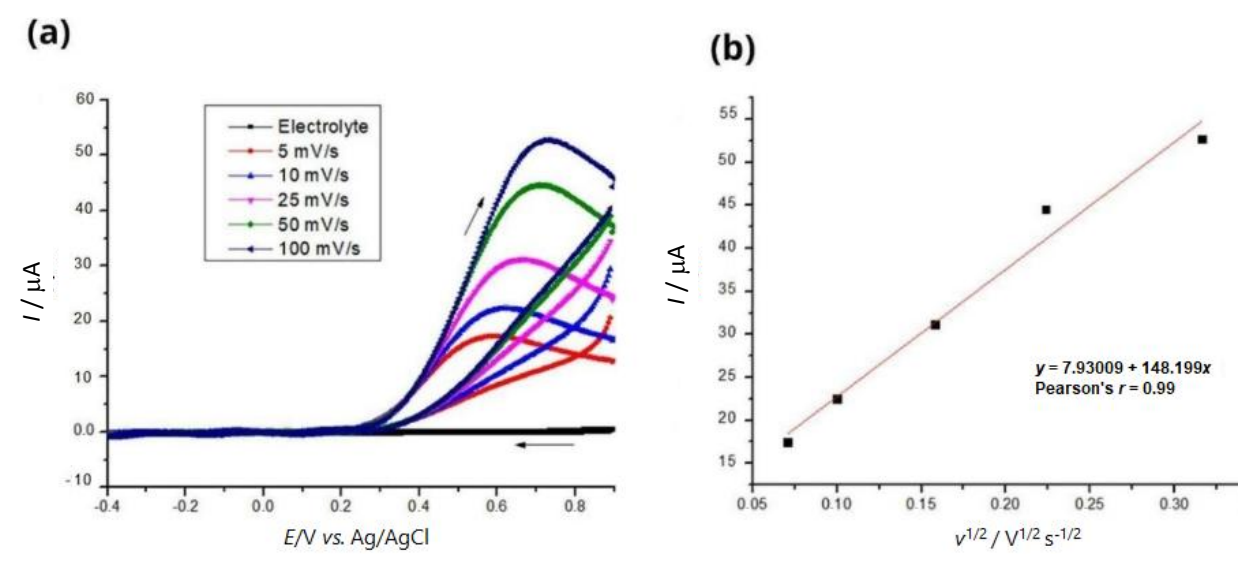


Figure 3. (a) Effect of scan rate on cyclic voltammetric response of GCE in 0.1 mol L^{-1} phosphate buffer, pH 5.5, and final AA concentration of 4.76 mmol L^{-1} ; (b) linear plot of peak current vs. square root of scan rate

Analysis of standard ascorbic acid using CPE

The AA oxidation profile was scrutinized for concentration variations, this time employing the CPE. Similar to the GCE, anodic peaks emerged upon adding aliquots of the AA solution, signifying its oxidation. These peaks are manifested at +0.75 V, denoting the potential at which AA undergoes oxidation, as confirmed by the recorded electron transfer. Notably, there was a slight shift in oxidation potential, transitioning from 0.6 to 0.75 V in comparison to the peaks observed with the GCE. This shift was attributed to the excess of paraffin in the CPE, which acts as a binder, filling the interstitial spaces between the particles and consequently adjusting the AA oxidation reaction to a slightly higher potential. Subsequently, mirroring the procedure with the GCE, a graph correlating current with concentration was constructed using the standard AA (Figure 4a). This graph reaffirms the linear relationship between the current (μ A) and the concentration of AA (mmol L⁻¹) (Figure 4b), as expected for an irreversible reaction [10]. Utilizing the linear fit equation, y = a + bx, we derived the values of b and a, corresponding to the angular and linear coefficients of the line, respectively. These values were b = 14.17 μ A mmol L⁻¹ and a = 14.58 μ A.

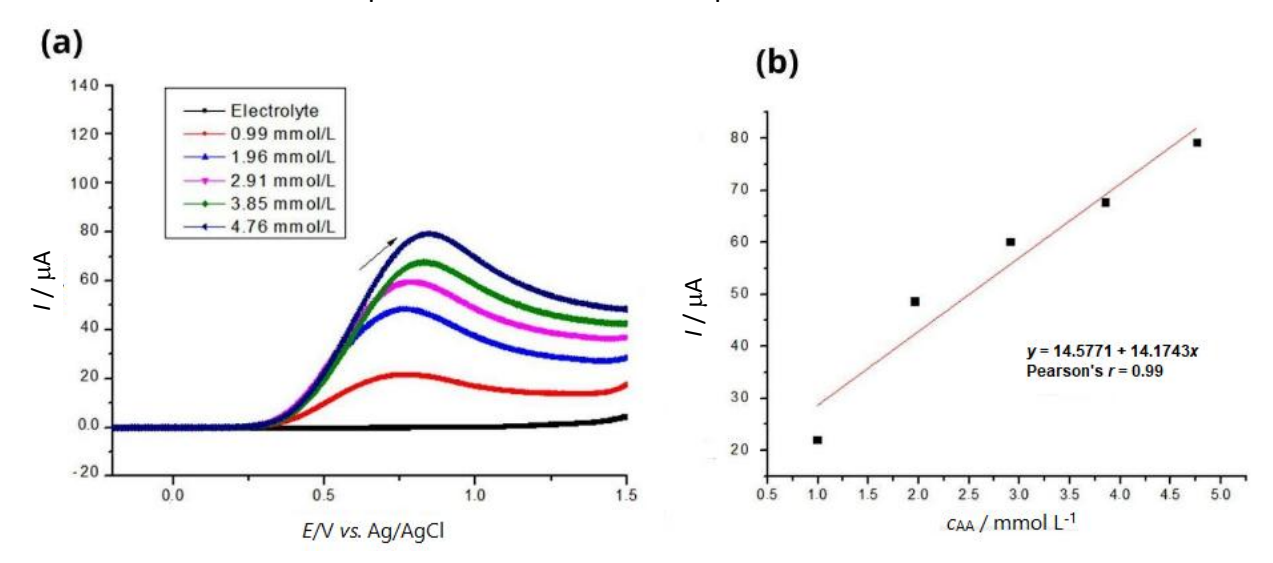


Figure 4. (a) Linear sweep voltammograms (LSV) at 50 mV s⁻¹of CPE in 0.1 mol L⁻¹ phosphate buffer, pH 5.5, and varying the AA final concentration from 0.99 to 4.76 mmol L⁻¹; (b) linear correlation between peak current and AA concentration

As previously mentioned, the closer the correlation coefficient is to 1, the stronger the linearity between the two variables. Consequently, the coefficient determined using the analytical curve, r = 0.97, confirms this linearity and establishes the direct proportionality between electrolyte concentration and current intensity. Finally, the limit of detection (LoD) was calculated by Equation (2):

LoD =
$$3s/m = (3.6.5 \,\mu\text{A})/((60 \,\mu\text{A}/(4.76-0.99) \,\text{mmol}\,\,\text{L}^{-1}) = 1.2 \,\text{mmol}\,\,\text{L}^{-1}$$
 (2)

The determined LoD is 1.2 mmol L^{-1} , which is a value above the AA concentration of the first addition (0.99 mmol L^{-1}) and below the others, demonstrating that the amounts of analytes chosen were significantly different from the blank (electrolyte-phosphate buffer solution pH 5.5), with the exception of the first addition, which is unreliable. Therefore, the results for CPE could be validated only for concentrations between 1.96 and 4.76 mmol L^{-1} .

In the following, the analysis of AA oxidation was extended to varying scan rates, now for the CPE (Figure 5a). This dataset facilitated the creation of linear plots illustrating peak potential against the square root of the scan rate (Figure 5b). From this graph, a direct correlation was evident between the peak current and the square root of the scanning rate (r = 0.987). This indicates that the

oxidation process on the electrode surface primarily follows a diffusion-controlled reaction rather than an adsorption-controlled one. This observation aligns with previous findings using the glassy carbon electrode and is consistent with conclusions drawn in other studies [2].

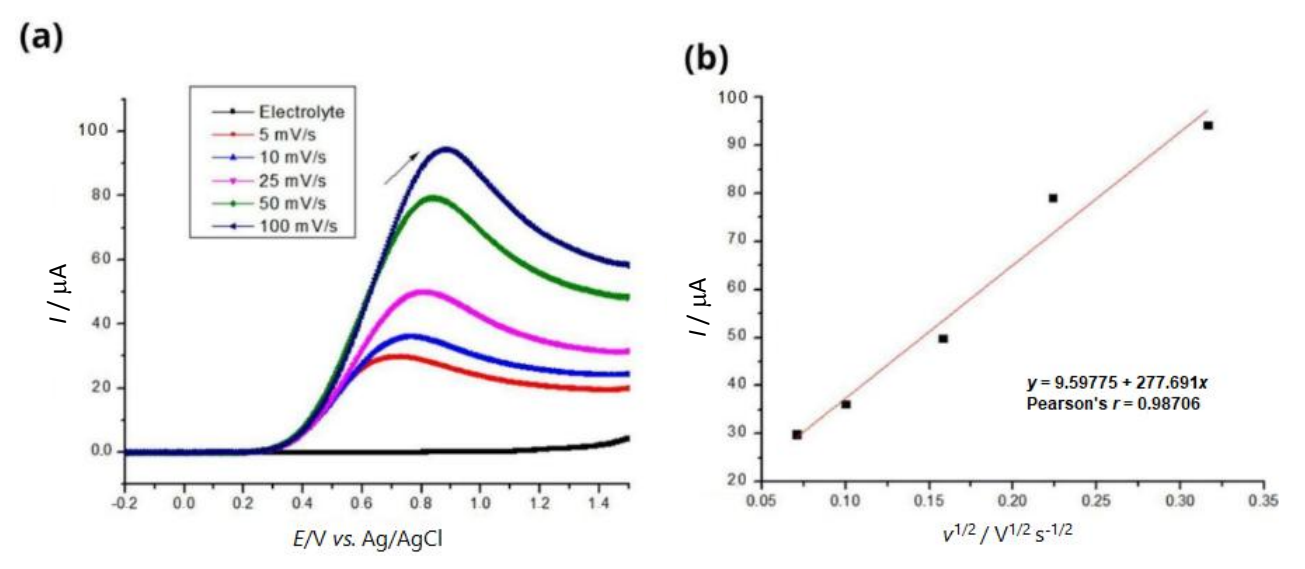


Figure 5. (a) Effect of scan rate (5 to 100 mV s^{-1}) on LSV responses of CPE in 0.1 mol L^{-1} phosphate buffer, pH 5.5, and final AA concentration of 4.76 mmol L^{-1} ; (b) linear plot of peak current vs. square root of scan rate

Analysis of standard ascorbic acid using carbon screen-printed electrode

To compare the three electrodes, an analysis was carried out using standard ascorbic acid at somewhat higher concentrations than those used for GCE and CPE in order to ensure its electrochemical response.

In this phase, the oxidation profile of AA was scrutinized with varying concentrations. With new volumes of standard AA solution, the anodic peaks shifted to a potential of +0.8 V. This shift was attributed to the escalated AA concentrations. Additionally, it was noted that the anodic current surged in tandem with concentration increments. This observation aligns with the previously emphasized principle that conductivity is directly linked to analyte concentration [9].

Upon the completion of the analyses utilizing the standard AA, a graph correlating current to concentration was developed, mirroring the procedure applied to the other electrodes (Figure 6b). Once again, the linearity between peak current (μ A) and the concentration of AA (mmol L⁻¹) was evident [10]. Through the equation derived from the linear fit, y = a + bx, we derived the coefficients b and a. Specifically, the angular and linear coefficients were determined to be b = 16.4118 μ A mmol L⁻¹ and a = -77.7762 μ A, respectively (Figure 6b).

The obtained Pearson correlation coefficient (r = 0.983) from the analytical curve affirms a direct proportionality between the electrolyte concentration and current intensity. Moving on to the calculation of the limit of detection (LoD), a critical parameter for sensitivity, since it is the smallest amount of analyte in the test sample that can be truly distinguished from zero, Equation (3) [9] is applied:

LoD =
$$3s/m = (3.47.9 \,\mu\text{A})/(115 \,\mu\text{A}/(30-23.9) \,\text{mmol L}^{-1}) = 7.63 \,\text{mmol L}^{-1}$$
 (3)

LoD value of 7.63 mmol L⁻¹ is notably lower than the initial AA concentration of 23.9 mmol L⁻¹ introduced, underscoring the robust sensitivity of the printed electrode. This ensures that the selected analyte concentrations were significantly distinct from the blank (electrolyte-phosphate buffer solution at pH 5.5), substantiating the validity of the obtained results.

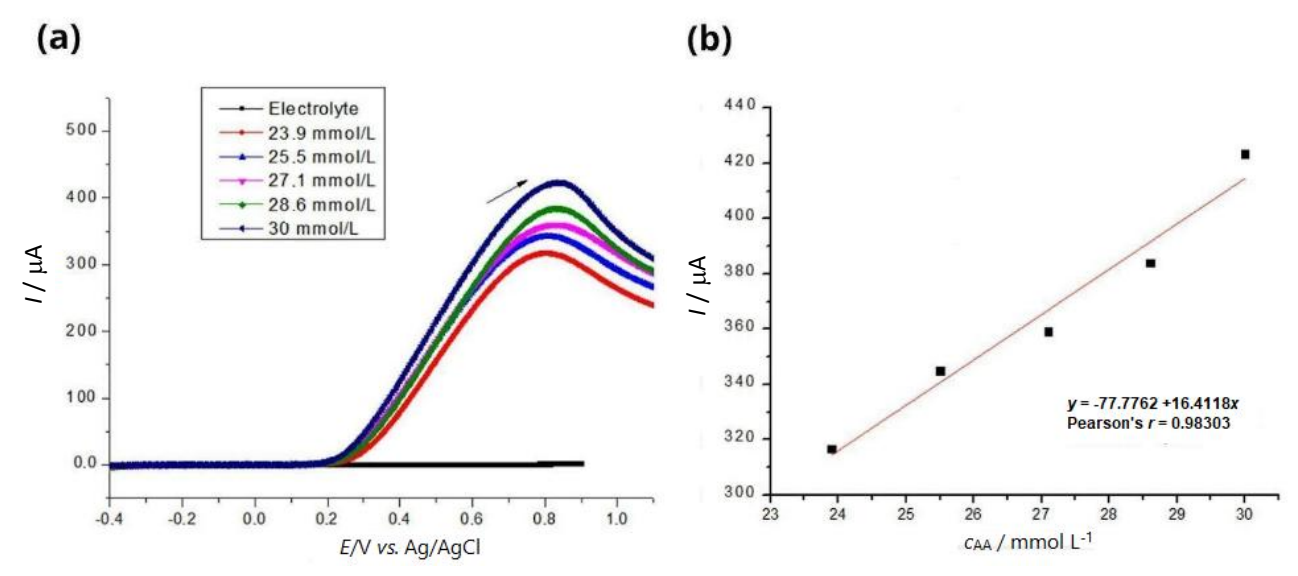


Figure 6. (a) LSV curves at 50 mV s^{-1} of C-SPE in 0.1 mol L^{-1} phosphate buffer, pH 5.5, and varying the AA final concentration from 23.9 to 30 mmol L^{-1} ; (b) linear correlation between peak current and AA concentration

To investigate the behavior of ascorbic acid oxidation concerning varying scan rates, Figure 7a stands as a crucial source of insights. The voltammograms within the figure distinctly portray a notable trend, a discernible shift in the oxidation potential towards more positive values as the scan rate progressively increases. Alongside this observation, it becomes evident that the anodic peak current experiences a surge in intensity concomitant with the escalating scan rates. It is worth noting that a scan rate of 50 mV $\rm s^{-1}$ was employed in the other experiments, and as a result, the additional peaks linked with the carbon screen-printed electrode (C-SPE) were distinctly identified at a potential of 0.8 V.

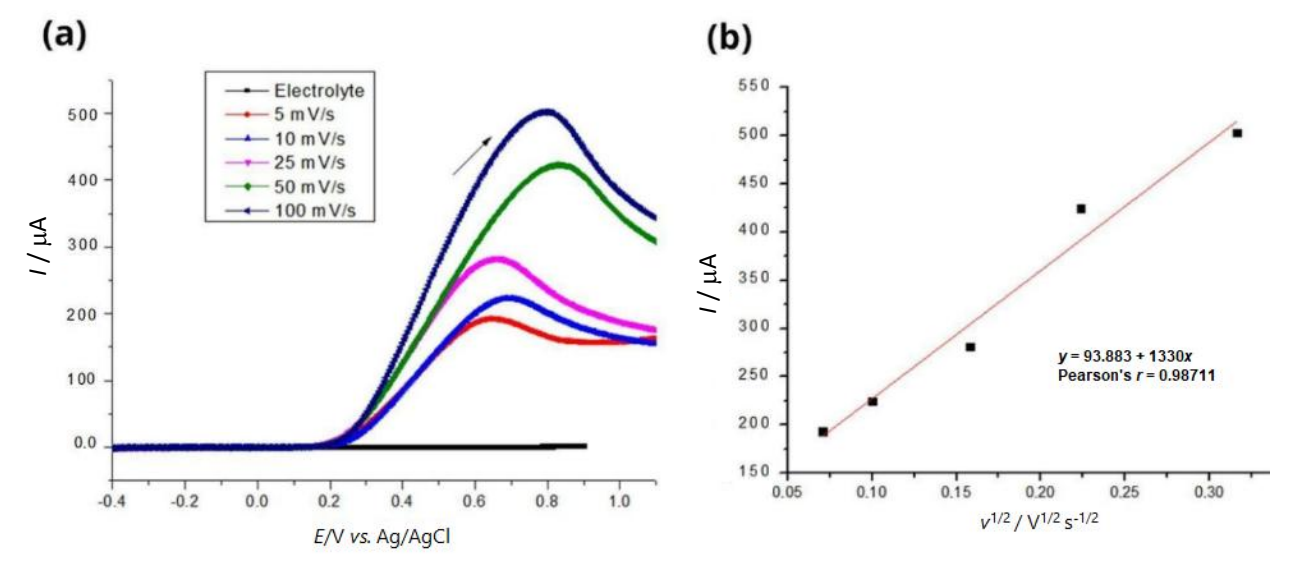


Figure 7. (a) Effect of scan rate on LSV responses of C-SPE in 0.1 mol L^{-1} phosphate buffer, pH 5.5, and final AA concentration of 30 mmol L^{-1} ; (b) linear plot of peak current vs. square root of scan rate

Valuable insights into the oxidation behavior of ascorbic acid under varying scan rates can be obtained from LSV curves presented in Figure 7a. A graph depicting the peak current in relation to the square root of the potential sweep rate ($v^{1/2}$) is presented in Figure 7b, unveiling a strikingly linear relationship between the peak current and the square root of the scan rate (with a correlation coefficient of r = 0.987). This observation indicates that the oxidation process transpiring on the electrode surface is predominantly governed by diffusion as opposed to adsorption. This finding is

in alignment with prior observations utilizing GCE, CPE, and corroborating studies [2], which have likewise arrived at a similar conclusion. This insight further contributes to the comprehensive understanding of the intricacies governing the oxidation behavior of ascorbic acid.

Comparison of standard ascorbic acid analysis using the three electrodes

To compare the three electrodes, an analysis was carried out using standard ascorbic acid in the same concentrations as those used for GCE and CPE. It can be seen that using C-SPE at lower concentrations, the anodic peaks showed potentials of +0.3 V to +0.6 V. As shown in the previous analyses, this shift occurs as the concentration of ascorbic acid increases.

Again, a graph correlating current to concentration was developed, from which it is possible to observe the linearity between peak current (μ A) and the concentration of AA (mmol L⁻¹). Using the equation derived from the linear fit, y = a + bx, it is possible to obtain the angular and linear coefficients, which correspond to b = 28.7375 μ A mmol L⁻¹ and a = -5.69623 μ A, respectively (Figure 8b).

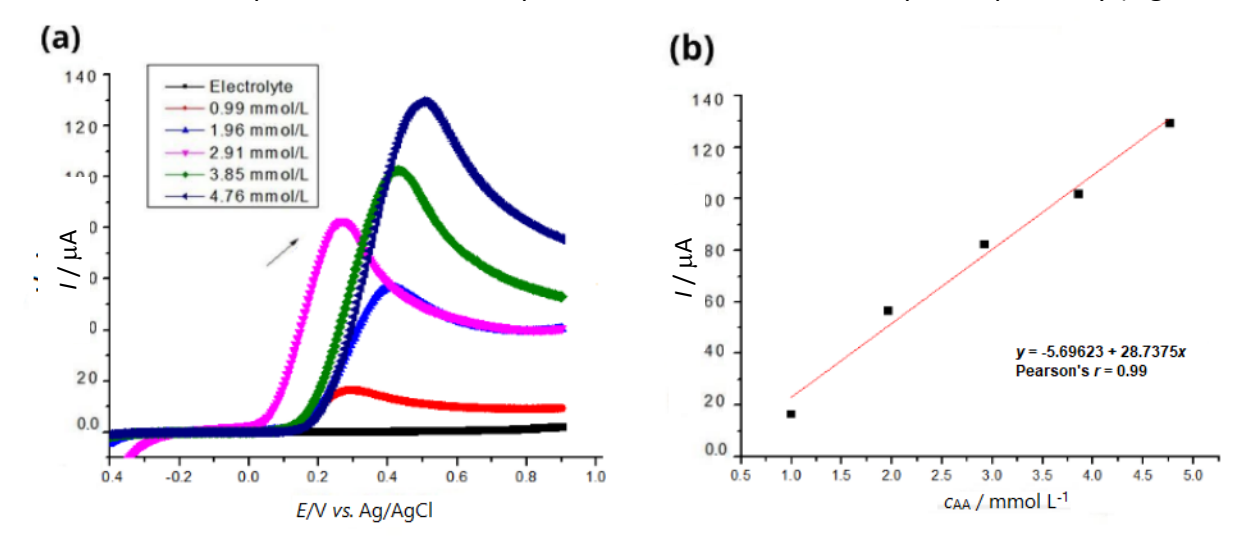


Figure 8. (a) LSV curves at 50 mV s^{-1} of C-SPE in 0.1 mol L^{-1} phosphate buffer, pH 5.5, and varying the AA final concentration from 0.99 to 4.76 mmol L^{-1} ; (b) linear correlation between peak current and AA concentration

The obtained Pearson correlation coefficient (r = 0.99) from the analytical curve affirms a direct proportionality between the electrolyte concentration and current intensity. Moving on to the calculation of the limit of detection (LoD), a critical parameter for sensitivity, since it is the smallest amount of analyte in the test sample that can be truly distinguished from zero, the equation by [9] is applied:

LoD =
$$3s/m = (3.6.32404 \,\mu\text{A})/(120 \,\mu\text{A}/(4.96-0.99) \,\text{mmol L}^{-1}) = 0.63 \,\text{mmol L}^{-1}$$
 (3)

The determined LoD is 0.63 mmol L⁻¹, a value lower than the initial AA concentration of 0.99 mmol L⁻¹ introduced, underscoring again the robust sensitivity of the printed electrode, demonstrating that the selected analyte concentrations were significantly distinct from the blank (electrolyte-phosphate buffer solution at pH 5.5) and proving the validity of the obtained results.

Finally, comparing the three electrodes, GCE, CPE and C-SPE, at the same concentration of 4.76 mmol L^{-1} , we obtain the results shown by the voltammograms in Figure 9. A notable potential shift was observed in the three voltammograms. It transitioned from +0.5 to +0.7 V when moving from the C-SPE to the GCE and then further to +0.8 V from the GCE to the CPE. In an intriguing departure from theoretical expectations [1], the anodic peak current registered for the CPE (80 μ A) exceeded that of the GCE (52.9 μ A). This trend persisted across all other concentrations and rates.

This inversion suggests that the custom-made electrode demonstrated heightened sensitivity compared to the conventional electrode, possibly attributed to the lower ohmic resistance of the paste in contrast to the GCE.

In addition, the C-SPE demonstrated a notably higher current response, registering at 129 μ A, compared to the unmodified GCE. This observation aligns with the anticipated outcomes as indicated in prior research [11]. Furthermore, it surpassed the peak current recorded by the CPE, showcasing superior sensitivity in comparison to the other electrodes.

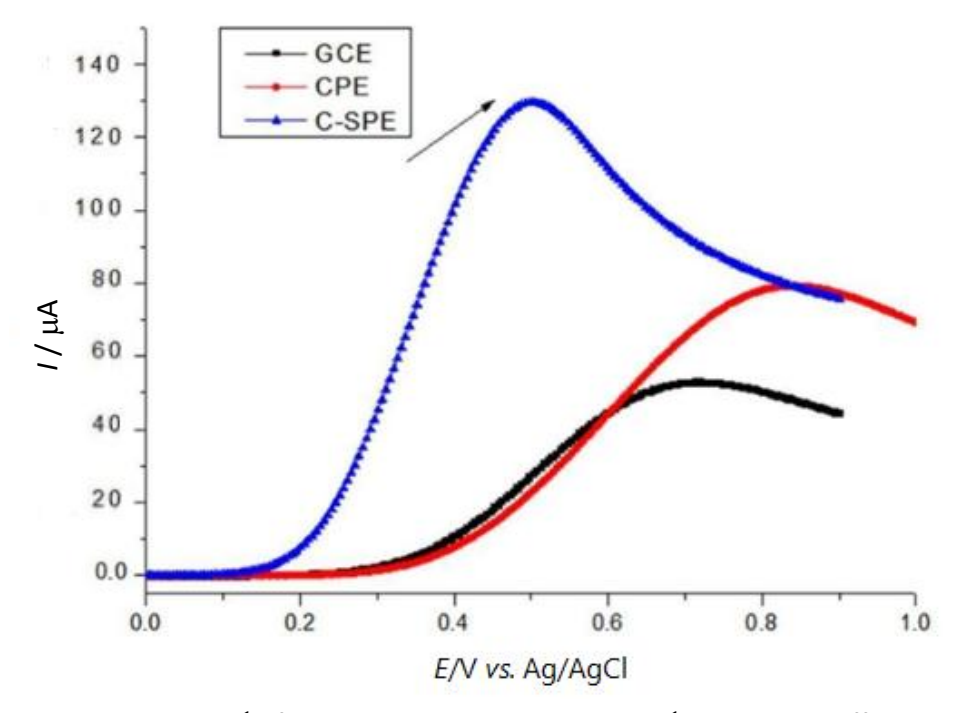


Figure 9. LSV curves at 50 mV s⁻¹ of GCE, CPE and C-SPE in 0.1 mol L^{-1} phosphate buffer, pH 5.5, with the AA final concentration 4.76 mmol L^{-1}

It is worth noting that all electrodes proved efficient in generating the AA oxidation profile. They exhibited high sensitivity while maintaining a low background current, indicating minimal noise interference in the readings.

Determining the concentration of ascorbic acid in different juice samples using C-SPE

Due to its superior characteristics, as shown in the comparison above, C-SPE was used for AA determination in different juice samples (pear-orange, Tahiti lemon, and Ponkan tangerine). A standard addition method was employed, following a well-established protocol in which a sample of unknown initial concentration of analyte C_{X_1} exhibits a signal intensity of I_X . Subsequently, a precisely measured quantity of known standard S is introduced into an aliquot of the sample, resulting in an observed signal denoted as I_{S+X} for this solution. The addition of the standard induces a change in the original concentration of the analyte due to dilution.

Application of standard addition method for ascorbic acid quantification

For notation purposes, let C_{X_f} represent the diluted concentration of the analyte, where 'f' signifies "final". Similarly, the concentration of the standard in the final solution is denoted as C_{S_f} . It is important to note that the chemical species X and S are identical [9]. As per the fundamental principle, the signal is directly proportional to the concentration of the analyte.

The standard addition method involves adding known concentrations of a standard solution to a sample with an unknown initial concentration of the analyte, ascorbic acid. This process results in a change in the original concentration of the analyte due to dilution, allowing for precise determination. Equation (4) represents this relationship:

$$\frac{C_{x_i}}{C_{s_i} + C_{x_i}} = \frac{I_x}{I_{s+x}}$$

The equation above shows that the signal is directly proportional to the concentration of the analyte, where C_{X_i} is the concentration of the analyte in the initial solution, $C_{S_f} + C_{X_f}$ is the concentration of the analyte plus the standard in the final solution, I_X is a sign of the initial solution and I_{S+X} is signal of the final solution. The deduction mechanism is given by Equation (5):

$$I_{X} = kC_{X_{1}} \tag{5}$$

$$I_{S+X} = k(C_{S_f} + C_{X_f})$$
 (6)

where k is a constant of proportionality. Dividing Eq. (5) by Eq. (6), we get Equation (7):

$$\frac{I_{x}}{I_{s+x}} = \frac{kC_{x_{i}}}{k(C_{s_{i}} + C_{x_{i}})} = \frac{C_{x_{i}}}{(C_{s_{i}} + C_{x_{i}})}$$
(7)

For an initial volume V_0 of the unknown sample and the added volume V_s of standard with concentration C_{S_i} , the total volume is $V = V_0 + V_s$ and the final concentrations in equation (6) are presented by Equations (8):

$$C_{\mathsf{X}_{\mathsf{f}}} = C_{\mathsf{X}_{\mathsf{i}}} \frac{V_{\mathsf{0}}}{V} \tag{8a}$$

$$C_{\mathsf{S}_{\mathsf{f}}} = C_{\mathsf{S}_{\mathsf{i}}} \frac{V_{\mathsf{S}}}{V} \tag{8b}$$

The dilution factor, V_0/V , is crucial in these calculations. By expressing the diluted concentration of the analyte C_{X_i} in terms of the initial concentration C_{X_i} , we can solve for C_{X_i} , given that all other variables are known.

Determining the concentration of ascorbic acid in pear-orange

Experimental data in Figure 10a shows that the anodic current is directly proportional to the concentration of AA. The addition of specific volumes of standard AA solution leads to corresponding increases in current.

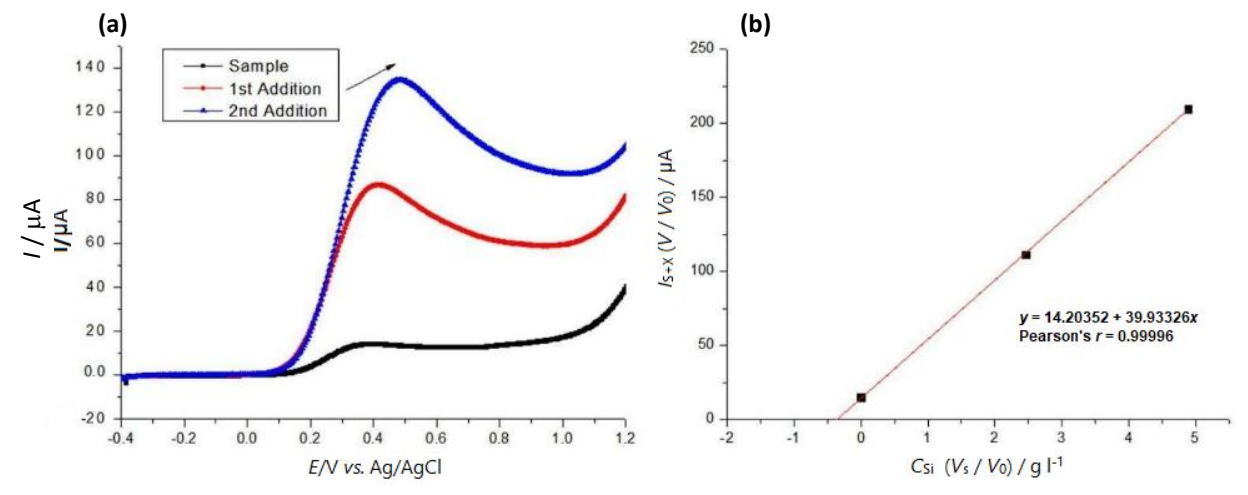


Figure 10. (a) LSV curves at 50 mV s⁻¹ of C-SPE in 0.1 mol L⁻¹ phosphate buffer pH 5.5 and AA sample present in the juice of a pear-orange and two added volumes (5 and 10 μ L) of 0.05 mol L⁻¹ AA standard solution; (b) determination of AA concentration in pear-orange using standard addition method

These data points and known parameters will be used to generate a linear equation for further analysis. A series of data points representing concentrations of standards added to the sample are calculated for the x-axis: $C_{X_i}(V_S/V_0)$, and corresponding signals (I_{S+X}) adjusted for volume ratios, are calculated for the y-axis: $I_{S+X}(V/V_0)$.

For the initial volume of unknown sample (V_0) = 0.018 mL and initial concentration of standard C_{S_i} = 0.05 M = 8.8 g L⁻¹, the needed parameters and calculated standard AA concentrations and corresponding currents are summarized in Table 1.

Table 1. Analytical parameters and calculated concentrations of standards and resulting current responses for AA determination in pear-orange by standard addition method: $V_0 = 0.018$ ml, $C_{S_i} = 0.05$ mol $L^{-1} = 8.8$ g L^{-1}

$V_{\rm S}$ / mL	$I_{S+X}/\mu A$	V / mL	$V_{\rm S}$ / $V_{\rm O}$	V/V_0	$C_{S_i}(V_S/V_0)/g L^{-1}$	I_{S+X} (V/V_0) / μA
0	14.72	0.018	0.000	1.00	0.00	14.72
0.0050	87.03	0.023	0.280	1.28	2.46	111.4
0.010	135.0	0.028	0.550	1.55	4.89	210.0

The linear Equation (9) shown in Figure 10b can be derived from the obtained data in Table 1:

$$y = 14.20352 + 39.93326x$$
 (9)

Using Eq. (9), it can be easily calculated that for y = 0, $x = |-0.36 \text{ g L}^{-1}| = 0.36 \text{ g L}^{-1}$ or 360 L⁻¹.

The experimental analysis revealed that the concentration of AA in the pear-orange sample was determined to be 360 mg L^{-1} . This value comes with a calculated uncertainty of \pm 32.4 mg L^{-1} , which was derived using the propagated errors of the coefficients obtained from the software.

This result implies that the actual concentration of AA in pear oranges lies within the range of 327.6 to 392.4 mg L⁻¹.

Repeatability study

It's worth noting that variations in fruit variety may account for the observed differences in AA concentration. To validate the repeatability of this experiment, it was conducted in triplicate using two additional samples from the same batch of oranges.

To evaluate the repeatability of the analysis, the same orange juice sample underwent two additional LSV analyses. The entire initial procedure was repeated. The first repetition is referred to as duplicate analysis, and the second as triplicate analysis, yielding new peak potential and current values, which are presented below.

Duplicate analysis: Upon conducting the duplicate analysis (Figure 11a and 11b), the linear Equation (10) derived from the obtained data was:

$$y = 24.07257x + 6.80553 \tag{10}$$

Solving for x when y = 0, $x = |-0.283 \text{ g L}^{-1}| = 0.283 \text{ g L}^{-1}$.

The concentration of AA found in the pear-orange through duplicate analysis was determined to be 283 mg L^{-1} . This measurement comes with an associated uncertainty of \pm 29 mg L^{-1} . Therefore, the experiment suggests that the concentration of AA within pear oranges is within the range of 254 to 312 mg L^{-1} .

Comparing this duplicate measurement to the value obtained in the initial analysis, the relative error ranged from -22.47 to -20.49 %. Notably, the concentration of AA in the duplicate analysis was lower than in the first assessment. However, it's essential to consider that both analyses were performed on the same orange, contributing to a reduced margin of error compared to literature data obtained from diverse experiments.

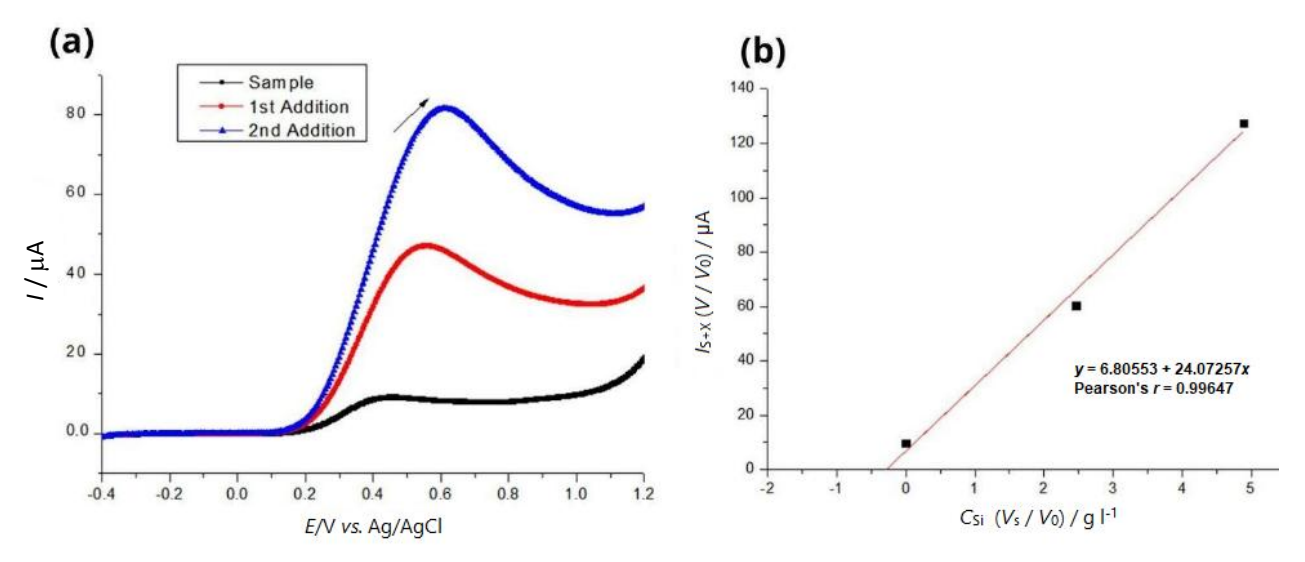


Figure 11. LSV curves at 50 mV s^{-1} of C-SPE for a duplicate of the AA sample present in the juice of a pear-orange and for two added volumes of 0.05 mol L^{-1} AA standard solution, in 0.1 mol L^{-1} , phosphate buffer pH 5.5, scan rate 50 mV s^{-1} ; (b) determination of AA concentration in duplicate pear-orange sample using standard addition method

Triplicate analysis (Figures 12a and 12b): Using the linear fit equation, y = a + bx, it is possible to obtain Equation (11) from Fig. 12b:

$$y = 24.34109x + 6.521 \tag{11}$$

Solving for x when y = 0, we find that $x = |-0.268 \text{ gL}^{-1}| = 0.268 \text{ g L}^{-1}$.

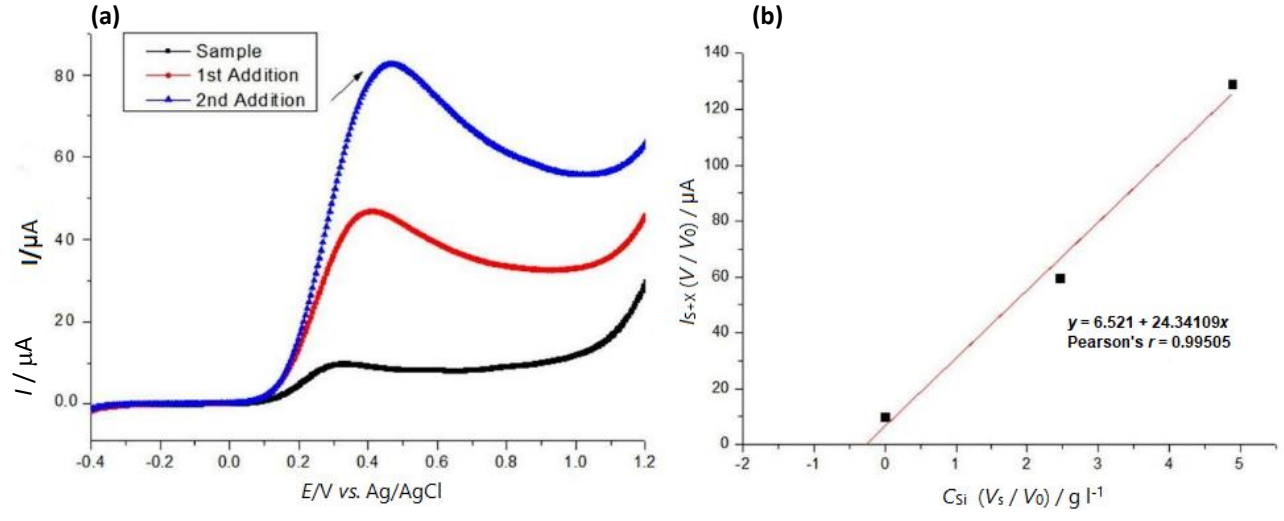


Figure 12. LSV curves at 50 mV s⁻¹ of C-SPE for a triplicate of the AA sample present in the juice of a pear-orange and for two added volumes of 0.05 mol L^{-1} AA standard solution in 0.1 mol L^{-1} , phosphate buffer pH 5.5; (b) determination of AA concentration in triplicate pear-orange sample using standard addition method

The concentration of AA found in the pear-orange was quantified to be 268 mg L^{-1} , with an associated uncertainty of \pm 34.2 mg L^{-1} . Based on this experiment, it can be inferred that the concentration of AA in pear-orange ranges from 233.8 to 302.2 mg L^{-1} . The standard deviation calculated for the three concentration values obtained was 49.36 mg L^{-1} .

Comparing this triplicate analysis to the value obtained in the first measurement, the relative error ranged from -28.63 to -22.99 %. This indicates that the concentration of AA in the triplicate analysis was also lower than in the first assessment.

To include the error bar of the replicates, a graph was generated (Figure 13) of the mean of the values corresponding to the y-axis by the values of the x-axis - the same for the three measurements since the dilution factor is maintained: 0 for the sample, 0.28 for the first addition and 0.56 for the second addition).

From the graph, it is possible to obtain the linear Equation (12):

$$y = 11.20558 + 28.40392x \tag{12}$$

Setting y = 0, the equation was solved for x, yielding |-0.394| g L-1, whose modulus corresponds to 0.394 g L-1, accompanied by an uncertainty of \pm 37.4 mgL⁻¹. The relative error of this value compared to the literature is from -36.27 to -13.77 %.

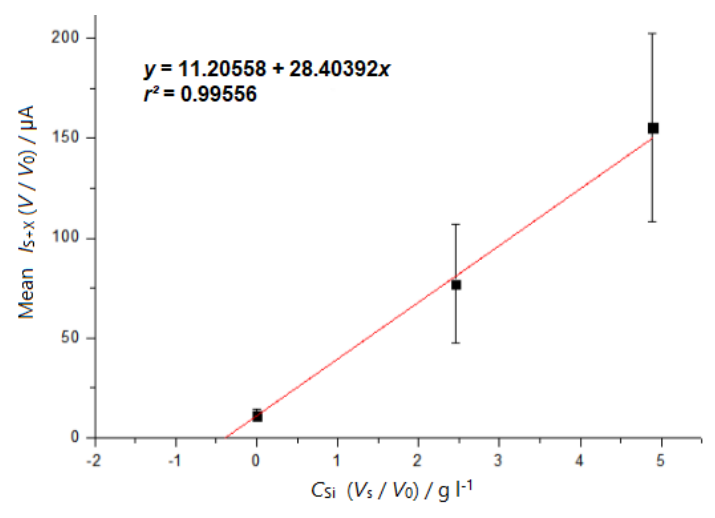


Figure 13. Determination of AA concentration in pear-orange using the standard addition method with error bars considering the mean of three measurements

Although the observed error, considering the three measurements, is reasonable (given the variety among the fruits themselves), when we look at each replicate individually, it is notable that in comparison to the duplicate analysis, the relative error of the triplicate was between -7.95 and -3.14 %. In other words, the concentration in the triplicate analysis was lower than in the first and second analyses. This discrepancy may be attributed to the degradation of AA over time, as these samples of juice originated from the same orange and were subjected to the environmental conditions of temperature, light, and oxygen. Hence, to ensure more precise results, the analyses conducted on Tahiti lemon and Ponkan tangerine were performed only once, preventing potential degradation of vitamin C due to prolonged exposure to ambient conditions.

Experimental determination of ascorbic acid concentration in Tahiti lemon

As seen in Figure 14a, the anodic currents measured at C-SPE in solutions containing juice sample of Tahiti lemon increase after additions of AA standard samples. For $V_0 = 0.018$ mL and $C_{S_i} = 0.1$ mol $L^{-1} = 17.6$ g L^{-1} , the needed parameters used for calculations of standard concentrations and corresponding currents are summarized in Table 2.

Table 2. Analytical parameters and calculated concentrations of standards and resulting current responses for AA determination in Tahiti lemon by standard addition method: $V_0 = 0.018$ ml, $C_{S_i} = 0.1$ mol $L^{-1} = 17.6$ g L^{-1}

$V_{\rm S}$ / mL	$I_{S+X}/\mu A$	V/mL	$V_{\rm S}/V_{\rm 0}$	V/V_0	$C_{S_i}(V_S/V_0)/g L^{-1}$	I_{S+X} (V/V_0) / μA
0.000	17.67	0.018	0.000	1.00	0.00	17.67
0.005	51.00	0.023	0.280	1.28	4.89	65.17
0.010	74.21	0.028	0.550	1.55	9.78	115.4

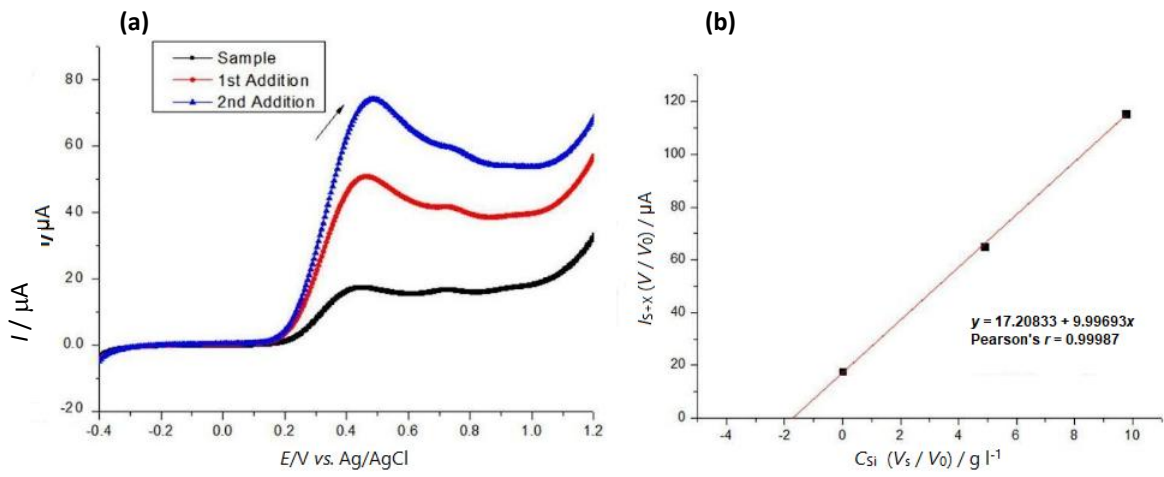


Figure 14. (a) LSV curves at 50 mV s⁻¹ of C-SPE in 0.1 mol L⁻¹ phosphate buffer pH 5.5 containing AA sample present in Tahiti lemon juice and two added volumes (5 and 10 μ L) of 0.01 mol L⁻¹ AA standard solution; (b) determination of AA concentration in Tahiti lemon juice using standard addition method

The linear equation derived from data in Table 2 and shown in Figure 14b is:

$$y = 17.20833 + 9.99693x \tag{13}$$

Setting y = 0, the equation was solved for x, yielding -1.72 g L⁻¹. This value was converted to a positive value, resulting in 1.72 g L⁻¹. Therefore, the concentration of AA in the Tahiti lemon was determined to be 1720 mg L⁻¹, accompanied by an uncertainty of \pm 131.4 mg L⁻¹.

Thus, the experiment indicates that the concentration of AA present in the Tahiti lemon is between 1588.6 and 1851.4 mg L^{-1} . Compared to the TACO Table [12], the AA content in a lemon weighing approximately 100 g is around 38.2 mg. Therefore, considering that the lemon used yielded 35 mL and weighed 120 g (the theoretical value is 45.84 mg and the experimental value is within the range of 55.6 and 64.8 mg), the relative error presented had a range of 21.29 to 41.36 %.

Determining the concentration of ascorbic acid in Ponkan tangerine

LSV curves for C-SPE in a solution containing Ponkan tangerine juice are presented in Figure 15a. For $V_0 = 0.018$ mL and $C_{S_i} = 0.05$ mol L⁻¹ = 8.8 g L⁻¹ the needed analytical parameters for calculations of standard concentrations and corresponding currents are summarized in Table 3.

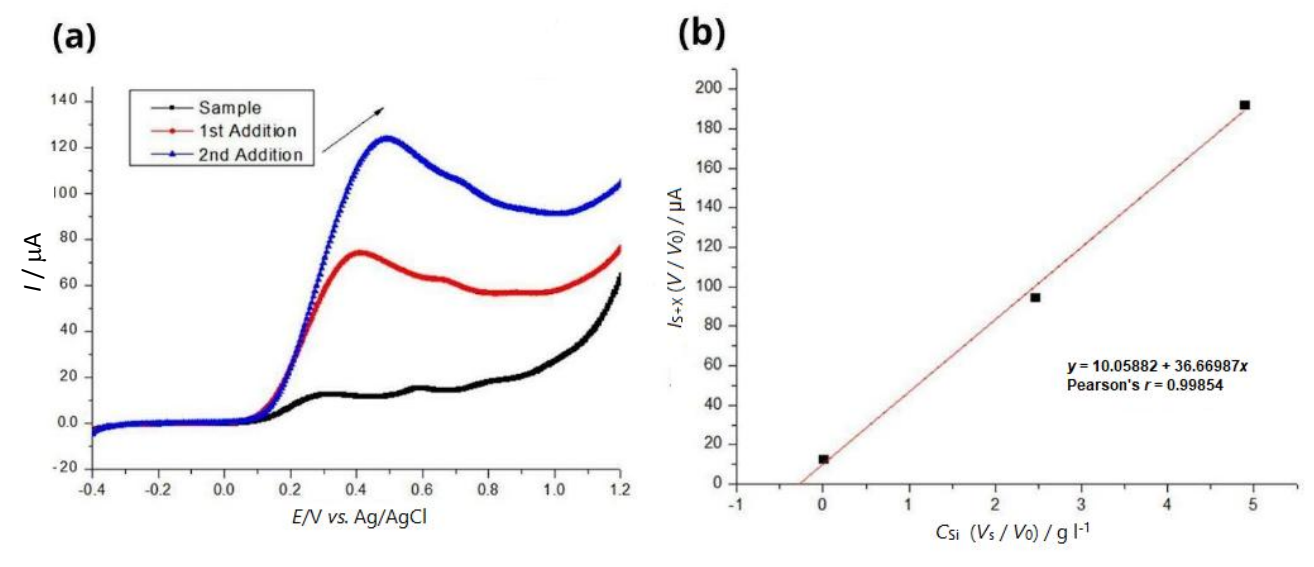


Figure 15. (a) LSV curves at 50 mV s⁻¹ of C-SPE in 0.1 mol L⁻¹ phosphate buffer pH 5.5 containing AA sample present in Ponkan tangerine juice and two added volumes (5 and 10 μ L) of 0.05 mol L⁻¹ AA standard solution; (b) determination of AA concentration in Ponkan tangerine juice using standard addition method

Table 3. Analytical parameters and calculated standard concentrations and resulting current responses for AA determination in Ponkan tangerine by standard addition method: $V_0 = 0.018$ ml, $C_{S_i} = 0.05$ mol $L^{-1} = 8.8$ g L^{-1}

V _s / mL	$I_{S+X}/\mu A$	V/mL	$V_{\rm S}$ / $V_{\rm O}$	V/V_0	$C_{S_i}(V_S/V_0)/g L^{-1}$	I_{S+X} (V/V_0) / μA
0.000	12.84	0.018	0.00	1.00	0.00	12.84
0.005	74.09	0.023	0.280	1.28	2.46	94.67
0.010	123.6	0.028	0.550	1.55	4.89	192.2

The linear Equation (14) derived from data in Table 2 and shown in Figure 15b is:

$$y = 10.05882 + 36.66987x \tag{14}$$

When y = 0, x = -0.27 g L⁻¹, equivalent to 0.27 g L⁻¹. Consequently, the concentration of AA found in the Ponkan tangerine was 270 mg L⁻¹ with an uncertainty of \pm 100 mg L⁻¹.

Thus, the experiment indicates that the concentration of AA present in the Ponkan tangerine is between 170 and 370 mg L⁻¹. Compared to the TACO table [13], the AA content in a Ponkan tangerine of approximately 100 g is around 48.8 mg. Therefore, considering that the tangerine used weighed 143.3 g (the theoretical value would be 69.93 mg) and yielded 60 mL of juice (experimental value between 10.2 and 22.2 mg), the relative error presented had a range of -85.4 to -68.2 %.

Again, the value found was lower (as with the pear-orange), which could be due to intra-species variation in the fruit itself but could also be due to losses during the procedure.

Conclusion

In summary, this study thoroughly evaluated the efficacy of various carbon electrodes (including the conventional glassy carbon electrode and highly sensitive carbon paste electrode) composed of graphite powder and paraffin, and the cost-effective commercial carbon screen-printed electrode. Among these, the C-SPE exhibited good performance in terms of anodic peak current, demonstrating its robustness, cost-effectiveness, and ease of use, thus positioning it as a compelling alternative for practical applications.

The effectiveness of the C-SPE was validated through its successful application in determining vitamin C concentrations in different citrus fruit samples using the standard addition method in conjunction with linear sweep voltammetry. The results for the ascorbic acid concentration in pear-orange ranged from 327.6 to 392.4 mg L⁻¹ in the first analysis, as subsequent analyses were affected by degradation. For Tahiti lemon and Ponkan tangerine, the concentrations were 1588.6 to 1851. mg L⁻¹ and 170 to 370 mg L⁻¹, respectively. These findings indicate that, among the fruits analyzed, Tahiti lemon is the richest source of vitamin C, making its consumption highly recommended for individuals needing to supplement this vitamin.

The applied voltammetric method, specifically LSV, for ascorbic acid determination, proved to be highly sensitive, rapid, and reproducible, particularly given the inherent variability among different fruit samples. These results underscore the considerable potential of C-SPE for practical applications in vitamin C analysis. Moreover, the development and utilization of specialized electrodes, such as C-SPE, reflect a broader trend in the field of food analysis, enhancing both precision and efficiency in nutrient quantification.

Acknowledgments: The authors are thankful to CAPES (CAPES, PROCAD-SPCF - File number process 88887.613955/2021-00), FAPESP (File numbers 2017/22401-8 and 2022/12189-0), and CNPq (File number 302742/2022-0) for financial support. The authors also thank Dr. Cynthia Maria de Campos Prado Manso, who revised and edited this full text.

References

- [1] A. M. Pisoschi, A. Pop, A. I. Serban, C. Fafaneata, Electrochemical methods for ascorbic acid determination, *Electrochimica Acta* **121** (2014) 443-460. https://doi.org/10.1016/j.electacta.2013.12.127
- [2] K. R. O. Araújo, Study on the determination of ascorbic acid in solution using a Nafion®-modified glassy carbon electrode, Master's Dissertation in Chemistry, Federal University of Goiás, Goiânia, Brazil, 2017.
- [3] A. K. Alkhawaldeh, Platinum nanoparticle electrode modified iodine using cyclic voltammetry and chronoamperometry for determination of ascorbic acid, *Analytical and Bioanalytical Electrochemistry* **12(6)** (2020) 780-792. https://www.abechem.com/article_43202.html
- [4] A. Pardakhty, S. Ahmadzadeh, S. Avazpour, V. Kumar Gupta, Highly sensitive and efficient voltammetric determination of ascorbic acid in food and pharmaceutical samples from aqueous solutions based on nanostructure carbon paste electrode as a sensor, *Journal of Molecular Liquids* **216** (2016) 387-391. https://doi.org/10.1016/j.molliq.2016.01.010
- [5] J. G. Manjunatha, M. Deraman, G. P. Mamatha, Simultaneous voltammetric measurement of ascorbic acid and dopamine at poly (vanillin) modified carbon paste electrode: A cyclic voltammetric study, *Der Pharma Chemica* 4(6) (2012) 2489-2497. <a href="https://www.derpharmachemica.com/pharma-chemica/simultaneous-voltammetric-measurement-of-ascorbic-acid-and-dopamine-at-poly-vanillin-modified-carbon-pasteelectrode-a-c.pdf
- [6] G. K. Jayaprakash, B. E. Kumara Swamy, S. C. Sharma, J. J. Santoyo-Flores, Analyzing electron transfer properties of ferrocene in gasoline by cyclic voltammetry and theoretical methods, *Microchemical Journal* **158** (2020) 105116. https://doi.org/10.1016/j.microc.2020.105116
- [7] G. M. Alvez, A. S. Castro, B. R. McCord, M. F. de Oliviera, MDMA Electrochemical Determination and Behavior at Carbon Screen-printed Electrodes: Cheap Tools for Forensic Applications, *Electroanalysis* **33** (2021) 635-642. https://doi.org/10.1002/elan.202060080
- [8] A. J. Bard, L. R. Faulkner, H. S. White, *Electrochemical methods: Fundamentals and Applications*, John Wiley & Sons, New York, USA, 2022. ISBN 978-1119334064. https://www.wiley.com/en-ae/Electrochemical+Methods%3A+Fundamentals+and+Applications%2C+3rd+Edition-p-9781119334057
- [9] D. C. Harris, *Quantitative Chemical Analysis*, W. H. Freeman Publ., New York, USA, 2015. ISBN-978-1429218153
- [10] D. A. Skoog, F. J. Holler, S.R. Courch, *Principles of Instrumental Analysis, 7th ed.*, Cengage Learning, Boston, USA, 2017. ISBN: 978-1337468039
- [11] N. A. S. Pereira, Characterization of carbon electrodes functionalized with perylene derivatives, Ph.D. Dissertation in Chemistry, University of Minho, Portugal, 2015. [Online]. Available: https://hdl.handle.net/1822/35644.
- [12] G. F. S. Alegre, Determination of bioactive compounds and antioxidant capacity in fresh and pasteurized orange juices, Master's Dissertation in Food and Nutrition, UNESP, Araraquara, Brazil, 2015. [Online]. Available: http://hdl.handle.net/11449/121868.
- [13] TACO, Brazilian Food Composition Table, NEPA/UNICAMP, Campinas, Brazil, 2011. [Online]. Available: https://www.cfn.org.br/wp-content/uploads/2017/03/taco-4-edicao-ampliada-e-revisada.pdf

© 2025 by the authors; licensee IAPC, Zagreb, Croatia. This article is an open-access article distributed under the terms and conditions of the Creative Commons Attribution license (https://creativecommons.org/licenses/by/4.0/)





Open Access : : ISSN 1847-9286

www.jESE-online.org

Original scientific paper

Ecofriendly synthesis of NiZnFe₂O₅ nanoparticle by papaya leaf extract for electrochemical detection of ascorbic acid in orange juice and pharmaceuticals

Gubbihalli Nanjundappa Chandana¹, Murudagalli Basavaraju Shivaswamy¹, Mandya Shivananju Asha², Shanthalingaiah Jeevitha¹, Honnegowdanahalli Shivabasappa Nagendra Prasad^{1,⊠}, Bendekere Shankarappa Hemanth^{1,4}, Madanahalli Ankanathappa Sangamesha³, Beejaganahalli Sangameshwara Madhukar¹, Lingappa Mallesha⁵, Jamballi G. Manjunatha⁶

¹Department of Chemistry, Sri Jayachamarajendra College of Engineering, JSS Science and Technology University, Mysuru-570 006, Karnataka, India

²Department of Studies and Research Centre in Chemistry (A Recognized Research Centre of University of Mysore), St. Philomena's College Bannimantapa, Mysuru 570015, Karnataka, India ³Department of Chemistry, The National Institute of Engineering, Mysuru-570008, Karnataka, India ⁴Centre for Nano and Material Sciences, JAIN (Deemed-to-be University), Jain Global Campus, Kanakapura, Bangalore, Karnataka-562112, India

⁵JSS College of Arts, Commerce and Science, Ooty road, Mysuru, Karnataka-570008, India ⁶Department of Chemistry, FMKMC College, Constituent College of Mangalore University, Madikeri, Karnataka-571201, India

Corresponding author: [™]<u>nprasad@jssstuniv.in</u>

Received: August 21, 2024; Accepted: November 30, 2024; Published: December 11, 2024

Abstract

A green technique has been employed to synthesize the NiZnFe $_2O_5$ nanoparticles using papaya leaf extract. The X-ray diffraction investigated the structural characteristics and crystalline size. The morphology of the synthesised nanoparticle is analysed by scanning electron microscopy. The average diameter of the nanoparticle is 47.93 nm, which was determined using the dynamic light scattering method. UV/Vis diffuse reflectance spectrum results revealed that the NiZnFe $_2O_5$ NPs band gap is 1.8 eV. It was calculated using the Kubelka-Monk function and energy dispersion X-ray spectroscopy analysis was used to identify the synthesized nanoparticle's elements. The electrochemical behaviour of NiZnFe $_2O_5$ modified glassy carbon electrode (GCE) and bare GCE was studied to detect ascorbic acid using cyclic voltammetry and differential pulse voltammetry. Compared to unmodified GCE, NiZnFe $_2O_5$ nanoparticles modified GCE exhibit excellent electrocatalytic activity towards the AA oxidation, which was proved by the increase in peak current and decrease in peak potential. Electrochemical impedance analysis suggests that the

NiZnFe2O5 nanoparticles significantly enhance the charge transfer rate. The linear response of the peak current on the concentration of AA was obtained in the range of 0.2-50 μ M. The detection limit was found to be 1.038 μ M. The present work serves as a systematic benchmark to assess the electrochemical sensing potential of NiZnFe₂O₅ NPs towards AA in orange juice and pharmaceuticals.

Keywords

Green synthesis; glassy carbon electrode; cyclic voltammetry; differential pulse voltammetry; vitamin-C tablets

Abbreviations

PLE - Papaya leaf extract

 $NiZnFe_2O_5\ NPs\$ - Nickel zinc ferrite oxide nanoparticle

NPs - Nanoparticles

AA - Ascorbic acid

XRD - X-ray powder diffraction

JCPDS - Joint committee on powder diffraction standards

SEM - Scanning electron microscopy

EDX - Energy dispersion X-ray spectroscopy

UV-Vis DRS - Ultraviolet visible diffusion reflectance spectroscopy

DLS - Dynamic light scattering

GCE - Glassy carbon electrode

EIS - Electron impedance spectroscopy

CV - Cyclic voltammetry

DPV -Differential pulse voltammetry

Rct - Charge transfer resistance

*I*_{pa} - Anodic peak current

LOD - Limit of detection

Introduction

Nanoparticles are synthesised due to their unique properties and are applied to various fields such as biomedical, materials science, and environmental treatment. Compared to other techniques of nanoparticle synthesis [1], green synthesis, which uses naturally occurring sources such as plant extracts, algae, bacteria, and fungi, is more affordable, scalable, and environmentally friendly. The natural product has abundant bioactive properties that help stabilize and reduce nanoparticles during synthesis. *Carica* papaya leaf extract acts as a stabilizing and reducing agent due to the presence of flavonoids like quercetin and kaempferol, which help reduce metal ions to their nano size [2]. Papain and other alkaloids have chelating qualities that stabilize the nanoparticles by preventing agglomeration. Further aiding in the manufacturing process are additional bioactive substances, including phenolic acids and terpenoids, which supply functional groups for encasing the nanoparticles. *Carica* papaya leaf extract is also a great option for green synthesis because of its many benefits, which include biocompatibility, cost-effectiveness and availability.

Ferrites are generally understood to be ferromagnetic compounds made up of iron oxides. Nevertheless, they can also be chemically combined with other metals to give them magnetic and dielectric qualities. Within this category, spinel ferrites have been used in sensors recently because of their distinct qualities, including their high reactivity, high specific area, environmental friendliness, insensitivity to moisture, and scalability [3]. In the ultra-thin form, nickel ferrites (NiFe₂O₄) display a non-collinear spin structure and an inverted spinel structure varying with ferromagnetic and superparamagnetic properties of ferrites having a significant influence. It finds use in the medical domain,



including magnetic resonance imaging, medication delivery, and cancer therapies. They also have applications in electronics, including sensors, telecommunications, catalysts and high-frequency transformers [4].

The iron(III) oxide nanocomposite and reduced graphene oxide modified GCE are used to detect AA electrochemically [5,6]. L-ascorbic acid (AA) is a water-soluble vitamin with strong antioxidant properties that neutralizes harmful free radicals. The human body can only get the necessary amount of ascorbic acid from outside sources, unlike plants and the majority of animals that can synthesise AA from glucose [7]. Real samples such as orange juice, AA pills, avocado pear, garlic, green beans and cucumber contain AA. However, there may be health consequences from excessive or insufficient ingestion, which is why accurate detection techniques are important concerning their sensitivity, affordability, ease of use and possibility for real-time monitoring, electrochemical sensors present a promising method for the sensitive and selective detection of ascorbic acid. This work describes a straightforward electrochemical sensor production method that modified GCE to enable the sensing and targeted detects AA using NiZnFe₂O₅ NPs. It is important to note that the work also represents electrochemical detection in real samples such as orange juice and vitamin C tablets.

Experimental

Chemicals and reagents

Nickel nitrate (Ni(NO₂)₂), zinc nitrate (Zn(NO₂)₂), ferric nitrate (Fe(NO₂)₃), potassium chloride (KCl), ascorbic acid, ethylene glycol ($C_6H_8O_2$) and liquid ammonia were purchased from Sigma Aldrich chemical industries, Bengaluru, Karnataka, India and these compounds were used without any further purification in the experiment.

Extraction procedure

The *carica* papaya leaves of red leady bread were collected from the garden located in Bogadi, Mysuru, Karnataka, India. The leaves were initially washed two times with tap water, then washed with deionized water and ethanol wash to remove certain pests, steam from the leaf, and dried for 15 days, then blended to make a powder. 20 g of leaf powder was taken in a 250 ml beaker and 30 ml of deionized water was added with a constant stirring at a temperature of 80 °C for 2 hours. Cool the mixture at room temperature, then filter the mixture using a clean muslin cloth by a hand-pressing method and collect the filtrate. The obtained filtrate is PLE, which is further used as a fuel for nanoparticle synthesis.

Synthesis of nickel zinc ferrite (NiZnFe₂O₅) nanoparticles

NiZnFe₂O₅ NPs were synthesized using the solution combustion method. Nickel nitrate (Ni(NO₂)₂), zinc nitrate (Zn(NO₂)₂), and ferric nitrite (Fe(NO₂)₃) are used as precursor materials and PLE as a reducing agent. Stoichiometrically weighed 0.025 M zinc nitrite (Zn(NO₂)₂) and 0.05 M ferric nitrite (Fe(NO₂)₃) were taken in a 250 ml beaker containing 50 ml of ethylene glycol and continuously stirred for about 30 minutes. Then, stoichiometrically calculated 0.025 M nickel nitrate (Ni(NO₂)₂) was slowly added to the above solution, followed by adding 5 ml of PLE. Further, 1 ml of liquid NH₃ was periodically added during the synthesis to maintain the pH between 7 and 8. The mixture is stirred and heated at 50 °C for 3 hours to obtain a gel. Then, the calcination is carried out using a muffle furnace at a temperature of 600 °C for 4 hours. Similarly, the other two sets of solutions are prepared using 10 ml and 15 ml PLE. Eco-friendly synthesized nanoparticles are confirmed by different characterization techniques and used for electrochemical applications [8].

Characterization of nickel zinc ferrite (NiZnFe₂O₅) nanoparticles

The XRD (3proto A - XRD equipped with Cu K α radiation λ = 0.15406 nm, Mysuru) is utilized to determine the crystal structure and crystallite size of materials of the synthesized nanoparticle. The SEM (VEGA3 TESCAN, Brno, Czech Republic, Bangalore) is employed in the morphological investigation and surface features of NiZnFe₂O₅ nanoparticles. It provides high-resolution images, allowing us to observe the shape and surface structure of the nanoparticles. EDX (SWIFT 3000 SDD DETECTOR, Mysuru) is employed to determine the material's elemental composition. It provides quantitative evidence regarding the fundamental composition present in the sample, verifying the presence of specific elements and assessing their uniform distribution of elements within the nanoparticles. UV-Vis diffuse reflectance spectroscopy (PE Lambda20 Spectroscopy, Mysuru) is utilized to measure the absorption, reflectance and optical properties of the nanoparticle. The Malvern Zeta sizer Nano ZS-90 (Malvern Instruments, Mysuru) was used to estimate particle size along with size distributions in aqueous or physiological solutions at 25 °C. A CHI 608D electrochemical analyser was used to work on the electrochemical sensor.

Electrochemical sensors

The electrochemical sensor activity of synthesized NiZnFe₂O₅ NPs was investigated using a computer-controlled CHI 608D analyser. The CHI instrument is made up of three electrode systems:

- 1) reference electrode (silver-silver chloride electrode),
- 2) counter electrode (platinum electrode), and
- 3) working electrode (glassy carbon electrode).

Working electrode surfaces were polished with different sizes of alumina powder (0.3, 0.1 and 0.05 μ m) and rinsed with deionized water. Synthesized NiZnFe₂O₅ NPs (1 mg) were sonicated in water and ethanol for 20 to 30 minutes until fully dispersed. Then, the working electrode surface was drop cast with dispersed NiZnFe₂O₅ NPs, which were allowed to dry at room temperature. The modified electrode was used for electrochemical sensors.

Real sample preparation

The orange fruits were obtained at the local market and peeled the covering and squeezed completely. The collected orange juice samples were transferred into a 250 ml beaker. The tablets were brought from nearby medical shops, crushed using a mortar, and transferred to a 250 ml beaker containing deionized water. Then, the sample was centrifuged for further analysis.

Results and discussion

X-ray diffraction

XRD patterns are used to examine the crystallinity of the NiZnFe₂O₅ NPs. Figure 1 displays the XRD analysis of NiZnFe₂O₅ NPs. The peaks appearing at 2θ = 31.83, 56.63 and 70.05° were corresponded to Zn (100), Zn (110), and Zn (201) planes, respectively (JCPDS Card No. 22-1012) [9]. Peaks appearing at 2θ = 30.15, 35.56, 43.20, 53.43, 57.03 and 62.65°, these correspond to Fe (220), Fe (311), Fe (400), Fe (422), Fe (511) and Fe (440) planes respectively (JCPDS Card No.10-0325). Peaks appearing at 2θ = 37.02, 62.65 and 74.11° correspond to Ni (111), Ni (220), and Ni (311) and are coordinated with a JCPDS Card No. 10-0325 [10].

A comparison of the XRD patterns of the synthesized nanoparticle revealed that the peaks associated with the NiZnFe $_2O_5$ NPs are sharpened with an increase in the volume of PLE in the synthesised samples [11].

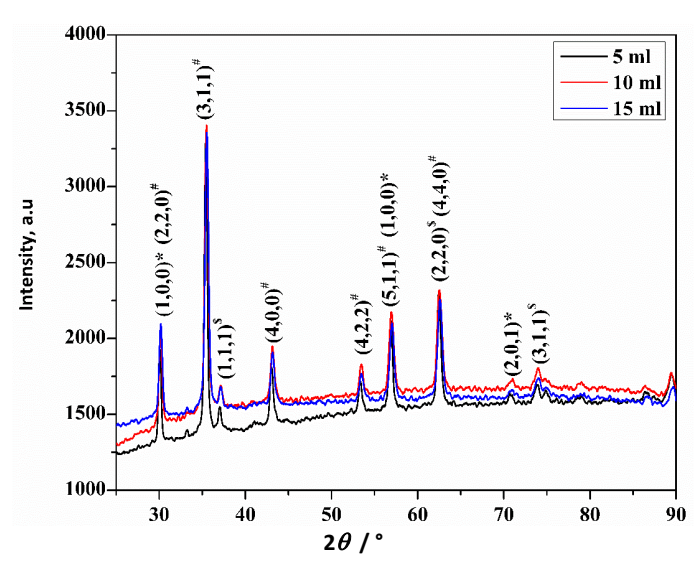


Figure 1. XRD spectra of NiZnFe₂O₅ NPs synthesised using three different volumes of PLE, 5, 10 and 15 ml (*, #, \$, indicate Zn, Fe, Ni, respectively)

The obtained peaks are narrow, which suggests that the synthesized NiZnFe $_2$ O $_5$ NPs are crystalline. The crystalline size of synthesized NiZnFe $_2$ O $_5$ NPs is calculated by Debye-Scherrer's length formula, Equation (1):

$$D = \frac{0.94\lambda}{\beta\cos\theta} \tag{1}$$

where λ is the wavelength of the X-ray radiation, β is the full-width at half maximum (FWHM) of the strongest intensity diffraction peak, θ is the angle of the strongest characteristic peak, and D is the average crystallite size. From Debye-Scherrer's length equation at the plane (311), the size of synthesized NiZnFe₂O₅ NPs ranges from 55 to 59 nm. Calculated data is given in Table 1.

 Volume of PLE added, mL
 β 2θ / °
 Scherrer's length, nm

 5
 0.2542
 35.56
 59.8

 10
 0.2655
 35.56
 57.2

 15
 0.2724
 35.56
 55.7

Table 1. XRD data of synthesized NiZnFe₂O₅ NPs (311) plane

Scanning electron microscopy and energy-dispersive X-ray spectroscopy

The development of NiZnFe $_2$ O $_5$ NPs was analysed via SEM and EDX, as shown in Figure 2 (A, B, C). The effect of PLE volume used in the synthesis of NiZnFe $_2$ O $_5$ NPs is noticeable. The synthesized NiZnFe $_2$ O $_5$ NPs present different shapes and are regular in size, with increased use of PLE in the synthesis process. EDX analysis shows that elements are evenly distributed across three samples. The nanoparticle surface exhibits the excellent distribution of nickel, zinc, iron, and oxygen with 9.78, 18.70, 56.10,15.43 wt.% for 5 mL of PLE added; 9.24, 18.13, 48.40, 28.81 wt.% for 10 mL of PLE added and 8.06, 16.30, 46.84, 24.22 wt.% for 15 mL of PLE added. The synthesized nanoparticles have high purity and no interference [12].

UV-vis diffuse reflectance spectroscopy

The diffuse reflectance spectra of NiZnFe₂O₅ NPs were displayed in Figure 3 and the band gap of the synthesized nanoparticle was calculated using Kubelka-Munk Equation (2).

$$F(R_{\infty}) = (1 - R_{\infty}^2)/2R_{\infty} = K/S \tag{2}$$

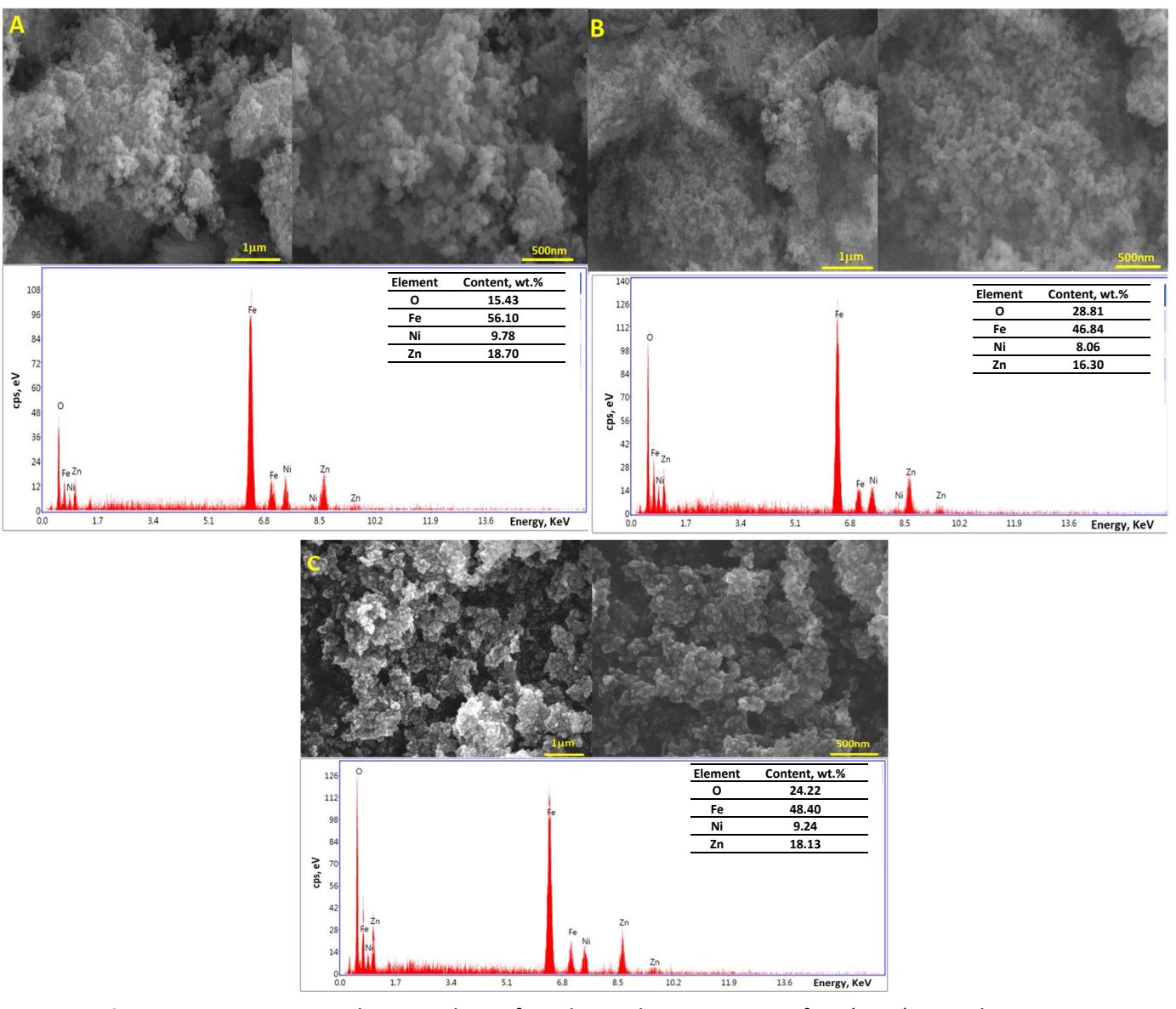


Figure 2. SEM images and EDX analysis of synthesized NiZnFe $_2O_5$ NPs for A) 5; B) 10 and C) 15 ml of PLE added

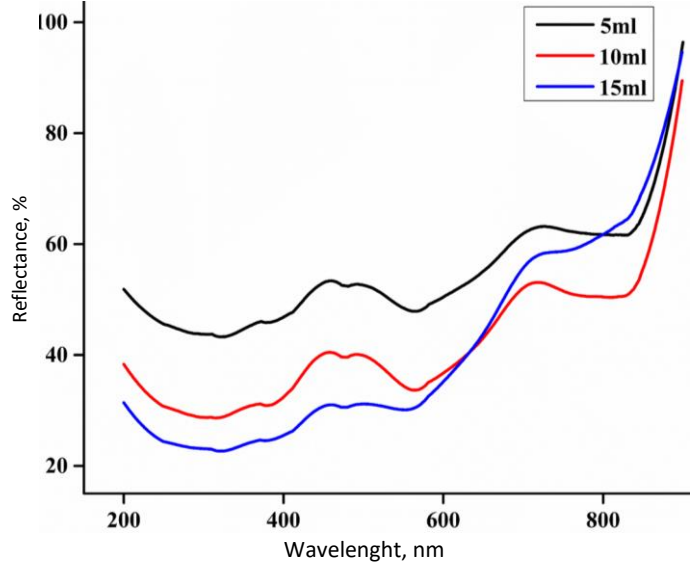


Figure 3. UV-vis diffuse reflectance spectroscopy of synthesized NiZnFe $_2O_5$ NPs with different volumes of PLE

with $F(R_{\infty})$ being the Kubelka-Munk function and R_{∞} being the diffuse reflectance of the nanoparticle, K is the absorption coefficient, and S is the scattering coefficient.

The result demonstrated that the band gap of NiZnFe₂O₅ NPs is about 1.8 eV. According to the literature, the calculated band gap of 1.8 eV was acceptable for catalytical activity for electrochemical sensor analysis [13].

Dynamic light scattering

Dynamic light scattering was used to determine the particle size. Figure 4 indicates the average crystalline size of 47.93 nm was obtained from a highly dispersed mixture in this experiment. NiZnFe $_2$ O $_5$ NPs show more stability in aqueous solutions, as indicated by the polydispersity index (PDI), which was 0.633. These values are consistent with the Scherer's length calculation from the XRD investigation [14]. This relates to the manufactured NiZnFe $_2$ O $_5$ NPs with 15 ml of PLE, a nanoscale composition.

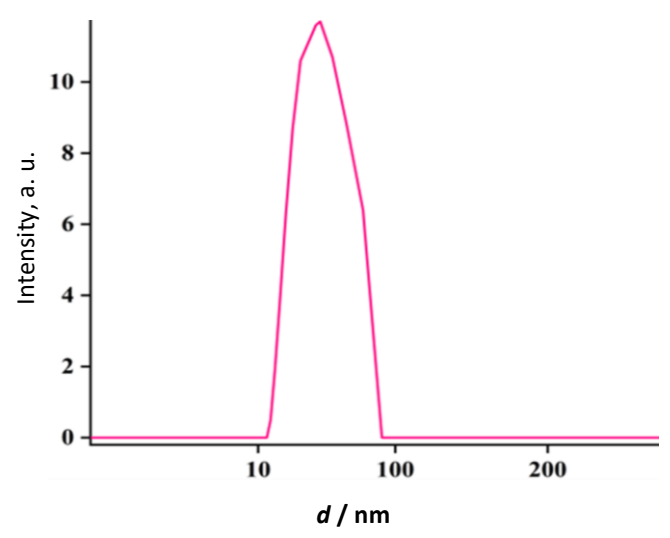


Figure 4. Dynamic light scattering (DLS) of synthesized NiZnFe₂O₅ NPs with a volume of PLE 15 ml

Electrochemical performance of NiZnFe₂O₅/GCE NPs

The electrochemical analysis of bare GCE and NiZnFe₂O₅ NPs/GCE modified electrodes were examined by CV in 0.1 M KCl (pH 7) with a scan rate of 0.5 V/s in the potential range of -1.4 to +1.4 V. Figure 5A represents the cyclic voltammograms of bare GCE and NiZnFe₂O₅/GCE NPs in the absence of an analyte. Bare GCE and NiZnFe₂O₅ NPs/GCE do not exhibit any current peak. The bare GCE and NiZnFe₂O₅ NPs/GCE electrodes were analysed using electrochemical impedance spectroscopy (EIS) and CV to investigate surface modifications. In Figure 5B, a redox peak appears due to the presence of [Fe(CN)₆]^{3-/4-} at a potential 0.42 V and 0.13 V, which confirms the modified NiZnFe₂O₅ NPs/GCE shows a higher peak current compared to bare GCE. According to Equation (3), the modified electrode has a greater surface area than the bare GCE at room temperature of 25 °C.

$$I_{pa} = (2.69 \times 10^5) n^{3/2} AC(Dv)^{1/2}$$
 (3)

In Equation (3) I_{pa} is the peak anodic current of the analyte, A is the electrochemically active surface area, n is the number of electrons, C is the analyte concentration, v is the scan rate and D is the diffusion coefficient of the analyte. The calculated electrochemical active area of NiZnFe₂O₅ NPs/GCE and GCE are 0.51685 and 0.243955 cm², respectively. The results show that NiZnFe₂O₅ NPs/GCE has approximately 2.12 times greater active surface area than GCE. Thus, NiZnFe₂O₅ NPs/GCE has much better electrochemical sensing properties than GCE [15,16].

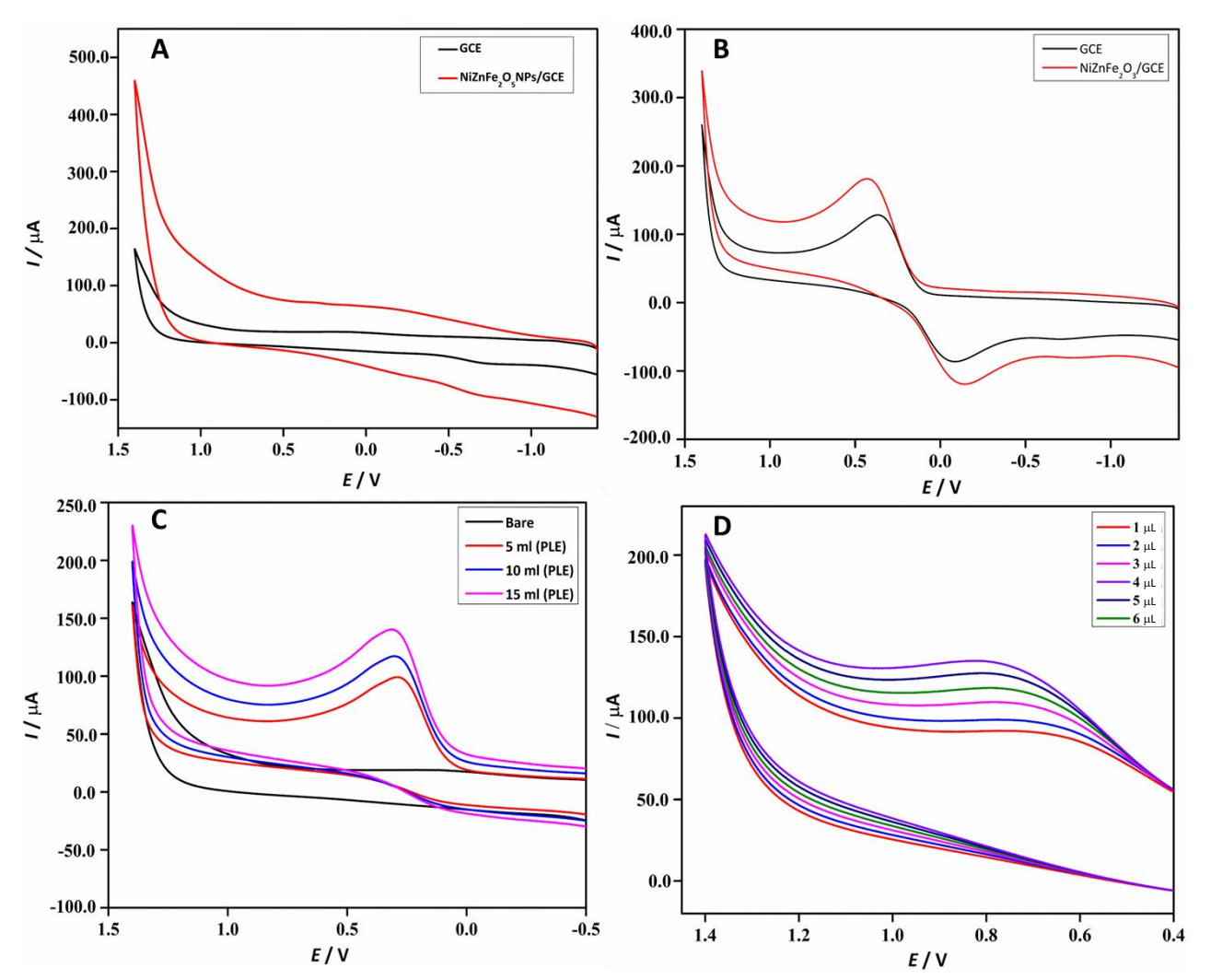


Figure 5. Cyclic voltammetry (0.5 V s⁻¹) of bare GCE and NiZnFe₂O₅ NPs/GCE in 0.1 M KCl: A) in the absence of analyte; B) in the presence of 3 mM [Fe(CN)₆]^{3-/4-}; C) with 2.5 μ M AA different volumes of PLE added; D) CV responses of NiZnFe₂O₅ NPs/GCE in 0.1 M KCl with 2.5 μ M AA for different drop-casting volumes of NiZnFe₂O NPs

In comparison to the bare GCE, the NiZnFe $_2O_5$ NPs/GCE modified electrode synthesized using different PLEs exhibits a substantially greater CV response. This enhanced performance is caused by the presence of NiZnFe $_2O_5$ NPs. Three distinct NPs with varying volumes of PLE and sensing capabilities exhibit responsiveness to a 2.5 μ M AA dose. Figure 5C clearly shows the high peak current for NiZnFe $_2O_5$ NPs synthesized using 15 ml of PLE.

The I_{pa} increases with the drop-casting volume in the range from 1.0 to 4.0 μ L. However, after 5.0 μ L, the I_{pa} gradually decreases with an increase in NiZnFe₂O₅ NPs concentration (Figure 5D). This is due to the increased resistance on GCE at higher drop-casting volumes. Thus, 4.0 μ L was used for drop-casting NiZnFe₂O₅ NPs modified GCE for further electrochemical investigations.

Electrochemical impedance spectroscopy

EIS is a widely used analytical technique for analysing the interfacial properties of the modified electrode's surface. The electron transfer characteristics of the electrode interface in 3.0 mM of $[Fe(CN)_6]^{3-/4-}$ with 0.1 M KCl and a scan rate of 0.5 V/s were examined using CV and EIS techniques. Based on the Nyquist plot, measured EIS spectra of the bare GCE and NiZnFe₂O₅NPs/GCE are displayed in Figure 6. Randles equivalent circuit in Figure 6 gives the R_{ct} values of 148.1 and 84.44 Ω for bare/GCE and NiZnFe₂O₅NPs/GCE, respectively.

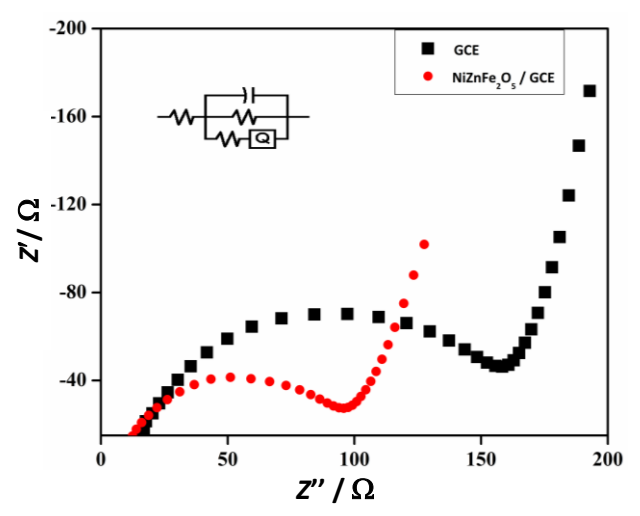


Figure 6. Impedance spectra of bare GCE and NiZnFe₂O₅ NPs/GCE in 0.1M KCl with 3 mM [Fe(CN)₆]^{3-/4-} and Randles equivalent circuit (insert)

Effect of scan rate

The electrocatalytic properties of NiZnFe $_2O_5$ NPs/GCE-modified electrodes were evaluated using CV in the presence of AA. CV was measured using 2.5 μ M AA in 0.1 M KCl (pH 7) with different scan rates from 0.25 to 2.0 V/s. Figure 7A indicates the increase in the peak current with the increase in the scan rate.

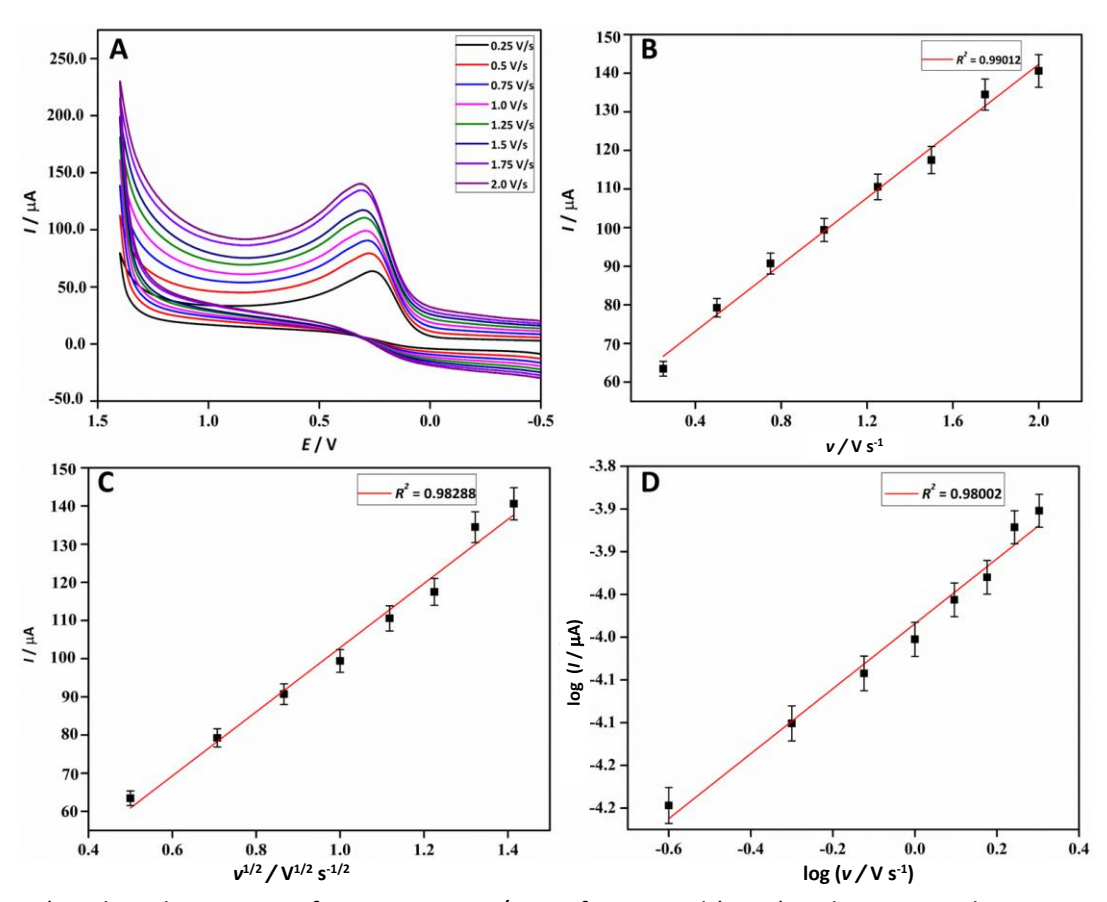


Figure 7. A) Cyclic voltammetry of NiZnFe $_2O_5$ NPs/GCE of 0.1 M KCl (pH 7) with 25μ M AA by varying the scan rates, B) anodic peak current vs. scan rate, C) anodic peak current vs. square root of scan rate.

D) anodic peak of log of anodic peak current vs. log of scan rate

Figure 7B shows a linear relationship between peak current vs. scan rate. According to Equation (4), the obtained regression coefficient value is 0.99012 (I_{pa}). Scan rate tests were conducted to

determine whether the process occurring on the surface of NiZnFe₂O₅NPs/GCE is diffusion-controlled or controlled by adsorption. Figure 7C indicates the direct correlation between the square root of the scan rate vs. peak current and from Equation (5), the exhibited correlation coefficient R² is 0.9828. A plot of the logarithm of scan rate vs. logarithm of scan rate peak current (Figure 7D) results in a straight line with a slope of 0.3814 in Equation (6). The obtained value of 0.3814 is near the theoretical value of 0.5 for a directly diffusion-driven process [17,18].

$$I_{pa} = 4.32266 \times 10^{-5} v + 5.58643 \times 10^{-5} (R^2 = 0.99012)$$
 (4)

$$I_{pa} = 8.40129 \ v^{1/2} + 1.88862 \ (R^2 = 0.98288)$$
 (5)

$$\log I_{\text{pa}} = 0.38014 \log v - 3.98423 (R^2 = 0.98002)$$
 (6)

Effect of ascorbic acid concentrations

The electrochemical behaviour of the modified electrode was examined by varying the analyte concentration from 0.8 to 6.2 μ M at a scan rate of 0.5 V/s. The peak current linearly increases with the increase in the concentration of AA from 0.8 to 6.2 μ M, as shown in Figure 8A. According to the data, NiZnFe₂O₅ NPs/GCE electrode acts as electrocatalysts for the electrochemical detection of AA. Figure 8B shows the calibration plot of current *vs.* concentration. It gives a linear relationship between concentration and current, and the regression coefficient value calculated using Equation (7) is 0.99592.

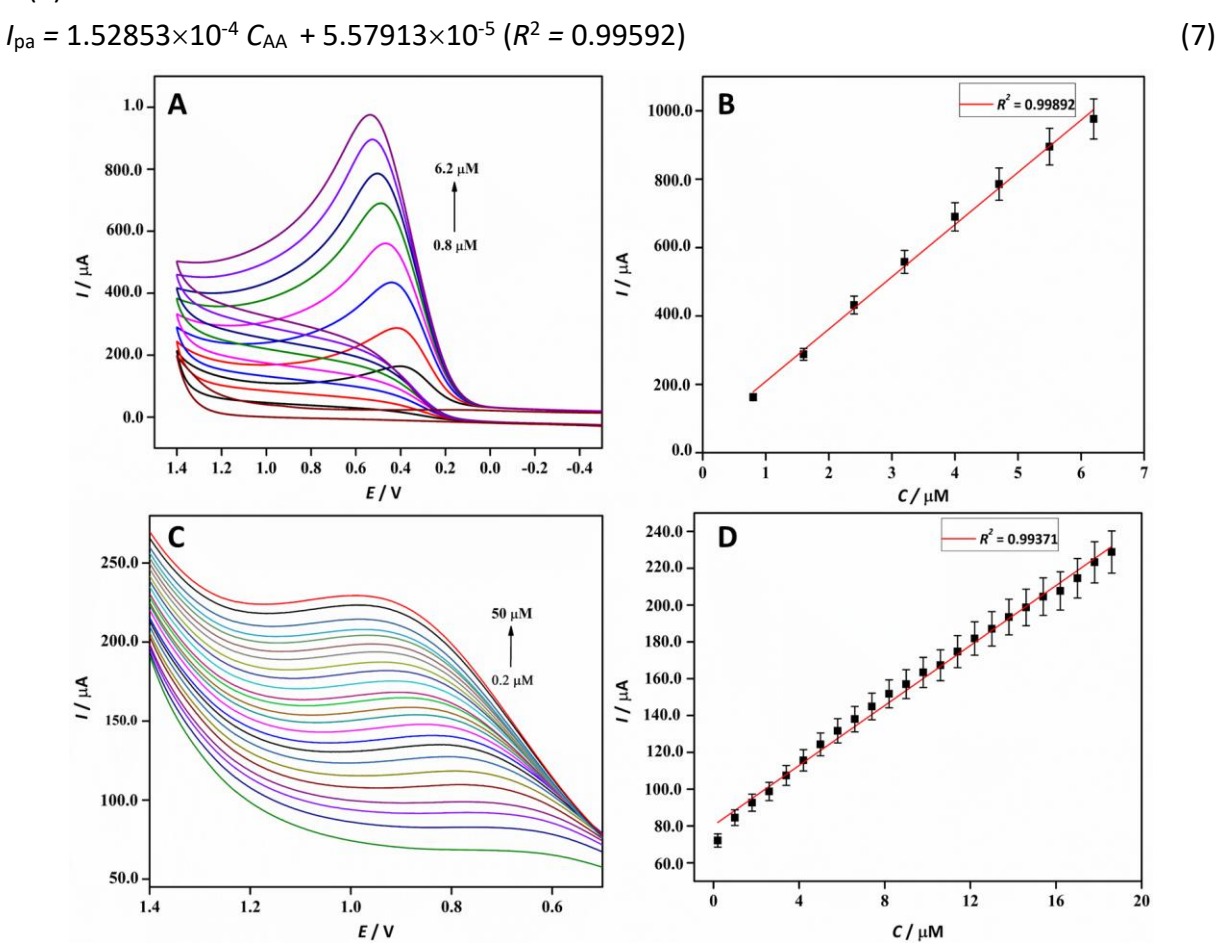


Figure 8. A) Cyclic voltammetry of NiZnFe₂O₅ NPs/GCE of 0.1 M KCl (pH 7) by varying the concentration of AA at scan rate 0.5 V s⁻¹; B) calibration plot of anodic peak current vs. concentration of AA; C) DPV representation of NiZnFe₂O₅ NPs/GCE for AA at a concentrations of 0.2-50.0 μM in (0.1 M KCl, pH 7) at scan rate of 0.5 V/s; D) calibration plot of DPV of current vs. AA concentration

The electrochemical response of AA on NiZnFe₂O₅ NPs/GCE was examined by the DPV technique. The peak current linearly increases with the increasing concentration of AA from 0.2 to 50.0 μ M in 0.1 M KCl (pH 7). As shown in Figure 8C, the electrochemical activity of NiZnFe₂O₅ NPs/GCE, which improves the electroanalytical function for AA oxidation, caused an increase in the I_{pa} with an increase in the concentration of AA. A linear plot of I_{pa} versus AA concentration is displayed in Figure 8D, similar to the other results from the literature [19,20]. The equivalent equation for the linear regression is Equation (8), which had a range of 0.2 to 50.0 μ M.

$$I_{pa} = 8.14601 \times 10^{-6} C_{DPV} + 8.03002 \times 10^{-5} (R^2 = 0.99371)$$
 (8)

The limit of detection, i.e. the lowest concentration of DPV can be determined using Equation (9):

$$LOD = 3.3 \,\sigma/S \tag{9}$$

where σ is the standard deviation of the response and S is the slope of the calibration curve. The limit of detection calculated using Equation (9) gives the value of 1.03897 μ M. The NiZnFe₂O₅ NPs/GCE electroanalytical potential was contrasted to those of previously released sensors to determine AA. Because NiZnFe₂O₅ NPs have a higher surface area, more active sites, and higher catalytic activity, the NiZnFe₂O₅ NPs/GCE performs better. Table 2 compares a few different AA electrochemical sensors. Our DPV sensor observes a larger linear dynamic range concentration than the previously published AA sensors. These findings could be explained by a notable rise in the GCE's active surface area when the NiZnFe₂O₅ NPs are present [21-29].

Table 2. Analysing the sensor's performance with other electrochemical sensors

Modified electrode	Method	Linear range, μM,	LOD, μM	Ref.
CCE/WCNT	DPV	15 to 100	7.71	[21]
GCE/CNO-NiMoO ₄ -MnWO ₄	DPV	1 to 100	0.33	[22]
GCE/ZnS/rGO/CTAB	Amperometry	50 to 1000	30.00	[23]
GCE/rGO/Au-Pd	DPV	50 to 290	2.83	[24]
SPCE	CV	0 to 10000	1360.00	[25]
CCE/BN	DPV	30 to 1000	3.76	[26]
GCE/TiO ₂ -RuO ₂	Amperometry	10 to 1500	1.80	[27]
e-GPE	DPV	20 to 400	2.00	[28]
GCE/MWCNT/CTAB-CO	DPV	5 to 300	1.00	[29]
xNiZnFe ₂ O ₅ NPs/GCE	DPV	0.2 to 50.0	1.03897	Present

e-GCE - exfoliated graphite paper electrode, CCE - Ceramic carbon electrode, BN - Boron nitride, GCE- Glassy carbon electrode, BN - Boron nitride, SPCE - Screen-printed carbon electrode

Scheme 1 illustrates the probable electrochemical oxidation pathway of AA at NiZnFe $_2O_5$ NPs/GCE. It is clear that AA is catalytically oxidized into dehydroascorbic acid by removing two electrons.

Scheme 1. Electrochemical oxidation of AA

Effect of Interference, reproducibility, pH and storage stability studies

CV was used to evaluate the selectivity of the NiZnFe $_2$ O $_5$ NPs/GCE sensor on AA in the presence of different biological compounds and certain metals. The CV curves of 2.5 μ M AA and threefold

concentrations of different interfering compounds, such as glucose, aspirin, cerium, copper, and molybdenum, are displayed in Figure 9A. Five distinct NiZnFe $_2O_5$ NPs/GCE were tested for repeatability using CV in 2.5 μ M AA Figure 9B. A tiny change in the current response magnitude is anticipated for each of the five electrodes. It confirms the five NiZnFe $_2O_5$ NPs/GCE-modified GCE electrodes show good repeatability. The stability of the NiZnFe $_2O_5$ NPs/GCE was tested for about 22 days, as shown in Figure 9C. The CV was taken every 3-day intervals. It showed a small decrease in peak current intensity as good stability with the associated I_{pa} values at 100, 99.9, 98.8, 98.2, 97.99, 97.75 and 96.88 % current height. The current intensity of 96.88 % based on the original value was maintained after 22 days of storage, indicating that the NiZnFe $_2O_5$ NPs/GCE sensor has excellent storage stability. The pH of the analyte significantly influences the peak current and potential. Figure 9D shows the pH dependence of the current peak height. The current increased significantly when the pH increased from 3.0 to 7.0 and gradually decreased from 7.0 to 13.0. It is noted that pH 7.0 is the ideal pH value for an accurate, well-resolved, high-intense signal. The present prominent oxidation peak for AA was observed at pH 7.0. These observations led to using 0.1 M KCl (pH 7) in all electrochemical experiments conducted in this study.

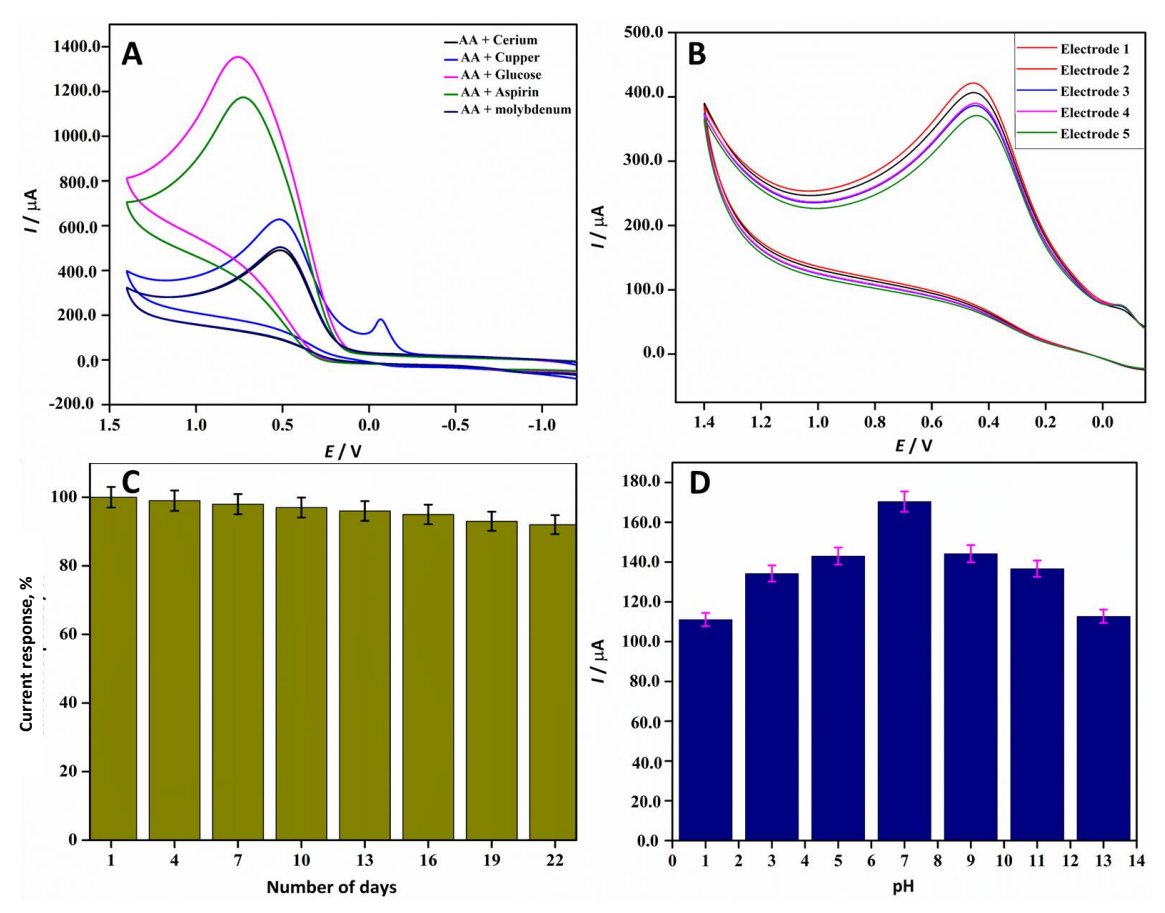


Figure 9. A) Selectivity of AA (2.5 μ M) detection at NiZnFe₂O₅ NPs/GCE in 0.1 M KCl, in presence of three-times higher concentrations of denoted interferents; B) repeatability of five separate NiZnFe₂O₅ NPs/GCE in 0.1 M KCl and 2.5 μ M AA; C) storage stability of NiZnFe₂O₅ NPs/GCE for AA detection; D) pH dependence of current peak height of 2.5 μ M AA at NiZnFe₂O₅ NPs/GCE in 0.1 M KCl

Real sample analysis

Orange fruit extract and vitamin C tablets were used for real sample analysis. The samples were analysed using a NiZnFe₂O₅ NPs/GCE modified electrode. CV evaluated the viability of using the NiZnFe₂O₅ NPs/GCE electrochemical sensor for the real-time detection of AA in real samples, including orange fruit and vitamin C tablets. The consistent findings are shown in Figure 10A. Prior



to the study, real samples were taken, and the samples showed no signs of AA [30]. The real samples were then spiked with an identified concentration of AA, and the electrochemical reactions were examined. The CV response and linear plot for orange fruit juice samples containing AA (1, 2, 3, 4, and 5 μ M) are displayed in Figure 10B. Similar to this, Figure 10C and Figure 10D show the CV curves of vitamin C tablet samples spiked with AA (1, 2, 3, 4, and 5 μ M) together with the matching linear plot. Table 3, which summarises the recovery results of the orange fruit juice and vitamin C tablet, shows that the NiZnFe₂O₅ NPs/GCE have a notable recovery for detecting AA in real samples.

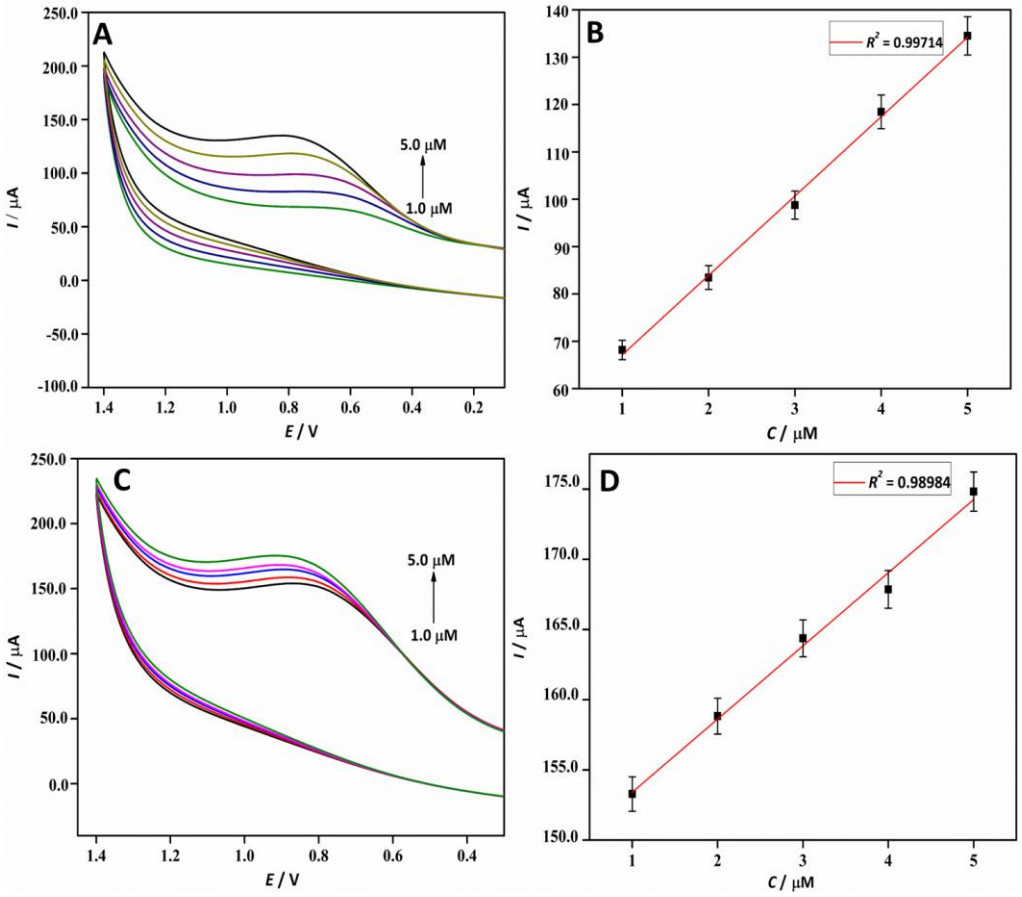


Figure 10. A) Cyclic voltammetry (0.5 V s^{-1}) of NiZnFe₂O₅ NPs/GCE in orange juice with varying concentrations of added AA; B) calibration plot of current vs. concentration of AA in orange juice sample; C) CVs (0.5 V s^{-1}) of AA tablet sample with varying concentrations of added AA; D) calibration plot of current vs. AA concentration in AA-tablet sample

Table 3. Ascorbic acid detection in a variety of real samples using the NiZnFe₂O₅ NPs/GCE

Pool cample	Amount, μM		Doggvery 0/	
Real sample	Added	Found	Recovery, %	
	1	1.23	123.00	
	2	2.20	110.00	
Orange juice	3	3.19	106.33	
	4	4.26	106.50	
	5	5.21	104.20	
	1	1.34	134.00	
	2	2.29	114.50	
Vitamin C tablet	3	3.26	108.66	
	4	4.31	107.75	
	5	5.32	106.40	

The linear regression coefficient follows Equations (10) and (11).

$$I_{pa} = 1.67686 C_{OJ} + 5.03633 \times 10^{-5} (R^2 = 0.99714)$$
 (10)

$$I_{pa} = 5.21224 \times 10^{-6} C_{AA} + 1.48195 \times 10^{-4} (R^2 = 0.98984)$$
 (11)

Conclusion

The present studies developed NiZnFe $_2O_5$ NPs using papaya leaf extract to investigate their potential for electrochemical sensing. The NiZnFe $_2O_5$ NPs electrochemical properties were examined by CV, EIS, and DPV. Their characterization was done by utilizing a variety of spectrophotometric methods, including XRD, SEM, EDX, UV-Vis DRS, and DLS. The NiZnFe $_2O_5$ NPs-modified GCE was used to detect AA. The DPV results, notably, showed a broad linear range from 0.2 to 50 μ M and a low LOD of 1.03897 μ M for AA detection. The suggested sensor also demonstrated excellent repeatability, strong stability, and anti-interfering activity. Moreover, the developed sensor's real-time applicability for calculating the AA content of AA and orange fruit(juice), with results showing notable recovery.

Acknowledgment: The authors are greatly thankful to Sri Jayachamarajendra College of Engineering (SJCE), JSS Science and Technology University, Mysuru.

Competing financial interests: The authors declare no competing financial interest.

Author Contribution: G. N. Chandana: Conducted the chemical experiment and tabulated data. S Jeevitha and M.S. Asha: Conducted the chemical experiment. M. B. Shivaswamy: Prepared the manuscript and analysed the characterization data. H.S. Nagendra Prasad: Supervisor and Design, lead the entire project and reviewed the manuscript. M. A. Sangamesha: Performed electrochemical analysis. B.S. Hemanth: Reviewed and improved the quality of the manuscript. B.S. Madhukar: Reviewed the manuscript L Mallesha: Reviewed the manuscript. J G Manjunath: Reviewed the manuscript and improved the quality of the manuscript.

References

- [1] P. G. Jamkhande, N. W. Ghule, A. H. Bamer, M. G. Kalaskar, Metal nanoparticles synthesis: An overview on methods of preparation, advantages and disadvantages, and applications, *Journal of Drug Delivery Science and Technology* **53** (2019) 101174. https://doi.org/10.1016/j.jddst.2019.101174
- [2] S. A. Farhan, R. Dadoosh, A. jassim, Evaluation of Phytochemical, Total phenolic and Antioxidant Activity of Carica Papaya Seed for Its Use in Biosynthesis of Gold Nanoparticles, *Egyptian Journal of Chemistry* **64** (2021) 4301-4310. https://doi.org/10.21608/ejchem.2021.63985.3371
- [3] G. Kesavan, N. Nataraj, S.-M. Chen, L.-H. Lin, Hydrothermal synthesis of NiFe ₂ O ₄ nanoparticles as an efficient electrocatalyst for the electrochemical detection of bisphenol A, *New Journal of Chemistry* **44** (2020) 7698-7707. https://doi.org/10.1039/D0NJ00608D
- [4] S. Z. Bas, N. Yuncu, K. Atacan, M. Ozmen, A comparison study of MFe2O4 (M: Ni, Cu, Zn)-reduced graphene oxide nanocomposite for electrochemical detection of bisphenol A, *Electrochimica Acta* **386** (2021) 138519. https://doi.org/10.1016/j.electacta.2021.138519
- [5] M. Derakhshi, T. Jamali, M. Elyasi, M. Bijad, R. Sadeghi, A. Kamali, K. Niazazari, M. R. Shahmiri, A. Bahari, S. Mokhtari, Synthesis and Characterization of NiO Nanoparticle as a High Sensitive Voltammetric Sensor for Vitamin C Determination in Food Samples, *Journal of the Serbian Chemical Society* 8 (2013) 8252-8263. https://doi.org/10.1016/S1452-3981(23)12884-7



- [6] T. Peik-See, A. Pandikumar, H. Nay-Ming, L. Hong-Ngee, Y. Sulaiman, Simultaneous Electrochemical Detection of Dopamine and Ascorbic Acid Using an Iron Oxide/Reduced Graphene Oxide Modified Glassy Carbon Electrode, *Sensors* **14** (2014) 15227-15243. https://doi.org/10.3390/s140815227
- [7] M. Dosedel, E. Jirkovsky, K. Macakova, L. Krcmova, L. Javorska, J. Pourova, L. Mercolini, F. Remiao, L. Novakova, P. Mladenka, Vitamin C-Sources, Physiological Role, Kinetics, Deficiency, Use, Toxicity, and Determination, *Nutrients* **13** (2021) 615. https://doi.org/10.3390/nu13020615.
- [8] S. Jeevitha, H. S. Nagendra Prasad, M. B. Shivaswamy, M. S. Asha, S. R. Arjun, G. N. Chandana, M. A. Sangamesha, B. S. Madhukar, B. S. Hemanth, Sabu Thomas, Facile green preparation of ZnFe2O4 nanoparticles using papaya leaf extract for electrochemical detection of acetaminophen in Zerodol P and Dolo drops, *Ionics* **30** (2024) 8617-8630. https://doi.org/10.1007/s11581-024-05879-6
- [9] P. Sivakumar, R. Ramesh, A. Ramanand, S. Ponnusamy, C. Muthamizhchelvan, Preparation and properties of nickel ferrite (NiFe2O4) nanoparticles via sol-gel auto-combustion method, *Materials Research Bulletin* 46 (2011) 2204-2207. https://doi.org/10.1016/j.materresbull.2011.09.010
- [10] H. M. Zaid, M. Adil, K. C. Lee, Structural and morphological evolution of metal oxide nanoparticles synthesised via sol-gel auto-combustion, *International Journal of Nanotechnology* **14** (2017) 284. https://doi.org/10.1504/IJNT.2017.082478
- [11] H. R. Ebrahimi, M. Parish, G. R. Amiri, B. Bahraminejad, S. Fatahian, Synthesis, characterization and gas sensitivity investigation of Ni_{0.5}Zn_{0.5}Fe₂O₄ nanoparticles, *Journal of Magnetism and Magnetic Materials* **414** (2016) 55-58. https://doi.org/10.1016/j.jmmm.2016.04.043
- [12] S. Alaei, M. Haghighi, J. Toghiani, B. Rahmani Vahid, Magnetic and reusable MgO/MgFe2O4 nanocatalyst for biodiesel production from sunflower oil: Influence of fuel ratio in combustion synthesis on catalytic properties and performance, *Industrial Crops and Products* **117** (2018) 322-332. https://doi.org/10.1016/j.indcrop.2018.03.015
- [13] S. Landi, I. R. Segundo, E. Freitas, M. Vasilevskiy, J. Carneiro, C. J. Tavares, Use and misuse of the Kubelka-Munk function to obtain the band gap energy from diffuse reflectance measurements, *Solid State Communications* **341** (2022) 114573. https://doi.org/10.1016/j.ssc.2021.114573
- [14] B. S. Hemanth, M. J. Deviprasad, M. B. Shivaswamy, H. S. Nagendra Prasad, S. Sumathi, R. Aswathy, M. A. Sangamesha, A. P. Ananda, H. S. Jayanth, T. N. Lohith, Synthesis of citral-tryptamine fused selenium nanospheres (CT@SeNP's) and exploration of their anticancer, antibacterial, and electrochemical sensor applications, *Journal of Molecular Structure* 1310 (2024) 138240. https://doi.org/10.1016/j.molstruc.2024.138240
- [15] M. P. Ujwal, S. R. Yashas, H. P. Shivaraju, N. Kumara Swamy, Gadolinium ortho-ferrite interfaced polyaniline: Bi-functional catalyst for electrochemical detection and photocatalytic degradation of acetaminophen, *Surfaces and Interfaces* **30** (2022) 101878. https://doi.org/10.1016/j.surfin.2022.101878
- [16] M. K. Manju, J.G. Manjunatha, K. Bhimaraya, S. A. Aldossari, S. Mohammad, M. Sillanpää, Simultaneous electrochemical detection of hydroquinone and catechol using a carbon nanotube paste electrode modified with electrochemically polymerized L-alanine, *Chemical Papers* **78** (2024) 8019-8030. https://doi.org/10.1007/s11696-024-03652-7
- [17] A. A.Rashak, F. F. Karam, Preparation of graphene oxide and multi-walled carbon nanotubes, and they are used to modify the glassy carbon electrode for sensing Enalapril Maleate, *Results in Chemistry* **8** (2024) 101597. doi.org/10.1016/j.rechem.2024.101597

- [18] R. Santhosh Kumar, K. Govindan, S. Ramakrishnan, A. R. Kim, J.-S. Kim, D. J. Yoo, Fe3O4 nanorods decorated on polypyrrole/reduced graphene oxide for electrochemical detection of dopamine and photocatalytic degradation of acetaminophen, *Applied Surface Science* **556** (2021) 149765. https://doi.org/10.1016/j.apsusc.2021.149765
- [19] M. B. Shivaswamy, P. Karthikdev, B. S. Madhukar, B. S. Hemanth, M. J. Deviprasad, R. Kavya, M. A. Sangamesha, A. P. Anand, H. P. Spoorthy, H. S. Nagendra Prasad, Silver fused multifunctional CeIn2O5 nanoparticle: Photocatalytic, antibacterial and electrochemical sensor studies, *Chemistry of Inorganic Materials* 2 (2024) 100042. https://doi.org/10.1016/j.cinorg.2024.100042
- [20] S. Kubendhiran, R. Sakthivel, S.-M. Chen, R. Anbazhagan, H.-C. Tsai, A novel design and synthesis of ruthenium sulfide decorated activated graphite nanocomposite for the electrochemical determination of antipsychotic drug chlorpromazine, *Composites Part B: Engineering* **168** (2019) 282-290. https://doi.org/10.1016/j.compositesb.2018.12.082
- [21] B. Habibi, M. H. Pournaghi-Azar, Simultaneous determination of ascorbic acid, dopamine and uric acid by use of a MWCNT modified carbon-ceramic electrode and differential pulse voltammetry, *Electrochimica Acta* **55** (2010) 5492-5498. https://doi.org/10.1016/j.electacta.2010.04.052
- [22] M. Saleh Mohammadnia, E. Marzi Khosrowshahi, E. Naghian, A. Homayoun Keihan, E. Sohouli, M. E. Plonska-Brzezinska, A. Sobhani-Nasab, M. Rahimi-Nasrabadi, F. Ahmadi, Application of carbon nanoonion-NiMoO4-MnWO4 nanocomposite for modification of glassy carbon electrode: Electrochemical determination of ascorbic acid, *Microchemical Journal* 159 (2020) 105470. https://doi.org/10.1016/j.microc.2020.105470
- [23] Y. J. Yang, One-pot synthesis of reduced graphene oxide/zinc sulfide nanocomposite at room temperature for simultaneous determination of ascorbic acid, dopamine and uric acid, *Sensors and Actuators B* **221** (2015) 750-759. https://doi.org/10.1016/j.snb.2015.06.150.
- [24] L. Zhang, G. Wang, D. Wu, C. Xiong, L. Zheng, Y. Ding, H. Lu, G. Zhang, L. Qiu, Highly selective and sensitive sensor based on an organic electrochemical transistor for the detection of ascorbic acid, *Biosensors and Bioelectronics* **100** (2018) 235-241. https://doi.org/10.1016/j.bios.2017.09.006
- [25] J. K. Jadav, V. V. Umrania, K. J. Rathod, B. A. Golakiya, Development of silver/carbon screen-printed electrode for rapid determination of vitamin C from fruit juices, *LWT Food Science and Technology* **88** (2018) 152-158. https://doi.org/10.1016/j.lwt.2017.10.005
- [26] M. S. Raghu, L. Parashuram, K. Y. Kumar, B. P. Prasanna, S. Rao, P. Krishnaiah, K. N. Prashanth, C. B. P. Kumar, H. Alrobei, Facile green synthesis of boroncarbonitride using orange peel; Its application in high-performance supercapacitors and detection of levodopa in real samples, *Materials Today Communications* 24 (2020) 101033. https://doi.org/10.1016/j.mtcomm.2020.101033
- [27] P. Shakkthivel, S.-M. Chen, Simultaneous determination of ascorbic acid and dopamine in the presence of uric acid on ruthenium oxide modified electrode, *Biosensors and Bioelectronics* **22** (2007) 1680-1687. https://doi.org/10.1016/j.bios.2006.07.026
- [28] A. Murali, Y. P. Lan, P. K. Sarswat, M. L. Free, Synthesis of CeO2/reduced graphene oxide nanocomposite for electrochemical determination of ascorbic acid and dopamine and for photocatalytic applications, *Materials Today Chemistry* **12** (2019) 222-232. https://doi.org/10.1016/j.mtchem.2019.02.001
- [29] B. Kaur, T. Pandiyan, B. Satpati, R. Srivastava, Simultaneous and sensitive determination of ascorbic acid, dopamine, uric acid, and tryptophan with silver nanoparticles-decorated reduced graphene oxide modified electrode, *Colloids and Surfaces B: Biointerfaces* **111** (2013) 97-106. https://doi.org/10.1016/j.colsurfb.2013.05.023



[30] V. Vinothkumar, R. Sakthivel, S.-M. Chen, T. H. Kim, M. Abinaya, S. Kubendhiran, G. Gopu, Nanoarchitectured nickel phosphate integrated with graphene oxide for the toxicant diphenylamine detection in food samples, *Journal of Food Composition and Analysis* 111 (2022) 104628. https://doi.org/10.1016/j.jfca.2022.104628

©2024 by the authors; licensee IAPC, Zagreb, Croatia. This article is an open-access article distributed under the terms and conditions of the Creative Commons Attribution license (https://creativecommons.org/licenses/by/4.0/)



Open Access :: ISSN 1847-9286 www.jESE-online.org

Original scientific paper

Screen printed graphite electrode modified with two-dimensional leaf-like zeolitic imidazolate framework-L (Zn) for efficient electrochemical sensing of sulphite

Satar Jabbar Rahi Algraittee^{1,2}, Ban Waheed Hussein Bdair³, Firas Abdul Abass Sukir⁴, Raed Muslim Mhaibes^{5,⊠}, Mustafa Mudhafar^{6,7} and Qais R. Lahhob⁸

⁸Collage of Pharmacy, National University of Science and Technology, 64001 Dhi Qar, Iraq

Corresponding author: [™]Raid.mcm@uomisan.edu.iq; Tel./Fax: +009647721014811

Received: November 30, 2024; Accepted: December 21, 2024; Published: February 23, 2025

Abstract

In this paper, we describe the use of a screen-printed graphite electrode modified with a two-dimensional leaf-like zeolitic imidazolate framework-L (Zn), ZIF-L (Zn) for the determination of sulphite. We started by using linear sweep voltammetry to investigate the redox properties of the modified electrode at different scan rates (10 to 400 mV s⁻¹). Next, we evaluated sulphite oxidation at the modified electrode. Using differential pulse voltammetry (DPV), the linear dynamic range of 0.04-900.0 μ M and the limit of detection (3s/m) of 0.01 μ M were obtained. DPV was also used to quantify sulphite in various real samples using the standard addition method.

Keywords

Differential pulse voltammetry; metal-organic frameworks; electrochemical sensors; chemically modified electrodes; real sample analysis

Introduction

Food safety is a significant concern for consumers worldwide and health organizations. According to the World Health Organization (WHO), over 200 diseases can be transmitted to humans through food, and many people are unknowingly infected with foodborne illnesses. Food additives and

¹College of Medicine, University of Kerbala, Kerbala, Iraq

²College of Medicine, University of Al-Ameed, Kerbala, Iraq

³Department of Medical Microbiology, College of Medicine, University of Kerbala, Kerbala, Iraq

⁴Department of Radiology, College of Health & Medical Technology, Sawa University, Iraq

⁵Department of Biochemistry, College of Medicine, Misan University, Misan, Iraq

⁶Department of Medical Physics, Faculty of Medical Applied Sciences, University of Kerbala, 56001 Karbala, Iraq

⁷Department of Anaesthesia Techniques and Intensive Care, Al-Taff University College, 56001 Kerbala, Iraq

preservatives are substances added to certain foods in small quantities to extend their shelf life. These additives and preservatives are crucial for maintaining the quality, appearance, taste, safety, and flavour of food over time [1]. Sulphite is a key additive in many food products because it effectively prevents enzymatic and non-enzymatic browning during processing and storage. However, sulphite can trigger asthmatic reactions in a small percentage of individuals, and excessive amounts may lead to undesirable off-flavours in food. Furthermore, some sulphite added can diminish due to reversible and irreversible chemical reactions. Therefore, accurately measuring the sulphite levels in foods is often essential [2].

Common analytical methods for detecting sulphite include high-performance liquid chromate-graphy (HPLC)/ultraviolet spectrophotometric, colorimetric, fluorescent, HPLC-DAD-MS/MS, liquid chromatography-tandem mass spectrometry (LC/MS/MS), and LC-ICP-MS [3-9]. However, many of these techniques have drawbacks, such as the need for expensive equipment, lengthy result times, the use of hazardous solvents, and the requirement for highly skilled personnel. In contrast, electrochemical methods offer significant advantages, including simple sample preparation, relatively low instrument costs, rapid detection, and ease of miniaturization. These techniques are robust and versatile analytical tools that deliver high sensitivity and accuracy, a broad linear dynamic range (LDR), and cost-effective instrumentation. Electroanalytical sensors that utilize pulse techniques are particularly prevalent in the analysis of drugs in real samples [10].

Carbon electrodes have become increasingly popular for several reasons. They are easily modified, exhibit low background current, allow for simple renewal, show chemical stability, and are sensitive and cost-effective. These benefits make chemically modified carbon electrodes widely used for detecting a variety of analytes, such as food additives, vitamins, drugs, dyes, and amino acids [11].

One way to enhance the analysis in electroanalytical techniques is through the use of screen-printed carbon electrodes (SPGEs), which offer a simpler alternative to traditional electrochemical cells. SPGEs are relatively inexpensive, easy to manufacture, and suitable for mass production, aligning with green chemistry principles such as the development of safe products. Additionally, SPGEs enable fast analysis with a linear response, high sensitivity, low energy consumption, and effective operation at room temperature. These advantages contribute to their widespread application in various fields. Moreover, when paired with miniaturized potentiostats, SPGEs provide portability, making them ideal for point-of-care (POC) analysis. This technology has already seen commercial and academic applications [12].

Despite these advantages, electrochemical detection of analytes with bare electrodes often faces challenges related to poor sensitivity and reproducibility. Modifying the electrode surface can help reduce overvoltage and enhance the kinetics of various electrode processes [13]. Nanotechnology is a promising field that has shown significant progress and potential across many domains [14]. Recent advances in nanoscience provide new opportunities for electroanalytical techniques by facilitating electron transfer and thus improving sensitivity and selectivity. In electrochemistry, these benefits arise from an increased surface-to-volume ratio, which enhances the overall rate of diffusion processes, as well as from the greater number of molecules that can attach to or adsorb on inorganic nanoparticles [15].

Due to numerous exposed metal sites, metal-organic frameworks (MOFs) have recently gained attention for their well-defined structures, large specific surface areas, and strong catalytic activity. These advantages make MOFs widely applicable in solar cells, catalysis, biopharmaceuticals, biosensors and electrochemical sensor development. Zeolitic imidazolate frameworks (ZIFs) are a subclass of MOFs that also share many of their general properties and demonstrate excellent

thermal and chemical stability, making them particularly promising for adsorption applications. ZIFs are especially well-suited for electrochemical sensing because of their excellent dispersion and high adsorption capacity for small molecules [16].

A ZIF-L (Zn) modified screen-printed graphene electrode (SPGE) was created, resulting in a sensitive method for the electrochemical analysis of sulphite. The modified electrode demonstrated improved electrochemical performance for sulphite detection compared to the unmodified SPGE. This engineered sensor was effectively used to detect sulphite in real samples.

Experimental

Chemicals and materials

All salts and solvents, including sulphite, etc., were of high purity and obtained from Merck and Sigma Aldrich. The phosphate buffer solution, PBS, was prepared using H₃PO₄ and sodium hydroxide (NaOH) in specific proportions.

Instrumentation

Cyclic voltammetry (CV), linear sweep voltammetry (LSV), differential pulse voltammetry (DPV) and chronoamprometry were used for the electrochemical analysis. The measurements were carried out with a potentiostat/galvanostat Model PGSTAT 12 Autolab electrochemical system (Eco Chemie, Utrecht, The Netherlands), utilizing software linked to GPES (Eco Chemie). Electrochemical measurements were performed using an electrochemical cell containing a screen-printed electrode (Dropsense, Spain), including a silver pseudo-reference electrode, graphite working electrode, and graphite auxiliary electrode.

Synthesis of ZIF-L (Zn)

The synthesis and characterization of ZIF-L (Zn) were detailed in our previous study [16]. Figure 1 presents the FE-SEM image of ZIF-L (Zn).

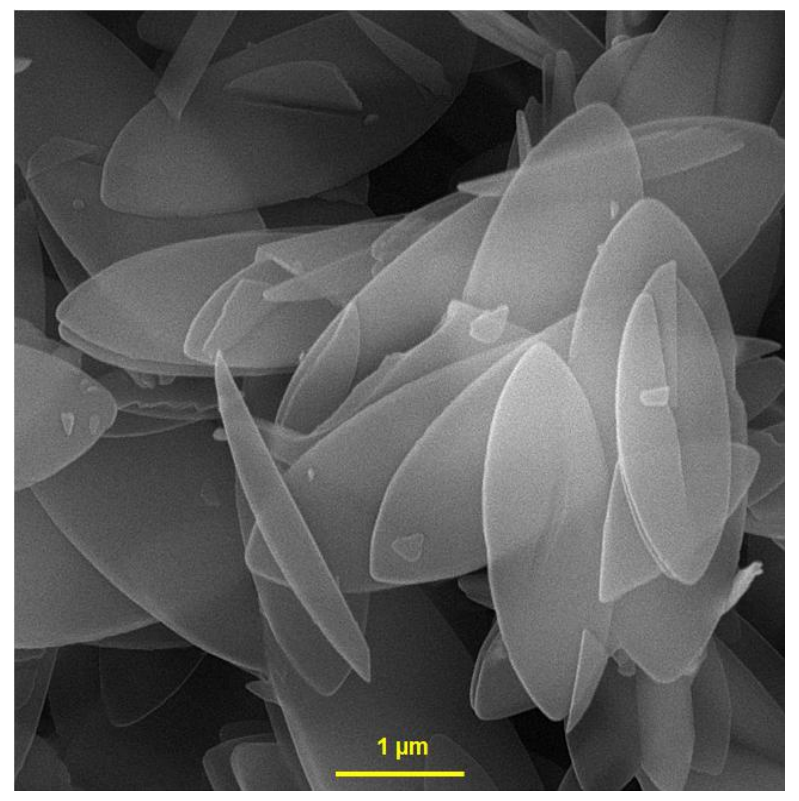


Figure 1. FE-SEM image of ZIF-L (Zn)

Preparation of modified SPGE

1.0 mg of ZIF-L (Zn) was suspended in 1000 mL of water. The suspension was dispersed using ultrasound for 20 min. Subsequently, 5 μ L of the ZIF-L (Zn) solution was applied dropwise onto the surface of the SPGE working electrode.

To determine the electroactive surface area of unmodified and modified SPGE, the CV responses of unmodified SPGE and ZIF-L (Zn) modified-SPGE were recorded for redox probe (1.0 mM K_3 [Fe(CN)₆]) in the presence of 0.1 M KCl solution at different scan rates. The Randles-Ševčik equation was applied to determine the surface areas. The electroactive surface area of unmodified SPGE (0.034 cm²) and ZIF-L (Zn) modified-SPGE (0.14 cm²) were calculated.

Procedure

All the experiments were performed at room temperature. After transferring the modified SPGE into a phosphate buffer solution, the oxidation signal of sulphite was obtained using DPV, with a scan rate of 40 mV s⁻¹ (step potential = 0.008 V and pulse amplitude = 0.01 V, initial potential = 580 mV, final potential = 960 mV). The data were baseline-corrected with GPES software. Five modified SPGEs were prepared identically, and the average signal of sulphite was obtained prior to each experiment for sulphite determination.

Results and discussion

Electrochemical oxidation of sulphite in the surface of bare SPGE and ZIF-L (Zn) modified-SPGE

Figure 2 shows the CVs in pH 7.0 PBS with 500.0 μ M sulphite. The anodic oxidation potential for bare SPGEs (trace a) is observed at 845 mV, with peak currents of 5.5 μ A, corresponding to the electrochemical oxidation of sulphite. In contrast, the ZIF-L (Zn)/SPGE (trace b) displays a peak at 750 mV, with peak currents of 11.0 μ A. This indicates that the ZIF-L (Zn)/SPGE achieves a higher peak current, making it more favourable for electroanalytical applications and potentially increasing sensitivity at lower concentrations. Therefore, modifying the SPGE with ZIF-L (Zn) enhances sensitivity and reduces overvoltage.

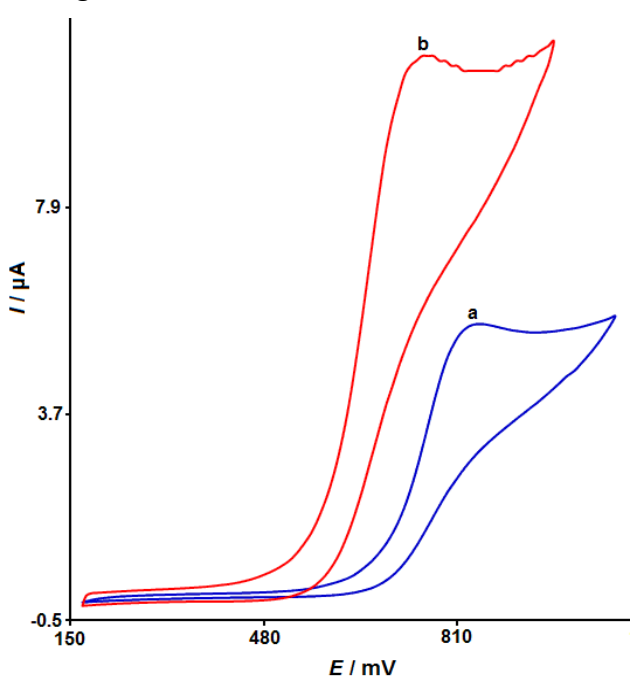


Figure 2. Cyclic voltammograms of bare SPGE (a) and ZIF-L (Zn) modified SPGE (b) for 500.0 μ M sulphite in 0.1 M PBS at pH 7.0 (scan rate: 50 mV/s)

Effect of scan rate

The influence of scan rate on the redox behaviour of 300.0 μ M sulphite was examined in 0.1 M PBS using LSV (Figure 3). As illustrated in Figure 4, the oxidation peak currents (I_p) of sulphite were directly proportional to the square root of the scan rate ($v^{1/2}$), which varied from 10 to 400 mV s⁻¹. These findings suggest that the electrochemical reaction of sulphite is a diffusion-controlled process.

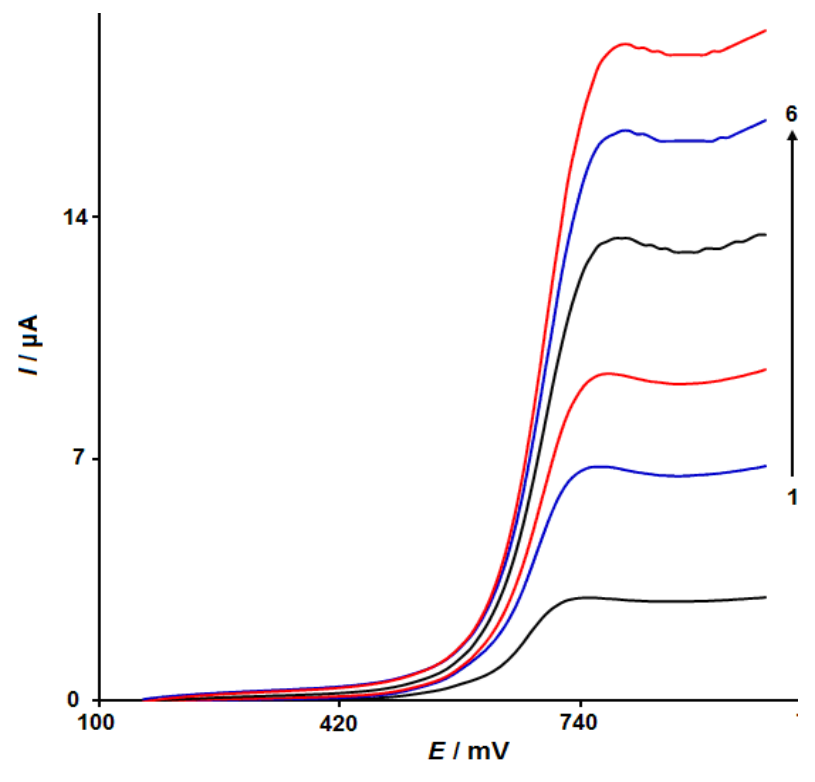


Figure 3. LSVs of ZIF-L (Zn) modified SPGE for 300.0 μ M sulphite in 0.1 M PBS at pH 7.0 at varying scan rates (1 - 10, 2 - 50, 3 - 100, 4 - 200, 5 - 300 and 6 - 400 mV/s)

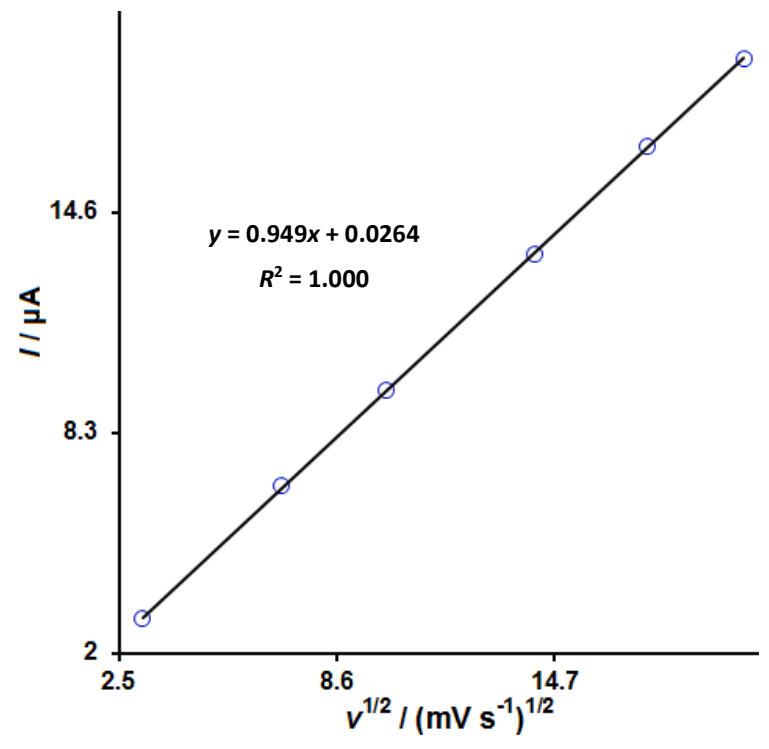


Figure 4. Linear dependence of peak currents on the square root of the scan rate

Chronoamprometry

To determine the diffusion coefficient (D) of sulphite at the ZIF-L (Zn)/SPGE, chronoamperometry was employed. Figure 5 presents the chronoamperometry studies conducted using ZIF-L (Zn)/SPGE at various sulphite concentrations, with the electrode potential set to 790 mV. The chronoamperometry data were analysed using the Cottrell equation [16]. Under diffusion-controlled conditions, the plot of current (I) versus time $t^{-1/2}$ is linear, allowing for the calculation of D from its slope. The plots of I versus $t^{-1/2}$ for sulphite are shown in Figure 6. The slopes of these linear plots were then plotted against the sulphite concentration (Figure 7), with the estimated value of D being 1.34×10^{-6} cm² s⁻¹.

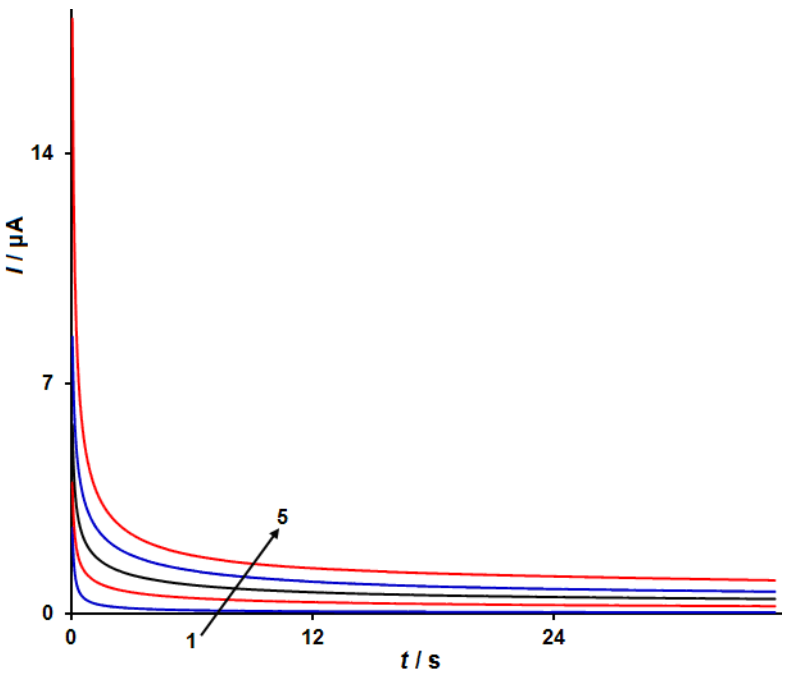


Figure 5. Chronoamperogram curves of ZIF-L (Zn) modified SPGE in 0.1 M PBS (pH 7.0) with sulphite concentrations of 1 - 0.1, 2 - 0.2, 3 - 0.3, 4 - 0.5 and 5 - 1.0 mM

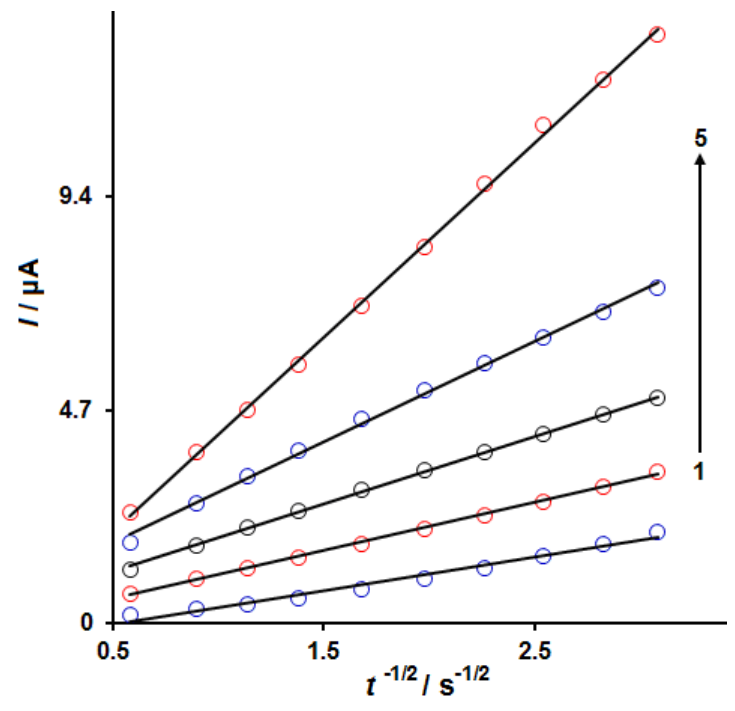


Figure 6. Plots of I versus $t^{-1/2}$ obtained from chronoamperograms for various sulphite concentrations (1 - 0.1, 2 - 0.2, 3 - 0.3, 4 - 0.5 and 5 - 1.0 mM)

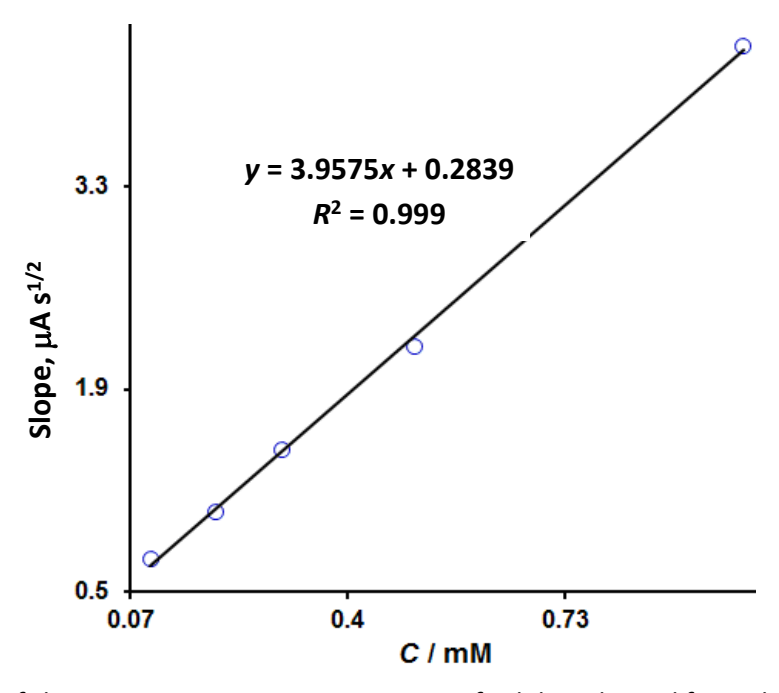


Figure 7. Plot of slope versus various concentrations of sulphite derived from chronoamperograms

DPV technique

The DPV technique was employed to quantitatively assess ZIF-L (Zn)/SPGE with varying sulphite concentrations from 0.04 to 900.0 μ M (Figure 8). A noticeable increase in peak current was observed as the sulphite concentration rose.

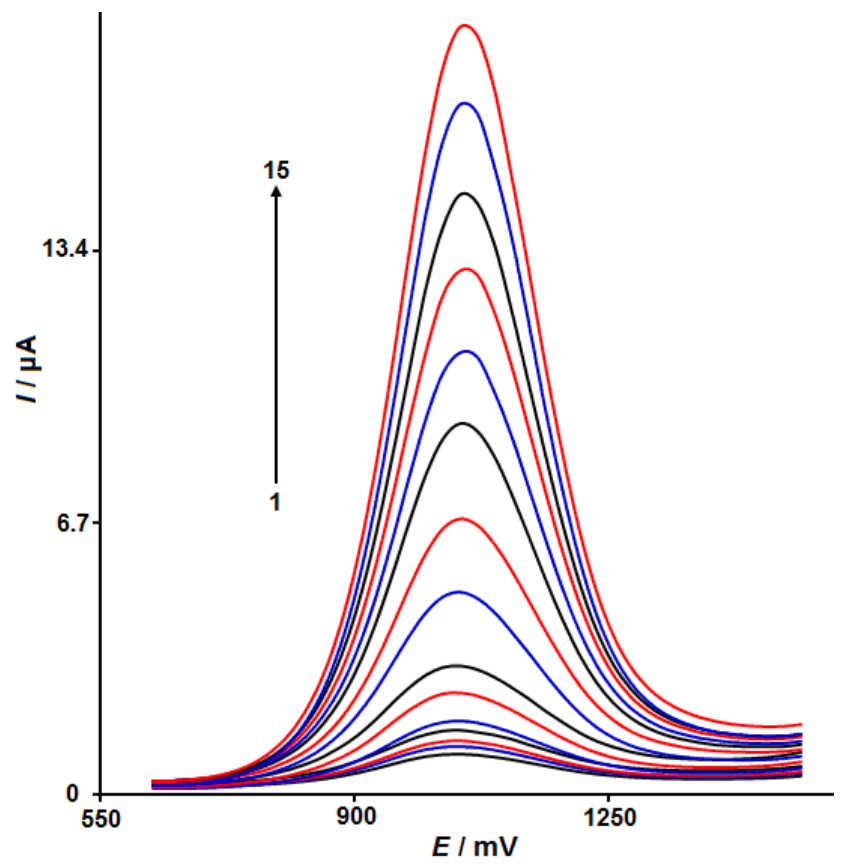


Figure 8. DPVs of ZIF-L (Zn) modified SPGE at different sulphite concentrations: 0.04, 0.5, 5.0, 15.0, 30.0, 70.0, 100.0, 200.0, 300.0, 400.0, 500.0, 600.0, 700.0, 800.0 and 900.0 μM, curves 1 to 15, respectively

As illustrated in Figure 9, the peak current signals at ZIF-L (Zn)/SPGE increased progressively with sulphite concentration, establishing a strong linear relationship within the concentration range, LDR, of 0.04-900.0 μ M. The limit of detection, LOD, was calculated to be 0.01 μ M. This value of LOD can be compared with some recent works, 16.5 μ M [17] and 3.3 μ M [18]. As can be seen, the obtained LOD in this work is better than the values obtained in these previous works.

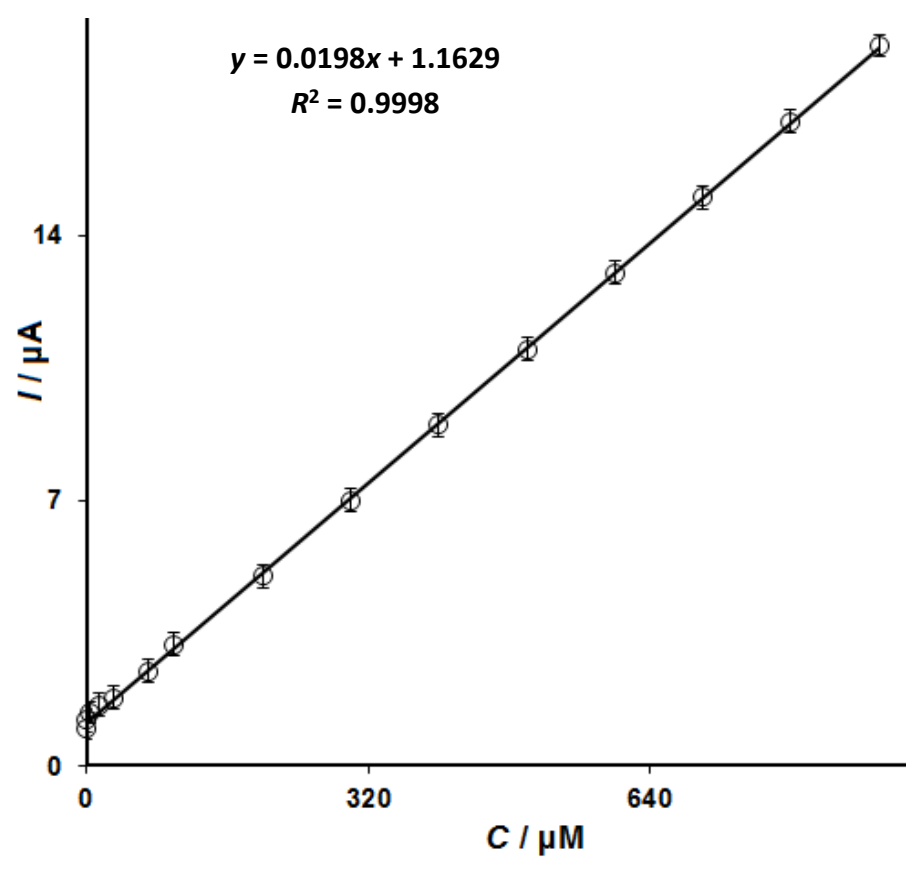


Figure 9. Plot of the linear relationship between peak current and sulphite concentrations

Stability of the ZIF-L (Zn)/SPGE

The long-term stability of the ZIF-L (Zn)/SPGE was evaluated by storing the electrode at room temperature for 6 days. After this period, the current response decreased by just 3.7 %, confirming the stability of the modified electrode.

Interference studies

Real samples contain various species that can influence the detection and sensitivity capabilities of electrodes. To study the interference effects of these species, we observed changes in the oxidation peak current of sulphite. Consequently, the anti-interference ability of the modified electrode is a critical factor affecting monitoring accuracy. This study shows that the presence of various interferences at concentrations up to several times greater than that of sulphite does not significantly impact the sensitivity and detection capabilities of the modified electrode. The tolerance limit was defined as the maximum concentration of the interfering substance that caused an approximately ± 5 % relative error in the determination. For example, in the detection of sulphite using modified, a 20-fold concentration of KCl, MgCl₂, NaNO₃, NaCl, CaCl₂, Na₂SO₄, fructose, citric acid, tartaric acid, glucose, malic acid, iodide, oxalic acid, nitrite, sulphide, thiosulfate, and bromide resulted slight changes in the peak current (less than 5 %). Table 1 shows the effect of some possible interfering compounds on the signal change of sulphite (30.0 μ M).

Table 1. The effect of some possible interfering compounds in determination of 20 time lower concentration of sulphite (30.0 μ M) in phosphate buffer solution (0.1 M with pH 7.0)

Interfering compounds	Signal change, %
KCI	2.2
$MgCl_2$	2.7
NaNO₃	3.1
NaCl	1.9
CaCl₂	3.0
Na ₂ SO ₄	4.2
Fructose	4.1
Citric acid	4.3
Tartaric acid	3.4
Glucose	3.1
Malic acid	4.9
Iodide	2.2
Oxalic acid	3.1
Nitrite	2.6
Sulphide	4.0
Thiosulfate	2.1
Bromide	3.2

Analysis of real samples

To assess the usability of the ZIF-L(Zn)/SPGE sensor for determining sulphite in real samples, the DPV technique was applied to various water samples. The standard addition method was employed, and the results are presented in Table 2. The recoveries of sulphite obtained were acceptable, and the reproducibility of the results is indicated by the mean relative standard deviation (RSD).

Table 2. Determination of sulphite in real samples (n=5).

Sample —	Concentration, μM		Docovoru 0/	DCD 0/	
Sample	Spiked	Found	— Recovery, %	RSD, %	
	5.0	4.9	98.0	3.3	
Well water —	7.0	7.1	101.4	2.7	
well water —	9.0	8.8	97.8	2.5	
	11.0	11.4	103.6	2.2	
	5.0	5.1	102.0	2.1	
Tan water —	7.5	7.4	98.7	3.0	
Tap water —	10.0	9.9	99.0	2.4	
	12.5	12.9	103.2	2.6	

Conclusions

With the continuous emergence of food additives, there is a growing interest in developing new analytical tools for detecting and quantifying food additives using a reliable and simple method. In this study, we present the development of ZIF-L(Zn)/SPGE sensor for the detection of sulphite in real samples. The electrochemical properties of ZIF-L(Zn) modified SPGE were analysed using CV and DPV. This sensor showed a very good practical application for sulphite detection in real samples. The sensitivity of the sensor was determined and obtained a detection limit of $0.01~\mu M$.

References

- [1] L. Wu, *Analysis of food additives*, in *Innovative food analysis*, C. M. Galanakis, Ed., Academic Press, 2021, 157. https://doi.org/10.1016/B978-0-12-819493-5.00007-8
- [2] X. Ma, C. Liu, Q. Shan, G. Wei, D. Wei, Y. Du, A fluorescein-based probe with high selectivity and sensitivity for sulfite detection in aqueous solution, *Sensors and Actuators B* **188** (2013) 1196-1200. https://doi.org/10.1016/j.snb.2013.08.007
- [3] R. F. McFeeters, A. O. Barish, Sulfite analysis of fruits and vegetables by high-performance liquid chromatography (HPLC) with ultraviolet spectrophotometric detection, *Journal of Agricultural and Food Chemistry* **51** (2003) 1513-1517. https://doi.org/10.1021/jf025693c
- [4] H. Tian, J. Qian, Q. Sun, H. Bai, W. Zhang, Colorimetric and ratiometric fluorescent detection of sulfite in water via cationic surfactant-promoted addition of sulfite to α , β -unsaturated ketone, *Analytica Chimica Acta* **788** (2013) 165-170. https://doi.org/10.1016/j.aca.2013.06.020
- [5] T. Gao, X. Cao, P. Ge, J. Dong, S. Yang, H. Xu, Y. Wu, F. Gao, W. Zeng, A self-assembled fluorescent organic nanoprobe and its application for sulfite detection in food samples and living systems, *Organic & Biomolecular Chemistry* **15** (2017) 4375-4382. https://doi.org/10.1039/C7OB00580F
- [6] S. Pati, P. Crupi, I. Benucci, D. Antonacci, A. Di Luccia, M. Esti, HPLC-DAD–MS/MS characterization of phenolic compounds in white wine stored without added sulfite, *Food Research International* **66** (2014) 207-215. https://doi.org/10.1016/j.foodres.2014.09.017
- [7] K. S. Carlos, L. S. de Jager, Determination of sulfite in food by liquid chromatography tandem mass spectrometry: collaborative study, *Journal of AOAC International* **100** (2017) 1785-1794. https://doi.org/10.5740/jaoacint.17-0033
- [8] K. S. Carlos, M. Treblin, L. S. de Jager, Comparison and optimization of three commercial methods with an LC–MS/MS method for the determination of sulfites in food and beverages, *Food Chemistry* **286** (2019) 537-540. https://doi.org/10.1016/j.foodchem.2019.02.042
- [9] Z. Ni, F. Tang, Y. Liu, D. Shen, R. Mo, Rapid determination of low-level sulfite in dry vegetables and fruits by LC-ICP-MS, Food Science and Technology Research **21** (2015) 1-6. https://doi.org/10.3136/fstr.21.1
- [10] T. R. Dadamos, M. F. Teixeira, Electrochemical sensor for sulfite determination based on a nanostructured copper-salen film modified electrode, *Electrochimica Acta* 54 (2009) 4552-4558. https://doi.org/10.1016/j.electacta.2009.03.045
- [11] R. Pauliukaite, R. Metelka, I. Švancara, A. Królicka, A. Bobrowski, K. Vytøas, E. Norkus, K. Kalcher, Carbon paste electrodes modified with Bi2O3 as sensors for the determination of Cd and Pb, *Analytical and Bioanalytical Chemistry* **374** (2002) 1155-1158. https://doi.org/10.1007/s00216-002-1569-3
- [12] W. J. Guan, Y. Li, Y. Q. Chen, X. B. Zhang, G. Q. Hu, Glucose biosensor based on multi-wall carbon nanotubes and screen printed carbon electrodes, *Biosensors and Bioelectronics* **21** (2005) 508-512. https://doi.org/10.1016/j.bios.2004.10.030
- [13] J. Liu, Y. Yin, G. Liu, Bipyridine-functionalized covalent-organic-framework-modified screen-printed electrode for ultrasensitive electrochemical determination of arsenic (III), International Journal of Electrochemical Science 19 (2024) 100720. https://doi.org/10.1016/j.ijoes.2024.100720
- [14] A. M. Sikkander, F. Bassyouni, K. Yasmeen, S. Mishra, V. Lakshmi, Synthesis of zinc oxide and lead nitrate nanoparticles and their applications: comparative studies of bacterial and fungal (E. coli, A. Niger), *Journal of Applied Organometallic Chemistry* **3** (2023) 255-267. https://doi.org/10.48309/JAOC.2023.415886.1115
- [15] T. Kant, K. Shrivas, K. Dewangan, A. Kumar, N. K. Jaiswal, M. K. Deb, S. Pervez, Design and development of conductive nanomaterials for electrochemical sensors: a modern approach,



Materials Today Chemistry **24** (2022) 100769. https://doi.org/10.1016/j.mtchem.2021.100769

- [16] H. Beitollahi, S. Tajik, Z. Dourandish, S. Z. Mohammadi, F. G. Nejad, R. Zaimbashi, The development of a disposable voltammetric sensor based on two-dimensional leaf-like ZIF-L (Zn) modified screen-printed graphite electrode for the simultaneous analysis of uric acid, dopamine and theophylline, *Inorganic Chemistry Communications* **170** (2024) 113158. https://doi.org/10.1016/j.inoche.2024.113158
- [17] T. Cazzotti Lozer, A. Carolina Miranda Prezilius, G. F.s Souza dos Santos, I. França Schaffel, T. Ramon Rosa, R. Queiroz Ferreira, Development of a portable electroanalytical methodology for determination of sulfite in wine using screen-printed carbon electrodes modified with carbon nanotubes, *Journal of Food Composition and Analysis* **116** (2023) 105052. https://doi.org/10.1016/j.jfca.2022.105052
- [18] J. Yang, X. Xu, X. Mao, L. Jiang, Xueliang Wang, An Electrochemical sensor for determination of sulfite (SO₃²⁻) in water based on molybdenum disulfide flakes/nafion modified electrode, *International Journal of Electrochemical Sciences* 15 (2020) 10304-10314. https://doi.org/10.20964/2020.10.48

© 2024 by the authors; licensee IAPC, Zagreb, Croatia. This article is an open-access article distributed under the terms and conditions of the Creative Commons Attribution license (https://creativecommons.org/licenses/by/4.0/)



Open Access :: ISSN 1847-9286 www.jESE-online.org

Original scientific paper

MoS₂ nanosheets-modified screen-printed electrode for the simultaneous detection of carmoisine and tartrazine

Hussein Jassim Abboud¹, Zaid H. Mahmoud², Aya Mohammed Saadoun³, Ekhlas A. Abdul Kareem², Mustafa Mudhafar⁴, Qais R. Lahhob⁶, and Raed Muslim Mhaibes⁻, ■

Corresponding authors: $^{\boxtimes}$ <u>qaisrlahhob@gmail.com</u>, $^{\boxtimes}$ <u>Raid.mcm@uomisan.edu.iq</u>

Received: December 9, 2024; Accepted: January 4, 2025; Published: March 3, 2025

Abstract

Solvothermal synthesis was used to create molybdenum disulfide nanosheets (MoS₂ NSs). A screen-printed electrode (MoS₂ NSs / SPE) was modified using the produced MoS₂ nanosheets and employed as the working electrode for the voltammetric measurement of carmoisine. For the oxidation of carmoisine, the MoS₂ NSs/SPE showed increased electrocatalytic activity. With a detection limit as low as 0.03 μ M under ideal circumstances, it was discovered that the oxidation peak currents of carmoisine were linearly proportional to its concentration in 0.1 to 400.0 μ M. Additionally, the MoS₂ NSs / SPE showed promise for simultaneous detection of both chemicals by effectively identifying carmoisine even in the presence of tartrazine. The MoS₂ NSs / SPE was appropriate for simultaneous detection of tartrazine and carmoisine using differential pulse voltammetry as the oxidation peak potentials of the two azo dyes were adequately separated by 200 mV.

Keywords

Transition-metal dichalcogenide; Differential pulse voltammetry; electrochemical sensors, chemically modified electrodes, real sample analysis

Introduction

Food colorants, which are actually food additives, are extraneously added to food and drinks so as to improve their look through artificial coloration and produce the effect of the highest visual appealing to customers. For that reason, the food industry needed to apply various kinds of food-

¹Ministry of Education, Baghdad, Iraq

²University of Diyala, College of Sciences, Chemistry Department, Iraq

³Albayan University, Basic Science Department, Iraq

⁴Department of Medical Physics, Faculty of Medical Applied Sciences, University of Kerbala, 56001, Karbala, Iraq

⁵Department of Anesthesia Techniques and Intensive Care, Al-Taff University College, 56001, Kerbala, Iraq

⁶Collage of Pharmacy, National University of Science and Technology, Dhi Qar, 64001, Iraq

⁷Department of Biochemistry, College of Medicine, Misan University, Misan, Iraq

grade colorants. These were mainly different in color and either natural or artificial [1]. Azodyes, a synthetic colouring agents, have been the prominent colorant used to improve the look and colour of food products, but due to their consistent color, low water solubility, low microbial contamination risk, low production costs, and excellent stability in the presence of light, oxygen, and pH changes, making them an ideal choice for food industries [1-5].

Coal tar pitch is the source of carmoisine, also known as E 122, a synthetic red azo dye that is widely used as a food and beverage colorant. It has functional groups, including hydroxy, sulpho, azo, and aromatic ring structures connected to possible negative health consequences when ingested in excess [6]. Carmoisine is used extensively as a food and beverage colorant since it is a highly water-soluble dye with exceptional stability that does not degrade even when exposed to light and oxygen. Carmoisine is classified as an emerging contaminant because of its stability and water solubility, which cause it to persist in aquatic habitats and raise questions about its possible effects on the environment and human health [7]. High levels of carmoisine exposure have been demonstrated to have detrimental impacts on health, such as carcinogenic effects that raise the chance of cancer, toxic effects that damage cells and tissues, and mutagenic effects that change genetic material [8].

E 102, another name for tartrazine, is an orange azo dye that dissolves in water and is frequently used as a colorant in a variety of goods, such as food, cosmetics, and medications. However, because of its widespread usage, it has been released into the environment through industrial effluent, which has contaminated water supplies. To reduce possible health hazards, the recommended daily intake of tartrazine in non-alcoholic drinks should not be more than 0.01 g/ml [9]. The possible hazards of consuming excessive amounts of tartrazine are highlighted by the fact that it has been connected to a number of human health issues, such as reproductive toxicity, alterations in kidney and liver function, and even neurobehavioral toxicity. The potential health risks associated with excessive consumption of tartrazine and carmoisine underscore the need for rigorous monitoring of their concentrations in relevant products. This requires the development and implementation of a rapid, simple, sensitive, and cost-effective analytical method to ensure the safety of consumers and prevent adverse health effects. Several analytical techniques are available for detecting and quantifying tartrazine and carmoisine, including spectrophotometry [10], HPLC [11] and capillary electrophoresis [12], each offering a unique set of advantages and capabilities for monitoring these synthetic colorants. Despite their effectiveness, many of these analytical techniques are often complex and labor-intensive, requiring specialized expertise and expensive equipment, making them less accessible and practical for routine monitoring and analysis.

Electrochemical sensing systems offer a range of advantages, including being cost-effective, portable, and simple to use, with benefits such as low limits of detection, fast analysis times, wide linear dynamic ranges, and high selectivity, even in the presence of interfering substances, making them an attractive option for analytical applications [13]. Voltammetric techniques, such as differential pulse voltammetry (DPV), offer several advantages, including rapid response times, high sensitivity, and excellent selectivity, making them a valuable tool for analytical determinations [14].

Screen-printing electrodes (SPEs) have been widely used for the large-scale production of disposable electrochemical sensors, offering a cost-effective and efficient way to manufacture sensing systems for various applications [15]. Screen-printing electrodes (SPEs) offer a unique combination of affordability, mass production capabilities, and sufficient reproducibility while also providing the benefits of versatility and miniaturization, making them an attractive option for the development of electrochemical sensing systems [15].

The bare electrode exhibits poor electrocatalytic performance [15]. Modifying the electrode surface significantly enhances its sensitivity, reproducibility, and overall stability [16]. The incorporation of nanomaterials can substantially boost the detection of trace analyte levels by dramatically improving the surface characteristics and electroconductivity of the electrodes [16].

Nanomaterials possess distinct physical and chemical properties, making them a popular choice for augmenting the sensing capabilities of electrochemical methods [17,18].

In recent years, there has been a surge of interest in two-dimensional (2D) nanomaterials, driven by their exceptionally thin and unique structure. Particular attention has been given to 2D MoS₂, a material composed of a single layer of molybdenum atoms sandwiched between two layers of hexagonally arranged sulphur atoms, forming a unique monoatomic structure. MoS₂, a two-dimensional layered transition-metal dichalcogenide, exhibits outstanding electrical properties and remarkable optical characteristics, making it a highly promising material [19]. The top gate configuration of layered MoS₂ crystals often yields exceptionally high electronic performance, characterized by impressive onoff ratios comparable to those of graphene nanoribbons. Furthermore, due to their high surface-to-volume ratios, these graphene-like materials may offer the potential for ultra-high sensitivity in detecting a wide range of biological, dietary, and environmental compounds [20].

In order to detect carmoisine, this study suggested using MoS₂ nanosheets (NSs) in conjunction with a screen-printed electrode (SPE). It is crucial to note that DPV, chronoamperometry, and CV were among the electrochemical methods used to assess the electrochemical characteristics of carmoisine and the performance of the MoS₂ NSs/SPE. Subsequent research showed that the MoS₂ NSs/SPE sensor had both exceptional electrocatalytic activity for carmoisine and the capacity to detect carmoisine and tartrazine in combination with different and recognizable signals. The MoS₂ NSs/SPE sensor's promise for practical uses was demonstrated when it was successfully used to accurately determine the levels of tartrazine and carmoisine in real samples.

Experimental

Apparatus and chemicals

An Autolab potentiostat/galvanostat was used for electrochemical experiments. A three-electrode setup including a graphite working electrode (WE), a graphite auxiliary electrode (AE), and a silver pseudo-reference electrode (RE) was used in the screen-printed electrodes (SPEs) manufactured by DropSens (DRP-110, Spain). A Metrohm 710 pH meter was used to measure the pH. Every solution was made from scratch with double-distilled water. All chemicals used, including tartrazine and carmosine, were analytical grade and came from Merck. Orthophosphoric acid and its salts purchased from Merck were used to make the buffer solutions.

Synthesis of MoS₂ NSs

To synthesize MoS_2 NSs, 0.26 g of ammonium molybdate and 0.50 g of thiourea were first dissolved in 30 ml of deionized - water through 15 min of stirring. The resulting solution was then transferred to an autoclave, which underwent hydrothermal treatment at 190 °C for about 24 h. After the hydrothermal reaction, the sediments were collected, repeatedly washed with ethanol, and dried under vacuum at 65 °C overnight.

Preparation of MoS₂ NSs / SPE

To achieve this, 2 mg of MoS₂ NSs were dispersed in 1 milliliter of ultra-pure water through 15 min of dispersion. Subsequently, the working electrode was fabricated by casting 5 microliters of the MoS₂

NSs suspension onto it. The modified electrode was then obtained by allowing the solvent to evaporate. The MoS_2 NSs / SPE was formed after the evaporation of the solvent.

Preparation of real samples

15.0 ml of lemon juice was filtered using filter paper to create a sample. Next, 2.0 ml of PBS was mixed with 10.0 ml of the filtered sample to dilute it.

Six grams of the powder were dissolved in 70 ml of deionized water at fifty degrees Celsius in order to create a powdered juice sample. 10 ml of PBS was then added to the solution to further dilute it. A 0.45-micrometer membrane filter was then used to filter the diluted solution.

Results and discussion

The MoS₂ NSs were subjected to X-ray diffraction (XRD) examination in order to investigate the crystal structure of the produced material. As illustrated in Figure 1, the prepared sample's XRD pattern shows prominent diffraction peaks at 2θ values of 14.0, 33.5, 39.8, 42.9, 49.3, 59.1 and 69.6°. These values correspond to the hexagonal MoS₂ structure's (002), (100), (103), (006), (105), (110), and (200) planes and match the standard pattern (JCPDS 37-1492) [21].

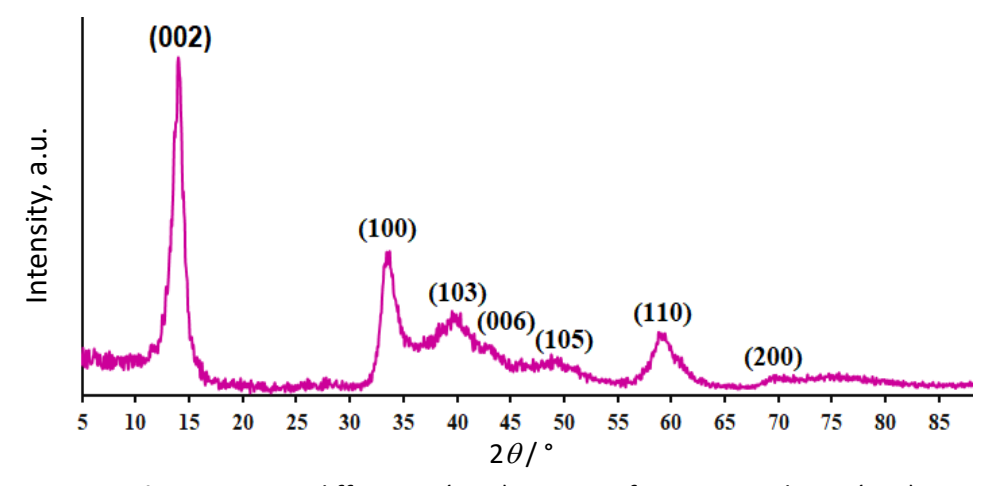


Figure 1. X-ray diffraction (XRD) pattern of MoS₂ nanosheets (NSs)

The produced MoS₂ NSs sample's FE-SEM pictures at various magnifications are shown in Figure 2.

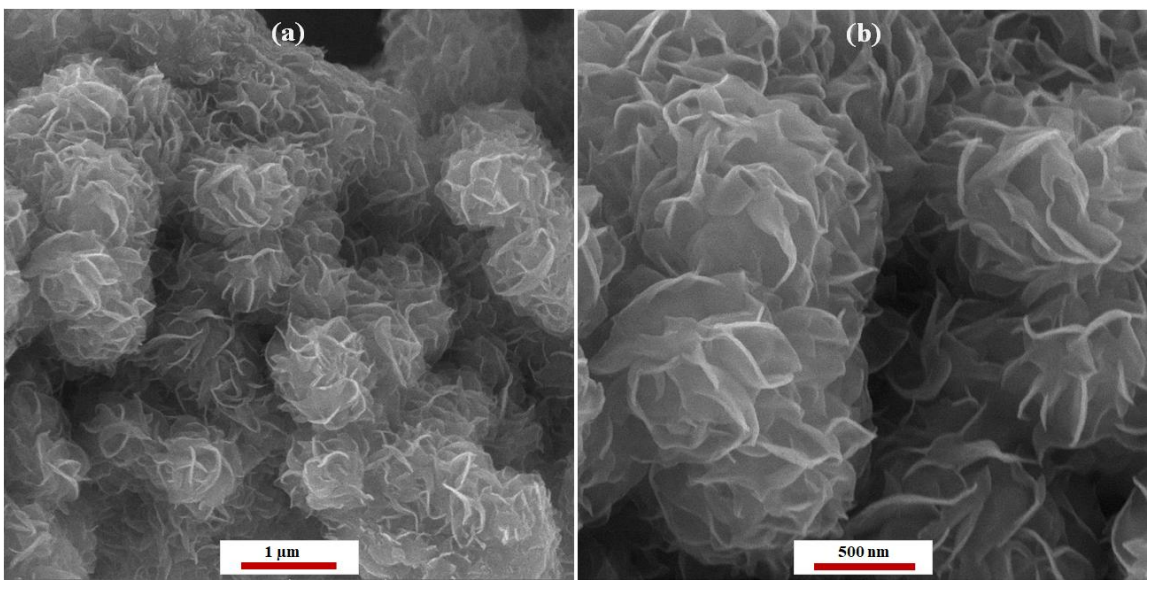


Figure 2. Field emission scanning electron microscopy images of MoS₂ nanosheets at different magnifications a) 1 μ m and b) 500 nm

The generated MoS₂ sample has spherical-like structures made up of many integrated nanosheets, as seen by the FE-SEM pictures.

Cyclic voltammetric study of carmoisine oxidation

Figure 3 shows the CVs for the electrochemical oxidation of 100.0 μ M carmoisine at the bare screen-printed electrode (SPE) (curve a) and the MoS₂ NSs-modified SPE (curve b). A comparison of the two curves reveals that the anodic peak potential for carmoisine oxidation at the MoS₂ NSs-modified SPE (curve b) is approximately 480 mV, which is significantly lower than the peak potential observed at the bare SPE (curve a), which is around 630 mV. A similar trend is observed for carmoisine oxidation, where the anodic peak current at the MoS₂ NSs-modified SPE (curve b) is substantially higher than the bare SPE (curve a), indicating a significant enhancement in the electrochemical response at the modified electrode. The results clearly demonstrate that the modification of the SPE with MoS₂ NSs significantly enhances the electrochemical characteristics of carmoisine oxidation, indicating improved performance of the modified electrode.

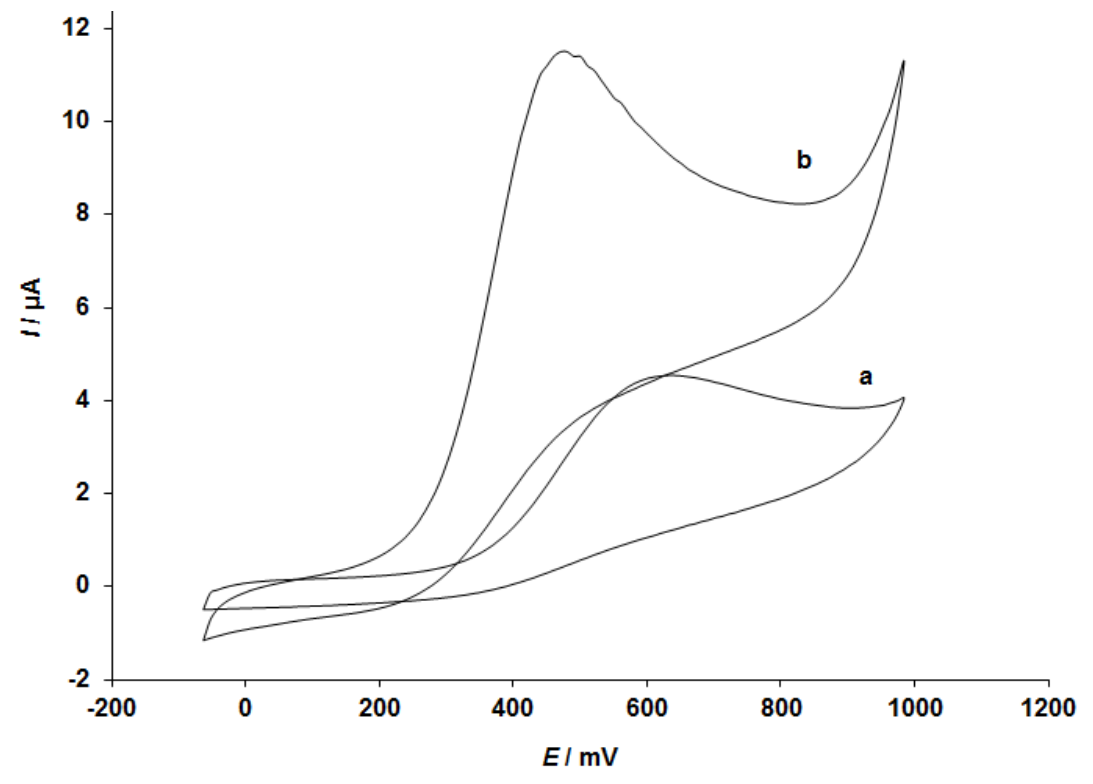


Figure 3. CVs of 100.0 μ M carmoisine at the surface of the unmodified screen-printed electrode (SPE) (a) and the MoS₂ NSs-modified SPE (b)

Effect of scan rate

The investigation was done with linear sweep voltammetry (LSV) and the effect of potential sweep rate on oxidation of carmoisine at the MoS_2 NSs-modified SPE is mentioned; the findings are shown in Figure 4A. It can be seen from a plot of the peak current (I_p) against the $v^{1/2}$ (5 to 400 mV/s) that oxidation of carmoisine at the MoS_2 NSs-modified SPE is not a diffusion-controlled process anymore but rather is a surface-controlled one at the overpotential, which is a sufficient value (Figure 4B).

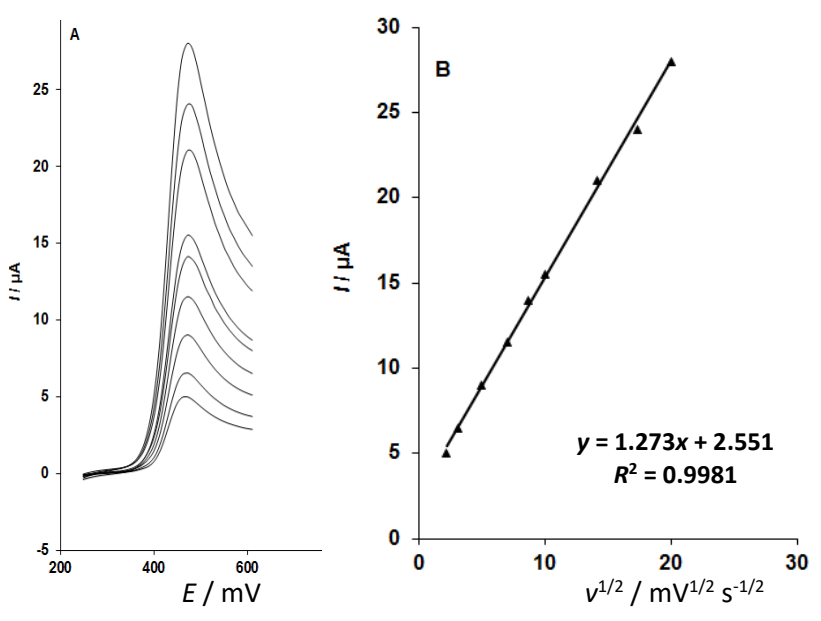


Figure 4. (A) shows the MoS₂ NSs-modified SPE's linear sweep voltammograms (LSVs) at scan rates of 5.0, 10.0, 25.0, 50.0, 75.0, 100.0, 200.0, 300.0, and 400.0 mV/s in 100.0 μ M carmoisine. (B) I against $v^{1/2}$

Chronoamperometric measurements

Chromatoamperometric experiments were conducted for carmoisine at the MoS₂ NSs-modified SPE. The current responses resulting from different carmoisine concentrations were recorded (Figure 5A).

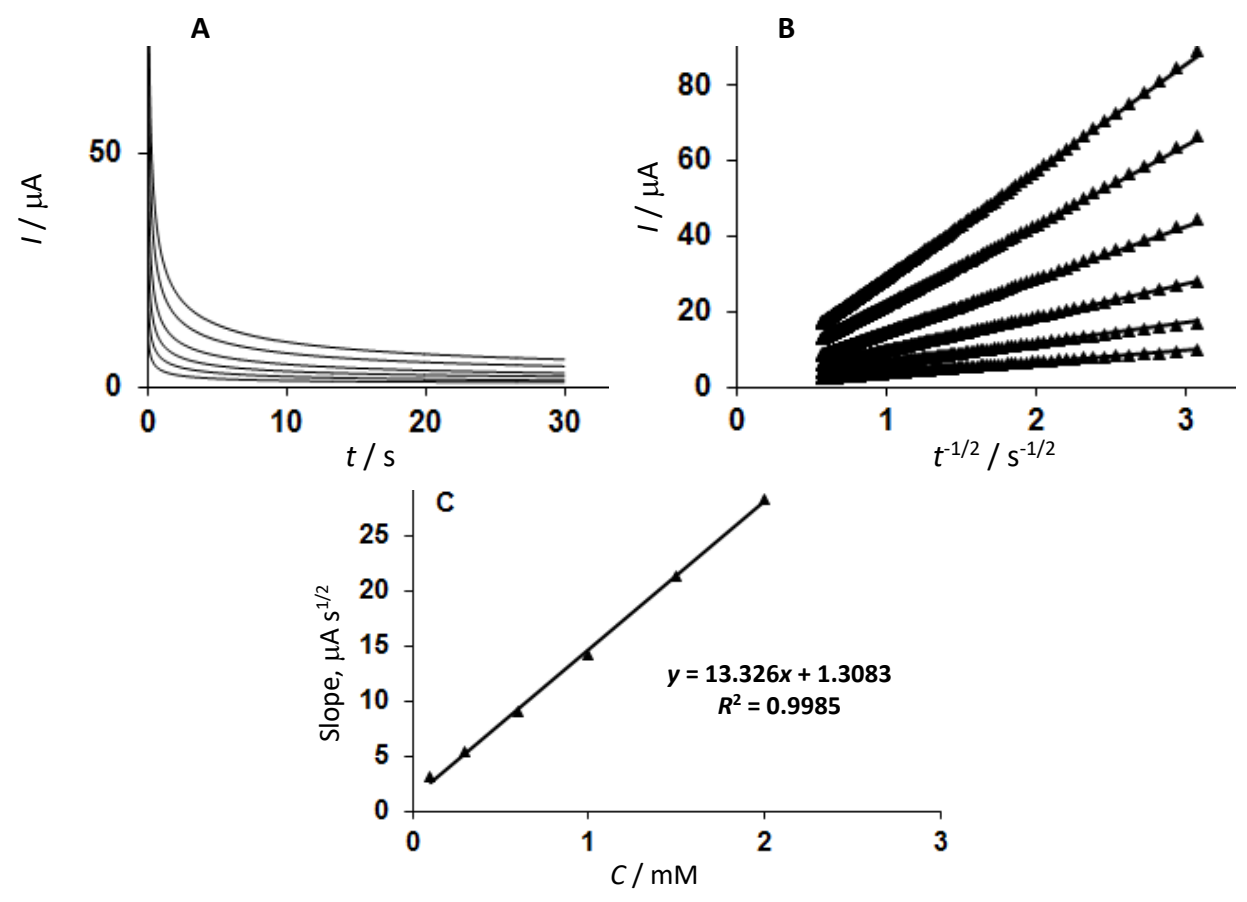


Figure 5. (A) Chronoamperometric responses obtained at the MoS₂ NSs-modified SPE for various concentrations of carmoisine (0.1, 0.3, 0.6, 1.0, 1.5, and 2.0 mM). (B) Cottrell plots of current versus $t^{-1/2}$ derived from the chronoamperograms. (C) Calibration plot of the slope of the straight lines from the Cottrell plots against carmoisine concentration

For carmoisine, the current-time response under mass transport limited conditions can be described by Cottrell Equation (1) [22]:

$$I = nFAD^{1/2}C/\pi^{-1/2}t^{-1/2}$$
(1)

The best fits for various carmoisine concentrations are displayed in Figure 5B, which is an experimental plot of current (I) against the inverse square root of time ($t^{-1/2}$). A curve was created by plotting the slope that emerged from the Cottrell plots (Figure 5B) against the carmoisine concentration (Figure 5C). The mean diffusion coefficient (D) of carmoisine was determined to be 6.1×10^{-5} cm²/s using the Cottrell equation and the slope derived from the calibration curve (Figure 5C).

Calibration plot and LOD

The quantitative measurement of carmoisine in solution can be based on the electrocatalytic peak current for carmoisine oxidation at the MoS_2 NSs-modified SPE. In order to do this, investigations utilizing the MoS_2 NSs-modified SPE with varying carmoisine concentrations were carried out using differential pulse voltammetry (DPV) (Figure 6A). A linear association with a slope of $0.1021\,\mu\text{A}/\mu\text{M}$ was found for the concentration range of 0.1 to 400.0 mM. It was determined that the detection limit (3σ) was $0.03~\mu\text{M}$ (Figure 6B). The findings of some recent work on the electrochemical determination of carmoisine are displayed in Table 1.

Table 1. Comparison the values of LOD and linear range of the MoS_2 NSs-modified SPE sensor with some of the previously published reports

	Modified electrode	Linear range, μΜ	LOD, μM	Ref.
	CaMgFe ₂ O ₄ hollow spheres-modified carbon paste electrode	10 to 900	0.86	[23]
Ī	Mesoporous Pr ₆ O ₁₁ /Ionic liquid/carbon paste electrode	0.09 to 135.00	0.0012	[24]
	MoS ₂ NSs-modified SPE	0.1 to 400.0	0.03	This work

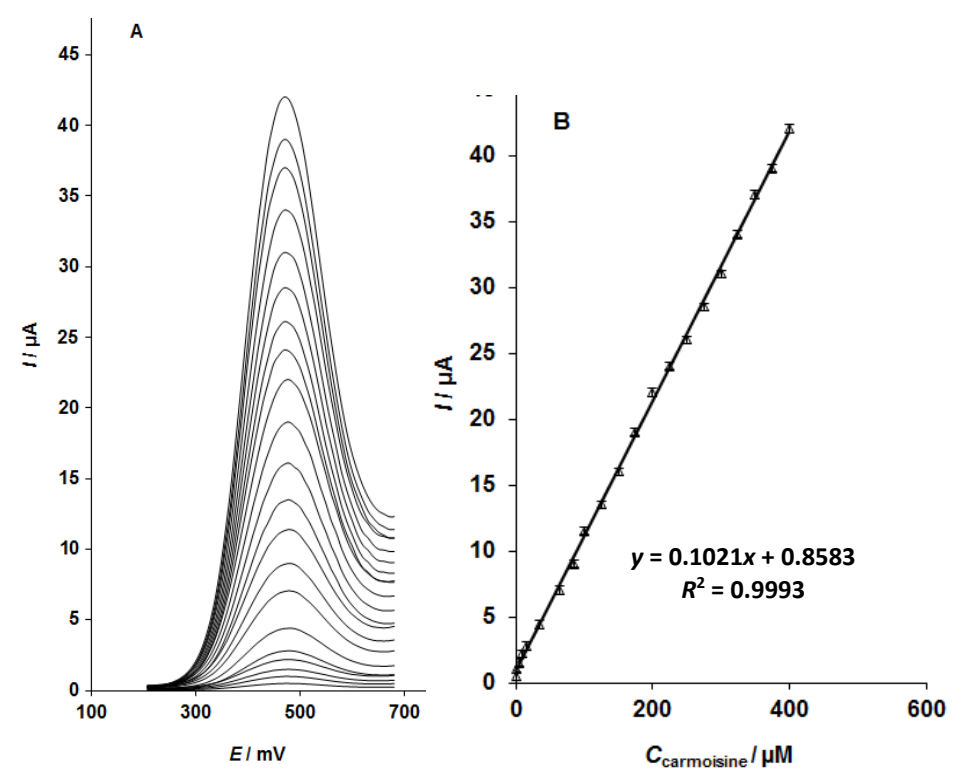


Figure 6. (A) Differential pulse voltammograms (DPVs) of the MoS₂ NSs-modified SPE containing various concentrations of carmoisine (0.1, 1.0, 5.0, 10.0, 15.0, 35.0, 65.0, 85.0, 100.0, 125.0, 150.0, 175.0, 200.0, 225.0, 250.0, 275.0, 300.0, 325.0, 350.0, 375.0, and 400.0 μ M). (B) Calibration plot of peak current versus carmoisine concentration

Simultaneous determination of carmoisine and tartrazine

No prior research has used MoS₂ NSs-modified SPE for the simultaneous analysis of carmoisine and tartrazine, and this is the first report on its application. As seen in Figure 7A, the simultaneous measurement of carmoisine and tartrazine was accomplished by altering the concentrations of both substances concurrently and recording the resulting differential pulse voltammograms (DPVs). The oxidation of carmoisine and tartrazine was represented by distinct anodic peaks in the voltammetric findings, which were obtained at potentials of 480 mV and 1170 mV. As shown in Figure 7A, this suggests that the MoS₂ NSs-modified SPE can identify these two chemicals at the same time.

The MoS $_2$ NSs-modified SPE's sensitivity to carmoisine oxidation was found to be 0.1031 μ A/ μ M, quite near the value measured without tartrazine. This implies that these chemicals' oxidation processes at the MoS $_2$ NSs/SPE are separate, making it possible to determine their mixes simultaneously without experiencing any major interferences.

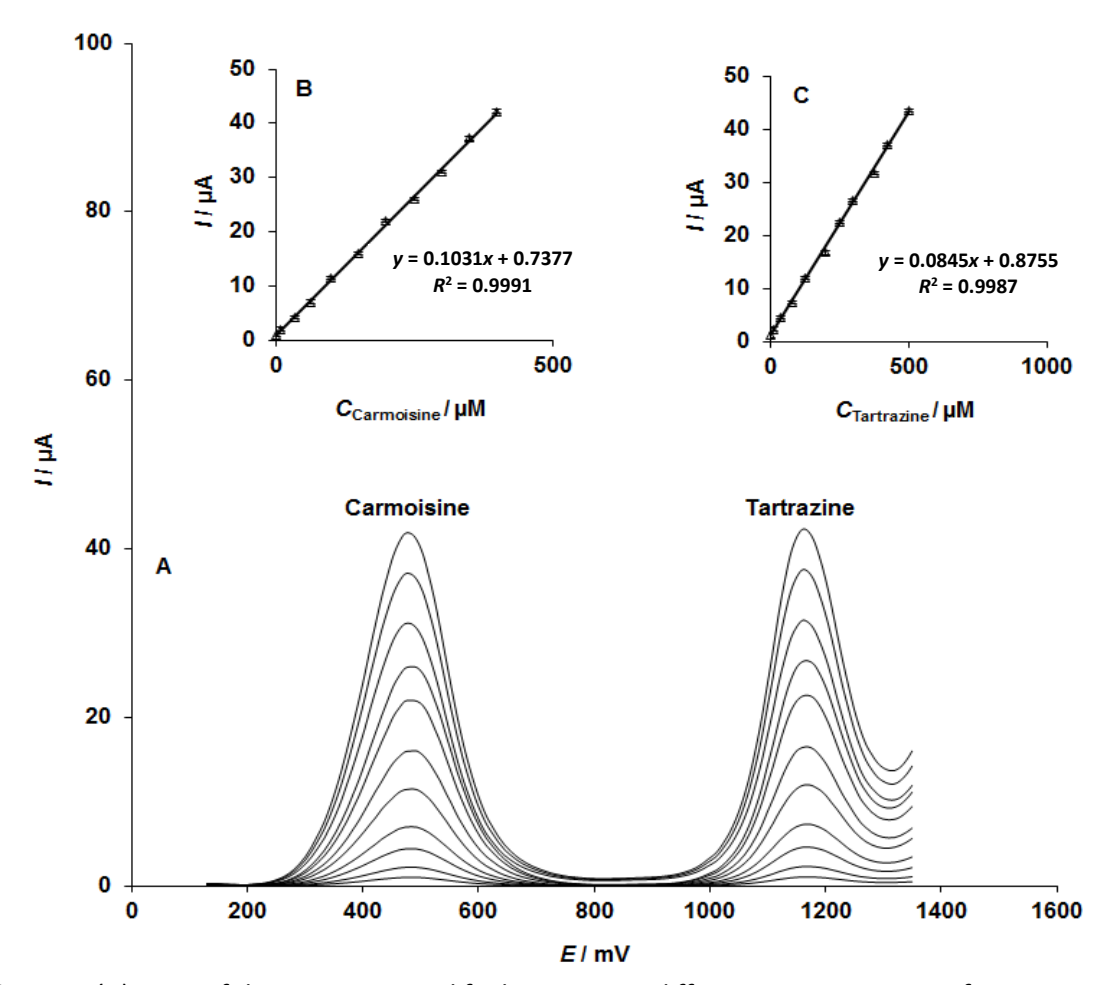


Figure 7. (A) DPVs of the MoS_2 NSs-modified, containing different concentrations of carmoisine and tartrazine (in μ M), from inner to outer: 1.0+2.0, 10.0+15.0, 35.0+40.0, 65.0+80.0, 100.0+125.0, 150.0+200.0, 200.0+250.0, 250.0+300.0, 300.0+375.0, 350.0+425.0, and 400.0+500.0, respectively. Insets: (B) Plot of Ip versus carmoisine concentration and (C) Plot of Ip versus tartrazine concentration

Stability, reproducibility, and repeatability

The MoS₂-NSs-modified SPE was air-stored at ambient conditions in order to verify its stability using the DPV technique. According to the findings, the modified electrode's peak carmoisine current (40.0 μ M) retained 97.5 % of its initial current after a week, indicating the sensor's remarkable long-term stability. Ten separate voltammetric measurements were made to assess the carmoisine electro-oxidation (40.0 μ M) on the same MoS₂ NSs-modified SPE electrode. The findings

showed that the generated sensor was highly repeatable, with an RSD of 3.4 %. The carmoisine response currents (40.0 μ M) on five MoS₂-modified SPE were compared under the same circumstances, and the findings demonstrated the remarkable repeatability of the generated sensor with an RSD of 3.7 %.

Interference study

It was examined how different alien species affected the measurement of 50.0 μ M carmoisine. With a relative inaccuracy of about ± 5 %, the tolerance limit was calculated as the highest concentration of invasive species. According to the results, there was no interference and the sensor's strong selectivity for carmoisine analysis was confirmed for Li⁺, Na⁺, Ca²⁺, F⁻, Br⁻, Fe², Mg²⁺, Zn²⁺, K⁺, Cl⁻, NO₃⁻, SO₄²⁻, Mn²⁺, Ca²⁺, citric acid, glucose, tryptophan, pantothenic acid, thiamine, indigo carmine and brilliant blue.

Determination of carmoisine and tartrazine in real samples

The mentioned procedure was implemented in the analysis of carmoisine and tartrazine in real samples, viz. powdered juice and lemon juice, to attempt its real analytic power. Table 2 contains the results of the analysis of tartrazine and carmoisine in the lemon juice and powdered juice samples. The accuracy and dependability of the suggested approach were evident from the satisfactory recovery rates achieved during the measurement of carmoisine and tartrazine in actual peptides. The repeatability of the approach was assessed by measuring the RSD, which was another way of making sure that the measurement was accurate, showing at the same time the reliability and dependability of the suggested approach.

Table 2. Results of the estimation of carmoisine and tartrazine in powdered juice and lemon juice samples
using the MoS $_2$ NSs / SPE method. The results are based on five replicate measurements (n=5).

	Concentration, μM				Pacovary %		RSD, %	
	Spil	Spiked Found		Recovery, %		N3D, 76		
Sample	Carmoisine	Tartrazine	Carmoisine	Tartrazine	Carmoisine	Tartrazine	Carmoisine	Tartrazine
	0	0	3.1	3.9	-	-	3.3	2.7
Davidarad	2.0	1.0	5.0	5.1	98.0	104.1	2.7	3.1
Powdered juice	4.0	3.0	7.3	6.7	102.8	97.1	1.9	2.9
	6.0	5.0	8.9	9.1	97.8	102.3	3.0	2.4
	8.0	7.0	11.2	10.7	100.9	98.2	2.4	2.5
	0	0	-	4.1	-	-	-	3.4
Lomon	5.0	2.0	5.1	6.0	102.0	98.4	2.0	1.8
Lemon juice	7.5	3.0	7.3	7.3	97.3	102.8	2.2	2.9
	9.5	4.0	9.4	8.0	98.9	98.7	3.3	2.7
	11.5	5.0	11.6	8.8	100.9	96.7	1.9	3.5

Conclusions

This work presents a simple process for creating molybdenum disulfide nanosheets (MoS_2 NSs), which were subsequently used with a screen printed electrode (SPE) to detect carmoisine electrochemically using voltammetry. MoS₂ NSs and SPE work together to provide a very efficient carmoisine detection system, and their synergy improves the system's overall detection capabilities. A broad and efficient detection range was shown by the developed sensor's linear response to carmoisine concentrations ranging from 0.1 to 400.0 μ M.

References

[1] M. V. Vieira, S. Noore, B. Tiwari, C. O'. Donnell, C. Gonçalves, L. M. Pastrana, P. Fuciños, Enhancing the stability and functionality of phycobili proteins as natural food colourants

- through microparticle formulation, *Food Chemistry* **465** (2025) 142077. https://doi.org/10.1016/j.foodchem.2024.142077
- [2] P. Barciela, A. Perez-Vazquez, M. A. Prieto, Azo dyes in the food industry: Features, classification, toxicity, alternatives, and regulation, *Food and Chemical Toxicology* **178** (2023) 113935. https://doi.org/10.1016/j.fct.2023.113935
- [3] R. B. Shakuntala, J. Keshavayya, K. M. Mussuvir Pasha, N. D. Satyanarayan, B. N. Nippu, B. Thippeswamy, Synthesis, Spectroscopic, Computational, and Biological Evaluation of Pyrazole mono azo dyes, *Journal of Molecular Structure* **1309** (2024) 138045. https://doi.org/10.1016/j.molstruc.2024.138045
- [4] S. D. Nagesh, D. Satheesh, R. Devi Ravi, R. Pachaiappan, K. Manavalan, L. Cornejo-Ponce, T. Sethuramachandran, An effective photocatalytic decomposition of azo dyes by NiO/ZnO/g-C₃N₄ ternary nanocomposite under solar light excitation, *Surfaces and Interfaces* **56** (2024) 105578. https://doi.org/10.1016/j.surfin.2024.105578
- [5] P. Vineis, R. Pirastu, Aromatic amines and cancer, *Cancer Causes Control* **8** (1997) 346-355. https://doi.org/10.1023/A:1018453104303
- [6] S. Sunil, B. Kumar Mandal, Facile synthesis of CQD/g-C₃N₄ as a highly effective metal-free photocatalyst for the degradation of carmoisine and indigo carmine dye, *Inorganic Chemistry Communications* **171** (2025) 113545. https://doi.org/10.1016/j.inoche.2024.113545
- [7] H. Barrera, J. Cruz-Olivares, B. A. Frontana-Uribe, A. Gomez-Diaz, P. G. Reyes-Romero, C. E. Barrera-Diaz, Electrooxidation-plasma treatment for azo dye carmoisine (Acid Red 14) in an aqueous solution, *Materials* **13** (2020) 1463. https://doi.org/10.3390/ma13061463
- [8] G. P. Ford, B. I. Stevenson, J. G. Evans, Long-term toxicity study of carmoisine in rats using animals exposed in utero, *Food and Chemical Toxicology* 25 (1987) 919-925. https://doi.org/10.1016/0278-6915(87)90285-7
- [9] K. Rovina, S. Siddiquee, S. M. Shaarani, A review of extraction and analytical methods for the determination of tartrazine (E 102) in foodstuffs, *Critical Reviews in Analytical Chemistry* **47** (2017) 309-324. https://doi.org/10.1080/10408347.2017.1287558
- [10] Z. Kiayi, T. Bagheri Lotfabad, A. Heidarinasab, F. Shahcheraghi, Microbial degradation of azo dye carmoisine in aqueous medium using Saccharomyces cerevisiae ATCC 9763, *Journal of Hazardous Materials* **373** (2019) 608-619. https://doi.org/10.1016/j.jhazmat.2019.03.111
- [11] F. Turak, M. Dinç, O. Dülger, M. O. Özgür, Four derivative spectrophotometric methods for the simultaneous determination of carmoisine and ponceau 4R in drinks and comparison with high performance liquid chromatography, *International Journal of Analytical Chemistry* **2014** (2014) 650465. https://doi.org/10.1155/2014/650465
- [12] H. Y. Huang, Y. C. Shih, Y. C. Chen, Determining eight colorants in milk beverages by capillary electrophoresis, *Journal of Chromatography A* **959** (2002) 317-325. https://doi.org/10.1016/S0021-9673(02)00441-7
- [13] F. Yang, S. Li, X. Zhang, L. Wang, S. Liu, Single-particle collision electrochemical biosensing for DNA and protein kinase via sulfhydryl group manipulation and biomodification-free Pt nanoparticle, *Sensors and Actuators B* **426** (2025) 137099. https://doi.org/10.1016/j.snb.2024.137099
- [14] C. Yengin, F. Gulay Der, I. Alcin, B. Cihan, E. Kilinc, Non-invasive electrochemical immunosensor for reverse iontophoretic determination of cardiac troponins (cTnT & cTnI) in a simulated artificial skin model, *Talanta* **256** (2023) 124276. https://doi.org/10.1016/j.talanta.2023.124276
- [15] P. Kelíšková, O. Matvieiev, L. Janíková, R. Šelešovská, Recent advances in the use of screen-printed electrodes in drug analysis: A review, *Current Opinion in Electrochemistry* **42** (2023) 101408. https://doi.org/10.1016/j.coelec.2023.101408



- [16] J. P. Chandhana, M. Roshith, S. P. Vasu, D. V. Ravi Kumar, T. G. Satheesh Babu, High aspect ratio copper nanowires modified screen-printed carbon electrode for interference-free non-enzymatic detection of serum creatinine in neutral medium, *Journal of Electroanalytical Chemistry* **971** (2024) 118605. https://doi.org/10.1016/j.jelechem.2024.118605
- [17] X. Shi, Lei Shi, J. Wang, Y. Zhou, S. Zhao, Defect engineering of nanomaterials for selective electrocatalytic CO₂ reduction, *Matter* **7** (2024) 4233-4259. https://www.cell.com/matter/fulltext/S2590-2385(24)00492-2
- [18] Y. Song, C. Tang, T. Wang, Y. Liu, X. He, C. Xie, G. Chen, C. Deng, Z. He, J. Huang, Nano FeNi-OH/Co(OH)₂/NF p-n heterojunction for efficient oxygen evolution reaction and electrocatalytic urea oxidation: Built-In electric field regulated charge distribution and mechanism exploration, *Applied Surface Science* **670** (2024) 160649. https://doi.org/10.1016/j.apsusc.2024.160649
- [19] A. T. Ezhil Vilian, B. Dinesh, S. M. Kang, U. Maheswari Krishnan, Y. S. Huh, Y. K. Han, Recent advances in molybdenum disulfide-based electrode materials for electroanalytical applications, *Microchimica Acta* **186** (2019) 203. https://doi.org/10.1007/s00604-019-3287-y
- [20] Z. Xie, S. Yu, X. Ma, K. Li, L. Ding, W. Wang, D.A. Cullen, H.M. Meyer III, H. Yu, J. Tong, Z. Wu, F.Y. Zhang, MoS₂ nanosheet integrated electrodes with engineered 1T-2H phases and defects for efficient hydrogen production in practical PEM electrolysis, *Applied Catalysis B:*Environmental 313 (2022) 121458. https://doi.org/10.1016/j.apcatb.2022.121458
- [21] M. Dinesh, K. Muthumalai, Y. Haldorai, R. Thangavelu Rajendra Kumar, MoS2 nanosheets decorated multi-walled carbon nanotube composite electrocatalyst for 4-nitrophenol detection and hydrogen evolution reaction, *Electroanalysis* **32** (2020) 2571-2580. https://doi.org/10.1002/elan.202060351
- [22] A .J. Bard, L. R. Faulkner, *Electrochemical Methods Fundamentals and Applications*, John Wiley & Sons, Inc., New York, USA, 2000. ISBN 978-0-471-04372-0
- [23] M. Karami, M. Shabani-Nooshabadi, Electro-sensing of carmoisine and tartrazine in foodstuffs based on triple-shell CaMgFe₂O₄ hollow spheres-modified sensor, *Materials Chemistry and Physics* 318 (2024) 129289. https://doi.org/10.1016/j.matchemphys.2024.129289
- [24] S. Hamzeh, H. Mahmoudi-Moghaddam, S. Zinatloo-Ajabshir, M. Amiri, S. A. Razavi Nasab, Eco-friendly synthesis of mesoporous praseodymium oxide nanoparticles for highly efficient electrochemical sensing of carmoisine in food samples, *Food Chemistry* **433** (2024) 137363. https://doi.org/10.1016/j.foodchem.2023.137363

© 2025 by the authors; licensee IAPC, Zagreb, Croatia. This article is an open-access article distributed under the terms and conditions of the Creative Commons Attribution license (https://creativecommons.org/licenses/by/4.0/)



Open Access : : ISSN 1847-9286

www.jESE-online.org

Original scientific paper

A new potential of sodium anthraquinone-2-sulfonate as a corrosion inhibitor for carbon steel in 0.5 M H₂SO₄

Roza Kenzhegalieva, Meruyet Khapiyeva, Gauhar Uzakbay, Aruzhan Talapova, Ruben Vardanyan and Nikolay Akatyev[⊠]

Makhambet Utemisov West Kazakhstan University, N. Nazarbayev Ave. 162, Uralsk 090000, The Republic of Kazakhstan

Corresponding authors: [™]nikolay.akatyev@wku.edu.kz

Received: September 21, 2024; Accepted: January 14, 2025; Published: January 22, 2025

Abstract

The present study investigates the inhibitory properties of sodium anthraquinone-2-sulfonate (AQ2SNa). Weight loss measurements, electrochemical tests, and metal surface analysis were carried out in this study to evaluate the adsorption behavior of the compound and its influence on the corrosion rate of carbon steel in 0.5 mol dm⁻³ H₂SO₄ solution. Density functional theory DFT/B3LYP/6-311+G(d,p) and molecular dynamic simulation (MD) were applied for theoretical studies to evaluate the inhibiting effect and understand the mechanism of interaction of inhibitor molecules with Fe (110) surface. It was found that the inhibition efficiency of AQ2SNa in 0.5 mol dm⁻³ H₂SO₄ solution reached up to 94.44 % at the maximum concentration (0.5 g dm⁻³). Thermodynamic parameters show that the adsorption process is spontaneous and endothermic, suggesting the conformance of strong interactions between inhibitor and metal surface according to the Langmuir adsorption model. The spontaneous physisorption ($\Delta G^0_{ads} > -20 \text{ kJ mol}^{-1}$) of the inhibitor molecules led to high efficiency. Analysis of dynamic polarization curves showed that AQ2SNa acts as an inhibitor of a mixed nature. The results also indicate that AQ2SNa significantly increases the contact angle, indicating increased hydrophobicity due to the formation of a stable film on the metal surface. Theoretical parameters were compared to experimental data. The results highlight the novel potential of AQ2SNa as an effective corrosion inhibitor to provide an effective solution for enhancing the protection of carbon steel in acidic media.

Keywords

Organic corrosion inhibitors; metal protection; weight loss; electrochemical tests, quantum chemical calculations

Introduction

Corrosion poses a significant challenge to various industries as the deterioration of metals and alloys can lead to structural failures, reduced efficiency and significant economic losses [1]. The

addition of corrosion inhibitors is still the most effective way of preventing metal corrosion. To prevent the corrosive destruction of metals, individual compounds of various nature (organic, inorganic) and origin (synthetic, natural), comprising mixed compositions [2], polymers and their composites [3], or extracts obtained from natural sources (plant [4], biomass [5]) or plant waste [6,7], can be used. Corrosion inhibitors adsorb onto the metal surface, forming a protective film that prevents corrosive agents from reaching the metal. This adsorption can be physical (physisorption) or chemical (chemisorption). The protective layer can be composed of oxides or other less reactive compounds than the base metal [8].

Anthraquinones form a large and diverse subgroup within the quinone superfamily. The first study of the effect of anthraquinone and some of its derivatives on the corrosion resistance of metals in sulfuric acid solution was published in 1969 by Kuzyukov and Levin [9]. Three amide derivatives of 1-aminoanthraquinones synthesized from long chain fatty acids were investigated by Muthukumar as effective corrosion inhibitors. It has been shown that the inhibitory effectiveness of these compounds can reach 84 % [10]. Saqalli *et al.* [11] reported the influence of hydroxyl group number of some anthraquinone derivatives 1,2,4-trihydroxyanthraquinone (purpurin) and 1,4-dihydroxyanthraquinone (quinizarin) on their corrosion inhibition efficiency. Electrochemical studies and quantum chemical calculations revealed that the compound containing supplementary group (OH) presents the highest inhibition efficiency (91.5 %). The anticorrosive properties of alizarin (also a hydroxy derivative of anthraquinone) as a cathodic inhibitor of mild steel corrosion in 1.0 M HCl solution are well known [12]. Furthermore, Bensouda *et al.* demonstrated that *Mentha piperita* essential oil, containing 1-(p-fluorophenyl) anthraquinone as the main component (42.8 %), showed an inhibitory effect of up to 87 % for mild steel in HCl solution [13].

Sodium anthraquinone-2-sulfonate (AQ2SNa, Figure 1) is a water-soluble anthraquinone derivative that can be prepared by sulfonation of anthraquinone.



Figure 1. Chemical structure and ball-and-stick model of AQ2SNa with atomic enumeration

Nowadays, the AQ2SNa has a wide range of applications. It is used in high-performance supercapacitors [14], in photochemistry [15], as a co-catalyst [16], and for developing nano-antibacterial materials [17] and multifunctional sensors [18]. Articles dealing with anti-corrosion properties of AQ2SNa are exclusively concerned with the use of AQ2SNa as a self-deoxidizing additive to an electrolyte of aqueous-zinc batteries to prevent zinc anode corrosion and dendrite growth [19]. In related studies, sulfonate-rich layers have been shown to modulate ion transport at the anode-electrolyte interface. These layers create electrostatic repulsion that blocks harmful species from reaching the zinc surface while facilitating the desolvation of zinc ions. This mechanism helps in reducing undesirable side reactions and promotes uniform zinc deposition [20]. Nevertheless, nowadays, there is no information on using AQ2SNa as a corrosion inhibitor of other metals in liquid media or against any other type of corrosion.

Therefore, the aim of the present study is to investigate the corrosion protection properties of AQ2SNa for carbon steel in acidic media.

Experimental

Materials and solution

A freshly prepared corrosive medium comprising 0.5 mol dm⁻³ sulfuric acid (H_2SO_4) solution obtained by diluting high-grade concentrated sulfuric acid (98.3 %) with double distilled water (DDW) was utilized in this study. The corrosion inhibitor was incorporated into the solution at concentrations spanning 0.05, 0.1, 0.2, 0.3, 0.4 and 0.5 g dm⁻³. Analytical grade (\geq 98 %) AQ2SNa as a monohydrate was purchased from commercial suppliers and used without further purification.

Sample preparation

Carbon steel specimens containing 97.8 wt.% Fe, 0.22 wt.% C, 0.65 wt.% Mn, 0.30 wt.% Si, 0.04 wt.% P, 0.05 wt.% S, 0.30 wt.% Cr, 0.30 wt.% Ni, 0.30 wt.% Cu and 0.01 wt.% N, with dimensions of 25.0×35.0×3.0 mm, were acquired from the industrial sector for corrosion testing. Before the experiment, the samples were polished in sequence using emery paper with grit numbers between 250 and 1200. The specimens were washed in running water and DDW to remove oxides and dust and then cleaned and degreased with ethanol and acetone. The specimens were prepared and kept in a desiccator with silica gel until the upcoming corrosion tests.

Weight loss (gravimetric) measurements

The weight loss experiments were performed to evaluate the corrosion rate (CR), degree of surface coverage (θ), and inhibition efficiency (IE). Every sample was placed in a beaker preliminarily filled with 100 ml of corrosion medium at room temperature. Samples were removed from the beaker following the soaking time and gently scrubbed with a soft brush under tap water and DDW. Then, they were immersed in a mixture of 50 % NaOH and 100 g of zinc dust [21] to remove any leftover corrosion product residues. Before being reweighted, the samples were rewashed in tap water and DDW, followed by rinsing in ethanol, acetone, and drying. The Ohaus Adventurer Pro AV264 analytical balance was utilized for all weighing tasks with a precision of ± 0.1 mg.

Equations (1) to (3) were employed for the determination of the corrosion rate (CR / g m⁻² h⁻¹), inhibition efficiency (IE / %), and degree of surface coverage (θ), respectively:

$$CR = \frac{\Delta m}{S\tau} \tag{1}$$

$$IE = \frac{CR_0 - CR_i}{CR_0} 100 \tag{2}$$

$$\theta = \frac{IE}{100} \tag{3}$$

where Δm / g is the weight loss of the carbon steel specimen after the immersion time τ / h, S / m² is the surface area of the carbon steel specimen, CR₀ is the corrosion rate of carbon steel without inhibitor, and CR_i is the corrosion rate of carbon steel with the addition of inhibitor.

Activation parameters calculations

The activation energy was determined in accordance with the logarithmic form of the Arrhenius Equation (4) as follows:

$$\log CR = \log A - \frac{E_a}{2.303 RT} \tag{4}$$

where A is the Arrhenius pre-exponential factor, T/K is absolute temperature, and R is the universal gas constant (8.314 J mol⁻¹ K⁻¹). The plots of log CR against 1 / 2.303 RT exhibit straight lines with a slope corresponding to E_a and intercept to log A.

Enthalpy ($\Delta H^*/\text{ kJ mol}^{-1}$) and entropy ($\Delta S^*/\text{J mol}^{-1}\text{K}^{-1}$) of activation were obtained from the slope $-\Delta H^*/2.303\text{R}$ and intercept [log $R/Nh + (\Delta S^*/2.303\,R)$] respectively from the plot of log (CR/T) versus 1 / T in accordance with the following alternative form of Arrhenius Equation (5):

$$\log \frac{CR}{T} = \frac{-\Delta H^*}{2.303R} \left(\frac{1}{T} \right) + \left| \log \frac{R}{N_A h} + \left(\frac{\Delta S^*}{2.303R} \right) \right|$$
 (5)

where h signifies Planck's constant, N_A denotes Avogadro's number, T represents thermodynamic temperature, R denotes the universal gas constant, ΔS^* is the entropy change, and ΔH^* signifies the enthalpy change.

Adsorption and thermodynamics

In corrosion science, adsorption isotherms describe the adsorption behavior of corrosion inhibitors on metal surfaces. They help to determine the thermodynamic parameters and the nature of the interaction of inhibitors with the metal surface (physisorption or chemisorption), as well as estimate the efficiency of these interactions. For this purpose, the adsorption models of Langmuir, Temkin, Freundlich, Flory-Huggins, Frumkin and El-Awady (Equations (6) to (11)) are usually used. Every model has its own mathematical form, allowing graphical determination of the necessary parameters [22]. In our study, we evaluated the applicability of all the above models to the adsorption of AQ2SNa on the surface of carbon steel in accordance with their mathematical expressions, where $C_{\rm inh}$ / g dm⁻³ - inhibitor concentration, θ - degree of surface coverage, $K_{\rm ads}$ - the equilibrium constant for adsorption-desorption processes:

Langmuir adsorption isotherm

$$\frac{C_{\text{inh}}}{\theta} = \frac{1}{K_{\text{ads}}} + C_{\text{inh}} \tag{6}$$

• Temkin adsorption isotherm

$$\theta = \ln C_{\rm inh} + K_{\rm ads} \tag{7}$$

• Freundlich adsorption isotherm

$$\log \theta = \log K_{\text{ads}} + \frac{1}{n} \log C_{\text{inh}}$$
 (8)

where n is a dimensionless constant indicating the intensity of the adsorption process.

• Flory-Huggins adsorption isotherm

$$\log \frac{\theta}{C_{\text{inh}}} = b \log(1 - \theta) + \log K_{\text{ads}}$$
 (9)

where b is the parameter representing the interaction between the adsorbate and the adsorbent.

Frumkin adsorption isotherm

$$\log \left[C_{\text{inh}} \left(\frac{\theta}{1 - \theta} \right) \right] = 2\alpha \theta + 2.303 \log K_{\text{ads}}$$
 (10)

where α is the interaction parameter that quantifies the interactions between adsorbed molecules on the surface.

• El-Awady adsorption isotherm

$$\log\left(\frac{\theta}{1-\theta}\right) = y\log C_{\text{inh}} + \log K \qquad K_{\text{ads}} = K^{\frac{1}{y}}$$
(11)

where *y* is the parameter that represents the number of active sites occupied by one inhibitor molecule on the metal surface.

The values of K_{ads} obtained from the isotherms are usually used to calculate the Gibbs free energy according to the known relationship:

$$\Delta G_{ads}^{0} = -RT \ln(55.5 K_{ads}) \tag{12}$$

where ΔG^0_{ads} is the Gibbs free energy of adsorption, R is the universal gas constant, T is the thermodynamic temperature, and 55.5 is the molar concentration of water in mol dm⁻³.

Electrochemical measurements

The steel specimens used in the electrochemical experiment and weight loss tests underwent the same pretreatment. The NOVA 2.1.6 software installed in the Autolab PGSTAT 101 Metrohm potentiostat/galvanostat was used for the electrochemical test. Electrochemical measurements were conducted using a three-electrode configuration: a reference electrode (Ag/AgCl filled with 3.0 mol dm⁻³ KCl), a counter electrode (platinum), and a working electrode (steel sample). An electrochemical cell was created using a beaker with 100 ml of 0.5 mol dm⁻³ H_2SO_4 , with and without inhibitor. During open circuit potential (OCP) testing, the working electrode, with an exposed area of 1.0 cm², was stabilized. Linear polarization measurements were carried out immediately following the OCP using linear sweep voltammetry (LSV) staircase and corrosion rate analysis. Potentiodynamic scanning was conducted by applying a scan rate of 0.01 V s⁻¹ within the range of -0.50 to +0.50 V. The corrosion potential (E_{corr}) and corrosion current density (E_{corr}) were determined from Tafel polarization curves.

Equation (13) was utilized to calculate the inhibition efficiency (IE_j , %) based on the corrosion current density:

$$IE_{j} = \frac{j_{\text{inh}} - j_{\text{corr}}}{j_{\text{inh}}} 100 \tag{13}$$

where j_{inh} and j_{corr} are the corrosion current densities determined by extrapolating the Tafel slopes with and without inhibitors, respectively, A cm⁻².

The calculation of inhibition efficiency through polarization resistance (IE_R , %) was derived using the Equation (14):

$$IE_{R} = \frac{R_{p}^{inh} - R_{p}^{0}}{R_{p}^{inh}} 100$$
 (14)

where $R_{\rm p}^{\rm inh}$ and $R_{\rm p}^{\rm 0}$ / Ω represent the charge transfer resistance with and without inhibitor, respectively.

Metal surface analysis

Contact angle measurement

The hydrophilicity of the steel coupons was assessed by measuring the contact angle between a water drop and the steel surface using an Ossila Contact Angle Goniometer equipped with the Ossila Contact Angle software *ver.* 4.2.0. The water drops were mounted on the surface of the carbon steel sample using a micro-syringe with a needle diameter of 0.4 mm. The reported contact angles were an average of at least three measurements from different areas of the surface. Photos of water drops were obtained using a high-resolution video camera and the above software.

Scanning electron microscopy surface analysis

Scanning electron microscopy (SEM) accurately reflect the morphology of the metal surface after corrosion and provides a very valuable reference for evaluating corrosion inhibitor performance. A scanning electron microscope JEOL 6390LV was used to observe the surface morphologies of the carbon steel specimens after immersion in 0.5 mol dm $^{-3}$ H₂SO₄ solution with and without inhibitor for 24 h. Tested specimens were compared with the polished specimens to analyze the corrosion inhibition efficiency. Before the experiments, the carbon steel surface was thoroughly cleaned with ethanol and acetone. Then, the polished specimen and the specimens after immersion in 0.5 mol dm $^{-3}$ H₂SO₄ solution were examined in the absence or presence of AQ2SNa for 24 h.

Computational details

Computer modeling methods such as density functional theory (DFT) calculation and molecular dynamic (MD) simulation are required for the theoretical study of new corrosion inhibitors. For this purpose, both methods were used in this work.

Quantum chemical calculations

The molecular mechanism of corrosion inhibition can be well explained by quantum chemical calculations. It is a valuable tool for gaining deeper insight into the adsorption phenomena and the accompanying effects of electronics.

In an aggressive environment, corrosion inhibitors can undergo various chemical transformations [23]. In acidic environments, AQ2SNa can dissociate as an ionic compound *via* Equation (15) or form the corresponding acid according to the exchange reaction described by Equation (16). Acid formed can also dissociate in solution and produce ions described by Equation (17):

$$AQ2SNa = AQ2S^{-} + Na^{+}$$
 (15)

$$AQ2SNa + H^{+} \leftrightarrows AQ2SH + Na^{+} \tag{16}$$

$$AQ2SH \hookrightarrow AQ2S^- + Na^+ \tag{17}$$

According to Equations (15) to (17), in a solution, AQ2SNa can exist as a salt, an acid (AQ2SH), and sulfonate ions (AQ2S⁻). Therefore, quantum chemical calculations were carried out for the three indicated forms for a comparative assessment. The energy of the highest occupied molecular orbital (E_{HOMO}), the energy of the lowest unoccupied molecular orbital (E_{LUMO}), energy gap (ΔE_{gap}), the ionization potential (IP), the electron affinity (EA), electronegativity (χ), global hardness (η), softness (σ), electrophilic (ω) and nucleophilic (ε) indexes, back-donation energy ($E_{\text{b-d}}$), total negative charge (TNC, TNC/n) were considered (n - total number of atoms in molecule) [24].

All quantum chemical calculations were performed on a desktop PC with Windows 11, a 12th generation Intel(R) Core (TM) i7-12700H 2.30 GHz, 16GB RAM) with GAMESS software [25]. Initially, full geometry optimization was achieved using the Molecular Mechanics (MM+) force field. The results from MM+ were further selected as input and re-optimized using semi-empirical AM1 to obtain the equilibrium geometry. Final geometry optimization and quantum chemical parameters were obtained by density functional theory (DFT) calculations. DFT is the most widely accepted *ab initio* approach for modeling ground states of molecules. To calculate optimized geometrical structure, atomic charges, and energies, the Lee-Yang-Parr Becke's three-parameter hybrid functionnal method (B3LYP) with the split-valence double-zeta polarized basis set 6-311+G(d,p) was used. All DFT calculations were done in the aqueous phase because it is well-known that the electrochemical corrosion always appears in an aqueous medium. The solvent (H₂O) was incorporated via the Conductor-like Screening Model (COSMO) [26].

Molecular dynamics simulation

The intensity of the interactions between the examined inhibitor and metal surface was determined using molecular dynamics (MD) simulations. MD simulation is a modern computational technique crucial for theoretical studies of the interaction between inhibitors and metal surfaces.

The corrosion system, which is composed of carbon steel, water, and a corrosion inhibitor structure, was constructed using Avogadro software. The MD simulations were carried out by using the GROMACS 2020.4 software [27]. Adsorption energy was calculated by Equation (18):

$$E_{\text{adsorption}} = E_{\text{total}} - (E_{\text{Fe}(110)+\text{solution}} + E_{\text{inhibitor}}) \tag{18}$$

where $E_{\rm adsorption}$ is the adsorption energy (or interaction energy) corresponds to the amount of energy released or absorbed as 1 mole of adsorbate molecules is adsorbed on the adsorbent, $E_{\rm total}$ is the total energy of the whole system (surface Fe(110) + solution + inhibitor molecule), $E_{\rm Fe(110)+solution}$ is the energy of the metal and the aqueous phase and $E_{\rm inhibitor}$ is the energy of the inhibitor molecule.

Binding energy is the energy required to separate a particle from a system. The greater the binding energy, the stronger the attraction force between the inhibitor and the metal surface, and hence the higher the inhibition efficiency. The binding energy is regarded as the reciprocal of the adsorption energy of the inhibitor molecule as follows (19):

$$E_{\text{binding}} = -E_{\text{adsorption}} \tag{19}$$

where E_{binding} is the binding energy.

Five layers of Fe (110) metal containing 960 Fe atoms were placed at the bottom of a simulation box, with the corrosion inhibitor molecule placed at the center of the box, surrounded by 800 water molecules (periodic boundary conditions). The Fe (110) metal structure was chosen due to its lowest surface energy, thermodynamic stability and the largest area of the Fe crystal [28]. Before the MD simulation, the system was optimized until the energy met the 0.10 J mol value. MD was conducted at a constant temperature of 298 K, with a 1 fs time step and a simulation time of 500 ps.

Results and discussion

Weight loss analysis

The weight loss tests were performed using the inhibitor concentrations of 0.05, 0.1, 0.2, 0.3, 0.4, and 0.5 g dm⁻³ for an exposure period of 2-24 hours. Figure 2 illustrates the impact of AQ2SNa concentration and exposure duration on the CR (A) and IE (B) of carbon steel in 0.5 mol dm⁻³ H₂SO₄ solutions.

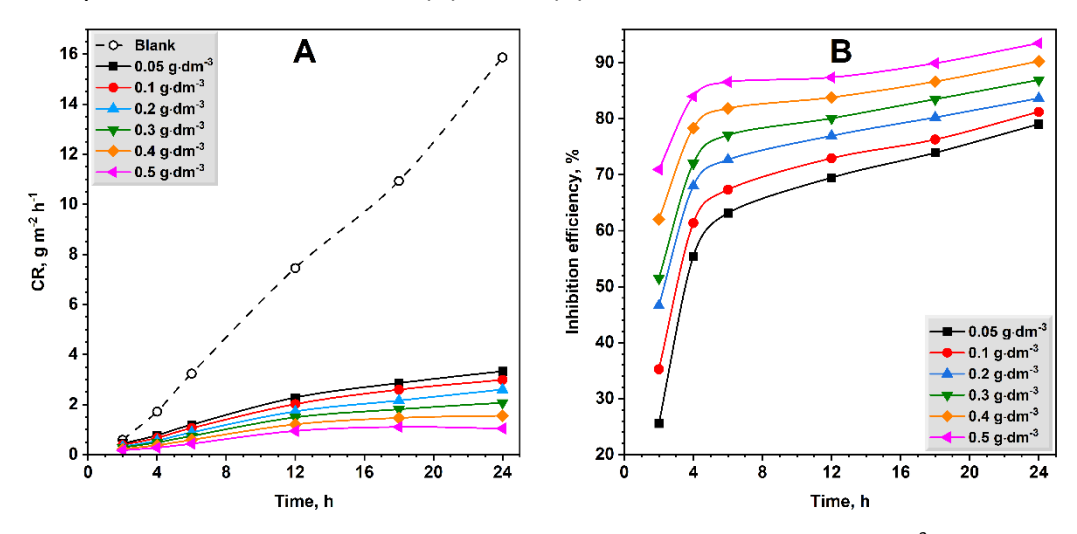


Figure 2. The relationship between CR (A) and IE (B) on carbon steel in 0.5 mol dm⁻³ H_2SO_4 solution and immersion time and inhibitor concentration at room temperature

Evidently, the presence of AQ2SNa significantly decreases the corrosion rate (Figure 2A). The IE of AQ2SNa in $0.5 \text{ mol dm}^{-3} \text{ H}_2\text{SO}_4$ depends on the inhibitor concentration and increases with the exposure time. The existence of an induction period indicates that the inhibitor forms the most effective protective layer on the carbon steel surface after at least 4 to 6 hours of immersion. The increase in the inhibitor concentration results in the augmentation of the protective properties. It was found that an inhibitor concentration of 0.5 g dm^3 provided the most effective corrosion inhibition. Accordingly, for the best possible inhibition, the inhibitor should be used in higher concentrations. The obtained results suggest that AQ2SNa has promising applications for preventing metal corrosion in a strongly acidic environment.

The corrosion rate (CR), inhibition efficiency (IE), and degree of surface coverage (θ) obtained from weight loss assay for carbon steel in 0.5 mol dm⁻³ H₂SO₄ solution at 298, 303, 313, 323 and 333 K in the absence and presence of AQ2SNa are given in Table 1.

Table 1. Corrosion parameters obtained from weight loss assay of carbon steel in 0.5 mol dm⁻³ H₂SO₄ containing various concentrations of AQ2SNa at different temperatures

containing vari	ous concentrations o	f AQ2SNa at different tempe	ratures
Inhibitor concentration / g dm ⁻³	CR / g m ⁻² h ⁻¹	IE / %	θ
	298	3 K	
0.00	6.30 ± 0.28	-	-
0.05	2.03 ± 0.12	67.81 ± 2.01	0.6781
0.10	1.89 ± 0.10	70.05 ± 1.25	0.7005
0.20	1.70 ± 0.08	73.04 ± 1.92	0.7304
0.30	1.38 ± 0.06	78.04 ± 1.79	0.7804
0.40	1.22 ± 0.05	80.66 ± 1.65	0.8066
0.50	1.01 ± 0.03	84.02 ± 1.85	0.8402
	303	3 K	
0.00	13.47 ± 0.84	-	-
0.05	3.78 ± 0.25	71.92 ± 2.38	0.7192
0.10	3.45 ± 0.19	74.38 ± 2.05	0.7438
0.20	3.09 ± 0.16	77.05 ± 1.99	0.7705
0.30	2.46 ± 0.13	81.72 ± 2.16	0.8172
0.40	2.12 ± 0.13	84.29 ± 2.48	0.8429
0.50	1.69 ± 0.10	87.49 ± 2.59	0.8749
	313	3 K	
0.00	27.97 ± 1.87	-	-
0.05	7.50 ± 0.82	73.19 ± 2.03	0.7319
0.10	6.64 ± 0.68	76.27 ± 2.60	0.7627
0.20	5.39 ± 0.52	80.74 ± 2.59	0.8074
0.30	4.31 ± 0.33	84.58 ± 2.75	0.8458
0.40	3.26 ± 0.27	88.36 ± 3.16	0.8836
0.50	2.18 ± 0.16	92.22 ± 3.38	0.9222
	323	3 K	
0.00	47.93 ± 3.24	-	-
0.05	9.72 ± 0.56	79.72 ± 2.29	0.7972
0.10	8.50 ± 0.32	82.26 ± 3.09	0.8226
0.20	7.18 ± 0.29	85.02 ± 2.94	0.8502
0.30	5.66 ± 0.28	88.20 ± 3.36	0.8820
0.40	4.39 ± 0.21	90.85 ± 3.24	0.9085
0.50	3.03 ± 0.16	93.67 ± 3.04	0.9367
	333	3 K	
0.00	65.06 ± 3.84	-	-
0.05	12.45 ± 1.03	80.86 ± 2.23	0.8086
0.10	10.88 ± 0.86	83.28 ± 2.81	0.8328
0.20	9.02 ± 0.72	86.13 ± 3.12	0.8613
0.30	7.12 ± 0.56	89.06 ± 3.27	0.8906
0.40	5.40 ± 0.47	91.69 ± 2.93	0.9169
0.50	3.62 ± 0.34	94.44 ± 3.11	0.9444

Table 1 shows that the best protective efficiency of 94.44 % is achieved at the highest temperature and concentration values. The obtained values of corrosion rates and protective effect clearly indicate an enhancement in the inhibitory effectiveness of AQ2SNa with the increased temperature and concentration in a given corrosion medium. At all temperatures, the IE reaches its maximum value at the highest concentration of the inhibitor. The results show that the presence of AQ2SNa decreases metal dissolution in 0.5 mol dm $^{-3}$ H₂SO₄ medium. This effect can be interpreted because of the formation of the protective layer of the inhibitor on the carbon steel surface.

Activation parameters

Graphical representation of activation parameters determined from the Arrhenius plots and transition state plots in accordance with Eqs. (4) and (5) are presented in Figure 3.

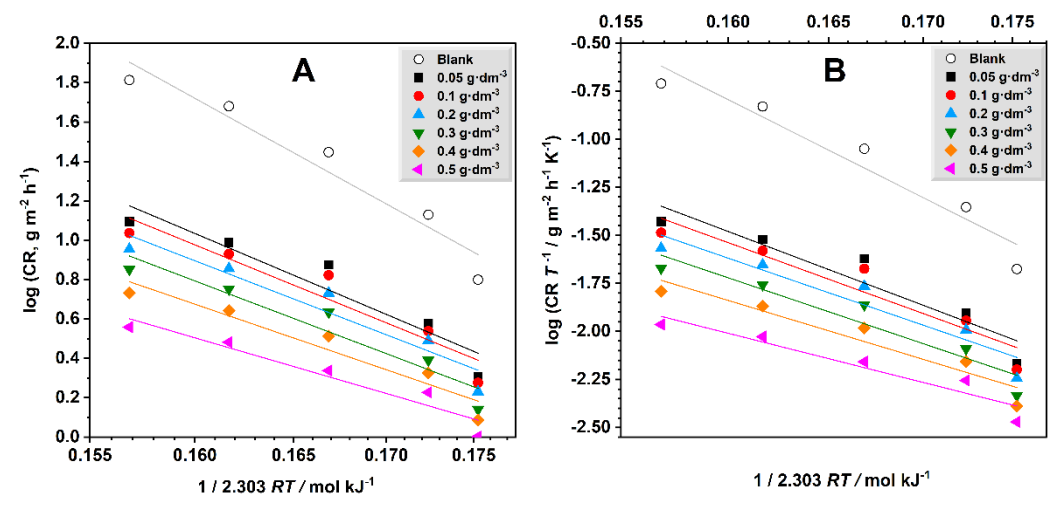


Figure 3. Arrhenius plots (A) and transition state plots (B) for carbon steel in 0.5 mol dm⁻³ H_2SO_4 solution in the absence and presence of AQ2SNa at different concentrations

The activation parameters of corrosion of carbon steel in 0.5 mol dm⁻³ H₂SO₄ in the absence and presence of different concentrations of AQ2SNa are given in Table 2.

Table 2 . Activation parameters of the dissolution of carbon steel in 0.5 mol dm ⁻³ H_2SO_4 in the absence and
presence of different concentrations of AQ2SNa

Inhibitor concentration / g dm ⁻³	Α	E _a / kJ mol ⁻¹	ΔH* / kJ mol ⁻¹	ΔS* / J mol ⁻¹ K ⁻¹
Blank	2.52·10 ⁷	27.95	-26.57	-378.80
0.05	8.98⋅10⁵	21.41	-20.03	-351.07
0.1	5.66⋅10⁵	20.62	-19.24	-347.24
0.2	3.11·10 ⁵	19.57	-18.19	-342.27
0.3	3.05⋅10⁵	19.23	-17.85	-342.10
0.4	9.73·10 ⁴	17.35	-15.97	-332.59
0.5	2.00·10 ⁴	14.72	-13.34	-319.44

In the presence of AQ2SNa, the activation energy is lower than that in the uninhibited sulfuric acid solution, which means that the inhibitor is effectively reducing the energy required for the corrosion reaction to proceed, thereby slowing down the corrosion rate. The decrease of activation energy with an increase in the inhibitor concentration leads to better surface coverage and more effective corrosion inhibition [29].

A decrease in the pre-exponential factor (A) with an increase in inhibitor concentration suggests a reduction in the frequency of effective molecular collisions, which can be attributed to various factors that hinder molecular interactions. In corrosion studies, this indicates that the inhibitor is effectively adsorbing onto the surface, forming a barrier that reduces the number of active sites available for the

reaction [30]. The negative values of the enthalpy of activation (ΔH^*) indicate that the process is exothermic, suggesting that the reaction is energetically favorable and tends to proceed spontaneously at lower temperatures [31]. An increase in ΔH^* with temperature suggests that at higher temperatures, the system needs more energy to sustain the reaction, and the energy barrier for the corrosion process becomes higher as the temperature rises. This behavior is often observed in systems where the inhibitor's effectiveness improves with temperature, leading to a more stable and protective adsorbed layer on the metal surface [32]. The negative values of the entropy of activation (ΔS^*) indicate that the transition state of the corrosion process is more ordered than the initial state. This implies that the formation of the activated complex involves a decrease in randomness or an increase in order. It also indicates that the activated complex is formed through an association process rather than dissociation, and the inhibitor molecules combine in a more ordered manner to form the transition state. The increase of the ΔS^* indicates that the rise in temperature corresponds to additional freedom of movement acquired by inhibitor molecules, leading to a less ordered transition state. This phenomenon often accompanies an endothermic process, where the adsorption and activation processes become more favorable at higher temperatures.

Adsorption and thermodynamics

Adsorption isotherms for AQ2SNa on carbon steel in 0.5 mol dm $^{-3}$ H $_2$ SO $_4$ surface, calculated according to Equations (6) to (11) at all experimental temperatures, are given in Figure 4. Figure 4A shows that C θ^{-1} presented *versus* inhibitor concentration at all experimental temperatures exhibits the best straight lines. High values of the linear regression coefficient ($r^2 > 0.995$) indicate that the Langmuir isotherm is the most suitable for describing the adsorption of AQ2SNa on the surface of carbon steel. The agreement of the adsorption process with the Langmuir model indicates that the inhibitor molecules form a monolayer on the metal surface, displacing the water molecules that initially occupy the adsorption sites, and no further adsorption occurs when the surface is completely covered [33]. It also demonstrates that all adsorption sites on the metal surface are identical and energetically equivalent and the adsorbed molecules do not interact with each other, meaning that the adsorption of one molecule does not affect the adsorption of another molecule [34]. For other isotherms, the value of the linear regression coefficient is significantly lower, rendering them unfit for describing the process of adsorption of AQ2SNa on a carbon steel surface under given experimental conditions.

The K_{ads} and Gibbs free energy values (ΔG^0_{ads}) for the AQ2SNa were calculated from the slopes and intercepts of the Langmuir adsorption isotherms in Figure 4A and presented in Table 3.

Table 3. Thermodynamic parameters of adsorption of AQ2SNa on carbon steel surface in 0.5 mol dm $^{-3}$ H $_2$ SO $_4$ solutionT / KSlopeIntercept r^2 K_{ads} / 10^{-3} dm 3 g $^{-1}$ ΔG^0_{ads} / kJ mol $^{-1}$ 2981.158230.028410.9970935.20-18.78

J mol ⁻¹
78
17
35
50
38

Negative values of ΔG^0_{ads} indicate that the absorption of AQ2SNa onto the carbon steel surface is spontaneous. The value of $\Delta G^0_{ads} > -20$ kJ mol⁻¹ clearly shows that the adsorption is physical (physisorption) and occurs as a result of electrostatic interaction between charged inhibitor molecules and the steel surface.

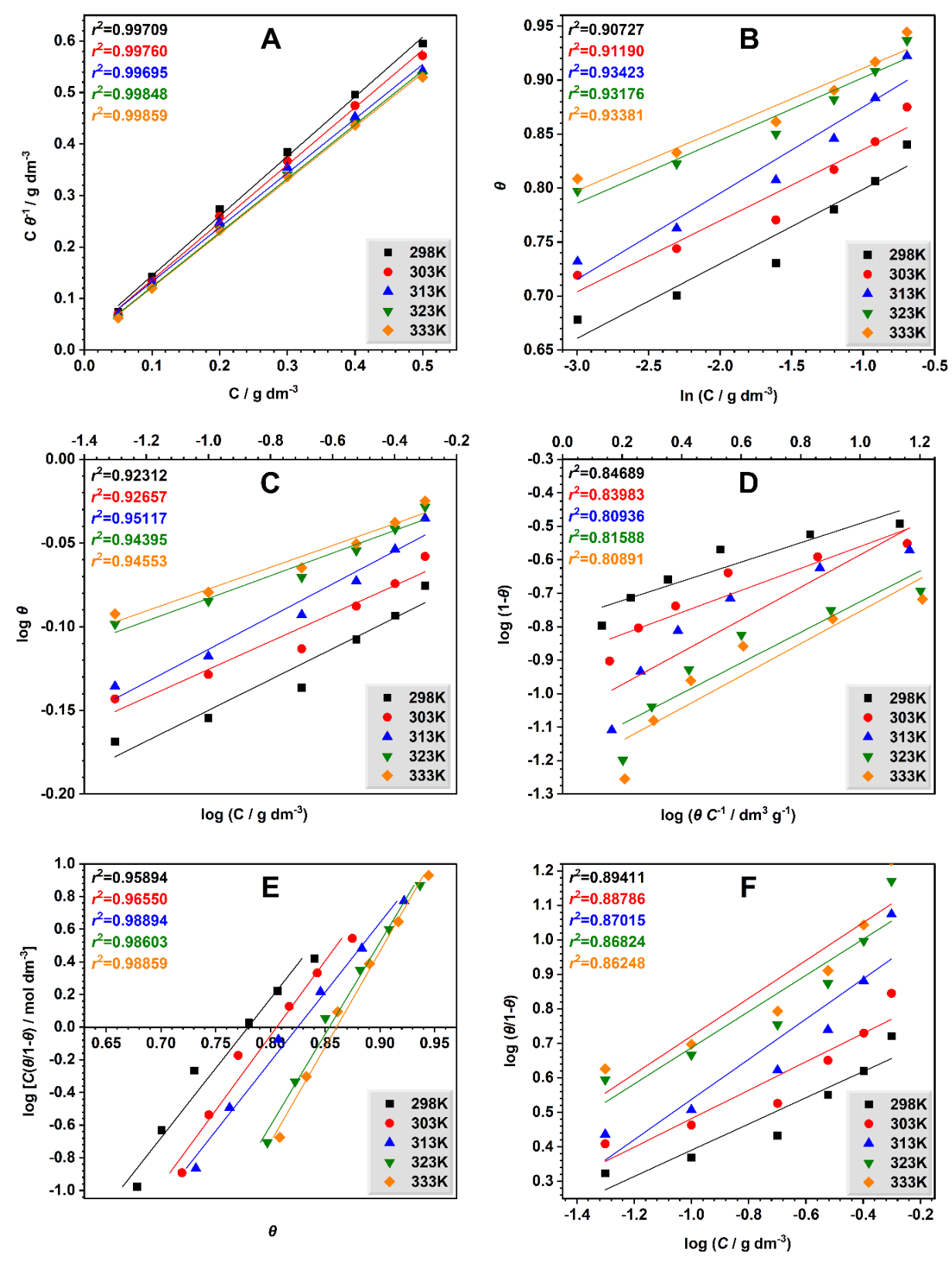


Figure 4. Adsorption isotherms for AQ2SNa in 0.5 mol dm⁻³ H_2SO_4 for 4 hours immersion period: A - Langmuir, B - Temkin, C - Freundlich, D - Flory-Huggins, E - Frumkin, F - El-Awady (r^2 - linear regression coefficient)

Increasing the temperature and concentration of the inhibitor accelerates the adsorption-desorption processes and promotes the formation of a stable, protective barrier on the metal surface [35]. A decrease in the Gibbs free energy value indicates that with an increase in temperature, adsorption occurs more efficiently, which contributes to better corrosion protection.

The values of ΔH^0_{ads} and ΔS^0_{ads} were calculated from the obtained values of ΔG^0_{ads} using the rearranged Gibbs-Helmholtz Equation (20):

$$\Delta G^0_{\text{ads}} = \Delta H^0_{\text{ads}} - T \Delta S^0_{\text{ads}} \tag{20}$$

The slope and intercept of the plot of the relationship between ΔG^0_{ads} and T allow to determine the values of ΔS^0_{ads} and ΔH^0_{ads} , respectively (Figure 5).

The positive value of ΔH^0_{ads} (11.62 kJ mol⁻¹) reveals that the adsorption of inhibitor molecules is an endothermic process and suggests physical adsorption (physisorption). It also indicates that the adsorption process becomes more favorable at higher temperatures, as the increased thermal energy helps to overcome the activation barrier for the adsorption reaction [36].

A positive value of ΔS^0_{ads} (102.28 J mol⁻¹ K⁻¹) for AQ2SNa indicates an increase in disorder at the metal-solution interface during the adsorption of inhibitor molecules onto the metal surface. Such values of ΔS^0_{ads} are often associated with endothermic adsorption (positive ΔH^0). Since the adsorption of inhibitor molecules onto the metal surface in aqueous corrosion media occurs with the displacement of water molecules, their subsequent desorption into the solution increases the overall disorder, thus contributing to a positive ΔS^0 value.

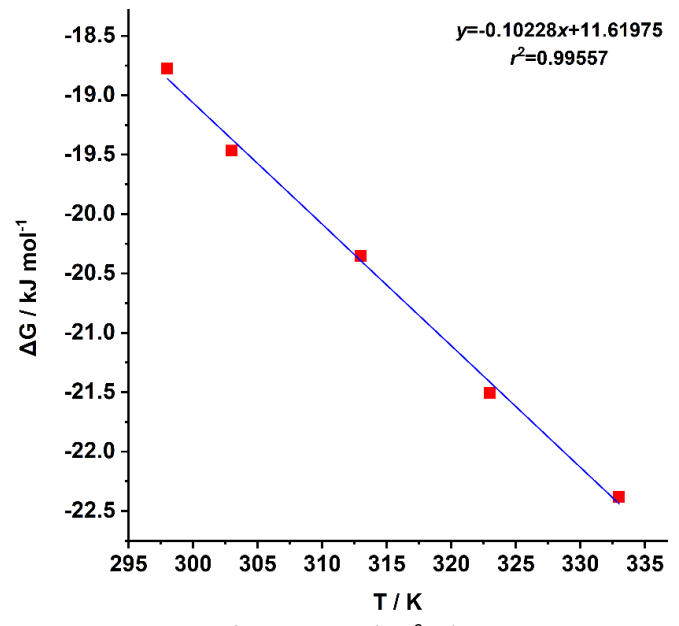


Figure 5. The relationship between Gibbs free energy (ΔG^0_{ads}) and absolute temperature for adsorption of AQ2SNa on carbon steel in 0.5 mol dm⁻³ H₂SO₄ solution

Metal surface analysis

Contact angle measurement was carried out to verify the formation of a protective layer of AQ2SNa inhibitor molecules on the carbon steel surface by evaluating changes in surface properties. This experiment provides insights into the surface wettability and the effectiveness of the inhibitor. A higher contact angle indicates increased hydrophobicity, suggesting that the inhibitor forms a protective layer on the metal surface, reducing its wettability and potentially enhancing corrosion resistance. Figure 6 displays the values of the contact angles for the carbon steel surface both with and without the inhibitor, taken before and after immersion in a 0.5 mol dm $^{-3}$ H₂SO₄ solution.

Figure 6 shows that the contact angle on the clean carbon steel surface is $55.96\pm0.82^{\circ}$ before immersion in a corrosive environment. After 24 hours of exposition in 0.5 mol dm⁻³ H₂SO₄ without the addition of an inhibitor, the contact angle was determined as $64.17\pm0.73^{\circ}$.

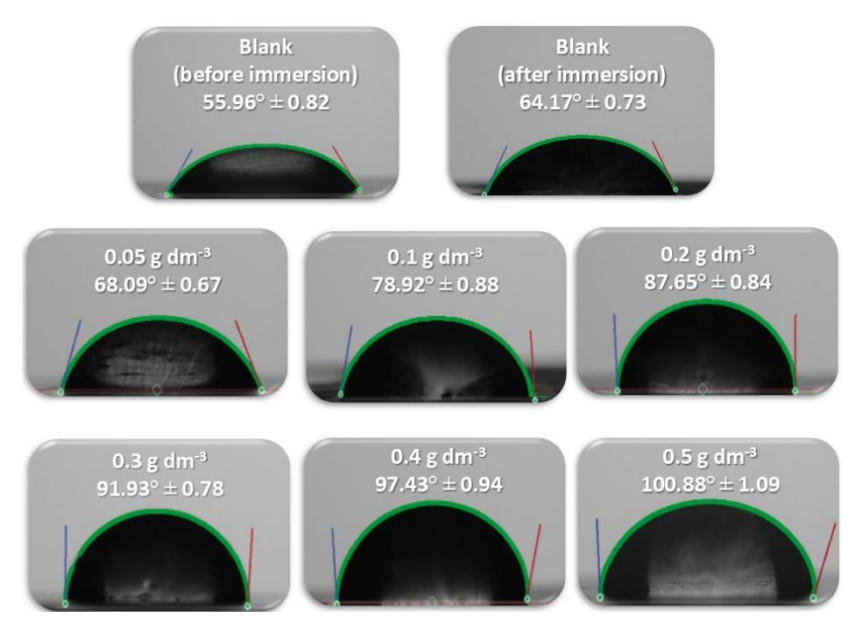


Figure 6. Contact angle values before and after immersing the carbon steel in 0.5 mol dm⁻³ H_2SO_4 solution for 24 hours in the presence of different AQ2SNa inhibitor concentrations

In the presence of an inhibitor, the contact angle increases significantly depending on the inhibitor concentration and reaches 100.88±1.09° at the maximal AQ2SNa concentration after 24 hours of immersion. The increase in the contact angle with increasing inhibitor concentration indicates increased hydrophobicity of the carbon steel surface. This suggests that the inhibitor effectively adsorbs on the surface, forming a protective layer that reduces wettability. As the inhibitor concentration increases, this layer becomes more robust, preventing the corrosive solution from interacting with the metal surface.

Scanning electron microscopy surface analysis

In order to explore the inhibitory properties of AQ2SNa better, the surface morphology of carbon steel was analyzed. Figure 7 shows the SEM micrographs of the polished steel and carbon steel immersed in $0.5 \text{ mol dm}^{-3} \text{ H}_2\text{SO}_4$ solution at 298 K for 24 h in the absence and presence of 0.5 g dm^{-3} AQ2SNa.

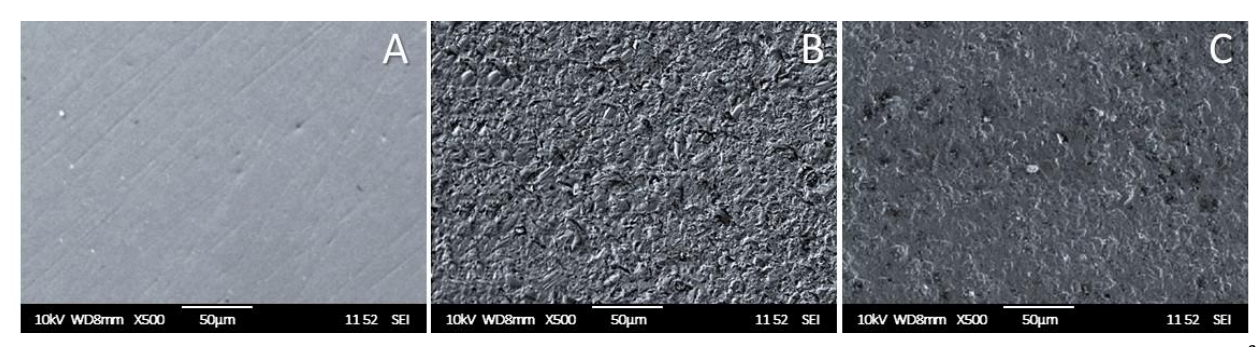


Figure 7. SEM micrographs of mild steel polished (A), after immersion without (B) and with (C) 0.5 g dm⁻³ AQ2SNa in 0.5 mol dm⁻³ H₂SO₄ solution

As can be seen, before immersion into the corrosion medium, the surface of the polished carbon steel was smooth, homogeneous with metallic lustre and a clearly defined structure, and the entire surface had some negligible roughness and scratches which are caused by sanding the prepared specimen (Figure 7A). After an immersion period without inhibitor, a drastic change in the metal surface structure is observed, forming a uniform dark, friable layer with noticeable pits and cracks. It can be observed that without the inhibitor, the carbon steel surface was severely corroded and

oxidized and corrosion pits appeared (Figure 7B). Compared with the fresh steel, the specimen surface was seriously damaged due to the corrosive acid solution in the absence of the inhibitor. This indicated carbon steel was corroded in 0.5 mol dm⁻³ H_2SO_4 solution. The presence of AQ2SNa induces the formation of a protective layer and the disappearance of the metallic lustre; however, the structure of the metal surface remains almost completely intact and visible corrosion damage to the surface is significantly reduced, which indicates that AQ2SNa exhibits excellent corrosion inhibition on carbon steel surface (Figure 7C). When the inhibitor was added to the corrosion medium, the carbon steel surface became smoother and cleaner because a protective film formed. These observations indicated that the inhibitor molecules adsorbed on the surface of carbon steel to form a protective film, which prevents the corrosion resulting from the corrosive medium.

Electrochemical experiments

Figure 8 displays the OCP vs. time curves and Tafel polarization curves for carbon steel corrosion in 0.5 mol dm⁻³ H₂SO₄. The OCP evaluation was performed during 60 seconds of immersion, both with and without AQ2SNa.

Figure 8 clearly demonstrates the anodic and cathodic polarization responses of carbon steel coupons, while Table 4 enlists the related corrosion outcomes and inhibition efficiencies obtained from polarization curves through corrosion rate analysis. The OCP reached an equilibrium state prior to the 60-second expiry. A shift in the OCP value at various AQ2SNa concentrations indicates that inhibitor molecules have adsorbed to the surface of the carbon steel. As can be seen, AQ2SNa primarily inhibits the anodic process, as indicated by a positive shift in OCP.

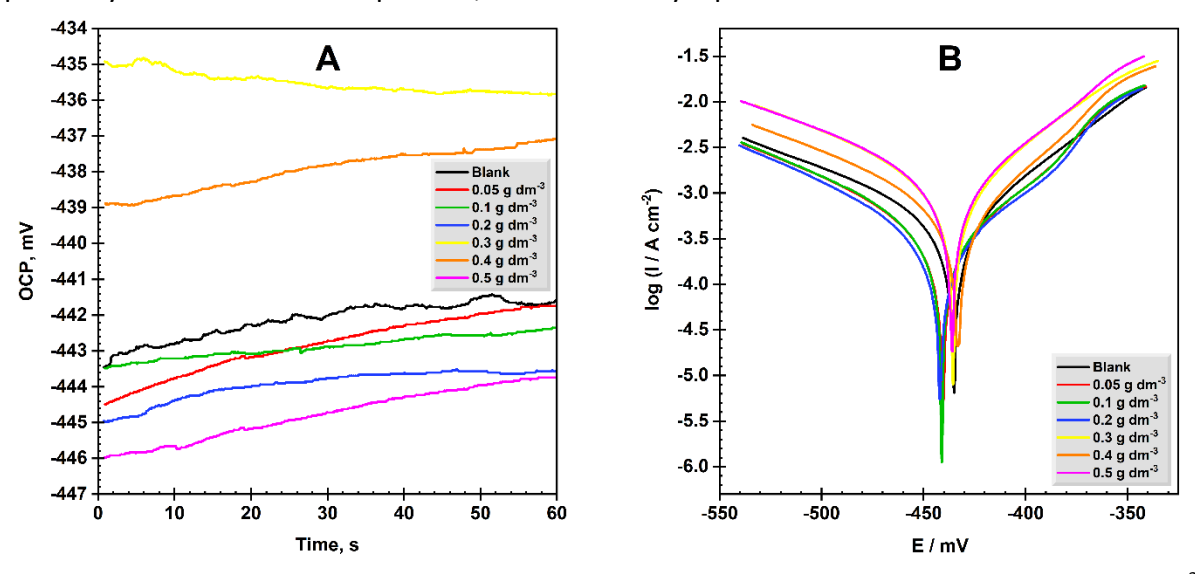


Figure 8. OCP vs. time diagram (A) and Tafel polarization curves (B) for carbon steel in 0.5 mol dm⁻³ H_2SO_4 solution with and without AQ2SNa at room temperature

Table 4. The electrochemical parameters of carbon steel corrosion in 0.5 mol dm⁻³ H_2SO_4 in the absence and presence of different concentrations of aqueous solution of AQ2SNa at room temperature

Inhibitor concentration / g dm ⁻³	-E _{corr} /mV	j _{corr} / 10 nA cm ⁻²	IE;/%	<i>b</i> _a / mV dec ⁻¹	<i>b</i> _c / mV dec ⁻¹	R_p/Ω	IE _R / %
Blank	432.98 ± 9.28	315 ± 9.5	-	71.13	91.09	60.37 ± 2.96	-
0.05	435.08 ± 8.36	87.2 ± 1.9	72.39	76.75	113.58	300.51 ± 12.33	79.91
0.1	440.46 ± 7.09	82.4 ± 2.2	73.88	88.68	121.26	354.85 ± 14.81	82.99
0.2	436.05 ± 6.53	74.5 ± 1.7	76.39	81.21	113.49	362.94 ± 16.86	83.37
0.3	435.08 ± 7.15	67.7 ± 2.1	78.55	75.13	105.56	370.34 ± 19.21	83.70
0.4	433.96 ± 6.13	61.1 ± 1.2	80.65	81.14	110.07	436.91 ± 22.78	86.18
0.5	432.98 ± 8.41	56.1 ± 1.5	82.23	84.05	113.14	451.91 ± 23.57	86.64

The corrosion rate of carbon steel in 0.5 mol dm⁻³ H_2SO_4 is significantly reduced in the presence of AQ2SNa. The presence of the inhibitor leads to significantly lower corrosion current density (J_{corr}) values, indicating that the metal surface is sufficiently protected from corrosion by AQ2SNa. The addition of an inhibitor leads to an increase in the values of polarization resistance (R_p), which confirms the formation of a protective layer on the steel surface, thereby preventing corrosion damage [37]. Apparently, the presence of an inhibitor causes a discernible shift in both the cathodic and anodic sites of the polarization curves, due to which AQ2SNa slows down both the cathodic and anodic reactions and acts as a mixed-type inhibitor. The anodic $|b_a|$ shift is smaller than the cathodic site shifts $|b_c|$, indicating the greater effect of the inhibitor on cathodic polarization rather than anodic polarization.

The values of the inhibitory effect, ascertained by applying Equations (13) and (14) based on corrosion current and polarization resistance, respectively, in the presence of the AQ2SNa aqueous solution, rise noticeably as the concentration of the inhibitor increases. This suggests that the investigated inhibitor has a high potential to stop the corrosion of carbon steel in a solution of 0.5 mol dm⁻³ H₂SO₄.

Quantum chemical calculations

Top and side views of the optimized structures calculated using DFT/B3LYP/6-311+G(d,p) of AQ2SNa, AQ2SH, and AQ2S⁻ are shown in Figure 9.

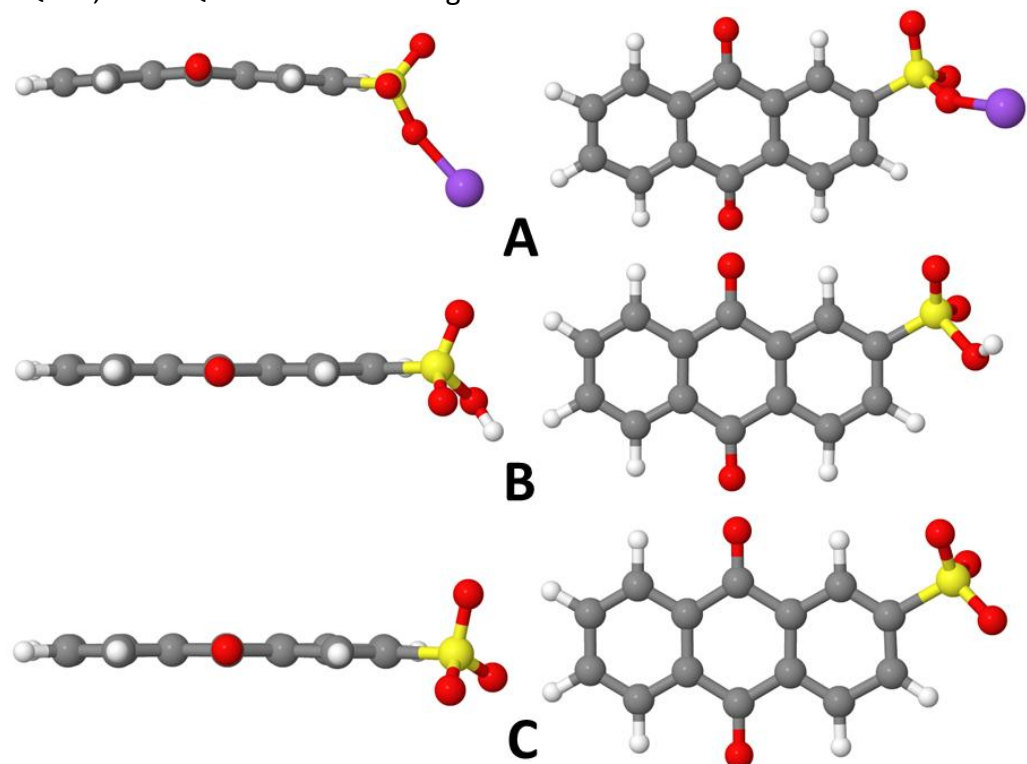


Figure 9. Top and side view of the optimized structures of AQ2SNa (A), AQ2SH (B) and AQ2S $^{-}$ (C) calculated using DFT/B3LYP/6-311+G(d,p)

As can be seen, the acidic and ionic forms of the inhibitor molecule are flat structures. Nevertheless, the sodium salt molecule is slightly bent in the middle at an angle of 172.1° and is not an absolutely flat structure. This indicates that the sorption of the inhibitor molecule in the form of a sodium salt could be relatively hindered.

Mulliken charges distribution

The distribution of electron density has a major impact on a molecule's chemical reactivity. The electrophilic and nucleophilic centers of the molecule can be identified through the use of Mulliken atomic charge distribution (MACD) analysis, which is a valuable parameter for the designation of the accountable atoms of the corrosion inhibitors that are prone to adsorption onto the metals. The carbon steel surface and the inhibitor molecules interact on the atoms with a large negative charge. The MACD with corresponding values of total negative charge (TNC) and TNC/n for different forms of the inhibitor molecule are shown in Table 5.

The MACD values in Table 5 indicate that the largest negative charges are in the ionic form (AQ2S⁻) of inhibitor molecule and located on oxygen atoms, indicating that these centers have the highest electron density and interact with Fe (110). This electron density is also visible in Figure 10 in the visualized molecular electrostatic potential (MEP) for inhibitor molecules.

TNC refers to the sum of the negative charges on all atoms within a molecule. Molecules with higher TNC tend to have a greater ability to donate electrons to the metal surface. A higher TNC indicates stronger interactions between the inhibitors and the metal surface. This is because the negatively charged regions of the molecule can interact more effectively with the positively charged metal atoms, enhancing the stability of the adsorbed layer [38].

The most negative values of TNC and TNC/n were calculated for the ionic form of the inhibitor molecule (-3.6542 and -0.1305, respectively). This indicates a greater tendency of the ionic form of the inhibitor to adsorb on the metal surface and, consequently, to exhibit inhibitory properties.

Table 5. Mulliken atomic charge distribution, TNC and TNC/n for different forms of AQ2SNa (atomic enumeration corresponds to Figure 1)

	,		<i>y</i> ,	
	Atom	AQ2SNa	AQ2SH	AQ2S-
	C(1)	-0.0912	-0.0806	-0.0861
	C(2)	-0.0770	-0.0796	-0.0859
	C(3)	-0.1338	-0.1036	-0.1126
	C(4)	0.0550	0.0396	0.0267
	C(5)	0.0189	0.0440	0.0258
	C(6)	-0.0892	-0.1062	-0.1110
	C(7)	0.3444	0.3525	0.3405
	C(8)	0.0299	0.0182	0.0284
	C(9)	0.0446	0.0425	0.0308
	C(10) 0.34	0.3444	0.3520	0.3473
MACD	C(11)	-0.1068	-0.1042	-0.1095
	C(12)	-0.0742	-0.0745	-0.0923
	C(13)	-0.1154	-0.1409	-0.1450
	C(14)	-0.1316	-0.1223	-0.1207
	O(15)	-0.4872	-0.4808	-0.4862
	O(16)	-0.4699	-0.4751	-0.5066
	S(17)	1.0872	1.1230	1.1212
	O(18)	-0.5407	-0.4052	-0.5894
	O(19)	-0.5142	-0.4744	-0.6018
	O(20)	-0.6854	-0.5971	-0.6071
	X(21)	0.7327 (Na)	0.3334 (H)	-
TNC		-3.5166	-3.2445	-3.6542
TNC/n		-0.1256	-0.1159	-0.1305

Frontier orbital energies and molecular electrostatic potential

Computational chemistry uses the highest occupied molecular orbital (HOMO) and the lowest unoccupied molecular orbital (LUMO) energies to predict the reactivity of molecules according to the frontier molecular orbital (FMO) theory. This approach allows for screening potential reactants and designing new molecules with desired reactivity profiles. The energies of HOMO and LUMO help identify the sites within a molecule that are most susceptible to electrophilic and nucleophilic attacks. In corrosion science, the HOMO and LUMO energies help in understanding the corrosion mechanism and inhibiting potential of compounds [39].

The FMO density distribution and molecular electrostatic potential (MEP) of different forms of the inhibitor molecule are presented in Figure 10.

The HOMO energy indicates the molecule's ability to donate electrons. The LUMO energy, in turn, represents the energy of the lowest occupied molecular orbital, indicating the molecule's ability to accept electrons. Molecules with higher E_{HOMO} and lower E_{LUMO} values can interact more effectively with the metal surface, enhancing their inhibition efficiency. The difference between HOMO and LUMO energies (energy gap, ΔE_{gap}) is an indicator of the stability and reactivity of inhibitors because electrons can be more easily excited from the HOMO to the LUMO, facilitating chemical reactions. A smaller ΔE_{gap} often indicates higher chemical reactivity, making the molecule more effective as a corrosion inhibitor. It also implies that the molecule can form a more stable adsorbed layer on the metal surface, providing better protection against corrosion. The calculated values of the HOMO, LUMO and ΔE energies indicate that the AQ2S⁻ anion demonstrates the best inhibitory activity.

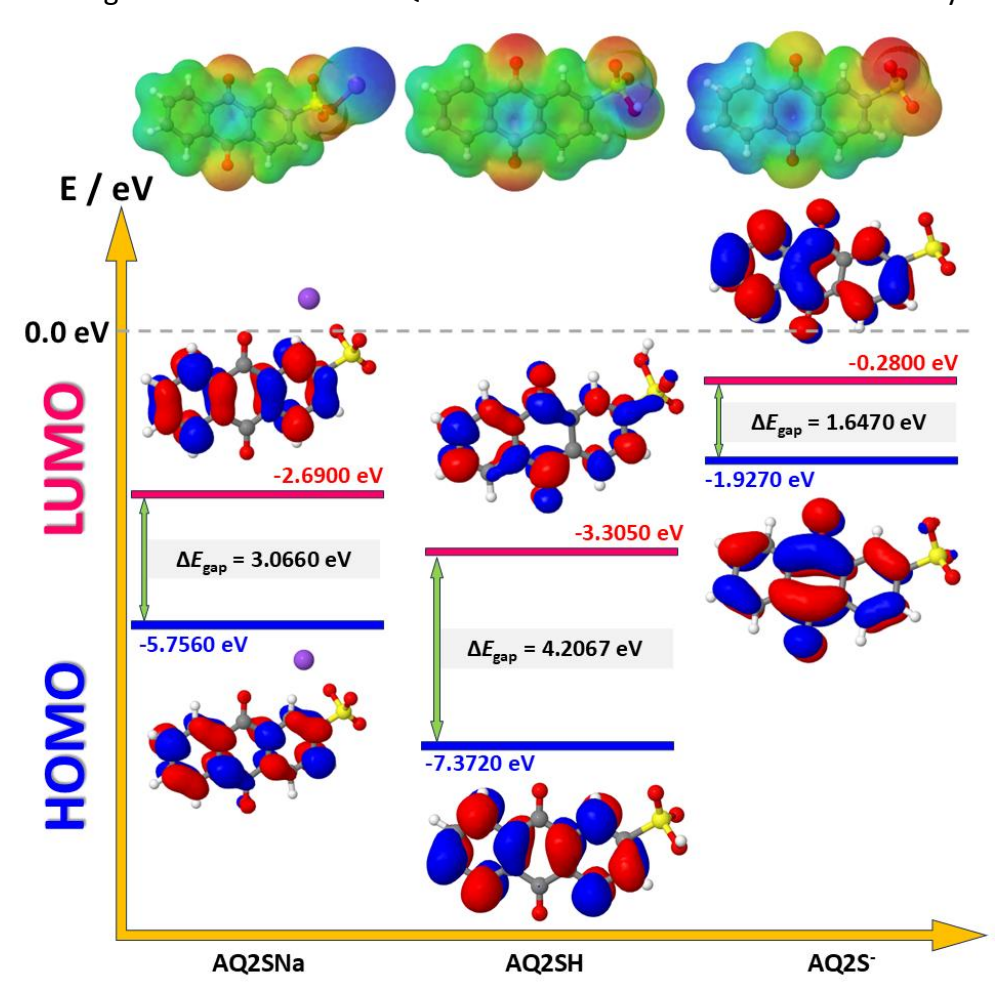


Figure 10. HOMO, LUMO energies and density distribution, energy gap (ΔE_{gap}), and MEP for AQ2SNa, AQ2SH, and AQ2S

Molecular reactivity

Quantum chemical descriptors provide rich details about molecules' electronic structure and properties, which are crucial for understanding and predicting molecular reactivity. These descriptors are used in combination with experimental data to explain the experimental results or predict the inhibition efficiency of new compounds.

Quantum chemical descriptors calculated for the inhibitor molecule in the form of sodium salt, acid and sulphonic anion are listed in Table 6.

In corrosion research, electron affinity (EA) and ionization potential (IP) are used to evaluate the tendency of a molecule to gain or lose electrons, which is critical for understanding the interaction of inhibitor molecules with the metal surface. A higher EA means the molecule can effectively accept electrons from the metal surface to form a stable adsorbed layer that protects against corrosion. According to the calculations, AQ2SH has the highest value of EA (3.3050 eV) and, therefore, should have the best inhibitory properties. The IP is directly correlated with the efficiency of corrosion inhibitors. Molecules with lower IP values tend to have higher inhibition efficiencies because they can more readily interact with the metal surface, forming a stable adsorbed layer that prevents corrosion. The ironic form of the inhibitor has the lowest value of IP and, therefore, should also have the best inhibitory properties.

Electronegativity (χ) and global hardness (η) provide an understanding of the electron-donating and accepting abilities of inhibitors.

Descriptor	Formula	AQ2SNa	AQ2SH	AQ2S
Ionization energy (IP), eV	$IP = - E_{HOMO}$	5.7560	7.3720	1.9270
Electron affinity (EA), eV	EA = - E _{LUMO}	2.6900	3.3050	0.2800
Electronegativity (χ), eV	$\chi = \frac{I + A}{2}$	4.2230	5.3385	1.1035
Chemical hardness (η), eV	$\eta = \frac{I - A}{2}$	1.5330	2.0335	0.8235
Chemical softness (σ), eV	$\sigma = \frac{1}{\eta}$	0.6520	0.4917	1.2143
Electrophilicity index (ω), eV	$\omega = \frac{\chi^2}{2}$	0.7665	1.0167	0.4117
Nucleophilicity index ($arepsilon$), eV	$\varepsilon = \frac{1}{\omega}$	1.3040	0.9835	2.4286
Back-donation energy (E_{b-d} , eV)	$\Delta E_{\text{b-d}} = -\frac{\eta}{4}$	-0.3830	-0.5083	-0.2058
Fraction of transferred electrons (ΔN)	$\Delta N = \frac{\chi_{\text{Fe}} - \chi_{\text{inhibitor}}}{2(\eta_{\text{Fe}} - \eta_{\text{inhibitor}})}$	0.5951	0.4533	0.9690

Table 6. Calculated reactivity descriptors for different forms of AQ2SNa in aqueous phase

Higher electronegativity and lower hardness are generally associated with better inhibition performance. Inhibitors with high electronegativity are better at accepting electrons from the metal surface, which can help in forming a protective layer. Global hardness is a measure of a molecule's resistance to the deformation of its electron cloud. Higher η indicates greater stability and lower reactivity, which can be beneficial for inhibitors as they are less likely to undergo unwanted chemical reactions. Global softness (σ), in turn, is the inverse of global hardness and measures the ease with which a molecule's electron cloud can be deformed. Higher global softness indicates higher reactivity, which can be advantageous for inhibitors as they can more easily interact with the metal surface to form a protective layer. Soft molecules are more polarizable and can form stronger interactions with the metal surface, leading to better adsorption and inhibition efficiency. A higher global softness

indicates that the molecule is more reactive and can easily interact with the metal surface, enhancing its corrosion inhibition properties. The calculation results show that the acidic form of the inhibitor molecule has the highest electronegativity. However, the ionic form has the lowest hardness and the highest softness values, indicating its increased anticorrosive activity compared with other forms of the inhibitor molecule. Electrophilicity (ω) and nucleophilicity (ε) indexes are also important quantum chemical descriptors that provide insights into the properties and effectiveness of corrosion inhibitors. A higher electrophilicity index indicates a greater ability to accept electrons, making the molecule more reactive towards electron-rich sites on the metal surface. The nucleophilicity index (ε) is a parameter reciprocal to the electrophilicity index, which is used to describe the ability of a molecule to donate electrons. Corrosion inhibitors with higher nucleophilicity indices are generally more effective because they can more readily form bonds with the metal surface. High values of this parameter are typical for inhibitors with heteroatoms like nitrogen, oxygen, and sulfur, which are known for their electron-donating properties. According to the calculated results, the ionic form of the inhibitor molecule has the highest nucleophilicity index, which also confirms its tendency to exhibit high inhibitory properties. Back-donation energy (E_{b-d}) in conjunction with electrophilicity and nucleophilicity indexes provides a comprehensive understanding of the inhibitor's reactivity and interaction with the metal surface. Back-donation energy refers to the energy change associated with the transfer of electrons from the metal surface back to the inhibitor molecule. A significant backdonation energy indicates a strong interaction between the inhibitor and the metal surface and the stability of the adsorbed layer. The ionic form of the AQ2SNa has the highest value of back-donation energy (-0.2058), which clearly indicates its significant inhibitory properties. The fraction of transferred electrons (ΔN) represents the number of electrons transferred from the inhibitor molecule to the metal surface. A higher ΔN value generally indicates a stronger interaction between the inhibitor and the metal, leading to better corrosion inhibition efficiency. A positive ΔN suggests that electron transfer occurs from the inhibitor to the metal, which helps in passivating the metal surface and preventing corrosion. The ΔN values calculated for all forms of the inhibitor are positive. At the same time, the highest value is characteristic of the ionic form (0.9690 eV), which indicates its greater tendency to transfer electrons to the metal surface and thereby also confirms its more significant inhibitory effectiveness.

The obtained calculation results show that the ionic form of the inhibitor molecule (AQ2S⁻) has higher inhibitory properties. The electron-donating ability is most pronounced for this form, contributing to its greater tendency to adsorb on the metal surface and forming a strong protective layer.

Molecular dynamic simulation and adsorption energy

The interaction between the active sites of different forms of the inhibitor and Fe (110) surface was explained using MD simulation. A deeper understanding of the interaction between each form of the inhibitor and Fe (110) metal surface was gained through MD simulation. The lowest energy configurations of different forms of the inhibitor in the simulated system are presented in Figure 11.

As can be seen, the inhibitor adsorbs in its anion form, lying flat on the Fe(110) surface. Acidic and salt forms of the inhibitor molecule are exhibited at an angle to the metal surface. This spatial arrangement of the inhibitor molecules is in excellent agreement with the results of quantum chemical calculations, in particular with the MACD and MEP. According to MACD, the flat-lying adsorption geometries suggest that this process is supported through oxygen atoms of both functional groups of the inhibitor molecule.

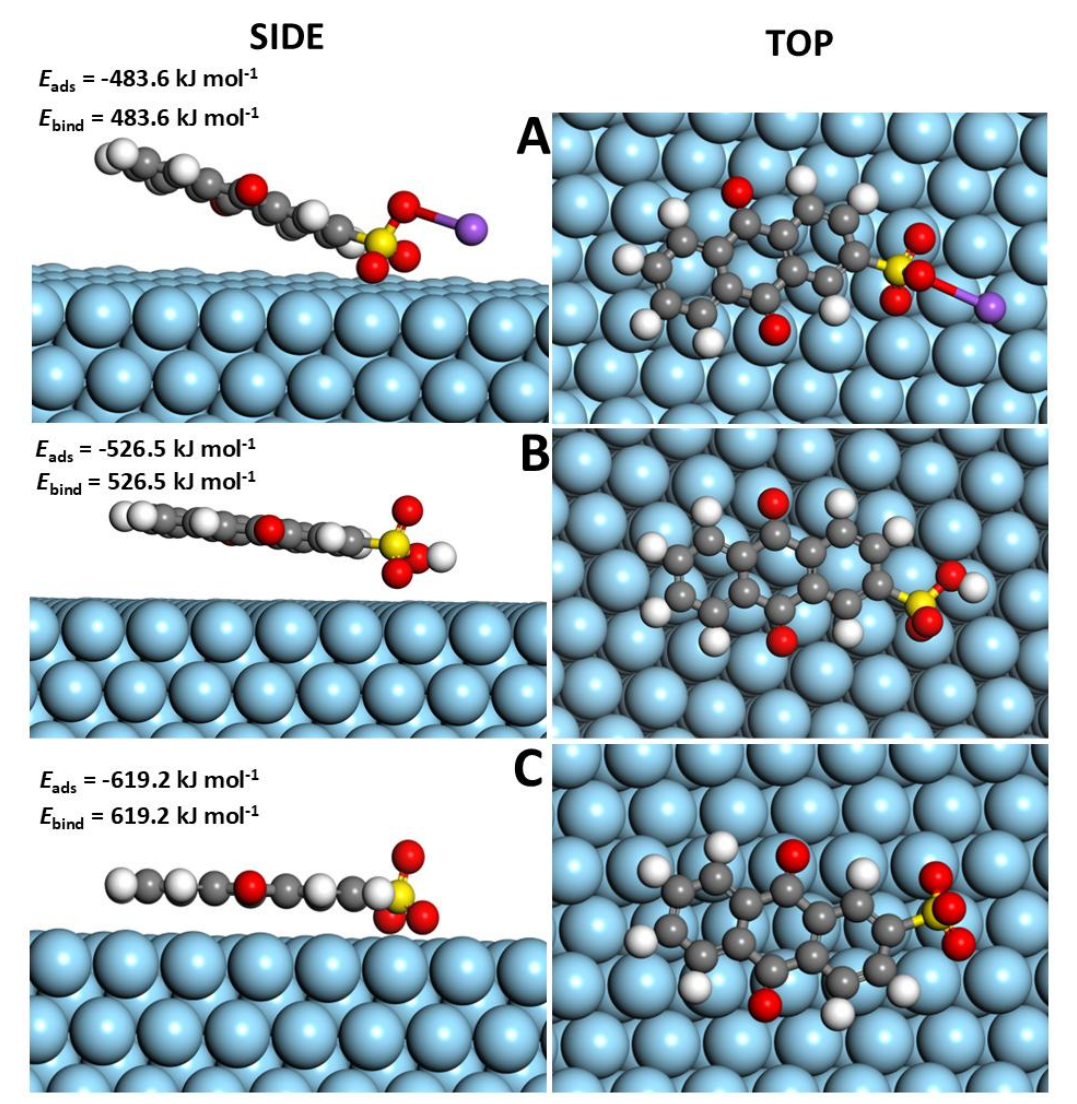


Figure 11. Side and top views of the most appropriate configuration for adsorption of AQ2SNa (A), AQ2SH (B), and AQ2S⁻ molecules (C) on the Fe (110) surface obtained by MD simulations in aqueous solution (water molecules were removed for clarity)

A more negative and evenly distributed charge on the oxygen atoms of the carbonyl groups in the anion contributes to a flatter arrangement of the molecule from the metal surface. In all three forms, the inhibitor molecules are adsorbed on a metal surface primarily due to two oxygen atoms of the sulfo group, since these atoms have the most negative charge. Binding energy quantifies the strength of the interaction between the inhibitor and the metal, providing insights into the stability of the adsorbed layer. The sorption and binding energy values clearly show that the anionic form sorbs better on the metal surface. Thus, it can be inferred that the inhibitor molecules adsorb on the metal surface to form a dense molecular layer, separating the metal surface from the water molecules to achieve the effect of corrosion inhibition.

Adsorption and corrosion inhibition mechanism

From the obtained experimental and theoretical results, we propose the adsorption mechanism presented in Figure 12. The results clearly show that the inhibitor adsorbs on the metal surface as a sulfonate anion. The inhibitor molecules bind to the negatively charged metal surface through attractive electrostatic forces. In parallel, the lone electron pairs of the oxygen atoms of the -C=O and -SO₃ $^-$ moieties and the π -electrons of the aromatic rings donate electrons to the vacant d-orbitals of the Fe atoms, which leads to the chemisorption.

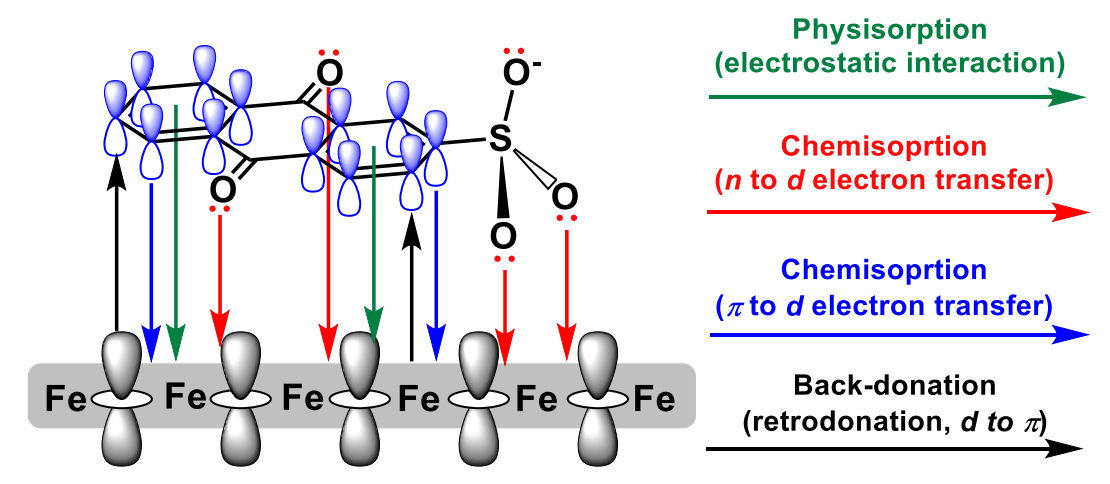


Figure 12. Representation of adsorption mechanism of AQ25 on Fe(110) surface

This transfer leads to the accumulation of electrons in the *d*-orbitals of the metal atoms, resulting in inter-electron repulsions. In order to avoid this repulsion phenomenon, a reverse transfer of electrons takes place from the *d*-orbitals of the surface metal atoms to the unoccupied molecular orbitals of the inhibitor molecules (retro-donation), thus reinforcing the adsorption of the inhibitor molecules on the metal surface.

It can be concluded that adsorption of the inhibitor on the Fe (110) surface in an acidic solution occurs through physisorption, chemisorption and retro-donation. In addition, theoretical studies show a good correlation with electrochemical studies, which show that AQ2SNa has high corrosion inhibition performance.

Conclusions

This study investigated the potential of AQ2SNa as a corrosion inhibitor on carbon steel in 0.5 mol dm⁻³ H₂SO₄ solution experimentally and theoretically. AQ2SNa showed significant inhibitory properties against the corrosion of carbon steel in a given medium. The maximum protection efficiency of the metal reaches up to 94.44 % at 333 K and an inhibitor concentration of 0.5 g dm⁻³. The adsorption of the inhibitor on the metal surface adheres to the Langmuir model. The protective film is formed due to spontaneous physisorption by creating a physical barrier between the metal surface and the corrosive environment. The inhibitor exhibits mixed-type properties, mainly reducing the rate of the cathodic process. An increase in the temperature and concentration of the inhibitor positively affects the anticorrosive performance of AQ2SNa. The increasing temperature and concentration of the inhibitor induce a significantly proportional increase in its protective effect. The data from the electrochemical experiments are in complete agreement with the results of the gravimetric measurements. An increase in polarization resistance and a decrease in corrosion current indicate a hindrance to the corrosion process in the presence of AQ2SNa. These suggest a robust protective layer forms on the metal surface, enhancing its resistance to acidic corrosive agents. Gravimetric and electrochemical results were rationalized by theoretical methods. The density functional theory calculations predicted that AQ2S⁻ ion is a real corrosion inhibitor in a model system with O atoms as the most possible adsorption centers. Moreover, the MD simulation revealed the strong adsorption interaction of AQ2S towards the Fe (110) surface. The obtained theoretical results are in agreement with the experimental ones. Thus, AQ2SNa is an effective inhibitor for corrosion protection of carbon steel in 0.5 mol dm⁻³ H₂SO₄ solution. The results of this study open up new prospects for the further application of this useful compound for anticorrosive protection of metals in acidic environments.

References

- [1] A. F. Hamood, H. S. Aljibori, M. A. I. Al-Hamid, A. A. Alamiery, W. K. Al-Azzawi, MOP as a Corrosion Inhibitor for Mild Steel in HCl Solution, A Comprehensive Study, *The Progress in Color, Colorants and Coatings* **17** (2024) 207-226. https://doi.org/10.30509/pccc.2023.1607176.1237
- [2] T. Seilova, Z. Kunasheva, R. Kubasheva, N. Akatyev, Development of new three-component BNP-inhibitor for carbon steel in 0.5 mol dm⁻³ HCl solution, Thermodynamic, adsorption and electrochemical studies, *The International Journal of Corrosion and Scale Inhibition* **13** (2024) 1268-1291. http://dx.doi.org/10.17675/2305-6894-2024-13-2-33
- [3] H. Bairagi, P. Vashishth, G. Ji, S.K. Shukla, E. E. Ebenso, B. Mangla, Polymers and their composites for corrosion inhibition application: development, advancement, and future scope a critical review, *Corrosion Communications* **15** (2024) 79-94. https://doi.org/10.1016/j.corcom.2023.10.006
- [4] M. Sheydaei, The Use of Plant Extracts as Green Corrosion Inhibitors: A Review, *Surfaces* **7** (2024) 380-403. http://dx.doi.org/10.3390/surfaces7020024
- [5] Q. Wang, R. Wang, Q. Zhang, C. Zhao, X. Zhou, H. Zheng, R. Zhang, Y. Sun, Z. Yan, Application of biomass corrosion inhibitors in metal corrosion control: a review, *Molecules* 28 (2023) 2832. http://dx.doi.org/10.3390/molecules28062832
- [6] G. Ji, Waste natural materials for sustainable corrosion prevention of steel: A mini review on their popularity, experimental and computational investigation, applications, challenges, and future strategy, *Journal of Molecular Liquids* 408 (2024) 125415 https://doi.org/10.1016/j.molliq.2024.125415
- [7] I. Pandey, A. V. Ullas, C. K. Rastogi, M. K. Singh, V. Kumar, B. Mangla, G. Ji, Extract Preparation of Waste Lady Finger Caps Using Ethanol, Generation of Extract's Layers on Copper Through Drop Casting Without and with NiO Nanoparticles, and Study of their Corrosion Performances in Saline Water, *Waste and Biomass Valorization* (2024). https://doi.org/10.1007/s12649-024-02729-4
- [8] S.B. Ade, Corrosion inhibition of mild steel in different acid medium by using various acidic groups of organic compounds, *International Journal for Research in Applied Science and Engineering Technology* **10** (2022) 367-373. http://dx.doi.org/10.22214/ijraset.2022.40288
- [9] A. N. Kuzyukov, I. A. Levin, Effect of anthraquinone and some of its derivatives on the corrosion resistance of metals in sulfuric acid solutions, *Chemical and Petroleum Engineering* 5 (1969) 787-788. https://doi.org/10.1007/BF01153172
- [10] N. Muthukumar, A. Ilangovan, S. Maruthamuthu, N. Palaniswamy, A. Kimura, 1 -Aminoanthraquinone derivatives as a novel corrosion inhibitor for carbon steel API 5L-X60 in white petrol—water mixtures, *Materials Chemistry and Physics* 115 (1) (2009) 444-452. https://doi.org/10.1016/J.MATCHEMPHYS.2008.12.027
- [11] L. Saqalli, M. Galai, N. Gharda, M. Sahrane, R. Ghailane, M. Ebn Touhami, Y. Peres-lucchese, A. Souizi, N. Habbadi, Corrosion inhibition of carbon steel by anthraquinones derivatives in 1.0 M HCl: Electrochemical and quantum calculations, *International Journal of Electrochemical Science* **13(5)** (2018) 5096-5119. https://doi.org/10.20964/2018.05.40
- [12] L. Saqalli, M. Galai, F. Benhiba, N. Gharda, N. Habbadi, R.Ghailane, M. Ebn Touhami, Y. Pereslucchese, A. Souizi, R. Touir, Experimental and theoretical studies of Alizarin as corrosion inhibitor for mild steel in 1.0 M HCl solution. *Journal of Materials and Environmental Science* 8 (2017) 2455-2467. https://www.jmaterenvironsci.com/Document/vol8/vol8 N7/264-JMES-2627-Sagalli.pdf
- [13] Z. Bensouda, M. Driouch, M. Sfaira, A. Farah, M. Ebn Touhami, B. Hammouti, K. M. Emran, Effect of *Mentha Piperita* essential oil on mild steel corrosion in hydrochloric acid,

- International Journal of Electrochemical Science **13** (2018) 8198-8221. https://doi.org/10.20964/2018.08.79
- [14] X. Miao, X. Zhang, S. Chen, Y. Liu, Y. Chen, J. Lin, Y. Zhang, Dual-redox enhanced supercapacitors with sodium anthraquinone-2-sulfonate and potassium bromide, *Electrochimica Acta* **374** (2021) 137889. https://doi.org/10.1016/j.electacta.2021.137889
- [15] P. R. Maddigapu, A. Bedini, C. Minero, V. Maurino, D. Vione, M. Brigante, M. Sarakha, The pH-dependent photochemistry of anthraquinone-2-sulfonate, *Photochemical & Photobiological Sciences* **9** (2010) 323. https://doi.org/10.1039/b9pp00103d
- [16] A. V. Losub, S. S. Stahl, Palladium-Catalyzed Aerobic Oxidative Dehydrogenation of Cyclohexenes to Substituted Arene Derivatives, *Journal of the American Chemical Society*, **137** (2015) 3454-3457. https://doi.org/10.1021/ja512770u
- [17] L. Zhang, P. Chen, Y. Xu, W. Nie, Y. Zhou, Enhanced photo-induced antibacterial application of graphene oxide modified by sodium anthraquinone-2-sulfonate under visible light, *Applied Catalysis B: Environmental* **265** (2020) 118572. https://doi.org/10.1016/j.apcatb.2019.118572
- [18] S.Khankaew, A. Mills, D. Yusufu, N. Wells, S. Hodgen, W. Boonsupthip, P. Suppakul, Multifunctional anthraquinone-based sensors: UV, O₂ and time, *Sensors and Actuators B: Chemical* **238** (2017) 76-82. http://dx.doi.org/10.1016/j.snb.2016.07.037
- [19] R. Sun, D. Han, C. Cui, Z. Han, X. Guo, B. Zhang, Y. Guo, Y. Liu, Z. Weng, Q.-H. Yang, A Self-Deoxidizing Electrolyte Additive Enables Highly Stable Aqueous Zinc Batteries, *Angewandte Chemie International Edition* **62** (2023) e202303557. https://doi.org/10.1002/anie.202303557
- [20] L. Zhang, J. Huang, H. Guo, L. Ge, Z. Tian, M. Zhang, J. Wang, G. He, T. Liu, J. Hofkens, D.J.L. Brett, F. Lai, Tuning Ion Transport at the Anode-Electrolyte Interface via a Sulfonate-Rich Ion-Exchange Layer for Durable Zinc-Iodine Batteries, *Advanced Energy Materials* **13** (2023) 2203790. http://dx.doi.org/10.1002/aenm.202203790
- [21] ISO 8407-2021: Corrosion of metals and alloys Removal of corrosion products from corrosion test specimens (2021). Geneva, Switzerland.
- [22] L. T. Popoola, Organic green corrosion inhibitors (OGCIs): a critical review, *Corrosion Reviews* **37(2)** (2019) 71-102. https://doi.org/10.1515/corrrev-2018-0058
- [23] Ya. G. Avdeev, Yu. I. Kuznetsov, Chemical transformation of corrosion inhibitors in the aggressive environment/metal system, *International Journal of Corrosion and Scale Inhibition* **12(4)** (2023) 1751-1790. https://dx.doi.org/10.17675/2305-6894-2023-12-4-19
- [24] C. G. Zhan, J. A. Nichols, D. A. Dixon, Ionization potential, electron affinity, electronegativity, hardness, and electron excitation energy: molecular properties from density functional theory orbital energies, *The Journal of Physical Chemistry A* **107(20)** (2003) 4184-4195. https://doi.org/10.1021/jp0225774
- [25] M. W. Schmidt, K. K. Baldridge, J. A. Boatz, S. T. Elbert, M. S. Gordon, J. H. Jensen, S. Koseki, N. Matsunaga, K. A. Nguyen, S. Su, T. L. Windus, M. Dupuis, J. A. Montgomery Jr, General atomic and molecular electronic structure system, *Journal of computational chemistry* 14(11) (1993) 1347-1363. https://doi.org/10.1002/jcc.540141112
- [26] A. Klamt, The COSMO and COSMO-RS solvation models, WIREs Computational Molecular Science **8(1)** (2017) e1338. https://doi.org/10.1002/wcms.1338
- [27] M. J. Abraham, T. Murtola, R. Schulz, S. Pall, J. C. Smith, B. Hessa, E. Lindahl, GROMACS: High performance molecular simulations through multi-level parallelism from laptops to supercomputers, *SoftwareX* 1 (2015) 19-25. https://doi.org/10.1016/j.softx.2015.06.001
- [28] N. Mazlan, K. Jumbri, M. A. Kassim, R. A. Wahab, M. B. A. Rahman, Density functional theory and molecular dynamics simulation studies of bio-based fatty hydrazide-corrosion inhibitors

- on Fe (110) in acidic media, *Journal of Molecular Liquids* **347(1)** (2022) 118321. https://doi.org/10.1016/j.molliq.2021.118321
- [29] M. Husaini, M.B. Ibrahim, Thermodynamic and Kinetic study on the corrosion, of aluminium in hydrochloric acid using benzaldehyde as corrosion inhibitor, *International Journal of Engineering and Manufacturing* **9(6)** (2019) 53-64. https://doi.org/10.5815/ijem.2019.06.05
- [30] L. Afia, R. Salghi, A. Zarrouk, H. Zarrok, O. Benali, B. Hammouti, S. S. Al-Deyab, A. Chakir, L. Bazzih, Inhibitive action of argan press cake extract on the corrosion of steel in acidic media, *Portugaliae Electrochimica Acta* **30(4)** (2012) 267-279. https://doi.org/10.4152/PEA.201204267
- [31] A. A. Khadom, A. S. Yaro, H. A. A. Kadum, A. S. AlTaie, A. Y. Musa, The Effect of Temperature and Acid Concentration on Corrosion of Low Carbon Steel in Hydrochloric Acid Media, *American Journal of Applied Sciences* **6(7)** (2009) 1403-1409.

 https://doi.org/10.3844/ajassp.2009.1403.1409
- [32] J. Sirajudeen, M. M. Mohamed Mubashir, Statistical approach and assessment of physicochemical status of ground water in near proximity of South Bank Canal, Tamil Nadu, India, *Archives of Applied Science Research* **5(2)** (2013) 25-32.
- [33] A. A. Khadom, A. S. Yaro, A. A. H. Kadhum, Adsorption Mechanism of Benzotriazole for Corrosion Inhibition of Copper-Nickel Alloy in Hydrochloric Acid, *Journal of the Chilean Chemical Society* **55(1)** (2010) 150-152. https://doi.org/10.4067/s0717-97072010000100035
- [34] N. Mohanapriya, M. Kumaravel, B. Lalithamani, Theoretical and experimental studies on the adsorption of n-[(E)-pyridin-2-ylmethylidene] aniline, a Schiff base, on mild steel surface in acid media, *Journal of Electrochemical Science and Technology* **11(2)** (2020) 117-131. https://doi.org/10.33961/jecst.2019.00430
- [35] A. S. Fouda, H. E. Megahed, N. Fouad, N. M. Elbahrawi, Corrosion inhibition of carbon steel in 1 M hydrochloric acid solution by aqueous extract of *Thevetia peruviana*, *Journal of Bio- and Tribo-Corrosion* **2** (2016) 16. https://doi.org/10.1007/s40735-016-0046-z
- [36] M. Husaini, M. B. Ibrahim, Investigation of inhibition potential effect of organic compound for the corrosivity of phosphoric acid on aluminium, *International Journal of Engineering and Manufacturing* **10(1)** (2020) 41-53. https://doi.org/10.5815/ijem.2020.01.04
- [37] R. Solmaz, G. Kardaş, B. Yazıcı, M. Erbil, Adsorption and corrosion inhibitive properties of 2-amino-5-mercapto-1, 3, 4-thiadiazole on mild steel in hydrochloric acid media, *Colloids and Surfaces A: Physicochemical and Engineering Aspects* **312(1)** (2008) 7-17. https://doi.org/10.1016/j.colsurfa.2007.06.035
- [38] El S. H. El Ashry, A. El Nem, S. A. Essawy, S. Ragab, Corrosion inhibitors, part 31: quantum chemical studies on the efficiencies of some aromatic hydrazides and Schiff bases as corrosion inhibitors of steel in acidic medium, *Arkivoc* **11** (2006) 205-220. https://doi.org/10.3998/ARK.5550190.0007.B21
- [39] P. Dhakal, W. Gassaway, J. K. Shah, Mapping the frontier orbital energies of imidazolium-based cations using machine learning, *The Journal of Chemical Physics* **159** (2023) 064513. https://doi.org/10.1063/5.0155775

©2025 by the authors; licensee IAPC, Zagreb, Croatia. This article is an open-access article distributed under the terms and conditions of the Creative Commons Attribution license (https://creativecommons.org/licenses/by/4.0/)



Open Access :: ISSN 1847-9286 www.jESE-online.org

Original scientific paper

Evaluation of porphyrin molecules as effective corrosion inhibitors for copper alloy in sulfuric acid using both experimental and computational approaches

Metwally Abdallah^{1,2,⊠}, Majda Alfakeer^{3,⊡}, Rasha N. Felaly¹, Abdulaziz M. Almohyawi¹, Jabir H. Al-Fahemi¹, Salih S. Al-Juaid⁴, Doaa F. Seyam², Elsayed M. Mabrouk² and Kamal A. Soliman²

¹Chemistry Department, Faculty of Sciences, Umm Al-Qura University, Makkah, Saudi Arabia

²Chemistry Department, Faculty of Science, Benha University, Benha, Egypt

³Chemistry Department, Faculty of Science, Princess Nourah bint Abdulrahman University, Riyadh, Saudi Arabia

⁴Chemistry Department, Faculty of Science, King Abdulaziz University, Jeddah, Saudi Arabia

Corresponding author: $^{\boxtimes}$ <u>metwally555@yahoo.com</u>; $^{\boxtimes}$ <u>msalonazi@pnu.edu.sa</u>

Received: October 24, 2024; Accepted: January 6, 2025; Published: February 3, 2025

Abstract

The inhibition efficacies of two porphyrin molecules, namely, 5,10,15,20-tetra-[m-(methoxy) phenyl] porphyrin (m-TMPP) and 5,10,15,20-tetra-[p-(methoxy)phenyl] porphyrin (p-TMPP) on the corrosion of copper alloy (C12510) in 1.0 M H₂SO₄ solutions were examined. Some chemical, electrochemical measurements, density functional theory and Monte Carlo simulations were utilized to study the adsorption behaviour and corrosion inhibition efficiency of m-TMPP and p-TMPP on the Cu (111) surface in acidic media. Scanning electron microscopy analysis was employed to examine the surface morphologies of the tested C12510 surfaces. The outcomes of these techniques proved that the inhibition efficiency increases with increasing concentration of TMPP molecules and with lowering temperatures. The inhibition efficiency is reached to 96.23 and 97.61 % in the case of m-TMPP and p-TMPP, respectively, using the potentiodynamic polarization technique. The inhibitory effect of TMPP molecules is explained based on their spontaneous physicochemical adsorption on the surface of C12510. The adsorption process is obeyed by the Langmuir isotherm model. Additionally, some thermodynamic activation parameters were determined and discussed. It was discovered that the two TMPP compounds retarded the pitting corrosion of C12510 in chloride-containing solutions by shifting the pitting potential to a more noble direction. Based on all the approaches investigated, the inhibitory efficacy of p-TMPP is higher than that of m-TMPP at every concentration tested.

Keywords

Metal alloy corrosion; heterocyclic organic compounds; adsorption isotherm; pitting potential; surface morphology; quantum chemical calculations

Introduction

Copper is a vital element used in many strategic industries due to its numerous qualities, including its low price, electrical conductivity, and distinctive mechanical properties. It is mainly used in electrical appliances, chemical industries, printed circuit boards, copper strips for shielding wires, airbags, busbar terminals, electromagnetic switches, pen holders, and roof panels [1]. Copper is a corrosion-resistant metal. Usually, $1.0 \text{ M H}_2\text{SO}_4$ solution is applied in pickling, cleaning processes, and removing precipitation layers on the copper surface, but, unfortunately, corrosion of the copper occurs, causing many economic problems. Researchers have tried a variety of approaches to eliminate or slow down copper corrosion, the most significant of which is the utilization of corrosion inhibitors because of their simple operation and remarkable effects [2].

Many of the inhibitors used for copper corrosion in acidic solutions are organic molecules with heteroatoms; the most common ones are nitrogen, oxygen, phosphorus, and sulphur; they are employed as inhibitors for copper corrosion in acidic solutions. These organic compounds' ability to prevent corrosion is dependent upon the heteroatoms they contain and typically decreases in the following order: P > S > N > O [3]. Numerous compounds, including drugs, synthetic organic molecules, and plant extracts, have been demonstrated to have effective inhibition efficiency against copper corrosion [4-6]. The efficiency of an inhibitor was influenced by the environment it operated in, the metal surface characteristics, and the interface electrochemical potential [7]. It is widely recognized that the initial stage in the mechanism of inhibition of copper in sulfuric acid solution is the adsorption of the organic molecules onto its surface. The main factors determining the force of adsorption operation are the chemical structure of the adsorbed compound, its properties like electron density (orbitals that donate electrons), aromaticity, and functional groups [8]. Also, density functional theory (DFT) calculations allow the prediction of molecular properties, which are key indicators of the ability of a molecule to donate or accept electrons. These electronic descriptors are essential for understanding how well an inhibitor can interact with a metal surface. Porphyrin derivatives have previously been used as corrosion inhibitors for 304 stainless steel in acidic environments [9] and N80 steel in 3.5 % sodium chloride solution [10]. The inhibitory effect of these compounds is due to strong adsorption on the steel surface.

The main objective of this manuscript is to determine the success of novel synthetic porphyrin molecules in suppressing the corrosion of copper alloy (C12510) in 1.0 M sulfuric acid solution using chemical and electrochemical methods. Scanning electron microscopy (SEM) was used to analyze the surface morphology of the copper sample. We supported our results by confirming the experimental results with calculated quantitative chemical parameters obtained from DFT and Monte Carlo (MC) simulations. Additionally, this study attempts to explicate the adsorption of porphyrin molecules on copper surfaces and understand the role of porphyrin structure in the corrosion inhibition process.

Experimental

Materials

The composition of the copper alloy (C12510) applied in this study is as follows: Cu (99.9 wt.%), Pb (0.020 wt.%), Zn (0.080 wt.%), Fe (0.05 wt.%), P (0.03 wt.%), Sb (0.003 wt.%), Te (0.025 wt.%), Sn (0.05 wt.%), Ni (0.050 wt.%) and Bi (0.005 wt.%). All chemicals used in this study were analytical grade (Aldrich chemicals). Distilled water was used to prepare corrosive solutions. 1.0 M H_2SO_4 was prepared using H_2SO_4 (98 %). The desired temperature of each experiment was adjusted to ± 1 °C using an air thermostat.

Synthesis of inhibitors

Solvents and reagents were purchased from commercial suppliers and were applied without further purifying. A Buchi rotary evaporator was used to evaporate the solvent at a lower pressure.

 1 H NMR and 13 C NMR spectra were gathered at 600 MHz on a Bruker Avance III™ HD 600 MHz spectrometer in 5 mm diameter tubes. Signals are presented in δ / ppm, from δ = 0.00 ppm (tetramethylsilane). All was done with deuterated chloroform solvent at room temperature. Ultraviolet-visible absorption spectra were recorded on Shimadzu® UV-1800 Spectrophotometer in solvent as stated. IR spectra were recorded using a Shimadzu® IRSpirit Fourier transform infrared spectrophotometer.

Thin layer chromatography (TLC) was employed using TLC plastic sheets coated with Silica Gel 60 F_{254} (MERCK $^{\circ}$), and the compounds were visualized under short-wavelength UV light at 245 or 366 nm.

Scheme 1 presents the synthesis of 5,10,15,20-tetra-[p-(methoxy)phenyl] porphyrin (p-TMPP).

Scheme 1. Synthesis of p-TMPP

P-methoxybenzaldehyde (6.80 g, 50 mmol, 1 eq.) was added dropwise to newly distilled pyrrole (3.35 g, 50 mmol, 1 eq.) in refluxing propionic acid (100 ml) in a modified version of Adler's general procedure [11]. After allowing the mixture to cool to room temperature and refluxing it for 30 min at 150 °C, 150 ml of MeOH was added. The mixture was refrigerated for a week before being filtered and given another methanol cleaning. A recrystallization from chloroform/methanol afforded purple solid of title compound (1.82 g, 20 %); mp. >350 °C; Rf = 0.8 (Chloroform/Hexane; 1:1); 1 H NMR (600 MHz, CDCl₃) δ = 8.87 nm (s, 8H), 8.13 (d, J = 8.5 Hz, 8H), 7.29 (d, J = 8.5 Hz, 8H), 4.10 (s, 12H), -2.75 (s, 2H). 13 C NMR (151 MHz, CDCl₃) δ = 55.6, 112.2, 112.2, 119.7, 134.7, 135.6, 159.4 nm.

Scheme 2 presents the synthesis of 5,10,15,20-tetra-[m-(methoxy)phenyl] porphyrin (p-TMPP).

Scheme 2. Synthesis of m-TMPP

Freshly distilled pyrrole (3.35 g, 50 mmol, 1 eq.) was added dropwise to m-methoxybenzaldehyde (6.80 g, 50 mmol, 1 eq.) in refluxing propionic acid (100 ml) in accordance with a modified version of Adler's general approach [12]. The mixture was refluxed for 30 minutes at 150 °C. Once it had cooled to room temperature, 150 ml of methanol was added. After a week of refrigeration, the mixture was filtered and again cleaned with methanol.

A recrystallization from chloroform/methanol afforded purple solid of title compound (1.82 g, 20 %); mp.>350 °C; Rf=0.85 (Chloroform/Hexane; 1:1); 1 H NMR (600 MHz, CDCl₃) δ = 8.90 nm (s, 8H), 7.83 (d, J = 7.3 Hz, 4H), 7.80 (s, 4H), 7.65 (t, J = 7.9 Hz, 4H), 7.35 (dd, J = 8.4, 2.6 Hz, 4H), 3.99 (s, 12H), -2.78 (s, 2H). 13 C NMR (151 MHz, CDCl₃) δ = 55.5, 113.6, 119.9, 120.5, 127.5, 143.5 nm.

Weight loss technique

Thirteen coupons of C12510 were cut equally into $(2.5\times1.5\times1)$ cm³ cuboids and then polished with a series of emery papers (grades 320, 600, 800 and 1200) and then washed with bi-distilled water, acetone and distilled water before being air-dried. The C12510 samples were immersed in a blank solution of $1.0 \text{ M H}_2\text{SO}_4$ solution and solutions containing different concentrations of m-TMPP and p-TMPP. They were raised from their respective solutions after 2 hours, wiped with filter paper to remove the corrosion products and then weighed, all carefully done at approximately the same time. This process was repeated for different immersion periods (4, 6, 8, 10, 20 and 24 hours), at 298 K. WL technique was also performed for 1 M blank H_2SO_4 solution, $1.0 \text{ M } H_2SO_4$ solution containing 1 mM m-TMPP and $1.0 \text{ M } H_2SO_4$ solution containing 1 mM p-TMPP at temperatures of 313, 323, 333 and 343K. WL experiments were performed twice, and the average weight loss was calculated. The corresponding corrosion rate $(CR_W / \text{mg cm}^{-2} \text{ h}^{-1})$ and the inhibition efficiency (η) were estimated by Equations (1) and (2) [13]:

$$CR_{W} = DW / At$$
 (1)

$$\eta_{\rm W} = \frac{CR_{\rm un} - CR_{\rm in}}{CR_{\rm un}} 100 \tag{2}$$

where, t / h is the immersion time, A / cm² is the exposed area of the copper samples, ΔW / mg is the weight difference (before and after immersion) for the estimated time, and CR_{in} represent the corrosion rate in uninhibited and inhibited solution, respectively.

Electrochemical techniques

Potentiodynamic polarization (PP) and potentiodynamic anodic polarization (PAP) techniques were conducted employing a PGSTAT30 potentiostat/galvanostat with a three-electrode cell; a calomel electrode (SCE), a counter platinum electrode (Pt) and the copper alloy (C12510) working electrode, with the exposed surface area of 0.25 cm². After the electrode was submerged in the test solution for around 60 minutes, or until the steady state potential was attained, the polarization process was initiated. For the PP and PAP techniques, the scan rates were set at 2.0 and 0.1 mV s⁻¹, respectively. In a temperature-controlled system, all procedures were done at 303 K. The electrochemical impedance spectroscopy (EIS) technique was conducted at open circuit potential (OCP) *via* peak-to-peak AC signal, with an amplitude of 4.0 mV and frequency range of 100 kHz to 0.1 Hz. Before being used, the exposed portion of the C12510 electrode was polished, cleaned for five minutes with distilled water and acetone, and then dried. At room temperature (25 °C), the corrosion data were recorded once as the potential reached the steady state values. The quantitative parameters of the dissolving properties were computed after analyzing the Nyquist and Bode plots.

The inhibition efficiency (η) obtained from PP and EIS was determined by the Eqs. (3) and (4) [14]:

$$\eta_{\rm pp} = \left(\frac{i_{\rm un} - i_{\rm in}}{i_{\rm un}}\right) 100 \tag{3}$$

$$\eta_{\text{EIS}} = \left(\frac{R_{\text{ct,in}} - R_{\text{ct,in}}}{R_{\text{ct,in}}}\right) 100 \tag{4}$$

where, i_{un} and i_{in} , are corrosion current densities for uninhibited and inhibited solutions corresponddingly, while $R_{ct,un}$ and $R_{ct,in}$ are the resistance of charge transfer for uninhibited and inhibited solutions, respectively.

Scanning electron microscopy analysis

SEM analysis for specimens was done in 100 ml of blank 1.0 M H_2SO_4 solution and with 1.0 mM of m-TMPP and p-TMPP for 2 h. Then specimens were taken off, washed with acetone, and then dried. The analysis was done using a JSM-IT700HR/LA SEM, at a 15 kV acceleration voltage.

Density functional theory study

Density functional theory (DFT) is a frequently utilized instrument in corrosion research because of its ability to accurately model and predict the molecular properties of many substances. In this study, the molecular structures were drawn using GaussView software [15], while the Gaussian 09 suite was used for performing DFT calculations [16]. Specifically, the B3LYP functional with the 6-31G(d,p) basis set was employed to optimize the geometries of the m-TMPP and p-TMPP molecules [17]. To better represent the surrounding environment, calculations were performed for an aqueous phase using the conductor-like polarizable continuum model [18]. Using DFT, frontier molecular orbital (FMO) properties were calculated. These provide insights into the molecule's reactivity, as HOMO represents the molecule's electron-donating ability, and LUMO corresponds to its electron-accepting ability. Other key electronic descriptors derived from the FMO analysis include global hardness (γ), global softness (σ), and Fraction of transferred electrons (ΔN_{111}) that are calculated according to Equations (5) to (7):

$$\gamma = \frac{E_{\text{LUMO}} - E_{\text{HOMO}}}{2}.$$
 (5)

$$\sigma = \frac{1}{\gamma} \tag{6}$$

$$\Delta N_{111} = \frac{\varphi - \chi_{\text{inh}}}{2(\gamma_{\text{Cu}} + \gamma_{\text{inh}})} \tag{7}$$

where φ is the work function of Cu surface (4.94 eV), and χ is the electronegativity of inhibitor.

Monte Carlo simulation

To explore the interaction between m-TMPP and p-TMPP with the Cu (111) surface, we employed a Monte Carlo (MC) simulation approach to model the adsorption process at the atomic scale. The interaction energies and adsorption configurations were calculated using the Adsorption Locator module in Materials Studio 2017 software [19]. The Cu (111) surface was chosen for its stability and relevance in corrosion studies. We modelled a supercell of the copper surface using periodic boundary conditions to simulate an extended surface area. A slab model of the Cu (111) surface was generated, with a 3.0 nm vacuum in the *z*-direction above the surface. This setup represents a large enough surface area to explore multiple adsorption sites for the molecules and solvent interactions. The copper surface was constructed with 9×9 unit cells, resulting in a supercell with sufficient space to accommodate the inhibitors and solvent molecules. To simulate an acidic environment, which is crucial for studying the corrosion process, we

introduced 100 water molecules as the solvent, four hydronium ions (H_3O^+) and two sulphate ions ($SO_4^{2^-}$) were incorporated into the simulation box. The entire simulation system (Cu surface, water molecules, hydronium ions, sulphate ions, and inhibitors) was optimized using the Forcite module in Materials Studio. The COMPASS force field was applied for all components of the simulation [20]. The COMPASS force field is well-suited for organic and inorganic systems and has been validated for surface interactions, making it ideal for simulating the interaction of inhibitors with metal surfaces. Energy minimization was applied to find the most stable configuration of the system, ensuring that all components are at their lowest possible energy states.

Results and discussion

Open circuit potential measurement

The open circuit potential (OCP) was measured over one hour while the copper working electrode was immersed in a $1.0~M~H_2SO_4$ solution. Figure 1 shows that the OCP values stabilize after about ten minutes. Moreover, the investigated TMPP compounds considerably diminish the cathodic corrosion process, as the OCP values become more negative than the blank.

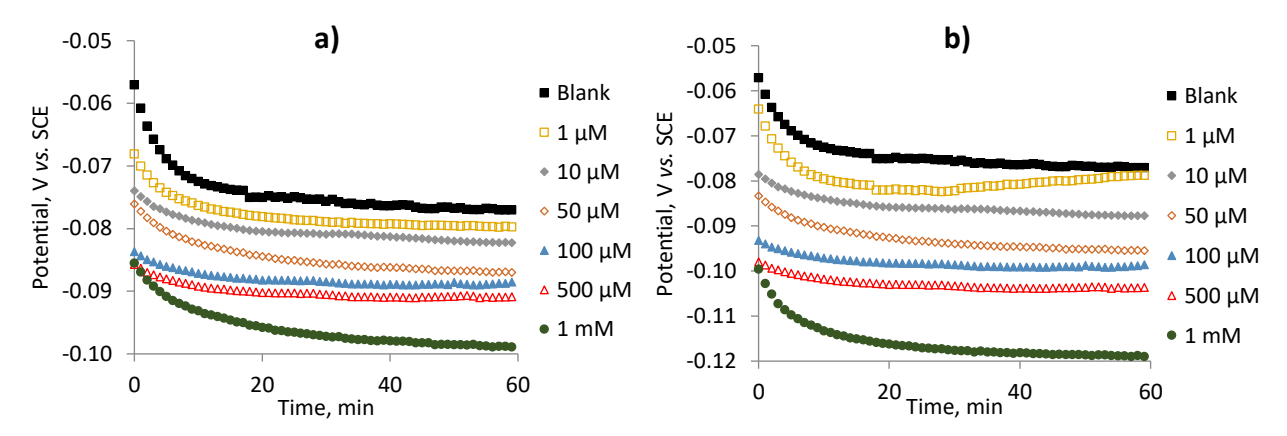


Figure 1. Open circuit potential of C12510 alloy versus time in 1.0 M H_2SO_4 solution without and with different concentrations of a) m-TMPP and b) p-TMPP

Potentiodynamic polarization technique

Figure 2 presents the PP curves of the C12510 electrode in blank 1.0 M H₂SO₄ and with different m-TMPP and p-TMPP molecule concentrations that vary from 10 μ M to 10 mM. The estimated parameters from the anodic and cathodic curves, such as Tafel slopes, anodic (β_a) and cathodic (β_c), corrosion potential (E_{corr}), corrosion current density (i_{corr}) and inhibition efficiency (η_{pp}), are listed in Table 1.

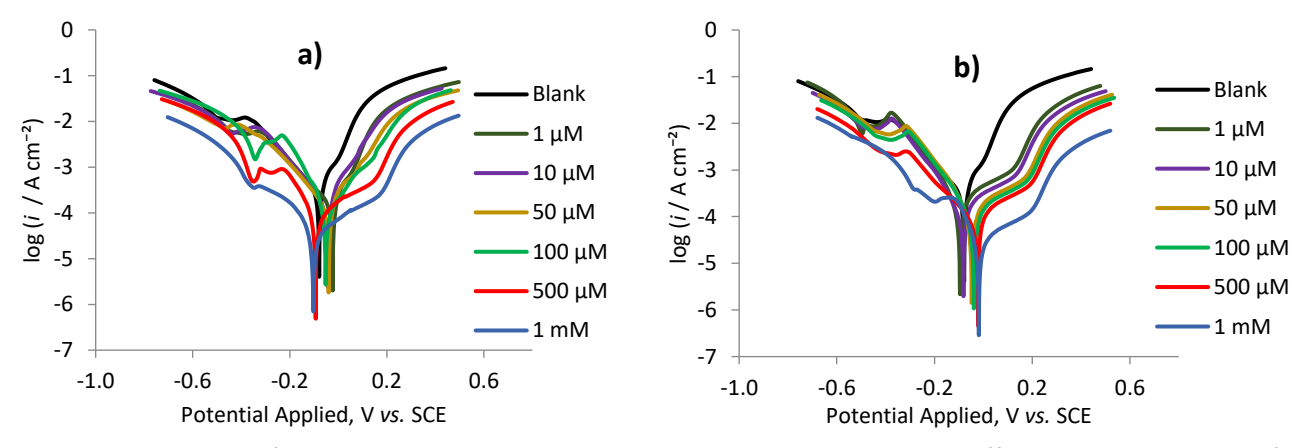


Figure 2. PP curves for C12510 alloy in 1.0 M H_2SO_4 solution without and with different concentrations of a) m-TMPP and b) p-TMPP, at scan rate 2.0 mV s^{-1} at 298 K

	C / μM (at 298 K)	$-eta_c$ / mV dec $^{ ext{-}1}$	$\beta_{\rm a}$ / mV dec ⁻¹	$^{\rm L}$ - $E_{\rm corr}$ / mV	/ i _{corr} / μA cm ⁻² C	R _{PP} / mm year	$^{ ext{-}1}$ $\eta_{ ext{PP}}$
Blank		48	62	79	2630.0	30.9	-
	1	49	63	23	1321.3	15.5	49.76
	10	50	65	44	864.4	10.2	67.13
m-TMPP	50	48	68	40	839.2	9.9	68.09
III-IIVIPP	100	45	70	52	680.5	8.0	74.13
	500	42	71	93	198.2	2.3	92.46
	1000	40	72	103	99.1	1.2	96.23
	1	34	58	96	844.0	9.9	67.91
	10	34	60	81	727.3	8.6	72.35
» TMDD	50	35	62	48	479.3	5.6	81.78
p-TMPP	100	35	63	39	468.8	5.5	82.17
	500	35	64	20	196.1	2.3	92.54
	1000	36	65	18	62.9	0.7	97.61

Table 1. Electrochemical corrosion parameters of C12510 alloy in 1.0 M H_2SO_4 solution and with different TMPP doses at scan rate 2 mV s⁻¹ and 298 K

The PP curves in 1.0 M H_2SO_4 in the absence and the presence of different concentrations of TMPP compounds shift to lesser current densities without a significant change in the shapes and slopes of the curves upon increasing the TMPP concentrations. This finding confirms the TMPP inhibitory ability of C12510 alloy against acid corrosion, by reducing the corrosion reaction rate without changing its mechanism. Anodic and cathodic current densities are significantly reduced with increasing m-TMPP and p-TMPP concentrations. This implies that the adsorption of porphyrin molecules, which probably blocks the active sites on the C12510 surface within the corrosive electrolyte, efficiently suppresses the dissolution of anodic metal and the development of cathodic hydrogen. The values of i_{corr} are reduced upon the increase of the TMPP concentrations and the η_{PP} increases, proving the inhibitory impact of these compounds.

The values of Tafel slopes (β_a and β_c) were nearly unchanged in the presence of porphyrin molecules. The change in θ_a is about 10 and 3 mV dec⁻¹ in the case of m-TMPP and p-TMPP, respectively, while the change in β_c is about 8 and 12 mV dec⁻¹ in the case of m-TMPP and p-TMPP. Also, the E_{corr} values change within less than ±85 mV away from the blank by increasing TMPP concentration. This implies that porphyrin compounds operate as mixed-type inhibitors via inhibiting both anodic and cathodic corrosion reactions [21].

A drop of the current density in the cathodic region is observed, followed by an irreversible increase as the potential decreases. Also, a potential plateau is seen where the Cu electrode crosses the Tafel polarization zone in the anodic region. In this region, the current value barely changes with the potential increase before its irreversible increase as the potential increases further. This phenomenon is probably due to the formation of the porous surface layer of corrosion products.

Potentiodynamic anodic polarization

PAP curves for a C12510 electrode in blank 1.0 M H_2SO_4 and with different quantities of NaCl added as a pitting corrosion factor at a scan rate of 0.1 mV s^{-1} are displayed in Figure 3. The slow scan rate reduces the chance for pitting at a lower potential [22]. The lack of a dissolving peak confirms the stability of the coating layer grown on the surface of C12510. Until a certain potential is achieved, the current increases rapidly due to the passive layer built on the surface of C12510 and the pitting corrosion progresses. This potential is known as the pitting potential ($E_{pitt.}$). The reduction of passivity can originate from the adsorption of Cl⁻ ions on the passive film that develops on the C12510 surface, which generates an electrostatic field through the film/electrolyte interface [23]. Thus, at a certain magnitude of the electrostatic field, the adsorbed anions start to enter the passive film and the pitting corrosion develops.

Assessment of the electrode surface after PAP tests showed visible pits, the number of which increased with increasing chloride ion content in the solution.

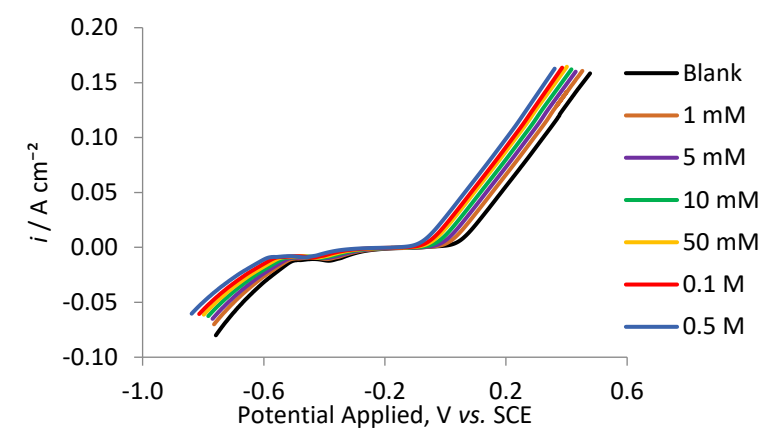


Figure 3. Potentiodynamic anodic polarization curves for C12510 alloy in 1.0 M H_2SO_4 solution and different concentrations of NaCl at room temperature, at scan rate 0.1 mV s⁻¹ and 298 K

The correlation between E_{pitt} and log Cl⁻ is described in Figure 4. A straight-line relationship that fulfils the equation below [24]:

$$E_{\text{pitt}} = \alpha - \beta \log C_{\text{Cl}}$$
 (8)

where α and β rely on the concentration of aggressive ions, as well as the type of metal or alloy. When the concentration of Cl⁻ ion increases, E_{pitt} values are moved to the active negative direction, proving that the Cl⁻ ion speeds the formation of pitting corrosion. TMPP molecules were tested as inhibitors for pitting corrosion utilizing the PAP technique.

The PAP curves for the C12510 electrode in a solution of 1.0 M $H_2SO_4 + 0.5$ M NaCl without and with certain concentrations of m-TMPP and p-TMPP molecules, respectively, are represented in Figure 5 at a scan rate of 0.1 mV s⁻¹.

It has been discovered that the E_{pitt} of the C12510 electrode is moved to more noble values with increasing the concentration of TMPP molecules. This implies increased protection of the C12510 electrode from pitting attack.

The relation between the logarithmic of the molar concentration of the TMPP molecules and E_{pitt} is displayed in Figure 6. Straight lines are acquired by satisfying Equation (9):

$$E_{\text{pitt}} = a - b \log C_{\text{TMPP}} \tag{9}$$

where a and b rely on the inhibitor employed as well as the type of metal or alloy.

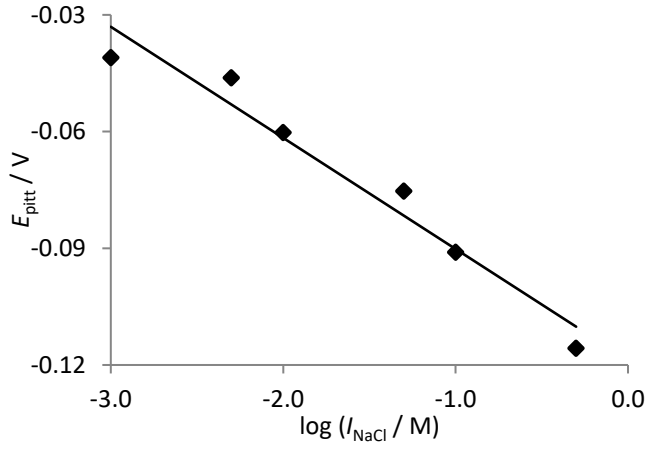


Figure 4. E_{pitt} vs. $log C_{Cl}$ ions for C12510 alloy in 1.0 M H_2SO_4 solution with various concentrations of NaCl, at scan rate 0.1 mV s⁻¹ and 298 K

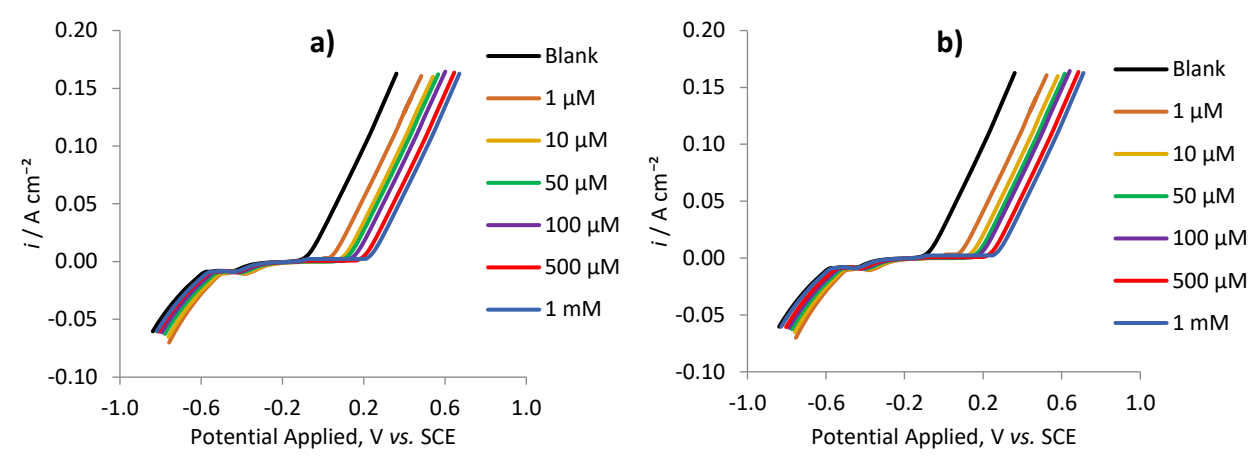


Figure 5. Potentiodynamic anodic polarization curves for C12510 alloy in (1.0 M $H_2SO_4 + 0.5$ M NaCl) solution with various concentrations of a) m-TMPP and b) p-TMPP, at scan rate 0.1 mV s⁻¹ and 298 K

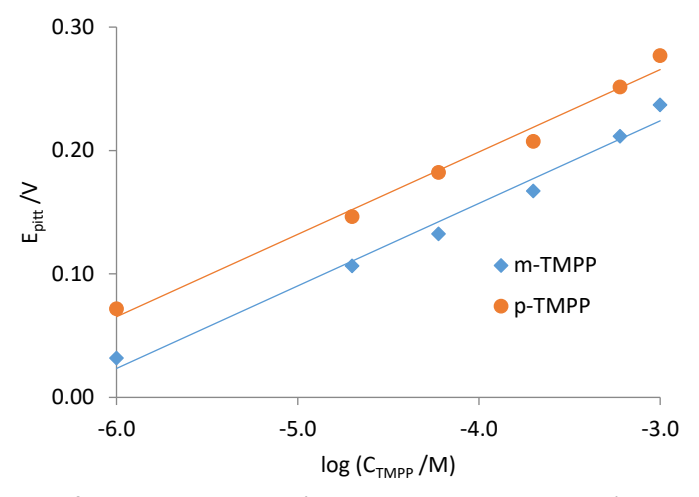


Figure 6. E_{pitt} vs. log C_{TMPP} for C12510 alloy in (1.0 M $H_2SO_4 + 0.5$ M NaCl) solution with concentrations of TMPP, at scan rate 0.1 mV s⁻¹ and 298 K

These findings verify that the presence of TMPP molecules increases the resistance to pitting corrosion. These molecules are categorized as inhibitors of pitting corrosion. The noble shift of $E_{\rm pitt}$, which suggests a greater ability to resist pitting corrosion, is greater for p-TMPP molecule than m-TMPP molecule at all concentrations tested.

Scanning electron microscopy analysis

The SEM is one of the most crucial instruments for surface analysis because of its capacity to offer a detailed microscopic view of metal surfaces. Figure 7 displays the SEM images of the surface of C12510 after PAP curves at a scan rate of 0.1 mV s^{-1} in (a) $1.0 \text{ M H}_2\text{SO}_4$, (b) $1.0 \text{ M H}_2\text{SO}_4 + 0.5 \text{ M NaCl}$, (c) $1.0 \text{ M H}_2\text{SO}_4 + 0.5 \text{ M NaCl} + 0.001 \text{ M m}$ -TMPP and (d) $1.0 \text{ M H}_2\text{SO}_4 + 0.5 \text{ M NaCl} + 0.001 \text{M p}$ -TMPP. It can be noticed in Figure 7a that the unsmooth surface was produced by the corrosion attack of H_2SO_4 solutions. Figure 7b shows that when 0.5 M NaCl was added as a pitting corrosion agent, the C12510 surface became more damaged and the pits can be clearly observed. By introducing the m-TMPP and p-TMPP molecules into the corrosive system (Figure 7c and d), the surface of C12510 is improved and the pits observed in the presence of NaCl disappeared. Pitting corrosion is avoided because the TMPP compound adsorbs on the surface of C12510 and creates a surface layer that separates the C12510 apart from the aggressive solution. It is evident that p-TMPP molecules form a good film on the C12510 surface with a higher inhibition efficiency and less damage caused by

corrosion than the film formed by m-TMPP molecules. This last film shows lower inhibition efficiency than p-TMPP, and some corrosion damage still happens.

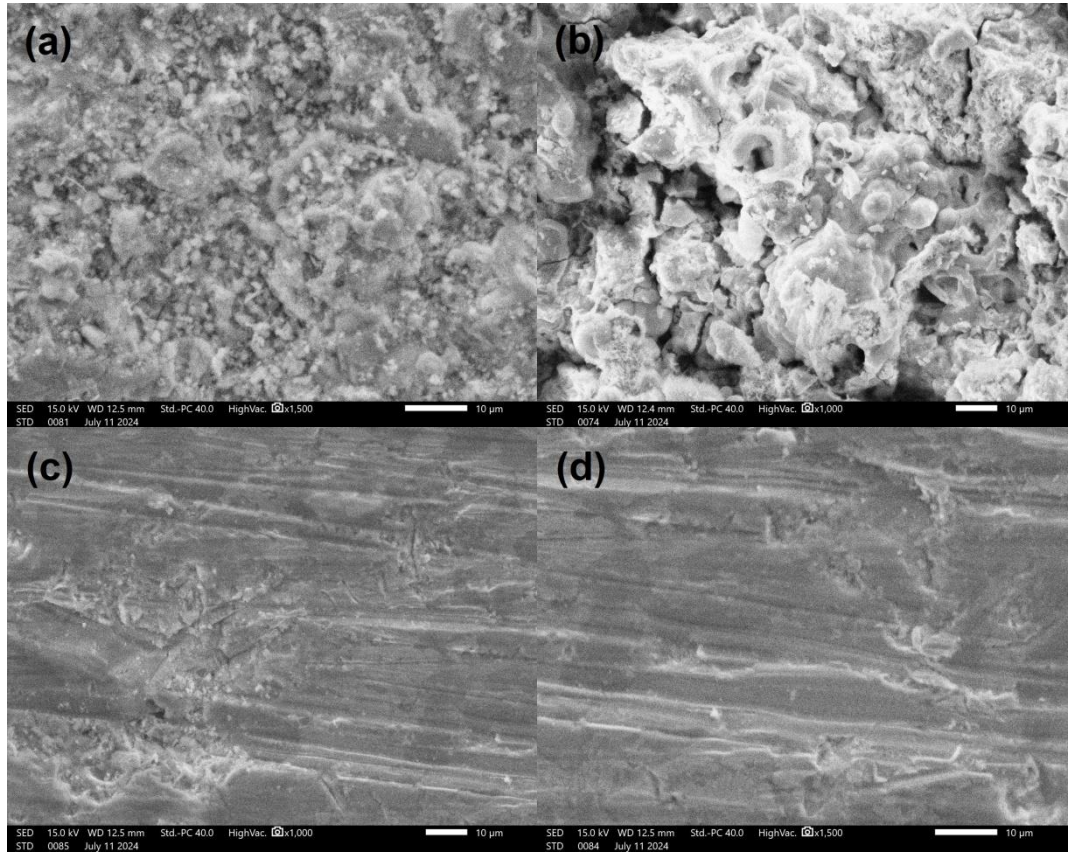


Figure 7. SEM images for C12510 alloy in (a) 1.0 M H_2SO_4 , (b) 1.0 M H_2SO_4 + 0.5 M NaCl, (c) 1.0 M H_2SO_4 + 0.5 M NaCl + 0.001 M m-TMPP and (d) 1.0 M H_2SO_4 + 0.5 M NaCl + 0.001 M p-TMPP

Electrochemical impedance spectroscopy

Electrochemical impedance spectroscopy (EIS) is a non-invasive technique helpful for understanding the electrochemical corrosion process of the metal and how organic molecules affect the reaction mechanism and prevent the metal dissolution [25,26]. This method effectively clarifies the electrolyte-electrode interface dynamics, providing insight into various physical and chemical properties, such as metal surface roughness and impurities [27]. The Nyquist and Bode plots for the C12510 electrode in a blank 1.0 M H_2SO_4 and with certain concentrations of m-TMPP and p-TMPP molecules ranging from 1 μ M to 1 mM are presented in Figure 8.

The measured Nyquist impedance graphs shown in Figure 8A display imperfect, not ideal semicircles. This is typically explained by the frequency dispersion of interfacial impedance arising from contaminants, surface roughness, grain boundaries, inhibitor adsorption, building up porous layers, and electrode surface homogenates. Also, the semicircles for the C12510 electrode, in the absence and presence of the TMPP compounds, are similar, implying that the TMPP inhibitors do not affect the corrosion mechanism, as previously reported by PP measurements [28]. The semicircular appearance seen in both blank 1.0 M H_2SO_4 solution and the presence of TMPP molecules claim that, in all cases, the charge transfer process governs the dissolution process of the C12510 electrode [29]. With increasing the concentration of TMPP molecules, the diameter of the capacitive loop increases, signifying higher charge transfer resistance, which appears due to the improved strength of the adsorbed inhibiting film.

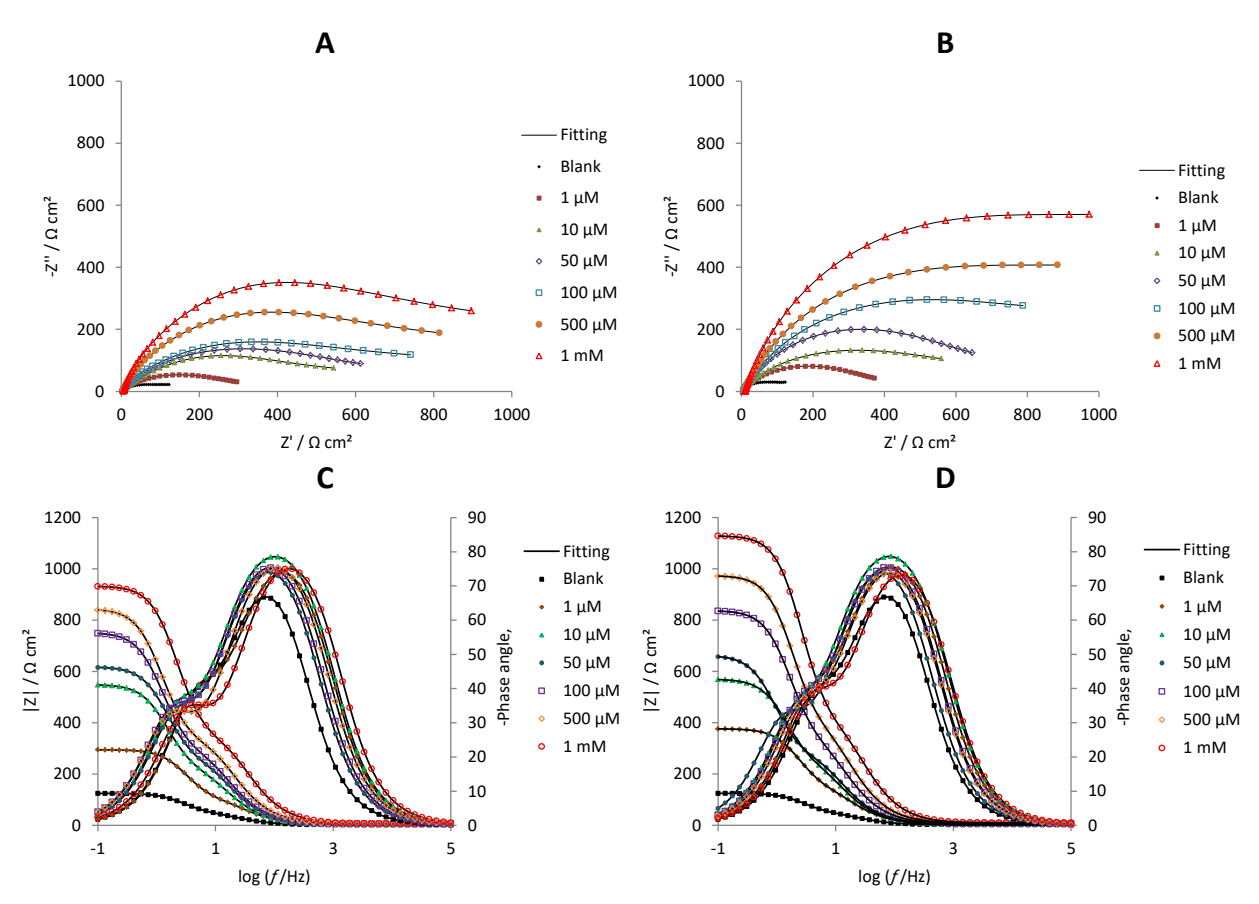


Figure 8. The Nyquist and Bode plots for C12510 alloy in 1.0 M H_2SO_4 solution without and with different concentrations of (A and C) m-TMPP and (B and D) p-TMPP molecules

Bode diagrams shown in Figure 8B represent the dependency of impedance modulus |Z| and phase shift on frequency. Bode plots show clear separation into two time constants, indicated by the appearance of a change in slope of impedance modulus |Z| and two phase angle maxima, effectively splitting the Bode plots into two sections, one at higher and another at lower frequencies. The impedance modulus increases with increasing the concentration of TMPP molecules, indicating the adsorption of TMPP molecules on the C12510 surface and strengthening the inhibitory effect against the H_2SO_4 solution [30]. Generally, higher concentrations of TMPP shift the phase-angle peaks to higher values, approaching the ideal capacitor values (-90°), an indication of their ordered distribution on the copper surface.

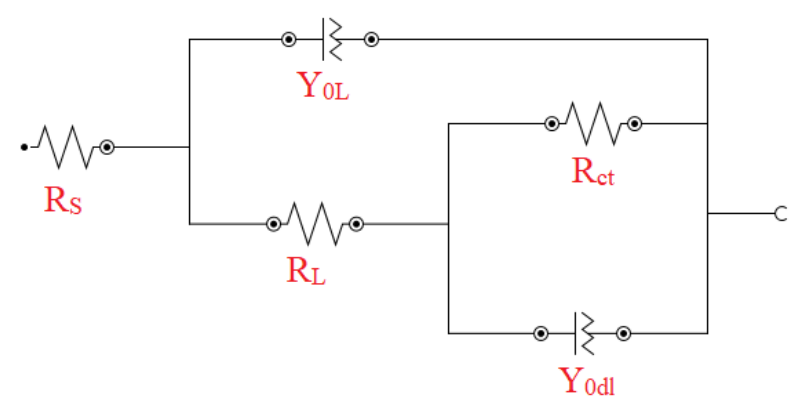


Figure 9. The electrical equivalent circuit used to fit electrochemical impedance data of C12510 alloy

The proposed electrical equivalent circuit designed for interpreting the impedance information is demonstrated in Figure 9. The recommended electrical equivalent circuit looks like this: initially, the

solution creates a resistance (R_S), followed by the impedance of an electrical double layer(Y_{Odl}) created by the corrosive solution in contact with the copper surface. Resistance to copper dissolution is denoted by charge transfer resistance (R_{ct}). Eventually, a chemical reaction occurs on the surface and chemical deposits are formed on the surface, creating a layer resistance (R_L), which arises from the formation of a barrier layer that impedes charge transfer during the electrochemical reaction. The capacitance of the barrier layer (Y_{OL}) is created with deposits acting as dielectrics. This phenomenon is supported by the PP results, as shown by the drops in the copper alloy's anodic and cathodic current densities at some potentials.

Table 2 summarizes impedance parameter values obtained by fitting the electrical equivalent circuit in Figure 9 to impedance spectra in Figure 8. The chi-square values (χ^2) are in the range of 10⁻⁴, suggesting the consistency of the simulation and experimental data. As shown in Table 2, when TMPP concentrations are raised, both R_{ct} and R_L increase, most likely due to the adsorption of TMPP molecules on the C12510 surface, ongoing with the formation of a barrier layer of the inhibitor molecules on the C12510/electrolyte interface, inhibiting the electrochemical corrosion reaction, hence η_{EIS} rises [31].

Table 2. AC impedance data for C12510 alloy in $1.0 \text{ M H}_2\text{SO}_4$ solution at room temperature with and without various TMPP concentrations

	C / μM (at 298 K)	χ^2	R_S / Ω cm ²	$n_{ m YOdI}$	Y _{0dl} / mS s ⁿ cm ⁻²	C _{dl} / mF cm ⁻²	$R_{\rm ct}$ / Ω cm ²	n _{YOL}	Y_{0L} / mS s ⁿ cm ⁻²	R_L / Ω cm ²	η_{EIS}
Blank		0.00015	2.17	0.61	18.93	527.58	63.05	0.54	1.10	49.48	-
	1	0.00024	2.52	0.62	4.81	122.62	453.41	0.54	0.55	73.95	86.09
	10	0.00011	2.54	0.61	4.17	116.89	583.73	0.56	0.47	172.67	89.20
TMDD	50	0.00090	5.75	0.64	3.98	90.55	616.23	0.59	0.37	205.69	89.77
m-TMPP	100	0.00054	5.47	0.65	3.93	77.19	707.71	0.52	0.33	238.15	91.09
	500	0.00032	6.01	0.66	3.81	68.62	850.25	0.57	0.23	282.08	92.58
	1000	0.00041	6.61	0.68	1.89	28.16	905.41	0.57	0.13	290.52	93.04
	1	0.00032	2.96	0.58	8.94	334.44	492.13	0.57	0.64	105.34	87.19
•	10	0.00018	2.86	0.58	7.20	252.72	622.09	0.59	0.54	188.96	89.86
- TMDD	50	0.00032	6.10	0.59	6.04	210.37	777.34	0.54	0.45	228.93	91.89
p-TMPP	100	0.00041	6.45	0.61	5.07	144.49	811.44	0.50	0.34	249.23	92.23
· _	500	0.00076	9.33	0.60	4.41	131.72	935.81	0.58	0.24	298.33	93.26
•	1000	0.00037	10.27	0.67	3.99	65.70	1085.88	0.55	0.14	307.55	94.19

True double-layer (C_{dl}) capacitance values were estimated by the following formula [32]:

$$C_{\rm dl} = Y_{\rm 0dl} \omega^{\rm n-1} = Y_{\rm 0dl} (2\pi f_{\rm max})^{\rm n-1} \tag{10}$$

where Y_{0dl} / S sⁿ cm⁻² is a parameter that describes the impedance of constant phase element (CPE), applied instead of a true double layer capacitor described by C_{dl} / F cm⁻² capacitance, n is CPE exponent, $\omega = 2\pi f$ is radial frequency, while f_{max} is the frequency at which the imaginary component of the impedance is maximal.

 $C_{\rm dl}$ values decrease with increasing TMPP concentration. These TMPP molecules could replace water molecules at the C12510/electrolyte interface, increasing its surface coverage and effectively shielding the copper from the corrosive surroundings. This led to increased double-layer thickness and a drop in $C_{\rm dl}$. The calculated $\eta_{\rm EIS}$ increases in the order p-TMPP > m-TMPP, as expected from the PP.

Weight loss technique

The corrosion behaviour of the C12510 sample was examined using the WL method at various concentrations of m-TMPP and p-TMPP molecules, ranging from 1 μ M to 1 mM, and across a variety of time intervals, from 2 to 24 hours. The results gathered for the m-TMPP and p-TMPP molecules



are listed in Table 3. According to Table 3, the addition of two studied compounds greatly lowered the corrosion rate of C12510 in the acid solution and enhanced inhibition efficiency (η_W). Therefore, it is reasonable to conclude that the two tested compounds are effective in preventing acid corrosion of C12510.

Table 3. Corrosion rates and inhibition efficacy of C12510 alloy in 1.0 H_2SO_4 solution with and without different TMPP concentrations for different immersion times

						In	hibitor conce	ntratio	n, μM					
Inhibitor	Time b	0	1		10		50		100		500		1000	
IIIIIDILOI	nine, n -	CR _W /	CR _W /	ηw/	CR _w /	ηw/	CR _w /	ηw/	CR _w /	ηw/	CR _w /	ηw/	CR _w /	ηw/
		mg cm ⁻² h ⁻¹	mg cm ⁻² h ⁻¹	%	mg cm ⁻² h ⁻¹	%	mg cm ⁻² h ⁻¹	%	mg cm ⁻² h ⁻¹	%	mg cm ⁻² h ⁻¹	%	mg cm ⁻² h ⁻¹	%
	2	1.45	1.33	8.28	1.24	14.48	1.12	22.76	0.97	33.10	0.85	41.38	0.65	55.17
	4	2.61	2.22	14.94	2.06	21.07	1.7	34.87	1.38	47.13	0.85	67.43	0.44	83.14
	6	3.42	2.8	18.13	2.51	26.61	2.15	37.13	1.62	52.63	0.95	72.22	0.53	84.50
m-TMPP	8	4.72	3.26	30.93	3.03	35.81	2.5	47.03	1.88	60.17	1.1	76.69	0.62	86.86
	10	5.63	3.57	36.59	3.32	41.03	2.74	51.33	2.06	63.41	1.21	78.51	0.68	87.92
	20	7.4	3.56	51.89	3.31	55.27	2.73	63.11	2.05	72.30	1.2	83.78	0.68	90.81
	24	8.16	3.58	56.13	3.33	59.19	2.75	66.30	2.07	74.63	1.21	85.17	0.68	91.67
	2	1.45	1.31	9.66	1.18	18.62	1.12	22.76	0.91	37.24	0.78	46.21	0.5	65.52
	4	2.61	2.12	18.77	1.81	30.65	1.57	39.85	1.16	55.56	0.7	73.18	0.43	83.52
	6	3.42	2.47	27.78	2.12	38.01	1.83	46.49	1.35	60.53	0.79	76.90	0.39	88.60
p-TMPP	8	4.72	2.98	36.86	2.55	45.97	2.21	53.18	1.63	65.47	0.96	79.66	0.47	90.04
	10	5.63	3.33	40.85	2.85	49.38	2.47	56.13	1.82	67.67	1.07	80.99	0.52	90.76
	20	7.4	3.44	53.51	2.95	60.14	2.55	65.54	1.88	74.59	1.1	85.14	0.54	92.70
	24	8.16	3.39	58.46	2.91	64.34	2.51	69.24	1.86	77.21	1.09	86.64	0.53	93.50

The results demonstrate that the η_W increases as TMPP concentration and immersion time increase. This finding could be attributed to the fact that more molecules are adsorbed, covering a larger surface area of the C12510 as the TMPP concentration increases. Consequently, the corrosion rate is reduced, and the inhibition efficiency increases. It's noteworthy to observe that there is a small range in which the η_W increases from the lowest to the greatest TMPP concentration. This behaviour is due to the formation of an isolating layer resulting from the adsorption of TMPP molecules on the C12510 surface. The η_W is of the order: p-TMPP > m-TMPP. Also, there is an obvious agreement between η_W values obtained using weight loss data and those obtained with the PP, PAP and EIS techniques.

Activation thermodynamic parameters

The influence of raising the temperature on the corrosion of C12510 in blank 1.0 M H_2SO_4 and inhibited by 1 mM m-TMPP and p-TMPP compounds for 2 h, was examined at temperatures ranging from 298 to 343 K. The calculated results presented in Table 4 show that with increasing temperature the values of CR_W rise, while the η_W are reduced. A decrease in the % η_W and an increase in the rate of elimination of the adsorbed TMPP from the surface of C12510 support the physical adsorption of the TMPP compounds on the C12510 surface.

The activation energy (E_a), the activation enthalpy (ΔH^*), and the activation entropy (ΔS^*) of C12510 in blank 1.0 M H₂SO₄ and solution containing 1 mM m-TMPP and p-TMPP molecules for 2 hours were assessed using Arrhenius equation and transition state relation [33]:

$$\ln CR_{\rm W} = \ln A - \frac{E_{\rm a}}{RT} \tag{11}$$

$$\ln\left(\frac{CR_{W}}{T}\right) = \left|\ln\left(\frac{R}{N_{A}h}\right) + \frac{\Delta S^{*}}{R}\right| - \frac{\Delta H^{*}}{RT} \tag{12}$$

where, A is the Arrhenius constant, h is the Planck's constant and N_A is Avogadro's number.

Solution	T / K	$CR_{\rm W}$ / mg cm ⁻² h ⁻¹	ηw/%	E_a / kJ mol ⁻¹	Δ <i>H</i> * / kJ mol ⁻¹	ΔS^* / J mol ⁻¹ K ⁻¹
	298	1.45	-			
	313	2.31	-	•		
1 M H₂SO₄	323	3.33	-	26.42	23.76	-162.16
	333	4.84	-	•		
	343	5.48	-	•		
	298	0.65	54.88			
1 M H ₂ SO ₄	313	1.23	46.82	•		
+	323	2.09	37.17	37.89	35.24	-130.42
1 mM m-TMPP	333	3.68	24.07	•		
	343	4.36	20.43	•		
	298	0.50	65.17			
1 M H ₂ SO ₄	313	1.17	49.42	•		
+	323	1.77	46.97	38.90	36.25	-128.65
1 mM p-TMPP	333	2.94	39.26	•		
	343	3.84	29.98	•		

Table 4. Thermodynamic activation parameters of C12510 alloy in 1.0 M H_2SO_4 solution both with and without 1 mM TMPP in different temperatures after 2 h of immersion time

Figures 10A and 10B exhibit the plots of log CR_W and log (CR_W/T) vs. 1/T for the C12510 sample in blank 1.0 M H₂SO₄ and with 1 mM concentrations of m-TMPP and p-TMPP molecules. Straight lines were produced with a coefficient of determination (R^2) close to unity.

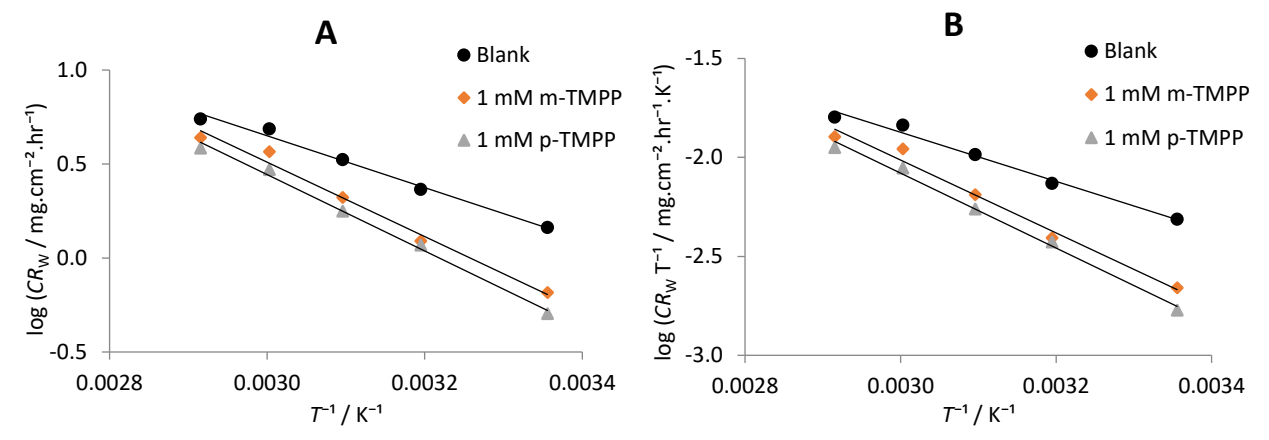


Figure 10. Arrhenius (A) and transition state (B) plots for C12510 alloy in $1.0 \text{ M H}_2\text{SO}_4$ solution with and without 1 mM concentrations of m-TMPP and p-TMPP

From the slope of the straight lines in Figure 10A, the values of E_a were computed and listed in Table 4. In the presence of TMPP molecules, the values of E_a are greater than in blank 1.0 M H₂SO₄, suggesting the physical adsorption of TMPP molecules on the C12510 sample. The higher value of E_a in the presence of TMPP molecules denotes the creation of a higher energy barrier against the corrosion process because an adsorbed layer has developed on the C12510 surface [34]. From the slopes and the intercepts of the straight lines in Figure 10B, the values of ΔH^* and ΔS^* were computed and listed in Table 4. The positive values of ΔH^* values imply an endothermic corrosion reaction, and when TMPP is added, the value rises, which suggests a greater need for heat for the reaction to proceed. The activated complex of the rate-determining step is association instead of dissociation, as indicated by the negative entropy change (ΔS^*) sign, which represents the formation of more arrangement when the reactant transforms to the activating complex.

Adsorption isotherm

Applying weight loss data, the surface coverage (θ) was determined for the varied concentrations of TMPP molecules to analyse the adsorption behaviour of TMPP on C12510 in 1.0 M H₂SO₄ solution.

The adsorption process can be thought of as an exchange process between the TMPP molecules in the aqueous solution [TMPP_(aq.)] and water molecules adsorbed on the C12510 [$H_2O_{(ads)}$] to donate the adsorbed TMP on the C12510 surface [TMPP_(ads.)], using Equation (13):

$$TMPP_{(aq.)} + H_2O_{(ads.)} \rightarrow TMPP_{(ads.)} + \beta H_2O_{(aq.)}$$
(13)

where β is the amount of water molecules exchanged by one TMPP molecule.

The interaction between the C12510 surface and TMPP molecules in 1.0 M H_2SO_4 solution is studied through the adsorption isotherm. The surface coverage value (θ) estimated from the WL technique is employed for several adsorption isotherms. It was found that the Langmuir isotherm matches the experimental data excellently, according to the following equation:

$$\frac{C_{\text{TMPP}}}{\theta} = \frac{1}{K_{\text{ads}}} + C_{\text{TMPP}} \tag{14}$$

where K_{ads} / M^{-1} is the equilibrium constant of adsorption.

Straight lines were obtained by plotting C_{TMPP}/θ versus C_{TMPP} with correlation coefficient (R^2) close to 1.0 as shown in Figure 11. The value of K_{ads} computed from the intercept reveals that a monolayer of TMPP molecules is formed on the C12510 surface with no side interactions between the adsorbed particles.

The standard free energy of adsorption (ΔG^{o}_{ads}) was estimated from Equation (15) [35]: $\Delta G^{o}_{ads} = -RT \ln (55.5K_{ads})$ (15)

where 55.5 is the molarity of water. The calculated values of ΔG^{o}_{ads} at all tested hours are negative, revealing that the TMPP molecules adsorb on the C12510 surface spontaneously, Table 5.

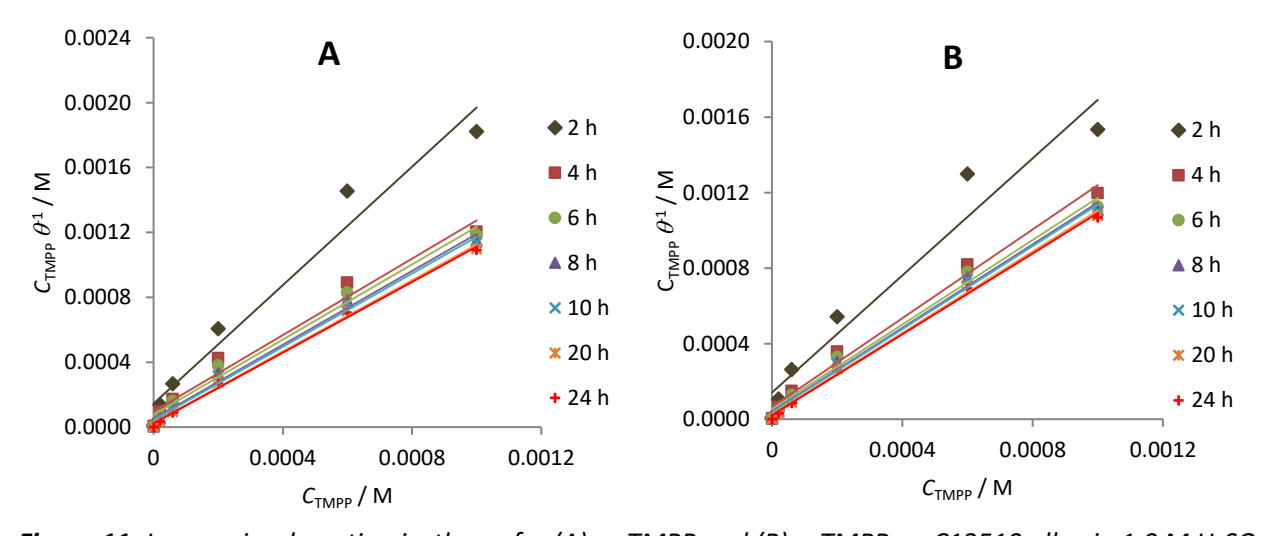


Figure 11. Langmuir adsorption isotherm for (A) m-TMPP and (B) p-TMPP on C12510 alloy in 1.0 M H_2SO_4 solution after different immersion times at 298 K

Also, it is known that the higher ΔG°_{ads} negative value, the more effective adsorption is. The values of ΔG°_{ads} ranged from -31.86 to -36.63 kJ mol⁻¹ and the high K_{ads} seen in the Langmuir model demonstrate that TMPP inhibitors are adsorbed on copper surfaces through a combination of physical and chemical adsorption process. The negative values of ΔG°_{ads} , after immersion for 2 hours through 24 hours for p-TMPP, range from -31.93 to -36.63 kJ mol⁻¹ and are somewhat larger than those for m-TMPP ranging from -31.86 to -36.38 kJ mol⁻¹, which is expected from weight loss measurements above. p-TMPP may show flatness and better spreading on the copper surface, which is reflected in the higher adsorption efficiency.

Inhibitor	Time, h	R^2	$K_{\rm ads}$ / mM ⁻¹	$\Delta G_{\rm ads}$ / kJ mol ⁻¹
	2	0.9654	6.91	-31.86
	4	0.9741	10.389	-32.87
	6	0.9845	13.088	-33.44
m-TMPP	8	0.9910	19.203	-34.39
	10	0.9930	22.820	-34.82
	20	0.9966	37.109	-36.03
	24	0.9973	42.756	-36.38
	2	0.9477	7.103	-31.93
	4	0.9893	15.552	-33.87
	6	0.9890	18.723	-34.33
p-TMPP	8	0.9925	24.308	-34.98
	10	0.9937	27.252	-35.26
p-TMPP	20	0.9966	40.161	-36.22
	2/	0.0074	47 207	26.62

Table 5. The equilibrium constant and adsorption standard free energy of various concentrations of TMPP on C12510 alloy in 1.0 M H₂SO₄ solution at room temperature

Inhibition mechanism

The inhibition of corrosion performance of the C12510 sample in blank $1.0 \, M \, H_2SO_4$ by the TMPP molecules using WL, PP, PAP, and EIS methods was found to depend on the concentration, kind and the position of the substitutes group in the molecule. The adsorption characteristics can be used to understand the nature of the inhibitor interaction on the metal surface during corrosion inhibition. The findings demonstrate that adsorption of the inhibitor at the solution interface inhibits corrosion. Some factors that influence the inhibitory efficacy of additive compounds are the amount of adsorption active sites and their charge density, the size of the molecule, the adsorption process, and the creation of metallic complexes.

The interaction between the TMPP molecule and C12510 surface ions may cause the stable complex to develop by forming four coordination bonds between the copper ion and the electron lone pairs of nitrogen atoms. The proposed structures of the complexes are presented in Figure 12. The results obtained from many methodologies in this study verify that p-TMPP has a somewhat higher inhibition efficiency order than m-TMPP. The molecular structure of the two TMPP compounds contains four methoxy groups ($-OCH_3$), contributing to their strong inhibitory efficacy. The methoxy group exhibits a negative inductive effect (-I) and a positive mesomeric impact (+M). The methoxy group's Hammett constant [36] is equivalent to $\sigma = -0.27$, which intensifies the molecule's delocalized π electrons. This group raises the molecule's electron charge density, increasing the inhibition efficiency.

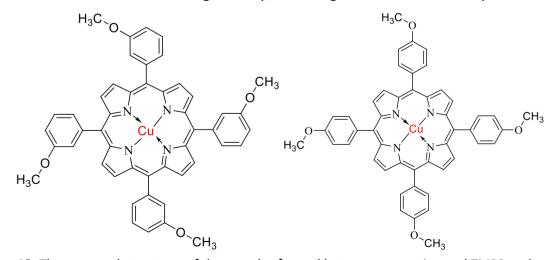


Figure 12. The proposed structures of the complex formed between copper ion and TMPP molecule

According to earlier findings on inhibition efficiency obtained from various methods, p-TMPP has a higher inhibition efficiency order than m-TMPP. The p-substituted group's inductive and mesomeric actions work in harmony to raise the degree of surface coverage and, as a result, the inhibitory efficiency. The efficacy of inhibition in the case of m-substituted groups depends on the resonance and inductive effects (+R, -I), which alter the electron density and activate the aromatic ring.

Density functional theory study

Theoretical calculations were conducted to complement experimental findings and provide insight at the molecular level. Among the available quantum chemical techniques for analysing corrosion inhibitors, density functional theory (DFT) has proven highly effective in identifying changes in the electronic structure that contribute to the inhibition mechanism. Recent advancements in DFT have enhanced its ability to accurately predict molecular properties and describe atomic interactions within molecules. Over the past decade, DFT has gained widespread popularity due to its precision and efficient use of computational resources, making it an invaluable tool for corrosion studies [37]. Figure 13 shows the optimized geometries of m-methoxy tetraphenyl porphyrin (m-TMPP) and p-methoxy tetraphenyl porphyrin (p-TMPP). The difference in the position of the methoxy group between the meta and para configurations results in slightly altered molecular geometries. The geometry optimization indicates that both structures retain the planar nature typical of porphyrins, but the subtle differences in bond angles and orientations of the phenyl groups are likely to influence the electronic properties of each molecule.

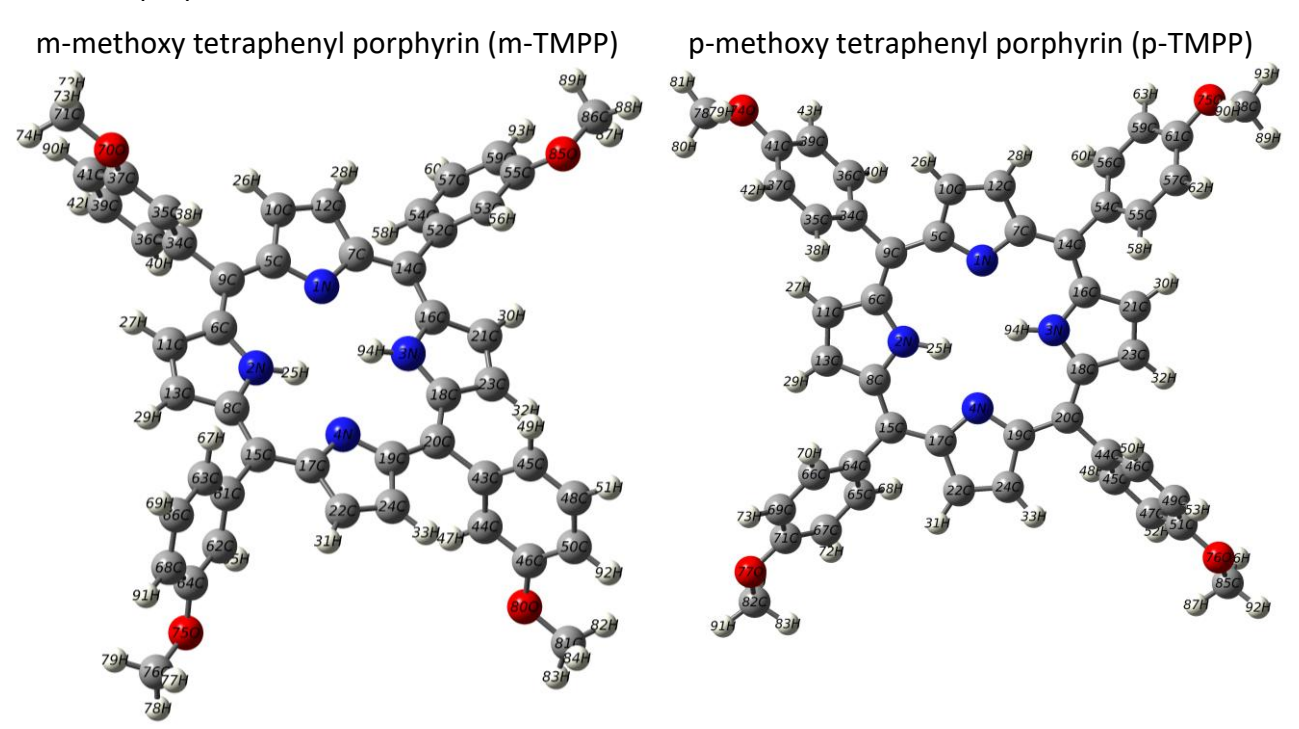


Figure 13. Optimized geometries of m-TMPP and p-TMPP molecules

In Figure 14, the LUMO (lowest unoccupied molecular orbital) and HOMO (highest occupied molecular orbital) maps, as well as the ESP (electrostatic potential) maps, are presented for m-TMPP and p-TMPP. The frontier orbitals play a significant role in determining the reactivity and interaction with surfaces or molecules. The HOMO for both m-TMPP and p-TMPP appears localized on the porphyrin ring, indicating that this area is responsible for electron donation. The LUMO, on the other hand, is slightly more delocalized, allowing for electron acceptance over a broader region. The ESP

maps show regions of electron-rich and electron-deficient areas, which are crucial for understanding intermolecular interactions. The different methoxy positions (meta *vs.* para) shift the electron density slightly, which may explain the differences in chemical reactivity.

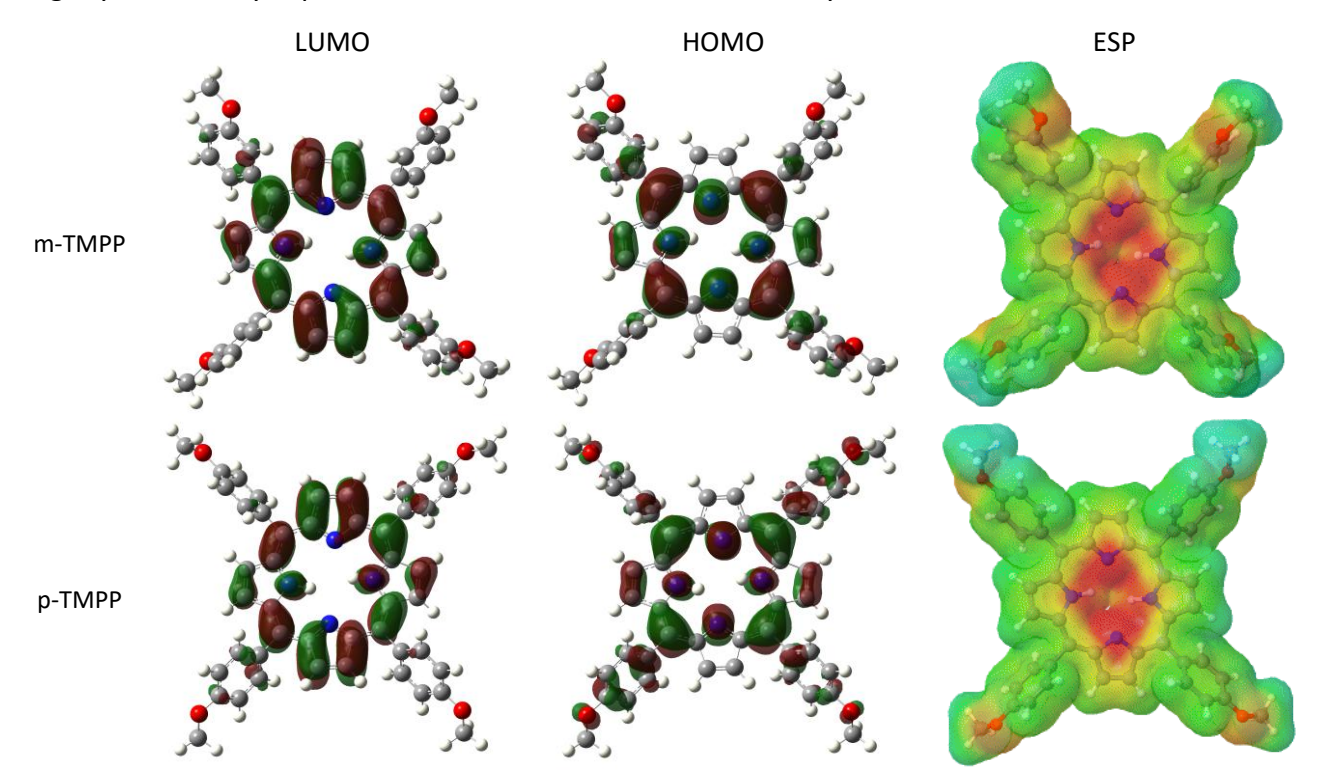


Figure 14. Frontier orbitals and ESP maps of m-TMPP and p-TMPP

The dipole moment vectors indicate the magnitude and direction of the molecular dipole. As shown in Figure 15, for m-TMPP, the dipole moment is relatively small at 0.79 debye, indicating that the electron distribution is relatively symmetrical. In contrast, p-TMPP shows a much larger dipole moment of 3.51 debye, suggesting a greater asymmetry in the charge distribution due to the parasubstitution of the methoxy group. This difference in dipole moments is significant, as a larger dipole moment can influence the interaction with polar environments and surfaces. p-TMPP has a larger dipole moment than m-TMPP, as indicated by both experimental results and DFT calculations.

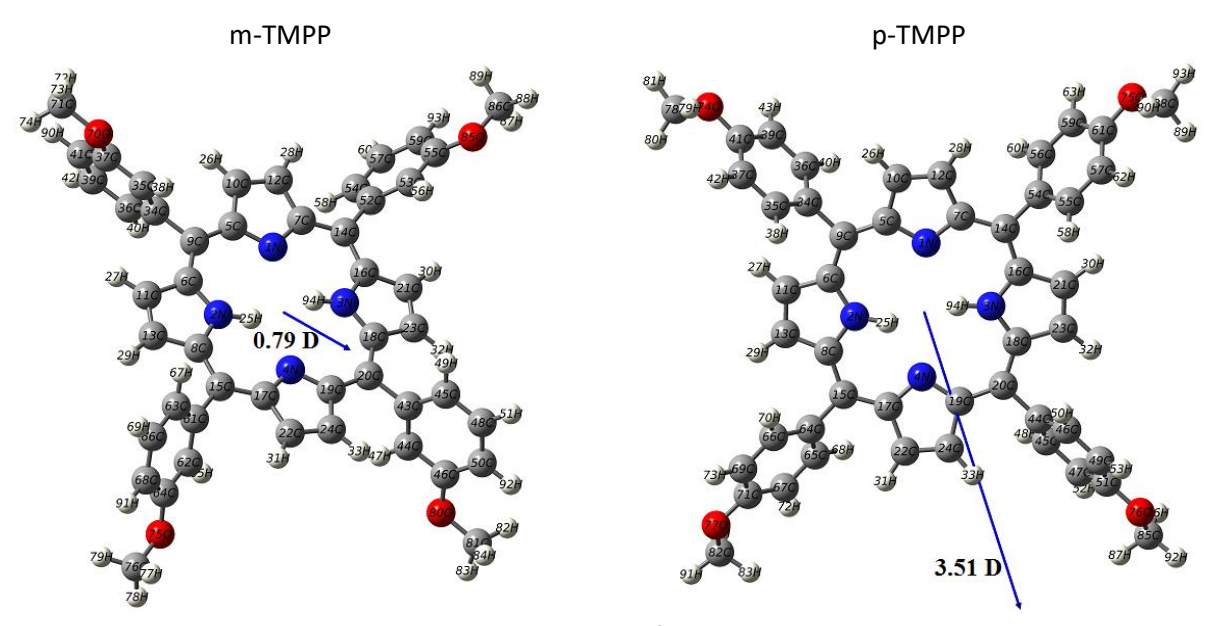


Figure 15. Dipole moment vectors for m-TMPP and p-TMPP

The larger dipole moment in p-TMPP increases its polarity, resulting in stronger electrostatic interactions between the inhibitor and the charged copper surface in acidic H_2SO_4 media. p-TMPP effectively reduces the rate of copper corrosion by creating a thicker and more protective adsorption layer as a result of the enhanced attraction. The quantum parameters for both m-TMPP and p-TMPP, as presented in Table 6, are essential for understanding their electronic properties. The energies of the frontier orbitals (E_{HOMO} and E_{LUMO}) provide key insights into the interaction between molecules and a copper surface. A higher E_{HOMO} indicates a greater ability for a molecule to donate electrons, which enhances its interaction with metal surfaces. In contrast, E_{LUMO} reflects the molecule's tendency to accept electrons; the lower the E_{LUMO} , the stronger its electron-accepting capability.

For m-TMPP and p-TMPP, the LUMO energy levels are -5.20 and -5.00 eV, respectively, while the HOMO levels are -2.58 eV for m-TMPP and -2.53 eV for p-TMPP as summarized in Table 6. These values indicate a subtle difference in electronic structure. The HOMO-LUMO gap is crucial in determining how well a molecule can interact with a metal surface. A smaller gap generally means a molecule can easily donate or accept electrons, facilitating stronger adsorption onto the metal. This process is key in forming a protective layer that prevents metal corrosion, especially in aggressive environments like acidic media (H₂SO₄). In this case, the slightly smaller band gap of p-TMPP as shown in Table 6, suggests a stronger affinity for the metal surface, thereby providing a better barrier against corrosive species compared to m-TMPP. In an aqueous phase, the protonation of p-TMPP and m-TMPP occurs on the nitrogen atom of the pyrrole unit, which carries the most negative charge. As seen in Figure 16, protonation decreases the energies of both frontier orbitals due to the increased electron-withdrawing nature of the positively charged pyrrole unit. However, the trend of p-TMPP having slightly higher HOMO and LUMO levels than m-TMPP remains consistent. Upon protonation, p-TMPP retains the smaller gap. The smaller band gap of p-TMPP in both protonated and non-protonated forms suggests a greater ease of electron transfer, which is critical for the formation of a robust protective barrier on the metal. This property makes p-TMPP more effective in environments such as acidic media.

The hardness and softness values of m-TMPP and p-TMPP are important indicators of their reactivity and inhibition efficiency in copper corrosion in H_2SO_4 media. Hardness (γ) is inversely related to a molecule's reactivity. A higher hardness value indicates that the molecule is more stable and less reactive, meaning it resists changes in its electronic configuration. Softness (σ), being the reciprocal of hardness, indicates how easily a molecule can donate or accept electrons.

Table 6. Quantum parameters of m-TMPP and p-TMPP inhibitors

Compound	LUMO, eV	HOMO, eV	ΔE / eV	Dipole moment, D	γ / eV	σ / eV ⁻¹	Number of electrons transferred
m-TMPP	-5.20	-2.58	2.62	0.79	1.31	0.763	3.37
p-TMPP	-5.00	-2.53	2.47	3.51	1.235	0.810	3.52

A higher softness value suggests higher reactivity and a stronger ability to interact with external species, such as metal surfaces. As seen in Table 6, p-TMPP is softer and, therefore, more reactive, making it a better electron donor or acceptor. This enables it to interact more strongly with the copper surface, leading to better adsorption and a more effective inhibition layer. The higher reactivity of p-TMPP also allows it to respond more efficiently to changes in the local environment, improving its ability to prevent the penetration of aggressive ions. m-TMPP, being harder and less reactive, would be less effective in forming strong interactions with the copper surface. While it can still act as a corrosion inhibitor, its lower softness means that it would not adsorb as strongly as p-TMPP and its ability to block corrosive species will be diminished.

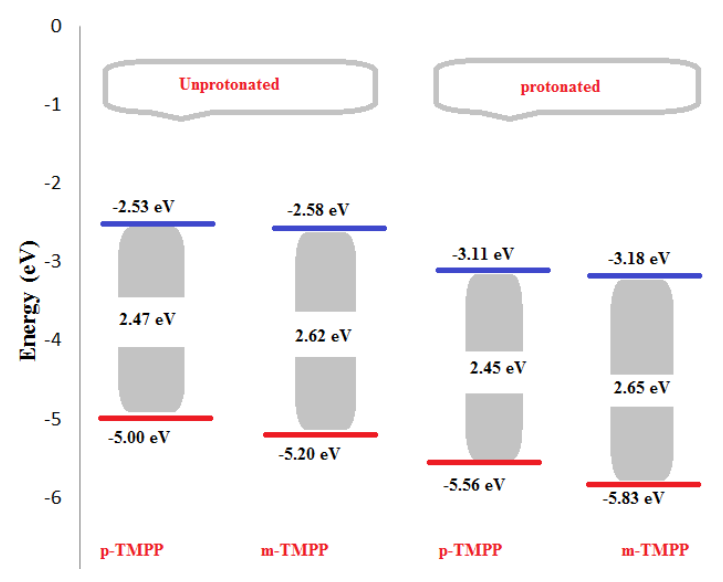


Figure 16. Frontier orbitals of m-TMPP and p-TMPP in unprotonated and protonated forms

The number of electrons transferred (ΔN) between the Cu surface and the inhibitor molecules m-TMPP and p-TMPP is a crucial indicator of how these molecules interact with the metal surface. According to Equation (7), the ΔN values represent the extent to which electrons are donated from the inhibitor molecules to the unoccupied 3d-orbitals of Cu, demonstrating their electron-donating capacity. As mentioned, positive ΔN values indicate that the inhibitors act as electron donors (or Lewis bases) [38]. Both m-TMPP and p-TMPP show positive ΔN values, which means they can donate electrons to the copper surface. This electron donation enhances the adsorption of the inhibitors on the copper surface, contributing to their ability to form a protective layer that inhibits corrosion. From Table 6, the ΔN values for m-TMPP and p-TMPP are 3.37 and 3.52 e, respectively. These values are less than 3.6 e, indicating moderate electron donation, but enough to create a strong interaction with the copper surface. The fact that p-TMPP has a slightly higher ΔN value than m-TMPP suggests that p-TMPP can transfer more electrons to the copper surface, making it a slightly more effective corrosion inhibitor.

Monte Carlo simulation

The adsorption of m-TMPP and p-TMPP on the Cu (111) surface was conducted to explore the interaction between the inhibitors and the copper surface. Figure 17 demonstrates the adsorption geometry of both molecules.

From the figure, it is evident that during the adsorption process, the inhibitors gradually approach the Cu (111) surface in a tilted orientation in the aqueous phase, with the phenyl methoxy groups pointing towards the copper surface. In the gas phase, both inhibitors adopt a parallel configuration, where the entire molecular plane aligns with the Cu (111) surface.

This specific orientation allows for increased surface coverage, as the phenyl methoxy groups enhance the adsorption of the molecules to the copper surface. The tilted configuration leads to a greater surface coverage compared to other orientations, which improves the overall inhibition efficiency (η). These findings align with previous discussions in this research, which suggest that better surface coverage leads to more effective corrosion protection. This interaction is also quantitatively illustrated in Table 7. The most stable configurations observed in the system are those associated with the lowest adsorption energies, indicating the most favourable adsorption interactions. The adsorption energy of p-TMPP is calculated to be -1120.73 kJ mol⁻¹, while m-TMPP

shows a slightly less negative adsorption energy of -1108.3 kJ mol⁻¹. These values indicate that both inhibitors have strong interactions with the surface, but p-TMPP demonstrates a stronger inhibitory efficiency due to its more negative adsorption energy.

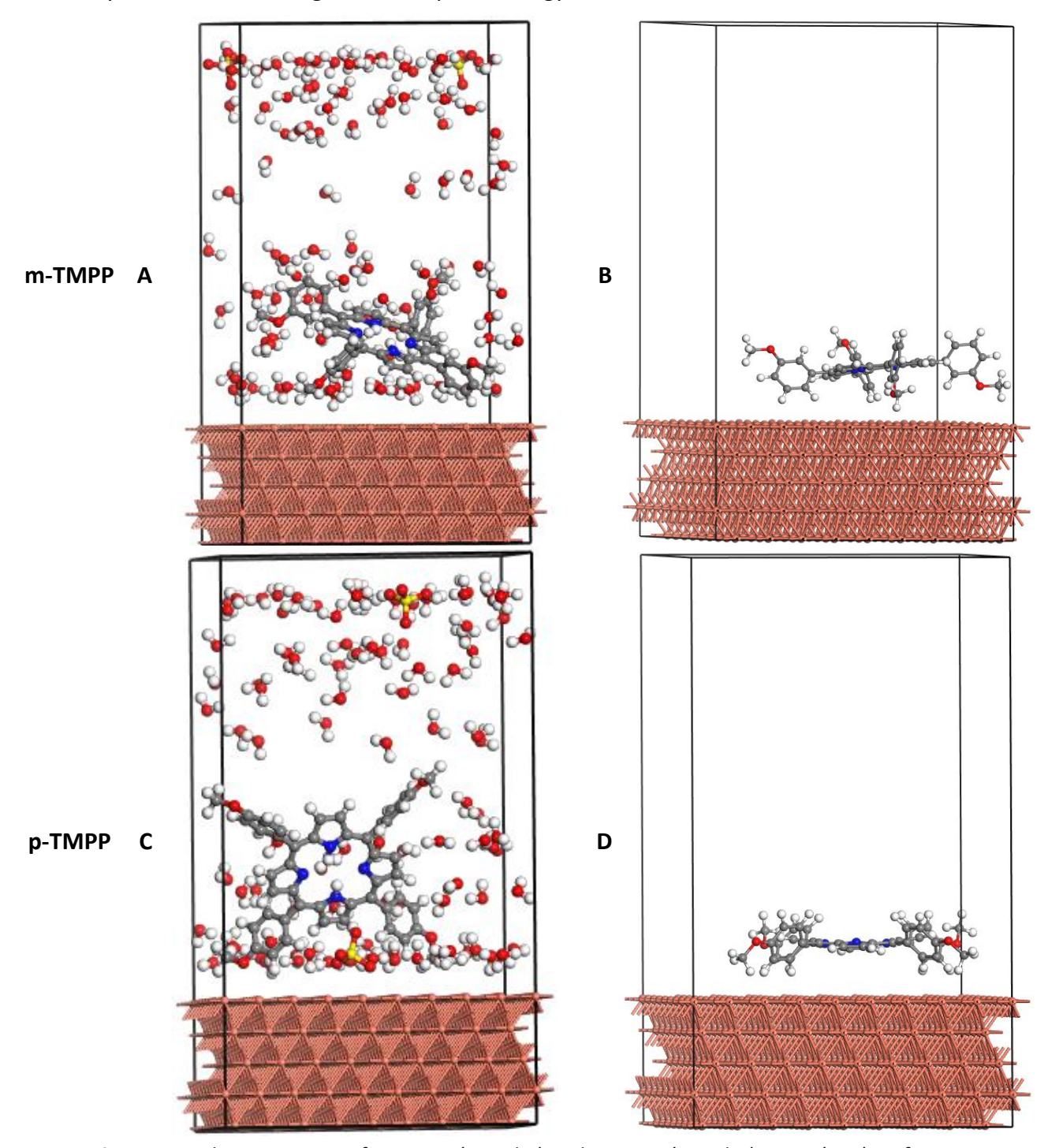


Figure 17. Adsorption view of m-TMPP (A and B) and p-TMPP (C and D) on Cu (111) surface in aqueous (A and C) and gas (B and D) media

Table 7. Adsorption energy for m-TMPP and p-TMPP inhibitors on Cu (111) surface

Phase	System	Adsorption energy, kJ mol ⁻¹
Varioone —	m-TMPP + Cu (111)	-1108.3
Aqueous —	p-TMPP + Cu (111)	-1120.73
Cos	m-TMPP + Cu (111)	-406.308
Gas —	p-TMPP + Cu (111)	-520.866

This observation supports the results previously discussed, confirming the enhanced ability of p-TMPP to adsorb onto and protect the surface, likely due to better surface coverage and stronger interaction with the Cu (111) surface. The higher magnitude of adsorption energies in the aqueous phase indicates stronger adsorption interactions compared to the gas phase. The solvation effects in water enhance the stabilization of the inhibitor-metal complex. Among the two, p-TMPP exhibits slightly stronger adsorption than m-TMPP, suggesting better inhibitor performance.

Comparison with previous studies

Table 8 compares the inhibition efficiency (η) due to m-TMPP and p-TMPP compounds with some other inhibitors used as corrosion inhibitors for copper and copper alloys in H₂SO₄ solution. All these inhibitors had a high percentage of inhibition efficiency due to their strong adsorption onto the copper surface.

Table 8. Comparison of the inhibition efficacy of m-TMPP and p-TMPP on copper alloy surface from the present work with some previous literature studies

Inhibitor	Substrate	Corrosive medium	Optimal inhibitor concentration	η / %	Ref.
Glycine, tyrosine, , valine	Cu	O ₂ -saturated 0.50 M H ₂ SO ₄	50 mM	98 for tyrosine, 91 for glycine and 75 for alanine and valine	[39]
Cauliflower extract	Cu	0.5 M H ₂ SO ₄	400 ppm	99.0	[40]
Montelukast sodium	Cu	0.5 M H ₂ SO ₄	50 ppm	99.0	[41]
Losartan potassium	Cu	0.5 M H ₂ SO ₄	40 ppm	94.9	[42]
Capsicum annuum L. leaf extract	Cu	0.5 M H ₂ SO ₄	500 ppm	93.9	[43]
m-TMPP	C12510 alloy	1.0 M H ₂ SO ₄	1 mM	96.23	Current
р-ТМРР	C12310 alloy	1.0 IVI H23O4	T IIIIVI	97.61	work

Conclusions

Two porphyrin molecules (m-TMPP and p-TMPP) provided efficient corrosion inhibition against copper alloy (C12510) in 1.0 M H₂SO₄ solution. Every technique (weight loss, potentiodynamic polarization, potentiodynamic anodic polarization, electrochemical impedance spectroscopy and Monte Carlo simulation) employed in the study confirmed the inhibitory potency of TMPP molecules. The inhibitory effectiveness of two TMPP molecules rose as their concentration increased and dropped with increasing temperature. The inhibitory mechanism was attributed to the spontaneous physicochemical adsorption of TMPP molecules onto the C12510 surface, as evidenced by the moderately high negative ΔG_{ads} values. According to the polarization data, these compounds exhibit mixed (cathodic and anodic) inhibitory action without affecting the corrosion mechanism. The adsorption of both inhibitor molecules matched Langmuir's isotherm properties. EIS approach demonstrated the charge transfer mechanism that governs metal dissolution (corrosion) reaction and the presence of the corrosion product layer on the copper alloy surface. In corrosive H₂SO₄ + NaCl solution, the TMPP molecules slowed the pitting corrosion, by shifting the pitting potential to a more noble direction. The inhibitory efficacy of p-TMPP is higher than m-TMPP at all concentrations tested. Also, this study highlights the utility of DFT and Monte Carlo simulations in evaluating the corrosion inhibition efficiency of organic inhibitors like m-TMPP and p-TMPP on copper surfaces. The results demonstrated that p-TMPP, with its higher dipole moment, lower HOMO-LUMO gap, and greater electron-donating ability, exhibits superior adsorption and interaction with the Cu (111) surface. This is further supported by the adsorption energies obtained from Monte Carlo simulations, where p-TMPP shows stronger interaction with the copper surface compared to m-TMPP.

Acknowledgment:The authors express their gratitude to Princess Nourah bint Abdulrahman University Researcher supporting project number (PNURSP2024R53). Princess Nourah bint Abdulrahman University, Riyadh, Saudi Arabia.

References

- [1] B. Tan, Y. Liu, Z. Gong, X. Zhang, J. Chen, L.-Guo, J.-Xiong, J.-Liu, R.-Marzouki, W.-Li, Pyracantha fortuneana alcohol extracts as biodegradable corrosion inhibitors for copper in H₂SO₄ media, *Journal of Molecular Liquids* **397** (2024) 124117. https://doi.org/10.1016/j.molliq.2024.124117
- [2] H. T. Hossein, M. G. Hosseini, Corrosion inhibition of copper in Sulphuric acid by some nitrogen heterocyclic compounds, *Anti-Corrosion Methods and Materials* **54** (2007) 308-313. https://doi.org/10.1108/00035590710822161
- [3] T. A. Farghaly, A. Fawzy, H. H. Alsharief, N. Alqarni, A. Al Bahir, S. M. Riyadh, Investigation of inhibition efficiencies of Novel *bis*-oxindole and *bis*(spiro(triazole-oxindole)) for the corrosion of copper in sulfuric acid medium, *Polycyclic Aromatic Compounds* **44** (2024) 1258-1272. https://doi.org/10.1080/10406638.2023.2191972
- [4] R. N. Felaly, M. Alfakeer, A. A. I. Ali, S. S. Al-Juaid, E. M. Mabrouk, A.Y. El-Etre, D. F. Seyam, M. Abdallah, Enhanced corrosion protection of copper alloy in 2.0 M HNO₃ solution using expired solo sept, slim-lax and well derm drugs, *International Journal of Electrochemical Science* **19** (2024) 100657. https://doi.org/10.1016/j.ijoes.2024.100657
- [5] A. S. Fouda, M. A. Ismail, M. A. Khaled, Experimental and computational chemical studies on the corrosion inhibition of new pyrimidinone derivatives for copper in nitric acid, *Scientific Reports* **12** (2022) 16089. https://doi.org/10.1038/s41598-022-20306-4
- [6] E. E. El-Katori, A. S. Abousalem, Impact of some pyrrolidinium ionic liquids on copper dissolution behavior in acidic environment: experimental, morphological and theoretical insights, *RSC advances* **9** (2019) 20760-2077. https://doi.org/10.1039/C9RA03603B
- [7] M. Abdallah, K.A. Soliman, M. Alshareef, A.S. Al-Gorair, H. Hawsawi, H.M. Altass, S.S. Al-Juaid, M.S. Motawea, Investigation of the anticorrosion and adsorption properties of two polymer compounds on the corrosion of SABIC iron in 1 M HCl solution by practical and computational approaches, RSC Advances 12 (2022) 20122–20137. https://doi.org/10.1039/D2RA03614B
- [8] M. Abdallah, M. Alfakeer, Mubark Alshareef, H. Hawsawi, Salih S. Al-Juaid, R.S. Abdel Hameed, M. Sobhi, Natural Sweet Almond Oil as an Effective Green Inhibitor for Aluminum Corrosion in Sulfuric Acid Medium, *International Journal of Electrochemical Science* **17** (2022) 220949. https://doi.org/10.20964/2022.09.18
- [9] A. Fouda, H. Abdel-Wahed, M. Atia, A. El-Hossiany, Novel porphyrin derivatives as corrosion inhibitors for stainless steel 304 in acidic environment: synthesis, electrochemical and quantum calculation studies, *Scientific Reports* 13 (2023) 17593. https://doi.org/10.1038/s41598-023-44873-2
- [10] A. Singh, Y. Lin, M. A. Quraishi, L. O. Olasunkanmi, O. E. Fayemi, Y. Sasikumar, B. Ramaganthan, I. Bahadur, I. B. Obot, A. S. Adekunle, Porphyrins as corrosion inhibitors for N80 steel in 3.5% NaCl solution: electrochemical, quantum chemical, QSAR and Monte Carlo simulations studies, *Molecules* 20 (2015) 15122-15146. https://doi.org/10.3390/molecules200815122

- [11] A. D. Adler, F. R. Longo, J. D. Finarelli, J. Goldmacher, J. Assour, L. Korsakoff, A simplified synthesis for meso-tetraphenylporphine, *The Journal of Organic Chemistry* **32** (1967) 476-476. https://doi.org/10.1021/jo01288a053
- [12] R. Dennington, T. A. Keith, J. M. Millam, GaussView 6.0. 16, Semichem Inc.: Shawnee Mission, KS, USA (2016) 143-150. https://gaussian.com/gaussview6/
- [13] A. S. Al-Gorair, T. Al-Habal, R. El-Sayed, S. S. Al- Juaid, R. S. Abdel Hameed, M. Abdallah, Investigations of non-ionic surfactants derived from triazoles and pyrroles as potent corrosion inhibitors for carbon steel in hydrochloric acid, *International Journal of Electrochemical Science* **18** (9) (2023) 100269. https://doi.org/10.1016/j.ijoes.2023.100269
- [14] A. D. Adler, F. R. Longo, W. Shergalis, Mechanistic Investigations of Porphyrin Syntheses. I. Preliminary Studies on *ms*-Tetraphenylporphin, *Journal of the American Chemical Society* **86** (1964) 3145-3149. https://doi.org/10.1021/ja01069a035
- [15] A. B. Nielsen, A. J. Holder, GaussView 5 Reference. Gaussian Inc., Pittsburgh, USA, 2009. https://chemistry4.me/Gaussian/G09W/gvref/gv5ref.pdf
- [16] M. J. Frisch, G. W. Trucks, H. B. Schlegel, G. E. Scuseria, M. A. Robb, J. R. Cheeseman, G. Scalmani, V. Barone, B. Mennucci, G. A. Petersson, H. Nakatsuji, M. Caricato, X. Li, H. P. Hratchian, A. F. Izmaylov, J. Bloino, G. Zheng, J. L. Sonnenberg, M. Hada, M. Ehara, K. Toyota, R. Fukuda, J. Hasegawa, M. Ishida, T. Nakajima, Y. Honda, O. Kitao, H. Nakai, T. Vreven, J. A. Montgomery, Jr., J. E. Peralta, F. Ogliaro, M. Bearpark, J. J. Heyd, E. Brothers, K. N. Kudin, V. N. Staroverov, R. Kobayashi, J. Normand, K. Raghavachari, A. Rendell, J. C. Burant, S. S. Iyengar, J. Tomasi, M. Cossi, N. Rega, J. M. Millam, M. Klene, J. E. Knox, J. B. Cross, V. Bakken, C. Adamo, J. Jaramillo, R. Gomperts, R. E. Stratmann, O. Yazyev, A. J. Austin, R. Cammi, C. Pomelli, J. W. Ochterski, R. L. Martin, K. Morokuma, V. G. Zakrzewski, G. A. Voth, P. Salvador, J. J. Dannenberg, S. Dapprich, A. D. Daniels, Ö. Farkas, J. B. Foresman, J. V. Ortiz, J. Cioslowski, D. J. Fox, Gaussian 09 Rev. D.01, Wallingford, CT (2009).
- [17] A. D. Becke, Density-functional exchange-energy approximation with correct asymptotic behavior, *Physical Review A* **38** (1988) 3098-3100. https://doi.org/10.1103/PhysRevA.38.3098
- [18] V. Barone, M. Cossi, Quantum Calculation of Molecular Energies and Energy Gradients in Solution by a Conductor Solvent Model, *The Journal of Physical Chemistry A* **102** (1998) 1995-2001. https://doi.org/10.1021/jp9716997
- [19] H. Bourzi, R. Oukhrib, B. El Ibrahimi, H. Abou Oualid, Y. Abdellaoui, B. Balkard, S. El Issami, M. Hilali, L. Bazzi, C. Len, Furfural Analogs as Sustainable Corrosion Inhibitors-Predictive Efficiency Using DFT and Monte Carlo Simulations on the Cu(111), Fe(110), Al(111) and Sn(111) Surfaces in Acid Media, *Sustainability* **12(8)** (2020) 3304. https://doi.org/10.3390/su12083304
- [20] H. Sun, P. Ren, J. Fried, The COMPASS force field: parameterization and validation for phosphazenes, Computational and Theoretical Polymer Science 8 (1998) 229-246. https://doi.org/10.1016/S1089-3156(98)00042-7
- [21] E. Echchihbi , R. Salim, M. Ouakki , M. Koudad , L. Guo , M. Azam, N. Benchat, Z. Rais, M. Taleb, Corrosion resistance assessment of copper, mild steel, and aluminum alloy 2024-T3 in acidic solution by a novel imidazothiazole derivative, *Materials Today Sustainability* **240** (2023) 100524. https://doi.org/10.1016/j.mtsust.2023.100524
- [22] M. Abdallah, Guar Gum as corrosion inhibitor for dissolution of carbon steel in NaCl solution, Portugaliae Electrochimica Acta 22 (2004) 161-175. https://doi.org/10.4152/pea.200402161
- [23] F. M. Abd El Wahab and A. M. Shams El Din, Effect of Gelatin on the Pitting Corrosion of Iron in Acid and Alkaline Solutions, *British Corrosion Journal* **13(1)** (1978) 39-44. https://doi.org/10.1179/000705978798358716



- [24] M. Abdallah, I. Zaafarany, K. S. Khairou, Y. Emad, Natural Oils as Corrosion Inhibitors for Stainless Steel in Sodium Hydroxide Solutions, *Chemistry and Technology of Fuels and Oils* **48(3)** (2012) 234-245. https://doi.org/10.1007/s10553-012-0364-x
- [25] M. Abdallah, K. A. Soliman, M. Alfakeer, A. M. Al-bonayan, M. T. Alotaibi, H. Hawsawi, O. A. Hazazi, R. S. Abdel Hameed, M. Sobhi, Mitigation effect of natural Lettuce oil on the corrosion of mild steel in sulfuric acid solution: Chemical, electrochemical, computational aspects, *Green Chemistry Letters and Reviews* 16(1) (2003) 2249019. https://doi.org/10.1080/17518253.2023.2249019
- [26] S. K. Gupta, R. K. Mehta, M. Yadav, O. Dagdag, V. Mehmeti, A. Berisha, E. E. Ebenso, Diazenyl derivatives as efficient corrosion inhibitors for mild steel in HCl medium: Gravimetric, electrochemical and computational approach, *Journal of Molecular Liquids* **382** (2023) 121976. https://doi.org/10.1016/j.molliq.2023.121976
- [27] M. R. Albayati, S. Kansız, H. Lgaz, S. Kaya, N. Dege, I. H. Ali, R. Salghi, I. Chung, Synthesis, experimental and theoretical characterization of (E)-2-((2,3-dimethylphenyl)amino)-N'- (furan-2-ylmethylene)benzohydrazide, *Journal of Molecular Structure* **1219** (2020) 128518. https://doi.org/10.1016/j.molstruc.2020.128518
- [28] J. Bessone, C. Mayer, K. Jüttner, W. J. Lorenz, AC-impedance measurements on aluminum barrier type oxide films, *Electrochimica Acta* **28** (1983) 171-175. https://doi.org/10.1016/0013-4686(83)85105-6
- [29] M. Abdallah, K. A. Soliman, R. Alfattani[,], A.S. Al-Gorair, A. Fawzy, M. A. A. Ibrahim, Insight of corrosion mitigation performance of SABIC iron in 0.5 M HCl Solutionby tryptophan and histidine: Experimental and computational approaches, *International Journal of Hydrogen Energy* **47(2)** (2022) 12782-12797. https://doi.org/10.1016/j.ijhydene.2022.02.007
- [30] S. K. Saha, A. Dutta, P. Ghosh, D. Sukul, P. Banerjee, Adsorption and corrosion inhibition effect of Schiff base molecules on the mild steel surface in 1 M HCl medium: a combined experimental and theoretical approach, *Physical Chemistry Chemical Physics* **17** (2015) 5679-5690. https://doi.org/10.1039/C4CP05614K
- [31] T. Gu, B. Tan, J. Liu, J. Chen, H. Wei, F. Zhang, N. Al-Zaqri, W. Li, Insight into the corrosion inhibition performance of Jasmine flower extract on copper in sulfuric acid medium using experimental and theoretical calculation methods, *Journal of Taiwan Institute of Chemical Engineers* **150** (2023) 105047. https://doi.org/10.1016/j.jtice.2023.105047
- [32] A.K. Singh, M.A. Quraishi, Inhibiting effects of 5-substituted isatin-based Mannich bases on the corrosion of mild steel in hydrochloric acid solution, *Journal of Applied Chemistry* **40** (2010) 1293-1306. https://doi.org/10.1007/s10800-010-0079-9
- [33] M.A. Hegazy, M. Abdallah, M. Alfakeer, H. Ahmed, Corrosion Inhibition Performance of a Novel Cationic Surfactant for protection of Carbon Steel Pipeline in Acidic Media, International Journal of Electrochemical Science 13 (2018) 6824-6842. https://doi.org/10.20964/2018.07.53
- [34] M. Prajila, A. Joseph, Controlling the Rate of Dissolution of Mild Steel in Sulfuric Acid Through the Adsorption and Inhibition Characteristics of (4-(4-Hydroxybenzylideneamino)-4H-1,2,4-Triazole-3,5-diyl)dimethanol (HATD), *Journal of Bio- and Tribo- Corrosion* **3** (2017) 10. https://doi.org/10.1007/s40735-016-0070-z
- [35] M. Abdallah, S. A. Ahmed, H. M. Altass, I. A. Zaafarany, M. Salem, A. I. Aly .E. M. Hussein, Competent inhibitor for the corrosion of zinc in hydrochloric acid based on 2,6-bis-[1-(2-phenylhydrazono)ethyl]pyridine, *Chemical Engineering Communications* **206(2)** (2019) 137-148. https://doi.org/10.1080/00986445.2018.1477761
- [36] M. Abdallah, T. Al-Habal, R. El-Sayed, M. I. Awad, R. S. Abdel Hameed, Corrosion control of carbon steel in acidic media by nonionic surfactant compounds derived from oxadiazole and

- thiadiazol, *International Journal of Electrochemical Science* **17** (2022) 221255. https://doi.org/10.20964/022.12.63
- [37] A. Soliz, P. P. Zamora, J. P. Muena, K. Bieger, J. Haribabu, E. Landaeta, A. Arulraj, R. V. Mangalaraja, Experimental and DFT analysis of the concentration dependency of corrosion inhibition by a pyridine Schiff base for mild steel in HCl solution, *Colloids and Surfaces A: Physicochemical and Engineering Aspects* 703 (2024) 135283. https://doi.org/10.1016/j.colsurfa.2024.135283
- [38] A. Berisha, F. Podvorica, V. Mehmeti, F. Syla, D. Vataj, Theoretical and experimental studies of the corrosion behavior of some thiazole derivatives toward MS in sulfuric acid media, *Macedonian Journal of Chemistry and Chemical Engineering* **34** (2015) 287-294. https://doi.org/10.20450/mjcce.2015.576
- [39] M. A. Amin, K. Khaled, Copper corrosion inhibition in O₂-saturated H₂SO₄ solutions, *Corrosion Science* **52** (2010) 1194-1204. https://doi.org/10.1016/j.corsci.2009.12.035
- [40] H. Li, S. Zhang, Y. Qiang, Corrosion retardation effect of a green cauliflower extract on copper in H₂SO₄ solution: Electrochemical and theoretical explorations, *Journal of Molecular Liquids* **321** (2021) 114450. https://doi.org/10.1016/j.molliq.2020.114450
- [41] B. Tan, S. Zhang, Y. Qiang, L. Feng, C. Liao, Y. Xu, S. Chen, Investigation of the inhibition effect of Montelukast Sodium on the copper corrosion in 0.5 mol/L H₂SO₄, *Journal of Molecular Liquids* **248** (2017) 902-910.https://doi.org/10.1016/j.molliq.2017.10.111
- [42] H. Li, S. Zhang, B. Tan, Y. Qiang, W. Li, S. Chen, L. Guo, Investigation of Losartan Potassium as an eco-friendly corrosion inhibitor for copper in 0.5 M H₂SO₄, *Journal of Molecular Liquids* **305** (2020) 112789. https://doi.org/10.1016/j.molliq.2020.112789
- [43] P. Hu, P. Cheng, Y. Wu, L. Guo, A. A. AlObaid, Insight into the corrosion inhibition performance of Capsicum annuum L. leaf extract as corrosion inhibitor for copper in sulfuric acid medium, *Journal of the Taiwan Institute of Chemical Engineers* **161** (2024) 105558. https://doi.org/10.1016/j.jtice.2024.105558

© 2025 by the authors; licensee IAPC, Zagreb, Croatia. This article is an open-access article distributed under the terms and conditions of the Creative Commons Attribution license (https://creativecommons.org/licenses/by/4.0/)



Open Access :: ISSN 1847-9286 www.jESE-online.org

Original scientific paper

Pyrazolone derivatives as corrosion inhibitors of copper in sulfuric acid solution

Rehab E. Azooz^{1,⊠}, Salah M. Abd El-Haleem² and Ahmed Diab²

¹Department of Physical Sciences, Chemistry Division, College of Science, Jazan University, P.O. Box. 114, Jazan 45142, Kingdom of Saudi Arabia

²Chemistry Department, Faculty of Science, Zagazig University, Zagazig, Egypt

Corresponding author: [™] <u>rramadan@jazanu.edu.sa</u>; Tel.: +966 532324115

Received: December 27, 2024; Accepted: February 5, 2025; Published: February 14, 2025

Abstract

This study examines the corrosion inhibition of copper in aerated H_2SO_4 solution using 5-methyl, 5-phenyl, and 5-methyl-2-phenyl derivatives of 2,4-dihydro-3H-pyrazol-3-one (Py) through electrochemical techniques, gravimetric method, SEM, DFT and Monte Carlo simulation. The results showed that these compounds exhibited good inhibition efficiency, increasing in the order: Py II (84.9 %) < Py III (87.9 %) < Py I (90.1 %) at 10 mM. The protection efficiency improved with higher inhibitor concentration and decreased with rising temperature. Thermodynamic parameters for the inhibition process were calculated, with ΔH_{ads}^0 values of -17.76±0.607, -15.8±0.101 and -16.24±0.118 kJ mol⁻¹ for Py I, Py II and Py III, respectively, confirming the exothermic nature of adsorption. The adsorption followed the Langmuir isotherm and occurred physically and spontaneously. Monte Carlo simulations indicated that PYs adsorbed in a parallel configuration, provide better coverage of the metal surface with high adsorption energy. SEM confirmed formation of a protective layer. Based on experimental and theoretical data, pyrazolone derivatives are recommended as corrosion inhibitors for copper in H₂SO₄ media.

Keywords

Metal corrosion; pyrazole compounds; inhibition efficiency; adsorption isotherm; DFT calculations; molecular dynamics simulations

Introduction

Owing to its favorable properties like high electrical and thermal conductivity, mechanical workability, malleability and resistance to atmospheric and chemical agents, copper is used in a wide range of industrial applications [1,2]. One of the most important applications of copper are industrial applications equipment, marine industry, power stations, coinages, electricity and desalination plants, heat exchanges and cooling power [3,4]. Despite its relatively noble character, copper dissolves in severe industrial environments like oxidizing acids e.g. HNO₃ and H₂SO₄. It also dissolves in acidic environments containing chloride, sulphates and nitrates [5,6] .

Because it is a stronger acid, generally more stable and safer to handle in a variety of industrial processes, sulfuric acid (H_2SO_4) is frequently used in corrosion studies instead of hydrochloric acid (HCl). It also has a higher degree of ionization, which can be helpful in reactions that require a strong acidic environment, and strong dehydrating properties that make it useful in reactions where water removal is crucial. Because it is less volatile than hydrochloric acid, which reduces the likelihood of hazardous vapors, it is a more versatile choice. It is also widely used in a variety of applications, including the production of detergents, dyes, and fertilizers.

As a result of the widespread use of copper within industrial acidic media, several studies were carried out using organic and inorganic materials as copper-based inhibitors. Aromatic compounds like amines and their derivatives containing a nitrogen atom that facilitates their adsorption on the metal surface and the formation of a protective barrier have been used extensively as organic corrosion inhibitors in acidic media [7]. Additionally, several investigations using organic compounds with 5-membered rings containing heteroatoms like oxygen, nitrogen, and sulfur were used to inhibit copper corrosion [8]. Copper corrosion has been observed to be inhibited in acidic environments by azoles and related derivatives. These compounds exhibit a remarkable inhibition efficiency due to their abundant donor atoms. The adsorption of these compounds frequently follows the Langmuir isotherm [9].

Pyrazole compounds are non-toxic, inexpensive and considered as a green and environmentally friendly inhibitor. They include functional groups like N, O, and pyrazolone rings. Their inhibitory action for copper and mild steel was explained using a range of methodologies, including electrochemical methods and weight loss assessments [10]. The mode of action of these compounds depends on their adsorption onto the metal surface. Lgaz *et al.* [11,12] used pyrazoline derivatives to inhibit mild steel corrosion in HCl solution. These compounds behave as mixed-type inhibitors and their adsorption obeys the Langmuir adsorption isotherm. On the other hand, Chaouiki *et al.* [13], used 2-(4-(3-phenyl-4,5-dihydro-1Hpyrazol-5-yl)phenoxy) acetic acid to inhibit the corrosion of mild steel in HCl solution using various techniques. The experimental results revealed that the studied compound gave a maximum inhibition efficiency of 87 % and the inhibition ability increased with raising of the inhibitor concentration. Computational calculations such as density functional theory (DFT) and molecular dynamic (MD) simulations correlate well with electrochemical parameters obtained.

The present investigation is concerned with the use of some pyrazolone derivatives as corrosion inhibitors for copper corrosion in H_2SO_4 using polarization and gravimetric methods. The investigation focused on the impact of inhibitor concentration, temperature, and duration immersion on the corrosion rate. The thermodynamic parameters associated with the inhibition process were computed. MD and DFT studies were performed to follow the adsorption configuration, adsorption energy, and quantum chemical descriptors. Upon integration of the experiment findings, the molecular-level mechanism of inhibitors surface adsorption could be elucidated, together with critical variables influencing the inhibitory performance.

Experimental

Experiments were carried out on copper sheets and/or rods with the following composition: 0.027 wt.% Ni, 0.067 wt.% Zn, 0.006 wt.% Se, and the remainder Cu 99.90 wt.%.

Solutions

Electrolyte solutions were prepared using analytical grade reagents and triple distilled water. H_2SO_4 solutions (BHD grade) with completely different concentrations were prepared. Figure 1

displays chemical configurations of the pyrazolone derivatives. The concentration range of the pyrazolone compounds (inhibitors) (Analytical grade purchased from Al-Gomhoria Company, Egypt and have high solubility in acidic medium) used was between 0.1 and 10 mM. The measurements were validated at 25±0.1 °C. The cell temperature was controlled with an ultra-thermostat from Polyscience (USA).

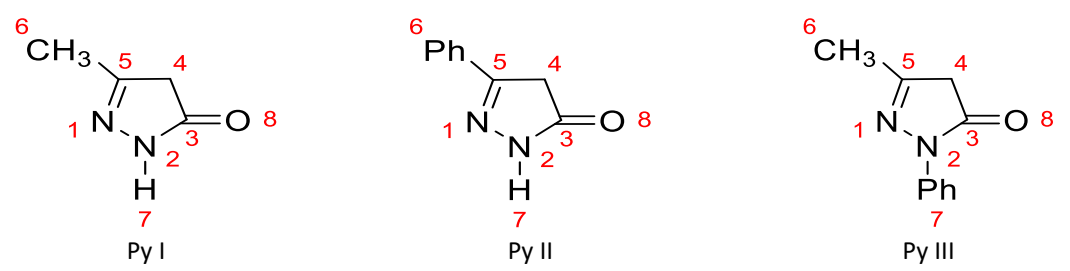


Figure 1. Chemical configurations of pyrazolone derivatives

Weight loss measurements

Five parallel copper sheets measuring $5.0\times2.0\times0.2$ cm were abraded with emery paper (grades 320–500–800) and then washed with demineralized water and dried with acetone After accurate weighing, the specimens were completely buried in a beaker containing 250 ml of the tested solution (sulfuric acid) without or with pyrazolone derivatives in varying concentrations. Following the appropriate immersion period, the specimens were pulled out, cleaned, dried, and precisely weighed. The average weight loss of five parallel copper sheets was obtained. The inhibitory efficiency (IE) and the surface coverage (θ) of pyrazolone compounds for the copper inhibition were calculated (equation 1) as follows [10]:

IE =
$$100 \theta = 100 (W^0 - W)/W^0$$
 (1)

where W^0 and W stand for the average weight loss for the free acid solution and in the presence of pyrazolone compounds, respectively.

Polarization measurements

In this section, testing was carried out in a cell with three openings: one for a standard reference electrode (SCE), one for a Pt counter electrode, and one for the working electrode. Using epoxy adhesive, the working electrode, a 0.350 cm diameter copper rod was inserted into a salt glass pipe, revealing 0.785 cm². A dense copper wire attached to the copper bar that was not in touch with the solution was used to create electrical connections. Using a Jean Wirtz TG 200 grinding machine, the metal conductor was consistently surface-prepared with successive 0-, 00-, and 000-grade sandpaper papers before use. It was then flushed with a solvent, cleaned with distilled water, and submerged in the solution.

The scanning rate used for all potentiodynamic polarization tests was 5 mV s⁻¹. By extrapolating the anodic and cathodic Tafel lines to obtain log i_{corr} the Stern-Geary method was utilized to quantify the corrosion current (i_{corr}) and the related corrosion potential (E_{corr}) for the tested solutions. The inhibition efficiency (IE) and surface coverage (θ) were then determined using the corrosion current density (i_{corr}), as shown by Equation 2 [10]:

$$IE = \left| 1 - \frac{i_{\text{corr(inh)}}}{i_{\text{corr(free)}}} \right| 100 = 100 \theta$$
 (2)

where, $i_{\text{corr (free)}}$ and $i_{\text{corr (inh)}}$ are corrosion current densities without and with pyrazolone compound solutions, respectively.

Computational study

Optimizing geometry for pyrazolone derivatives

All used pyrazolones were drawn using Chem-Draw 19.1 as portrayed in Figure 1, then uploaded to Gaussian 09, using density functional theory (DFT) based on the 6-31G basis set and B3LYP method as the level of theory to calculate energetic behavior and quantitative chemical descriptors. The most used quantum mechanical molecular descriptors include the highest occupied molecular orbital energy (E_{HOMO}) lowest unoccupied molecular orbital energy (E_{LUMO}), energy gap (E_{gap}), ionization potential (I), electron affinity (I), global hardness (I), global softness (I), absolute electrophilicity index (I), global electronegativity (I) and dipole moment (I). Where I0 and I1 were calculated from I1 and I2 were calculated from I3 and I4 were calculated from I4 and I5 and I6 and I7 and I8 and I8 are calculated from I8 and I9 and I1 and I9 and I1 and I1 are calculated from I1 and I2 and I3 are calculated from I3 and I4 are calculated from I4 and I5 are calculated from I6 and I8 are calculated from I8 and I9 are calculated from I9 and I1 are calculated from I9 and I1 are calculated from I9 and I1 are calculated from I1 and I1 are calculated from I1 and I3 are calculated from I3 and I4 are calculated from I4 and I5 are calculated from I6 and I8 are calculated from I8 are calculated from I8 are calculated from I8 and I9 are calculated from I9 and I1 are calculated from I1 and I1 are calculated from I1 and I2 are calculated from I3 and I4 are calculated from I4 and I5 are calculated from I6 and I6 are calculated from I8 are calculated from I8 and I9 are calculated from I9 and I9 are calculated from I9 and I9 are calculated from I9 are calculated from I9 and I9 are calculated from I9 are calculated from

$$E_{gap} = E_{LUMO} - E_{HOMO}$$
 (3)

$$I = -E_{\text{HOMO}} \tag{4}$$

$$A = -E_{\text{LUMO}} \tag{5}$$

Both I and A values are exploited to obtain χ and η of the inhibitory molecule [14] from Equations (6 and 7):

$$\chi = \frac{1}{2} (I + A) = \frac{1}{2} (E_{\text{LUMO}} + E_{\text{HOMO}})$$
 (6)

$$\eta = \frac{1}{2} (I - A) = \frac{1}{2} (E_{\text{LUMO}} - E_{\text{HOMO}})$$
 (7)

To compute the transferred fraction of electrons (ΔN), equation (8) [14], It is assumed that Cu_{bulk} atoms are softer than neutral Cu atoms, with a value of 4.48 eV/mol [15]. Additionally η_{Cu} is assumed to be 0 eV/mol. Considering that for a Cu_{bulk}, I = A [16]. Equation (8) can be expressed as follows

$$\Delta N = \frac{1}{2} \left(\frac{\chi_{\text{Cu}} - \chi_{\text{inh}}}{\eta_{\text{cu}} + \eta_{\text{inh}}} \right) \tag{8}$$

The formulas for the calculation of several descriptors mentioned are given by Equations (9) and (10) [17]:

$$\sigma = \frac{1}{\eta} \tag{9}$$

$$\omega = \frac{\chi^2}{2\eta} \tag{10}$$

The optimization process using the DMol3 module in BIOVIA Material Studio software was employed to determine the condensed Fukui function. This function is identified as the first derivative of electron density, $\rho(r)$, in proportion to the number of electrons, N, at a fixed external potential $\nu(r)$, which illustrates how a molecule changes electron density at a specific position as the counts of electrons vary [18,19]. Fukui indices (f_k^+, f_k^-) and f_k^0 are helpful to investigate the molecule responsiveness calculated from equations (11) to (15):

$$f(r) = \frac{\partial \rho(r)}{\partial N} \int_{\nu(r)}^{\nu(r)} dr$$

$$f_k^+ = [r_k(N) - r_k(N-1)]$$
 for nucleophilic attack (12)

$$f_{k} = [r_{k}(N+1) - r_{k}(N)]$$
 for electrophilic attack (13)

$$f_k^0 = 1/2 [r_k(N+1) - r_k(N-1)]$$
 for radical attack (14)

$$Df(k) = f_{k}^{+} - f_{k}^{-} \tag{15}$$

where for site k, the electronic densities of anionic, neutral, and cationic species are $r_k(N+1)$, $r_k(N)$ and $r_k(N-1)$ respectively. Df(k) is the dual descriptor, where, its positive and negative signs refer to

electrophilic species and nucleophilic species respectively. Sites with the highest probability of experiencing nucleophilic and electrophilic assaults are verified by the highest values of f_k^+ and f_k^- , respectively [20].

Molecular dynamic simulation

Although each orientation of Cu has unique benefits depending on its intended purpose, $Cu_{(111)}$ is widely utilized because of its stability and beneficial surface properties. Electrical and catalytic characteristics of copper surfaces are often studied, and different crystal orientations exhibit a variety of characteristics. Since $Cu_{(111)}$ is often copper's lowest energy face, its surface characteristics may be more consistent and distinct. Because it is typically more stable and less reactive than $Cu_{(110)}$ and $Cu_{(100)}$ surfaces, it is also less prone to reconstruction or surface flaws. The closely packed $Cu_{(111)}$ surface and its electrical characterization allow for better adsorption of some molecules, which may be useful in corrosion and catalytic processes [21].

Pure $Cu_{(111)}$ was enlarged to supercell to offer an extensive surface for the interaction with each inhibitor. The MD run in a 5×5 supercell featuring the force field of COMPASS, A temporal step of 1 fs, and an imitation period of 500 ps in a container of $(1.28 \times 1.28 \times 2.54 \text{ nm}^3)$ in even temperature of 303 K was employed with the Materials studio package.

Results and discussion

Weight-loss measurements

Effect of sulfuric acid concentration

When copper was soaked in a sulfuric acid solution, it became at risk of corrosion. The following equations (18) to (21) can be used to illustrate the different stages of the copper's dissolving reaction in the sulfuric acid solution [22,23]:

$$Cu \rightarrow Cu^{2+} + 2e^{-} \tag{18}$$

This reaction can be displayed in two steps, each involving one electron:

Step 1:
$$Cu \leftrightarrow Cu^+ + e^-$$
 (19)

Step 2:
$$Cu^+ \rightarrow Cu^{2+} + e$$
 (20)

where step 1 lies under equilibrium conditions and step 2 is the slower step in the sequence of the reaction, *i.e.* the copper dissolution is an activation-controlled process. In naturally aerated acid solutions, the rate-determining step during dissolution of copper is oxidation of (Cu⁺) [24]:

$$Cu^+ + 2H^+ + 1/2 O_2 \rightarrow Cu^{2+} + H_2O$$
 (21)

Equation (21) suggests that copper-anodic dissolution in naturally aerated acid solutions is an activation-controlled process. Gravimetric measurements were performed for copper specimens immersed through 10 to 60 hours of immersion time at 25 °C in different concentrations, ranging from 0.1 to 0.5 M H_2SO_4 . The weight loss variation for copper coupons in 250 ml of varying H_2SO_4 concentrations at 25 °C is shown in Figure 2 as a function of immersion time, where straight lines were obtained as results.

Figure 3 displays the plot of the log (weight loss) against the duration of immersion time to track the kinetics of the dissolution reaction of copper species at various sulfuric acid concentrations at 25 °C This figure shows straight-line correlations that indicate a first-order reaction for copper corrosion in sulfuric acid. The first-order rate law (Equation 22) was used to get the values of the rate constant (k) [25].

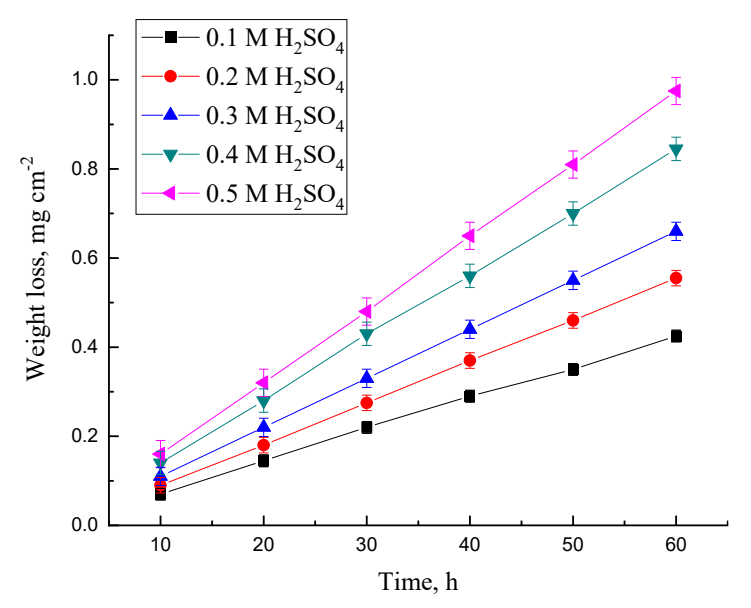


Figure 2. Variation of weight loss of copper with immersion time in different concentrations of H_2SO_4 solution at 25 °C

$$k = \frac{2.303}{t} \log W \tag{22}$$

where W is the weight loss of Cu after a period (t). From the parallel straight lines of Figure 3, the values of the slopes were calculated. By substituting these values in Equation (22), the rate constant (k) was calculated to be 3.915x10-3 h⁻¹ The half-life ($t_{1/2}$) was obtained by Equation (23) [25]:

$$t_{1/2} = \frac{0.693}{k} \tag{23}$$

Substituting the values of k into Equation (23), half-life time ($t_{1/2}$) for the copper dissolution process was found to be equal to 177 hours.

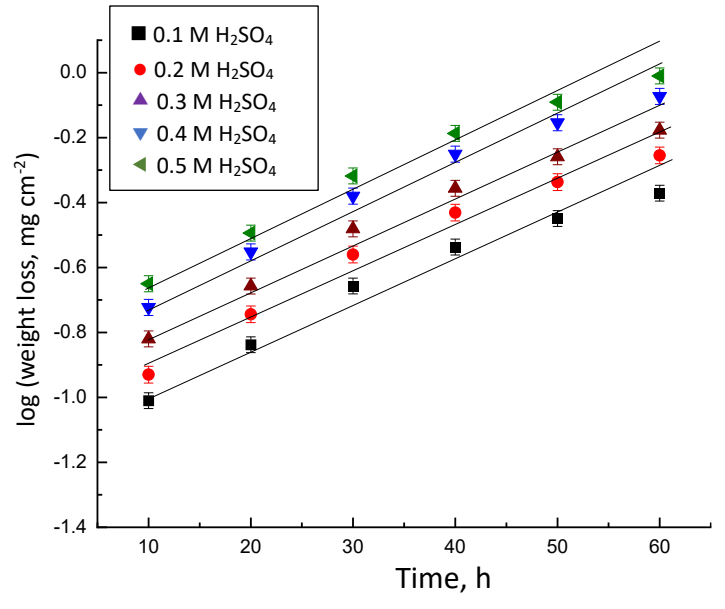


Figure 3. Log of weight loss versus immersion time for copper in different concentrations of sulfuric acid at 25 °C

Effect of temperature

The impact of raising the temperature from 25 to 55 °C on the copper corrosion rate in a naturally aerated 0.5 M H_2SO_4 solution is further investigated. The fluctuation of W for copper dissolution in 0.5 M H_2SO_4 solution at varying temperatures is shown in Figure 4 concerning immersion time (t).

The straight lines in Figure 4 demonstrate that as the temperature rises, the rate of corrosion of copper is markedly increased.

The Arrhenius equation (Equation (24)) can be used to express how temperature affects the rate of copper corrosion (r) [10]:

$$\log r = \text{constant} + \frac{\Delta E_{\text{a}}}{2.303RT} \tag{24}$$

where r is the corrosion rate, ΔH_{ads} is the activation energy of the corrosion reaction, T is the absolute temperature, and R is the universal gas constant. The Arrhenius plots for the copper corrosion rate in 0.5 M H₂SO₄ are displayed in Figure 5 (after 10 h of immersion). These findings produce a straight line with the slope from which the activation energy (ΔH_{ads}) can be determined. It was found that ΔH_{ads} equals 12.16 kJ mol⁻¹.

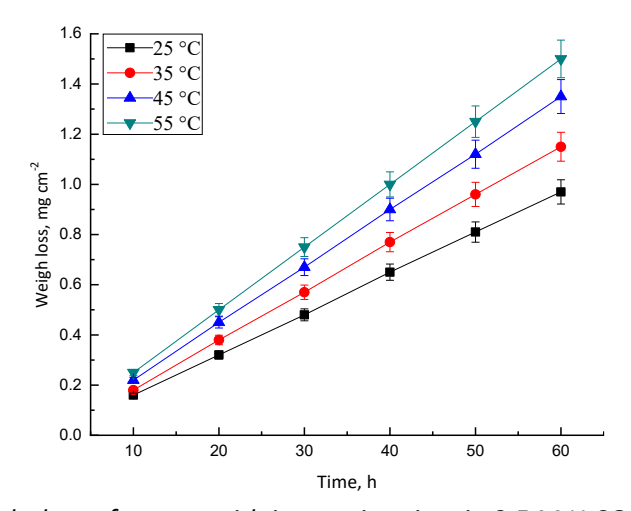


Figure 4. Variation of weight loss of copper with immersion time in 0.5 M H₂SO₄ at different temperatures

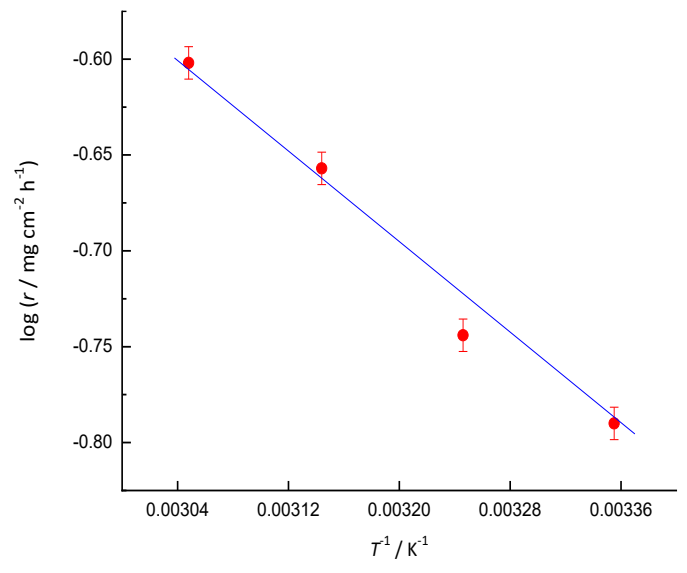


Figure 5. Arrhenius plot of corrosion rate against T⁻¹ for copper in 0.5 M H₂SO₄ after immersion time of 10 h

Effect of addition of pyrazolone derivatives

In the present part of this work, it was of interest to highlight the effect of some pyrazolone derivatives as inhibitors for the corrosion of copper in $0.5 \, M \, H_2 SO_4$ acid solution. Increasing concentrations of Py I, Py II and Py III were used to inhibit the corrosion of copper in $0.5 \, M \, H_2 SO_4$. Figure 6 represents the variation of weight loss of copper with immersion time in $0.5 \, M \, H_2 SO_4$ at increasing concentrations of Py at $25 \, ^{\circ}C$ (similar curves are obtained for other pyrazolone derivatives.).

Inspection of the curves of Figure 6, the values of weight loss of copper was decreased with increasing the concentrations of PY I. The curves of Figure 7 represent the variation of the weight loss of copper with immersion time at adjusted concentration of pyrazolone derivatives as 10 mM in 0.5 M H_2SO_4 at 25 °C.

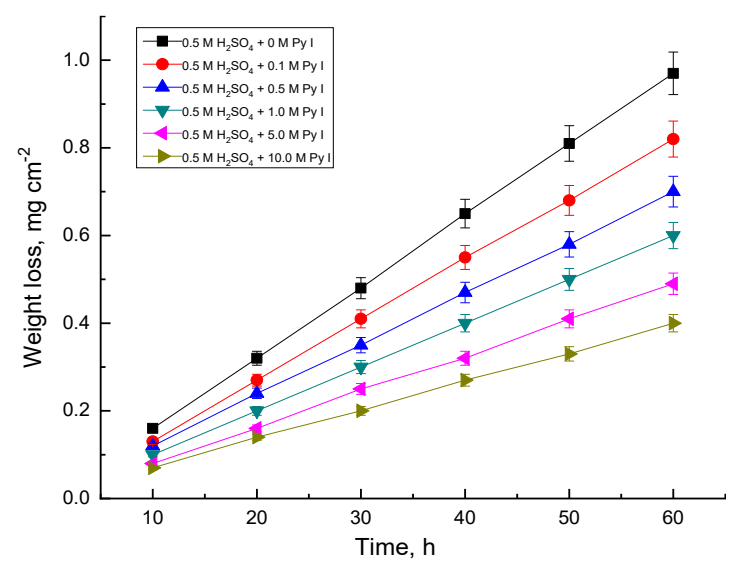


Figure 6. Variation of weight loss of copper with immersion time in 0.05 M H₂SO₄ without and with increasing concentrations of Py I at 25 °C

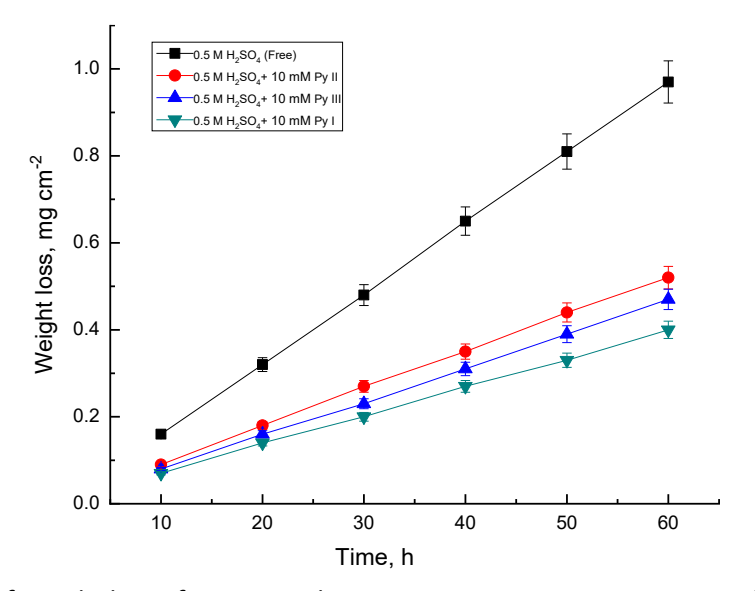


Figure 7. Variation of weight loss of copper with immersion time at 0.5 M H₂SO₄ without and with 10 mM concentration of three pyrazolone derivatives at 25 °C

This behavior could be attributed to the inhibiting effects of these compounds which retard the dissolution process and assist the inhibition process. It is clear from the curves of Figure 7 that the lowest values in the loss in weight for copper species dissolution in $0.5M~H_2SO_4$ occurs in presence of Py I than the other additives. Further inspection of Figure 7 indicates that the inhibition efficiency of these compounds increased in the following order: (low inhibition) Py II < Py III < Py I (high inhibition).

The action of the used pyrazolone additives as corrosion-inhibiting compounds could be detected from the values of the inhibition efficiency (IE) equation (25) for each additive which is defined by the following equation [10]:

$$IE = 1 - (W/W_0)100$$
 (25)

where W_0 and W are the weight loss in the absence and presence of inhibiting compounds, respecttively. The values of IE for the inhibiting compounds used (after 10 hours) can be seen in Table 1, which reveals the following conclusions to be drawn:

- IE of each inhibitor increases with increasing its concentration.
- At the concentration of the same additive, IE increases in the following order: Py II < Py III < Py I

Table 1. Variation of inhibition efficiencies of copper immersed in 0.5 M H_2SO_4 for 10 hours using various doses of pyrazolone derivatives, at 25°C

- / mN4		IE, %					
c_{Py} / mM	Pyl	PyII	PyIII				
0.1	19	6	13				
0.5	25	13	19				
1.0	38	25	31				
5.0	50	38	44				
10.0	57	44	50				

Polarization measurements

Potentiodynamic polarization behavior of the copper electrode in 0.1 to 0.5 M sulfuric acid at 25 °C, is illustrated in Figure 8. Inspection of the curves of Figure 8 reveals that on increasing the concentration of H_2SO_4 , shifts the anodic polarization curves to a more active direction, while the cathodic polarization curves shift to a more anodic direction.

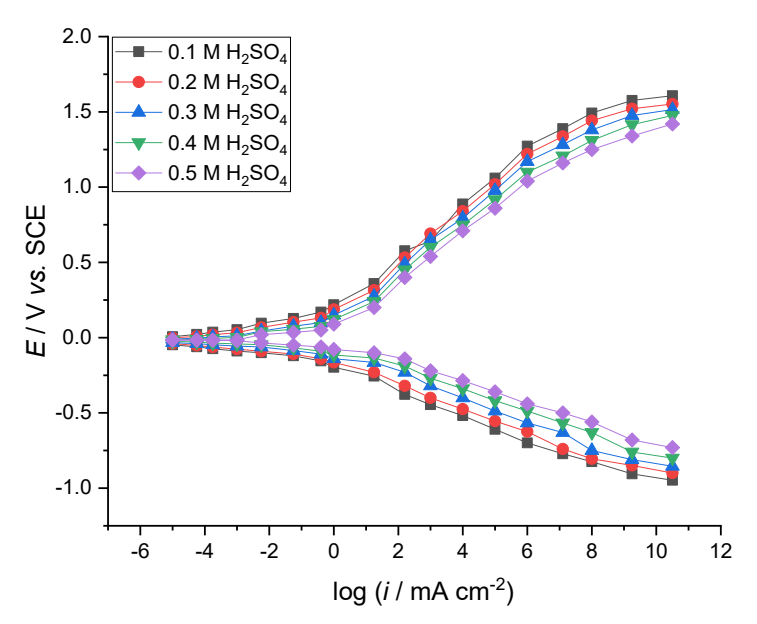


Figure 8. Potentiodynamic polarization curves of the copper electrode in various concentrations of H_2SO_4 solution at 25 °C and scanning rate 5 mV s^{-1}

The numerical values of the variation of corrosion current density (i_{corr}), corrosion potential (E_{corr}), and Tafel slopes (β_a and β_c), with the changing sulfuric concentrations are provided in Table 2. The polarization resistance was obtained from the Stern-Geary equation [26] and the corrosion rate of copper was determined from Equation (26) [27]:

Corrosion rate =
$$0.1288 i_{\text{corr}} \frac{w_{\text{eq}}}{D}$$
 (26)

where w_{eq} = 31.8 is the equivalent weight of metal (working electrode) and D = 8.96 g cm⁻³ is the density of metal. The computed data derived from Figure 8 and Table 2 show that Tafel-type

behavior is shown by the both cathodic and anodic curves. The anodic and cathodic polarization curves change to more active and noble directions, respectively, as the concentrations of H_2SO_4 increase. The values of i_{corr} increase, E_{corr} shifts to more active directions, R decrease, and the rates of corrosion increase. This trend indicates that when the concentration of sulfuric acid solution increases, copper electrode dissolution increased markedly and readily.

Table 2. Kinetic parameters of Cu electrode in various concentrations of H_2SO_4 solution at 25°C, as calculated from Figure 8 and Equation (26)

$c_{\rm H_2SO_4}$ / M	Corrosion rate, mm year ⁻¹	-E _{corr} /mV vs. SCE	$I_{\rm corr}$ / mA cm ⁻²	$eta_{\rm a}$ / mV dec $^{ ext{-}1}$	$\beta_{\rm c}$ / mV dec ⁻¹	$R_{\rm p}/{\rm k}\Omega$
0.1	0.005	19.8	0.013	239.3	-146.3	3.032
0.2	0.009	30.7	0.021	227.4	-128.8	1.701
0.3	0.027	36.2	0.062	213.5	-111.4	0.513
0.4	0.091	42.8	0.211	202.6	88.5	0.138
0.5	0.287	48.6	0.631	194.8	100.3	0.042

Figure 9 shows the impact of adding progressively higher concentrations of Py I (one of the evaluated pyrazolone derivatives) on the electrochemical behavior of copper in 0.5 M H_2SO_4 . Table 3 contains the electrochemical characteristics that were determined for the investigated pyrazolone derivatives, including E_{corr} , Tafel slopes (β_c and β_a), corrosion rates, and i_{corr} values.

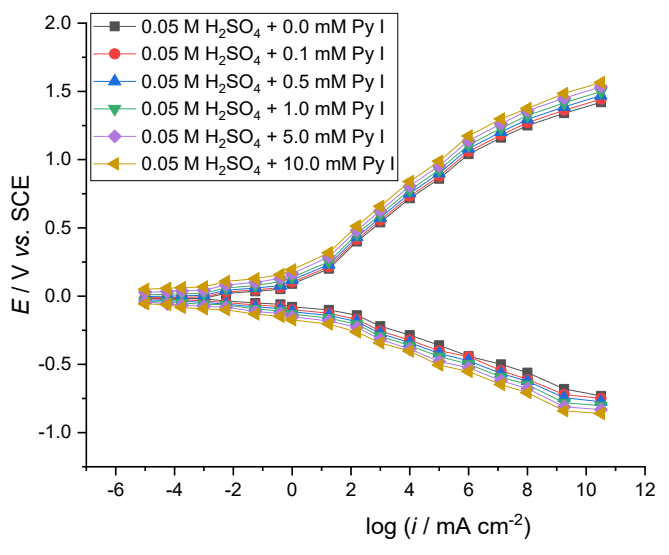


Figure 9. Potentiodynamic polarization patterns of the copper electrode in 0.5 M H_2SO_4 solution without and with increasing concentrations of Py I at 25 °C and scanning rate 5 mV s^{-1}

Examining the data in Figure 9 and Table 3 indicates that when the concentration of these additives increases, the corrosion potential (E_{corr}) of copper shifts towards more positive potentials, leading to increased adsorption on the copper surface [28]. The values of the corrosion rates decreased upon increasing the concentrations of added pyrazolone compounds. This behavior demonstrated the high inhibitory activity of these pyrazolones. Figure 10 represents Tafel-plots for copper electrode in 0.5 M H_2SO_4 in the absence and presence of different Py concentrations, the order of increasing IE is: (lower inhibition) Py II < Py III< Py I (higher inhibition). This is in good agreement with the behavior resulting from weight loss measurements and confirms the ability of those inhibitors to reduce corrosion of Cu in 0.5 M H_2SO_4 as compared to other derivatives listed in Table 4.

Table 3. Kinetic parameters for the inhibition of copper corrosion in 0.5 M H_2SO_4 without and with increasing pyrazolone derivative concentrations at 25 °C and computed using Equation 26 and Figure 10

c_{Py}/mM	Pyrazolone	Corrosion rate,	- E _{corr} /	I _{corr} /	$eta_{\!\scriptscriptstyle a}$ /	$eta_{ m c}$ /	$R_p/k\Omega$	θ	IE, %
CPy/ IIIIVI	derivate	mm year ⁻¹	mV (SCE)	mA cm ⁻²	mV dec ⁻¹	mV dec ⁻¹	Пр/ К52	U	11, 70
0.00	-	0.287±0.03	48.6	0.631	194.8	-88.5	0.042	-	-
0.11	_	0.181±0.05	36.6	0.398	204.2	-106.2	0.076	0.369	36.9
0.15	_	0.114±0.05	28.7	0.251	213.8	-119.7	0.133	0.602	60.2
1.00	Py I	0.072±0.05	17.4	0.158	227.6	-127.1	0.224	0.749	74.9
5.00	•	0.046±0.05	11.2	0.102	231.1	-138.5	0.368	0.838	83.8
10.00	•	0.028±0.05	5.5	0.063	238.7	-143.6	0.617	0.901	90.1
0.11	_	0.256±0.07	44.2	0.562	198.3	-92.7	0.049	0.109	10.9
0.15	_	0.162±0.07	39.8	0.355	207.4	-99.3	0.082	0.469	46.9
1.00	Py II	0.102±0.07	33.2	0.224	213.6	-106.4	0.138	0.645	64.5
5.00	•	0.064±0.07	25.3	0.141	221.8	-117.5	0.237	0.776	77.6
10.00	•	0.043±0.07	18.7	0.095	225.2	-124.3	0.366	0.849	84.9
0.11		0.218±0.06	41.3	0.478	199.8	-99.8	0.060	0.242	24.2
0.15		0.138±0.06	34.5	0.302	210.2	-111.2	0.105	0.521	52.1
1.00	Py III	0.087±0.06	26.4	0.191	219.5	-121.2	0.178	0.697	69.7
5.00		0.054±0.06	19.2	0.120	226.2	-130.4	0.299	0.809	80.9
10.00	-	0.036±0.06	10.3	0.079	233.4	-137.5	0.475	0.874	87.4

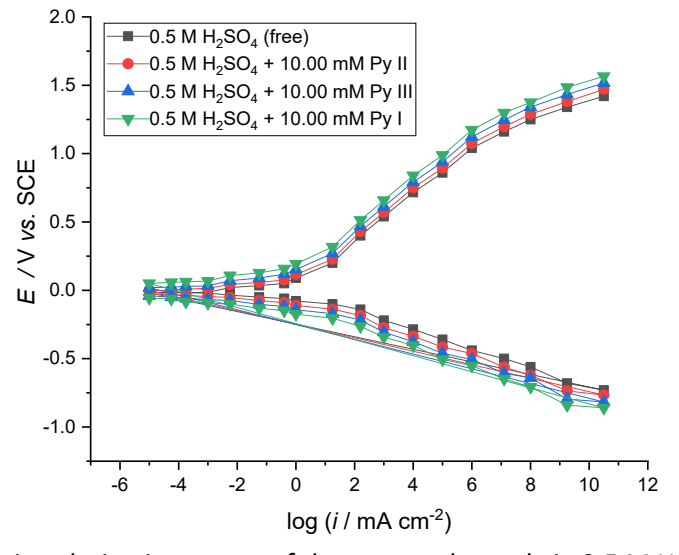


Figure 10. Potentiodynamic polarization curves of the copper electrode in 0.5 M H_2SO_4 solution without and with 10 mM of pyrazolone derivatives at 25 °C and scanning rate 5 mV s⁻¹

Table 4. List of pyrazolone derivatives utilized as corrosion inhibitors for various metals

Inhibitor	Electrode	Medium	IE %	Adsorption isotherm	Ref.
2-(4-(5-(p-tolyl)-4,5-dihydro-1H-pyrazol-3-yl)phenoxy)acetic acid (P1) and 2-(4-(5-(4-nitrophenyl)-4,5-dihydro-1H-pyrazol-3-yl)phenoxy)acetic acid (P2)	Mild steel	1.0 M HCl	>80	physisorption as well as chemisorption	[11]
2-(4-(4,5-dihydro-3-(4-methoxyphenyl)-1H-pyrazol-5-yl)phenoxy)acetic acid (PYR-1) and 2-(4-(4,5-dihydro-3-p-tolyl-1H-pyrazol-5-yl)phenoxy)acetic acid (PYR-2)	Mild steel	1.0 M HCl	>88	physisorption as well as chemisorption	[12]
1-Phenyl-3-Amino-5-Pyrazolone	Mild steel	0.5 M H ₂ SO ₄	98	physisorption as well as chemisorption	[29]
Halogen-substituted pyrazolo-pyrimidine derivatives: 3-methyl-6-oxo-4,5,6,7-tetrahydro-2H-pyrazolo[3,4-b]pyridine-5-carbonitrile (APP I), 3-methyl-6-oxo-4-(3-phenoxyphenyl)-4,5,6,7-tetrahydro-2H-pyrazolo[3,4-b]pyridine-5-carbonitrile (APP II) and 3-methyl-6-oxo-4-(thiophen-2-yl)4,5,6,7-	Copper	0.5 M H ₂ SO ₄	>70	Langmuir, chemisorption and physical absorption.	[30]

Inhibitor	Electrode	Medium	IE %	Adsorption isotherm	Ref.
-tetrahydro-2H-pyrazolo[3,4-b]pyridine-5 carbonitrile (APP III)					
Pyrazolone derivative	Mild steel	0.5 M H ₂ SO ₄	91	Langmuir & Temkin, physical adsorption	[31]
pyrazolone derivatives: 4-(2-(4-(N-(pyrimidin-2-yl)sulfamoyl) phenyl)hydrazono)-3-methyl-1-thiocarbamoyl-2-pyrazolin-5-one(PY1) and (4-methyl-3-phenylthiazol-2-ylidene)-3-methyl-1-thiocarbamoyl-2-pyrazolin-5-one (Py2)	Carbon steel	1.0 M HCl	>80	Temkin isotherm, physical adsorption	[32]
5-Methyl-2,4-dihydropyrazol-3-one and 5-methyl-2-phenyl-2,4-didhydropyrazol-3-one	Copper	0.1 M H ₂ SO ₄	76	Langmuir, physical adsorption	[33]
Imidazole derivatives	Copper	0.5 M H ₂ SO ₄	>9 5	Langmuir, chemisorption and physical adsorption	[34]
Aryl pyrazolo pyridines: 3-methyl-6-oxo-4,5,6,7-tetrahydro-2H-pyrazolo[3,4-b]pyridine-5-carbonitrile (APP I), 3-methyl-6-oxo-4-(3-phenoxyphenyl)-4,5,6,7-tetrahydro-2H-pyrazolo[3,4-b]pyridine-5-carbonitrile (APP II) and 3-methyl-6-oxo4-(thiophen-2-yl)-4,5,6,7-tetrahydro-2H-pyrazolo[3,4-b]pyridine-5-carbonitrile (APP III)	Copper	0.5 M HCl	92	-	[35]
pyrazolone derivatives: 2-(3-amino-5-oxo-4,5-dihydro-1 <i>H</i> -pyrazol-1-yl)(<i>p</i> -tolyl)methyl)malononitrile (PZ-1) and 2-((3-amino-5-oxo-4,5-dihydro-1 <i>H</i> -pyrazol-1-yl)(phenyl)methyl)malononitrile (PZ-2)	N80 Steel	15 % HCl	>90	-	[36]
Pyrazolo-pyrimidine derivatives	Copper	0.5 M H ₂ SO ₄	>70 %	-	[37]
H, 4H, 5H-pyrazolo[3,4-d]pyrimidine	Copper	synthetic seawater	>90	Langmuir, chemisorption	[38]
5-methyl, 5-phenyl, and 5-methyl-2-phenyl derivatives of 2,4-dihydro-3H-pyrazol-3-one (Py)	Copper	H ₂ SO ₄	>84	Langmuir, physical adsorption	This work

Adsorption isotherm

To fit the adsorption of the used additives, we tried to estimate the perfect adsorption isotherm realized our obtained results. Among the isotherms, Langmuir, Frumkin, Temkin, Freundlich, and Florry-Huggins, were checked using the degree of surface covering (θ) calculated from weight loss measurements. The experimental data showed that the Langmuir adsorption isotherm provided the most accurate description of adsorption of pyrazolone compounds on the copper surface. The Langmuir-isotherm can be expressed according to the Equation (27) and its logarithmic form, given by Equation (28) [39]:

$$c/\theta = 1/K + c \tag{27}$$

where K is the adsorption equilibrium constant, θ is the degree of inhibitor's surface covering, and C is the inhibitor concentration in the bulk electrolyte.

$$\log(c/\theta) = \log c - \log K \tag{28}$$

The Langmuir adsorption isotherm is the perfect one that fits the results of adsorption of pyrazolone derivatives on the surface of copper as detected from the linear relationship between $\log(c/\theta)$ and $\log c$ plots, shown in Figure 11.

From the intercepts of the straight lines of Figure 11, the equilibrium constant (K) values could be calculated. In the same way, K values can be calculated for the adsorption process of each pyrazolone compound at different temperatures (Table 5). Examination of data of Figure 11 reveals that K value declines in the following order at the test temperature: Py I > Py III > Py III. This could be attributed to the deceased tendency of adsorption of these additives. However, as the temperature is raised, the values of K decrease due to desorption of the inhibitors on rising the temperature [40].



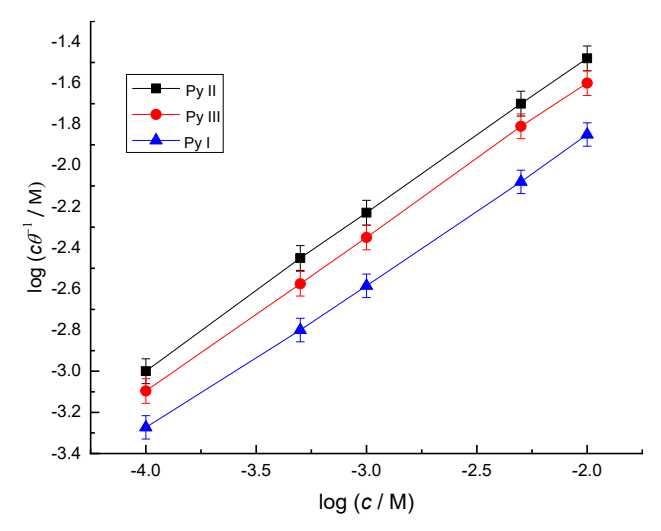


Figure 11. Plots of log (c/ θ) vs. log c, following 10 h immersion of copper in 0.5 M H₂SO₄ solution at 25 °C

The equilibrium constant of adsorption, K, is related to the free energy of adsorption (ΔG_{ads}) according to the Equation (29) [39]:

$$\Delta G^{\circ}_{ads} = -2.303 \, RT \log (55.5 \, K)$$
 (29)

The calculated ΔG^{o}_{ads} values were found to be negative and less than -40.0 kJ mol⁻¹ indicating that, although pyrazolone derivatives are physically and spontaneously adsorbed on the Cu-surface, the process is less favorable at high temperatures [41]. Equation (30) can also be used to compute the other thermodynamic functions [39]:

$$\Delta G^{o}_{ads} = \Delta H^{o}_{ads} - T\Delta S^{o}_{ads}$$
 (30)

where, ΔS^{o}_{ads} and ΔH^{o}_{ads} represent the entropy and enthalpy of the process, respectively.

Plotting the computed free energy values (ΔG°_{ads}) for the pyrazolone compounds utilized versus temperature (T) yielded straight lines, as illustrated in Figure 12.

Further inspection of the data of Table 5, the values of ΔS^{o}_{ads} for Py I are greater and more negative than those for the other pyrazolone compounds at the same temperature. This indicates an increased propensity for the inhibitory species to adsorb on the metal surface.

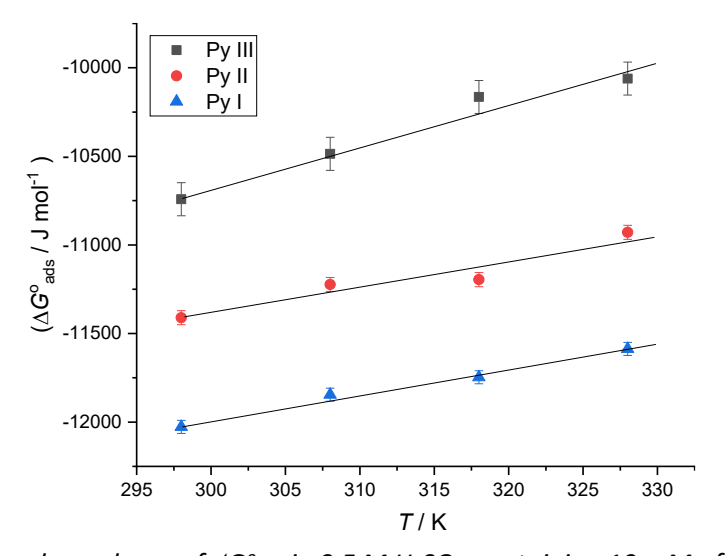


Figure 12. Temperature dependency of ΔG^{o}_{ads} in 0.5 M H₂SO₄ containing 10 mM of pyrazolone derivatives

Table 5 includes the values of ΔH^{o}_{ads} in the temperature range of 298 to 328 K for different pyrazolone derivatives. The exothermic nature of the adsorption of these additives on the Cu

surface is shown in the all-negative values of ΔH^{o}_{ads} [41]. In comparison with the other two pyrazolone derivatives, Py II and Py III exhibit less negative ΔH^{o}_{ads} . This suggests even more that Py I adsorbs less on the copper surface than the other two pyrazolone derivatives.

Table 5. Values of K, ΔG^{o}_{ads} , ΔH^{o}_{ads} and ΔS^{o}_{ads} for adsorption of pyrazolone derivatives on the copper surface at different temperatures (298 to 328 K)

Inhibitor	Parameter	Temperature, K							
	Parameter	298	308	318	328				
Py II	K / L mol⁻	76.33±0.41 60.00±0.52		46.72±0.14	40.00±0.67				
	$-\Delta G^{\circ}_{ads}$ / kJ mol $^{-1}$	10.74±0.06 10.49±0.18		10.17±0.00	10.06±0.05				
	$-\Delta H^{\circ}_{ m ads}$ / kJ mol $^{-1}$	15.80±0.10							
	$-\Delta S^{o}_{ads}$ / J mol ⁻¹	16.97±0.49	17.25±0.16	17.72±0.32	16.98±0.51				
Py III	K / L mol ⁻¹	100.00±0.77	100.00±0.77 80.00±0.28		55.00±0.60				
	-G° _{ads} / kJ mol ⁻¹	11.41±0.31	11.22±0.13	11.196±0.09	10.93±0.25				
	$-\Delta H^{\circ}_{ m ads}$ / kJ mol $^{-1}$	15.8±0.10							
	$-\Delta S^{o}_{ads}$ / J mol ⁻¹	16.97±0.49	16.97±0.49	16.97±0.50	16.97±0.49				
Ру І	K / L mol ⁻¹	128.20±0.81	102.20±0.54	85.00±0.09	70.00±0.11				
	$-\Delta G^{\circ}_{ads}$ / kJ mol $^{-1}$	12.03± 0.56	11.85±0.57	11.75± 0.53	11.59±0.30				
	$-\Delta H^{ m o}_{ m ads}$ / kJ mol $^{ m -1}$	17.76± 0.61							
	$-\Delta S^{o}_{ads}$ / J mol ⁻¹	19.23± 0.44	19.20±0.31	18.90±0.28	18.82±0.34				

Computational study

Optimizing geometry for pyrazolone derivatives

All quantum chemical data have been extracted by implementing geometric optimization concerning all nuclear coordinates using DFT based on the 6-31G basis set and B3LYP method as the level of theory. The optimal configuration of the examined chemical as well as their molecular electrostatic potential surface (MESP) is depicted in Figure 13.

Different colors clarify the electrostatic potential at various locations on the electron density surfaces. Electrophilic active areas, which have the highest negative electrostatic potential, are characterized by their red hue. Whereas the green color denotes a region of zero potential, the blue hue indicates the regions with the highest electrostatic potential (nucleophilic region). The possibility increases in the order green < blue < yellow < orange < red [42].

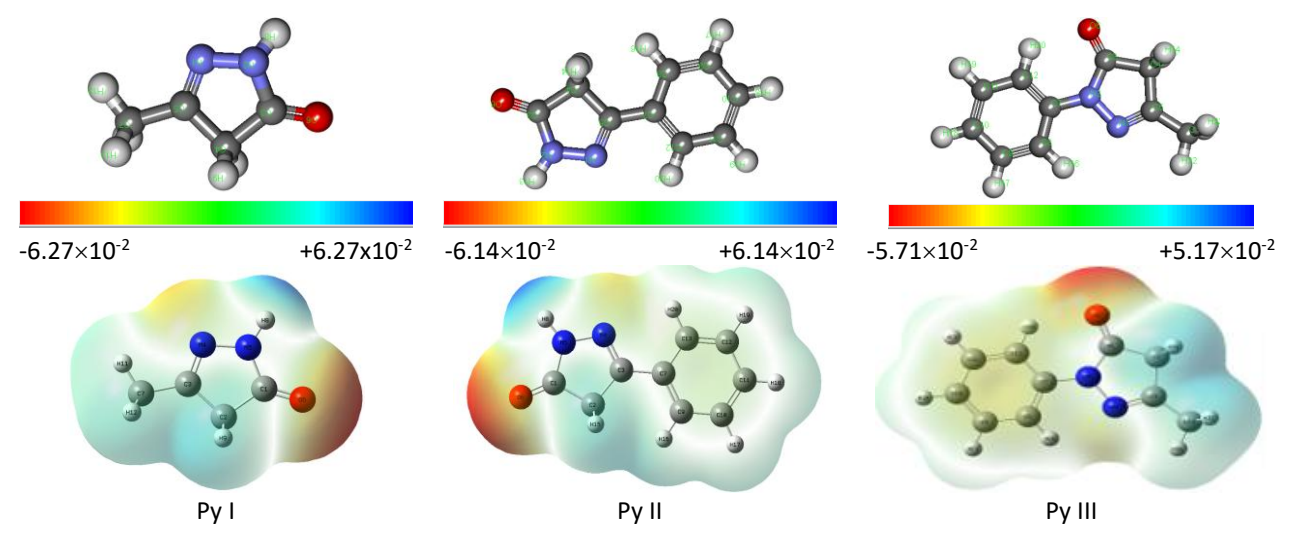


Figure 13. The optimized structures and electrostatics of examined pyrazolone molecules

Figure 13 displays the three compounds' electrostatic potential. Heteroatoms and conjugated double bonds are the main locations of the electron-rich areas. Negative areas that are conducive to electrophilic assaults are indicated by the N, NH, O and pyrazolone rings. Blue (positive sign) hydrogen atoms are more likely to be attacked by nucleophiles. The HOMO density location in the pyrazolone derivatives is mostly distributed near the nitrogen (*i.e.* NH or N), oxygen (=O) atoms, and pyrazolone rings, indicating that these are the preferred sites for adsorption [43], which is confirmed by both Mulliken negative charges and largest Fukui positive f_k^+ and f_k^- values for all inhibitors, whereas the LUMO density was distributed almost throughout the molecules. Table 6 shows the calculated DFT parameters of the examined compounds, where data show that, in the gas phase, PYI and PYI H+ show balanced stability and reactivity with moderate $\Delta E_{\text{(H-L)}}$ values (5.787 and 6.153 eV). PY II exhibits the strongest reactivity with the smallest $\Delta E_{\text{(H-L)}}$ value (4.586 eV) and the highest electronegativity (4.395 eV). PY III shows balanced stability and reactivity with a moderate gap (4.829 eV) and the highest ΔN value (0.191), indicating greater electron transport.

In the water phase, PYI and PYI H+ show balanced stability and reactivity with moderate ΔE values (5.872 and 6.366 eV). PY II has the smallest $\Delta E_{\rm gap}$ (5.998 eV) and the highest electronegativity (6.787 eV), indicating strong electron-accepting capacity. PY III exhibits balanced stability and reactivity with a moderate $\Delta E_{\rm gap}$ (5.059 eV) and the highest ΔN value (0.165), indicating greater electron transport.

Table 6. Calculated quantum chemical parameters of examined pyrazolone compounds

	E _{HOMO} / eV	E _{LUMO} / eV	$\Delta E_{\rm g}$ / eV	I / eV	A / eV	<i>X</i> / eV	H / eV	π/eV	σ/ eV ⁻¹	ω / eV	ω+ / eV	ω- / eV	Δω+ / eV	ΔΝ	$\Delta E_{ m back\ donation} / { m eV}$
	Gaseous state											_			
PYI	-6.706	-0.919	5.787	6.706	0.919	3.812	2.893	-3.812	0.3456	2.511	0.967	4.779	5.746	0.107	0.723
PYI H+	-7.007	-0.853	6.153	7.006	0.853	3.930	3.077	-3.930	0.325	2.510	0.9297	4.859	5.789	0.081	0.769
PYII	-6.275	-1.688	4.586	6.274	1.688	3.981	2.293	-3.981	0.436	3.456	1.7527	5.733	7.486	0.098	0.573
PYII H+	-7.103	-1.688	5.414	7.103	1.688	4.395	2.707	-4.395	0.369	3.568	1.709	6.104	7.813	0.006	0.677
PYIII	-5.922	-1.094	4.829	5.922	1.094	3.508	2.414	-3.508	0.414	2.549	1.100	4.604	5.701	0.191	0.604
PYIII H+	-6.805	-1.140	5.665	6.805	1.140	3.972	2.832	-3.972	0.353	2.785	1.153	5.126	6.279	0.081	0.708
							Liqı	uid (wat	ter)						
PYI	-6.746	-0.873	5.872	6.745	0.873	3.809	2.936	-3.809	0.341	2.471	0.933	4.742	5.675	0.106	0.734
PYI H+	-7.167	-0.801	6.367	7.167	0.801	3.984	3.183	-3.984	0.314	2.493	0.899	4.883	5.782	0.070	0.796
PYII	-8.934	-2.372	6.561	8.933	2.372	5.653	3.280	-5.653	0.305	4.871	2.454	8.107	10.560	-0.186	0.820
PYII H+	-9.787	-3.788	5.998	9.786	3.788	6.787	2.999	-6.787	0.333	7.681	4.662	11.449	16.111	-0.393	0.750
PYIII	-6.124	-1.064	5.059	6.124	1.064	3.594	2.530	-3.594	0.395	2.553	1.072	4.667	5.739	0.165	0.632
PYIII H+	-7.091	-0.485	6.606	7.091	0.485	3.788	3.303	-3.788	0.303	2.172	0.691	4.479	5.170	0.097	0.826

The obtained adsorption data of the three pyrazolone derivatives and the $Cu_{(111)}$ surface are tabulated in Table 7. The three molecules were adsorbed on a parallel position to the $Cu_{(111)}$ surface. The plane position leads to the maximum interaction between the active sites of the organic inhibitors and the metal surface [44] as shown in Figure 14.

Table 7. Lower adsorption configuration output results from the adsorption locator module

		En	$(dE_{ads}/dN_i)/kJ mol^{-1}$		
Structures	Total	Adsorption	Rigid adsorption	Deformation	(UE _{ads} /U/V _i)/ KJ IIIOI
Cu ₁₁₁ +PYI+ 98H ₂ O+ 2H ₂ SO ₄	-351.92	-238.756	-196.933	-41.8233	-238.756
Cu ₁₁₁ +PYII+ 98H ₂ O+ 2H ₂ SO ₄	-191.058	-190.272	-151.406	-38.8652	-190.272
Cu ₁₁₁ +PYIII+ 98H ₂ O+ 2H ₂ SO ₄	-370.468	-318.097	-290.081	-28.0202	-318.097

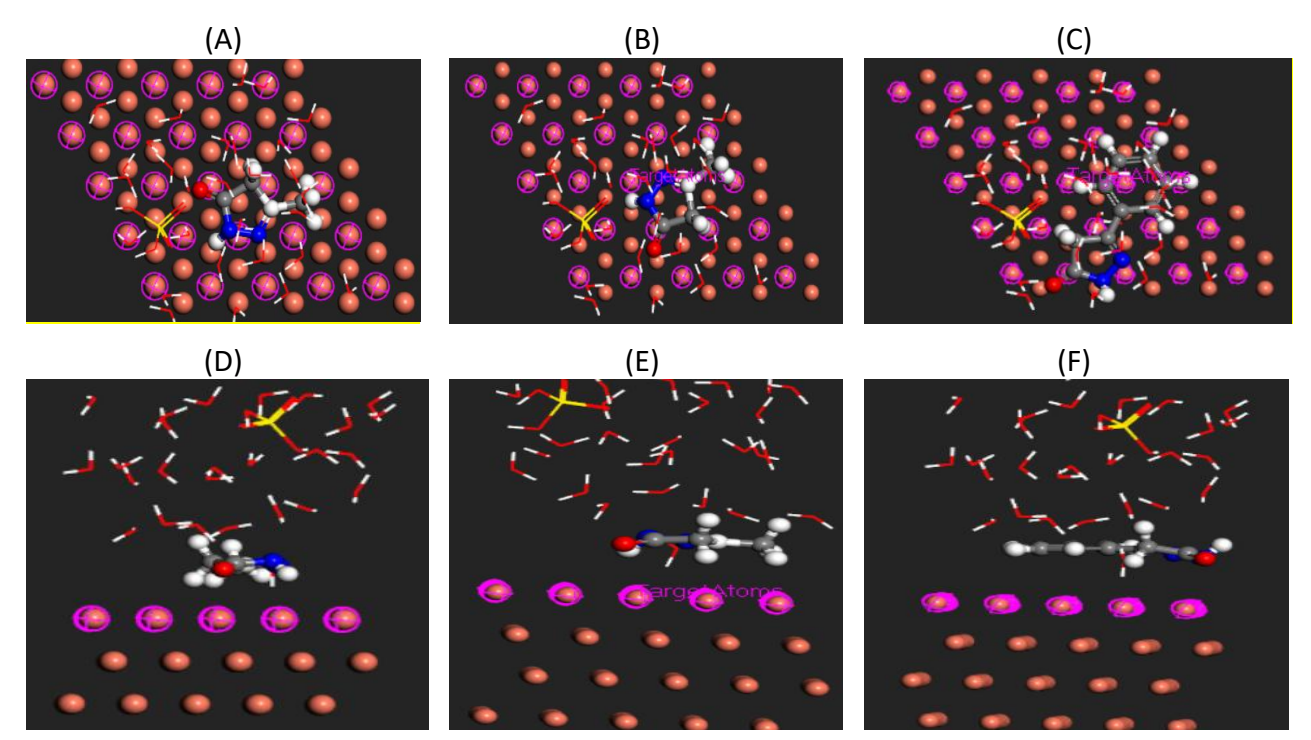


Figure 14. Side and top views of most stable adsorption configuration of Py I (A) and (D), Py II (B) and (E) and Py III (C) and (F) obtained by molecular dynamic simulations on $Cu_{111}/98 H_2O/2H_2SO_4$ surface

Inhibitory mechanism

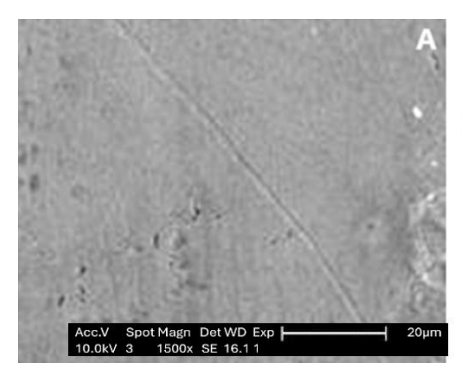
At least one polar unit, comprising atoms of N, O, S and, in certain situations Se and P, is required for the majority of organic compounds that can be employed as inhibitors. These kinds of substances are capable of donating electrons, and their mechanism of action is thought to be due to the adsorption of inhibitor molecules onto the surfaces of metals via an unshared pair of heteroatom electrons [45].

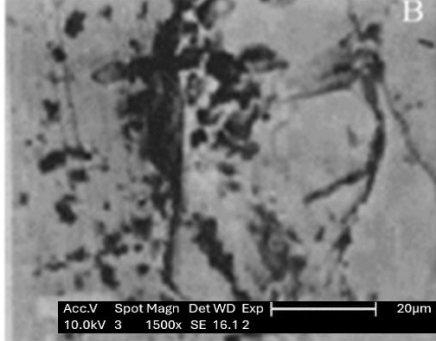
Figure 15. The keto-enol forms of Py I

Figure 15 shows the equilibrium of the keto and enol forms of Py I in an acidic medium. It is suggested that the interaction of the lone pair of electrons from the O-atom of the keto-enol, with the positively charged metal surface is the cause of the inhibition of Cu in an acidic medium. Other factors that must be taken into account in the corrosion inhibition process include the interaction of the electrons from the pyrazolone rings with the positively charged metal surface and the interaction of pyrazolone cations formed in acidic solutions with the negatively charged metal surface. Conversely, inhibitors' delocalized π -electrons enable high adsorption on the Cu-surface, which causes inhibition of corrosion [46]. Two factors may be responsible for Py I maximum inhibitory action: (i) the smallest molecule size; and (ii) the existence of an electron-donating group (-CH₃) that raised the pyrazolone ring electron density. These factors led to an increase in the adsorption process. The review of the literature also shows that pyrazolone derivatives are good corrosion inhibitors, particularly in acidic media, because of their strong adsorption through the

donation of O and N atoms' lone pairs of electrons to the metal surface [46] which is corroborated by Mulliken charges and Fukui indices.

SEM micrographs of the copper electrode surface taken before, after 10-hour immersion in 0.5 M sulfuric acid (free) and 0.5 M sulfuric acid with 10 mM Py I (an example of the utilized inhibitor) are shown in Figure 16. Examining these micrographs reveals that in H_2SO_4 free solution, the formation of little pits, some of which equally grew inward and laterally to produce some sizable attacked areas (compared by the Cu-surface before immersion in H_2SO_4 (Figure 16(A)). Traces of the corrosion products are seen inside these sizable regions, as shown in Figure 16(B). However, the number and size of pits created are significantly reduced in the presence of 10 mM Py I, as an example of organic inhibitors utilized (Figure 16(C)).





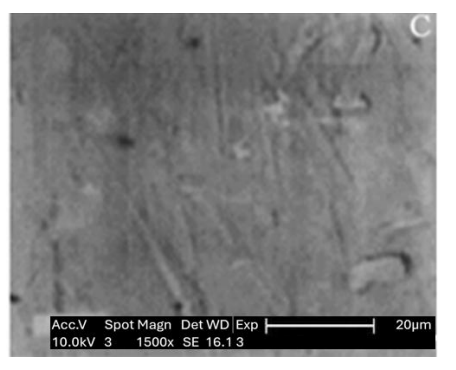


Figure 16. SEM micrographs of copper electrode surface: (A) after immersion for a period of 10 h in (B) 0.5 M sulfuric acid (free) and (C) 0.5 M sulfuric acid + 10 mM Py I.

Conclusions

The results of the present demonstrated the following:

Higher acid concentrations and longer exposure times cause copper to corrode more quickly in H_2SO_4 solutions. Weight loss and polarization measurements show that corrosion rates rise as temperature and acid concentration rise. The rates of copper corrosion in sulfuric acid are decreased by pyrazolone derivatives, and the efficiency of inhibition increases with increasing inhibitor concentration. The order of inhibitory efficiency at the same temperature is as follows: Py I < Py II < Py III. SEM demonstrates that these compounds significantly reduce corrosion regions. Quantum generally support lab results, strengthening the use of pyrazolone as a corrosion inhibitor for Cu in H_2SO_4 .

Declaration of competing Interest: The authors declare that they have no known competing financial interests or personal relationships that could have appeared to influence the work reported in this paper.

Acknowledgments: Authors are thankful to the Department of Chemistry, Faculty of Science, Zagazig University, Zagazig for providing laboratory facilities.

References

- [1] L. Nunez, E. Reguera, F. Corvo, E. González, C. Vazquez, Corrosion of copper in seawater and its aerosols in a tropical island, *Corrosion Science* 47 (2005) 461-484. https://doi.org/10.1016/j.corsci.2004.05.015
- [2] A.-Y. Zhu, J.-I. Chen, L. Zhou, L.-y. Luo, Q. Lei, L. Zhang, W. Zhang, Hot deformation behavior of novel imitation-gold copper alloy, *Transactions of Nonferrous Metals Society of China* **23** (2013) 1349-1355. https://doi.org/10.1016/S1003-6326(13)62603-5
- [3] E. T. Akinlabi, A. Andrews, S. A. Akinlabi, Effects of processing parameters on corrosion properties of dissimilar friction stir welds of aluminium and copper, *Transactions of*

- *Nonferrous Metals Society of China* **24** (2014) 1323-1330. https://doi.org/10.1016/S1003-6326(14)63195-2
- [4] B. Tan, S. Zhang, Y. Qiang, W. Li, H. Liu, C. Xu, S. Chen, Insight into the corrosion inhibition of copper in sulfuric acid via two environmentally friendly food spices: Combining experimental and theoretical methods, *Journal of Molecular Liquids* **286** (2019) 110891. https://doi.org/10.1016/j.molliq.2019.110891
- [5] A. Zarrouk, B. Hammouti, A. Dafali, F. Bentiss, Inhibitive properties and adsorption of purpald as a corrosion inhibitor for copper in nitric acid medium, *Industrial & Engineering Chemistry Research* **52** (2013) 2560-2568. https://doi.org/10.1021/ie301465k
- [6] R. Chadli, M. Elazouzi, I. Khellad, A. M. Elhourri, H. Elmsellem, A. Aouniti, J. K. Mulengi, B. Hammoutii, Electrochemical and theoretical study of pyrazole 4-(4,5-dihydro-1H-pyrazol-5-yl)-N,N-dimethylaniline (D) as a corrosion inhibitor for mild steel in 1 M HCl, Portugaliae *Electrochimica Acta* **35** (2017) 65-80. https://doi.org/10.4152/pea.201702065
- [7] K.-c. Shen, G.-h. Li, W.-m. Wang, Thermal expansion behavior, microhardness and electrochemical corrosion resistance properties of Au₅₂Cu₂₇Ag_{17-x} (NiZn0.5)_x alloys, *Transactions of Nonferrous Metals Society of China* **26** (2016) 2900-2909. https://doi.org/10.1016/S1003-6326(16)64419-9
- [8] M. Akrom, S. Rustad, A. G. Saputro, H. K. Dipojono, Data-driven investigation to model the corrosion inhibition efficiency of pyrimidine-pyrazole hybrid corrosion inhibitors, Computational and Theoretical Chemistry 1229 (2023) 114307. https://doi.org/10.1016/j.comptc.2023.114307
- [9] H. Chahmout, M. Ouakki, S. Sibous, M. Galai, N. Arrousse, E. Ech-chihbi, Z. Benzekri, S. Boukhris, A. Souizi, M. Cherkaoui, New pyrazole compounds as a corrosion inhibitor of stainless steel in 2.0 M H₂SO₄ medium: Electrochemical and theoretical insights, *Inorganic Chemistry Communications* 147 (2023) 110150. https://doi.org/10.1016/j.inoche.2022.110150
- [10] S. Abd El Rehim, S. Sayyah, M. El-Deeb, S. M. Kamal, R. E. Azooz, Adsorption and corrosion inhibitive properties of P (2-aminobenzothiazole) on mild steel in hydrochloric acid media, International Journal of Industrial Chemistry 7 (2016) 39-52. https://doi.org/10.1007/s40090-015-0065-5
- [11] H. Lgaz, R. Salghi, A. Chaouiki, Shubhalaxmi, S. Jodeh, K. S. Bhat, Pyrazoline derivatives as possible corrosion inhibitors for mild steel in acidic media: A combined experimental and theoretical approach, *Cogent Engineering* **5** (2018) 1441585. https://doi.org/10.1080/23311916.2018.1441585
- [12] H. Lgaz, S. K. Saha, A. Chaouiki, K. S. Bhat, R. Salghi, Shubhalaxmi, P. Banerjee, I. H. Ali, M. I. Khan, I. M. Chung, Exploring the potential role of pyrazoline derivatives in corrosion inhibition of mild steel in hydrochloric acid solution: Insights from experimental and computational studies, Construction and Building Materials 233 (2020) 117320. https://doi.org/10.1016/j.conbuildmat.2019.117320
- [13] A. Chaouiki, M. Chafiq, H. Lgaz, H. Shubhalaxmi, K. S. Bhat, I. H. Ali, S. Masroor, Y. El Aoufir, Experimental and theoretical insights into the corrosion inhibition activity of a novel pyrazoline derivative for mild steel in 1.0 M HCl, *Applied Journal of Environmental Engineering Science* 6 (2020) 2079-2093. https://doi.org/10.48422/IMIST.PRSM/ajees-v6i1.20261
- [14] N. A. Wazzan, I. Obot, S. Kaya, Theoretical modeling and molecular level insights into the corrosion inhibition activity of 2-amino-1,3,4-thiadiazole and its 5-alkyl derivatives, *Journal of Molecular Liquids* **221** (2016) 579-602. https://doi.org/10.1016/j.molliq.2019.117320
- [15] A.-B. Kamal, M. Mostfa, A. M. Ashmawy, M. S. El-Gaby, G. A. Ali, Corrosion inhibition behavior of the synthesized pyrazoline-sulfonamide hybrid of mild steel in aqueous



- solutions: Experimental and quantum investigations, Journal of Chemical Sciences **134** (2022) 90. https://doi.org/10.1007/s12039-022-02086-6
- [16] R. G. Pearson, Absolute electronegativity and hardness: applications to organic chemistry, The Journal of Organic Chemistry **54** (1989) 1423-1430. https://doi.org/10.1021/jo00267a034
- [17] S. Martinez, Inhibitory mechanism of mimosa tannin using molecular modeling and substitutional adsorption isotherms, *Materials Chemistry and Physics* **77** (2003) 97-102. https://doi.org/10.1016/S0254-0584(01)00569-7
- [18] R. G. Parr, L. V. Szentpály, S. Liu, Electrophilicity index, Journal of the American Chemical Society **121** (1999) 1922-1924. https://doi.org/10.1021/ja983494x
- [19] W. Yang, W. J. Mortier, The use of global and local molecular parameters for the analysis of the gas-phase basicity of amines, *Journal of the American Chemical Society* **108** (1986) 5708-5711. https://doi.org/10.1021/ja00279a008
- [20] C. Morell, A. Grand, A. Toro-Labbé, Theoretical support for using the Δf (r) descriptor, Chemical Physics Letters **425** (2006) 342-346. https://doi.org/10.1016/j.cplett.2006.05
- [21] Z. Qu, X. Wang, X. Shen, H. Zhou, Study of the Cu (111) Surface by Scanning Tunneling Microscopy: The Morphology Evolution, Reconstructions, Superstructures and Line Defects, Nanomaterials 12 (2022) 4278. https://doi.org/10.3390/nano12234278
- [22] M. Iwai, H. Majima, Y. Awakura, Dissolution of copper in hydrochloric acid solutions with dissolved molecular oxygen, *Hydrometallurgy* 20 (1988) 87-95. https://doi.org/10.1016/0304-386X(88)90028-X
- [23] M. Braun, K. Nobe, Electrodissolution kinetics of copper in acidic chloride solutions, *Journal of The Electrochemical Society* **126** (1979) 1666. https://iopscience.iop.org/article/10.1149/1.2128773/meta
- [24] L. Gao, S. Peng, X. Huang, Z. Gong, A combined experimental and theoretical study of papain as a biological eco-friendly inhibitor for copper corrosion in H₂SO₄ medium, *Applied Surface Science* **511** (2020) 145446. https://doi.org/10.1016/j.apsusc.2020.145446
- [25] A. A. Mahmmod, A. A. Khadom, A. A. H. Kadhum, A. Alamiery, Quinoxaline as a corrosion inhibitor for copper in nitric acid: Kinetics, statistical, and theoretical investigations, *Case Studies in Chemical and Environmental Engineering* **10** (2024) 100836. https://doi.org/10.1016/j.cscee.2024.100836
- [26] F. R. García-Galvan, S. Fajardo, V. Barranco, S. Feliu Jr, Experimental apparent stern—geary coefficients for AZ31B Mg alloy in physiological body fluids for accurate corrosion rate determination, *Metals* **11** (2021) 391. https://doi.org/10.3390/met11030391
- [27] C. Jeyaprabha, S. Sathiyanarayanan, K. Phani, G. Venkatachari, Influence of poly (aminoquinone) on corrosion inhibition of iron in acid media, *Applied Surface Science* **252** (2005) 966-975. https://doi.org/10.1016/j.apsusc.2005.01.098
- [28] R. T. Loto, C. A. Loto, A. P. Popoola, T. Fedotova, Inhibition effect of 2-amino-5-ethyl-1, 3, 4-thiadiazole on corrosion behaviour of austenitic stainless steel type 304 in dilute HCl solution, *Journal of Central South University* **23** (2016) 258-268. https://doi.org/10.1007/s11771-016-3069-1
- Y. Zhang, Y. Cheng, F. Ma, K. Cao, Corrosion inhibition of carbon steel by 1-phenyl-3-amino-5-pyrazolone in H₂SO₄ solution, International Journal of Electrochemical Science **14** (2019) 999-1008. https://doi.org/10.20964/2019.01.69
- [30] Y. Xu, S. Zhang, C. Liao, Y. Zhou, L.H. Madkour, Halogen-substituted pyrazolo-pyrimidine derivatives as corrosion inhibitors for copper in sulfuric acid solution, *International Journal of Corrosion and Scale Inhibition* **7** (2018) 236-249. https://doi.org/10.17675/2305-6894-2018-7-2-9

- [31] D. Nalini, K. Kohilah, R. Sowmya, A combined experimental and theoretical investigation on pyrazolone derivative as corrosion inhibitor for mild steel in 0.5 M sulphuric acid media, *Portugaliae Electrochimica Acta* **32** (2014) 109-123. https://doi.org/10.4152/pea.201402109
- [32] M. Deyab, A. Fouda, M. Osman, S. Abdel-Fattah, Mitigation of acid corrosion on carbon steel by novel pyrazolone derivatives, RSC Advances 7 (2017) 45232-45240. https://doi.org/10.1039/C7RA08761F
- [33] A. Díaz-Gómez, R. Vera, A. Molinari, A. Oliva, W. Aperador, 5-Methyl-2, 4-dihydropyrazol-3-one and 5-methyl-2-phenyl-2, 4-didhydropyrazol-3-one as copper corrosion inhibitors in acidic media, *International Journal of Electrochemical Science* **10** (2015) 4004-4019. https://doi.org/10.1016/S1452-3981(23)06597-5
- [34] T. Yan, S. Zhang, L. Feng, Q. Yujie, L. Lansi, F. Denglin, W. Yanan, C. Jida, L. Wenpo, T. Bochuan, Investigation of imidazole derivatives as corrosion inhibitors of copper in sulfuric acid: combination of experimental and theoretical researches, *Journal of the Taiwan Institute of Chemical Engineers* **106** (2020) 118-129. https://doi.org/10.1016/j.jtice.2019.10.014
- [35] M. Quraishi, The corrosion inhibition effect of aryl pyrazolo pyridines on copper in hydrochloric acid system: computational and electrochemical studies, *RSC Advances* **5** (2015) 41923-41933. https://doi.org/10.1039/C5RA03966E
- [36] K. Ansari, M. Quraishi, A. Singh, S. Ramkumar, I. B. Obote, Corrosion inhibition of N80 steel in 15% HCl by pyrazolone derivatives: electrochemical, surface and quantum chemical studies, *RSC Advances* **6** (2016) 24130-24141. https://doi.org/10.1039/C5RA25441H
- [37] Y. Xu, S. Zhang, W. Li, L. Guo, S. Xu, L. Feng, L. H. Madkour, Experimental and theoretical investigations of some pyrazolo-pyrimidine derivatives as corrosion inhibitors on copper in sulfuric acid solution, *Applied Surface Science* **459** (2018) 612-620. https://doi.org/10.1016/j.apsusc.2018.08.037
- [38] S. Echihi, N. Benzbiria, M. Belghiti, M. El Fal, M. Boudalia, E. M. Essassi, A. Guenbour, A. Bellaouchou, M. Tabyaoui, M. Azzi, Corrosion inhibition of copper by pyrazole pyrimidine derivative in synthetic seawater: experimental and theoretical studies, *Materials Today: Proceedings* **37** (2021) 3958-3966. https://doi.org/10.1016/j.matpr.2020.09.264
- [39] S. Abd El Rehim, S. Sayyah, M. El-Deeb, S.M. Kamal, R. E. Azooz, Poly (o-phenylenediamine) as an inhibitor of mild steel corrosion in HCl solution, *Materials Chemistry and Physics* **123** (2010) 20-27. https://doi.org/10.1016/j.matchemphys.2010.02.069
- [40] R. Zvauya, J. Dawson, Inhibition studies in sweet corrosion systems by a quaternary ammonium compound, *Journal of Applied Electrochemistry* **24** (1994) 943-947. https://doi.org/10.1007/BF00348786
- [41] P. Desai, R. Vashi, Inhibitive efficiency of sulphathiazole for aluminum corrosion in trichloroacetic acid, *Anti-Corrosion Methods and Materials* **58** (2011) 70-75. https://doi.org/10.1108/00035591111110714
- [42] S. S. Pingale, A. P. Ware, S. R. Gadre, Unveiling electrostatic portraits of quinones in reduction and protonation states, *Journal of Chemical Sciences* **130** (2018) 50. https://doi.org/10.1007/s12039-018-1450-3
- [43] M. Mostfa, H. Gomaa, I. M. Othman, G. A. Ali, Experimental and theoretical studies of a novel synthesized azopyrazole-benzenesulfonamide derivative as an efficient corrosion inhibitor for mild steel, *Journal of the Iranian Chemical Society* **18** (2021) 1231-1241. https://doi.org/10.1007/s13738-020-02106-7
- [44] Y. Boughoues, M. Benamira, L. Messaadia, N. Ribouh, Adsorption and corrosion inhibition performance of some environmental friendly organic inhibitors for mild steel in HCl solution via experimental and theoretical study, *Colloids and Surfaces A: Physicochemical*



- and Engineering Aspects **593** (2020) 124610. https://doi.org/10.1016/j.colsurfa.2020.124610
- [45] L. Herrag, A. Chetouani, S. Elkadiri, B. Hammouti, A. Aouniti, Pyrazole derivatives as corrosion inhibitors for steel in hydrochloric acid, *Portugaliae Electrochimica Acta* **26** (2008) 211-220. https://peacta.org/articles_upload/PEA_26_2_211_220.pdf
- [46] A. Zarrouk, B. Hammouti, A. Dafali, Inhibition of copper corrosion in acid solution by N-1-naphthylethylenediamine dihydrochloride monomethanolate: experimental and theoretical study: part-1, *Research on Chemical Intermediates* **38** (2012) 1079-1089. https://doi.org/10.1007/s11164-011-0444-2

© 2025 by the authors; licensee IAPC, Zagreb, Croatia. This article is an open-access article distributed under the terms and conditions of the Creative Commons Attribution license (https://creativecommons.org/licenses/by/4.0/)



Open Access :: ISSN 1847-9286 www.jESE-online.org

Original scientific paper

Electrooxidation of catechol in the presence of proline at different pH

Firoz Ahmed¹, Md Abdul Motin¹,⊠, Md A. Hafiz Mia¹ and Md A. Aziz²

¹Department Chemistry, Khulna University of Engineering & Technology (KUET), Khulna 9203, Bangladesh

²University of Global Village (UGV), Barishal, Bangladesh

Corresponding author: [™]motin@chem.kuet.ac.bd; Tel: +88 01920770333

Received: January 21, 2025; Accepted: February 12, 2025; Published: February 21, 2025

Abstract

The electrooxidation characteristics of catechol in the presence of different concentrations of proline in aqueous buffer solutions at different pH levels were examined using cyclic voltammetry, controlled potential coulometry, and differential pulse voltammetry. In the second potential scan, the reaction involving o-benzoquinone and proline occurred at higher proline concentrations. The product of catechol electrooxidation with proline is assumed to be (S)-1-(3,4-dihydroxyphenyl)pyrrolidine-2-carboxylic acid, which undergoes electron transfer at more negative potentials compared to catechol. The influence of the pH of catechol in the presence of proline was assessed by adjusting the pH of the buffer solution from 5 to 11. Both pH and proline concentration significantly affected the reaction, and the optimal conditions for this reaction were observed at a proline concentration of 150 mM and a catechol concentration of 2 mM in a buffer solution of pH 7. The reaction pathway exhibited characteristics of an electron transfer, chemical reaction and electron transfer (ECE) type, followed by a diffusion mechanism.

Keywords

Electrosynthesis, catechol-proline adduct, oxidation reaction pathway, voltammetry techniques, controlled potential coulometry

Introduction

Catechol is an important foundational compound in organic synthesis, and it is produced on an industrial scale for use as a precursor in pesticides, fragrances, and pharmaceuticals [1]. It is also present in various natural products, particularly those with antioxidant properties [2]. A notable feature of catechols is their susceptibility to oxidation, primarily because of their antioxidant capabilities and low oxidation potentials [3]. The oxidation results in the formation of reactive and electron-deficient o-quinones. Electrochemical oxidation is one of the most effective methods for generating these reactive o-quinone species [4]. Several studies have documented the electro-

oxidation of catechols to create o-quinones, which act as reactive intermediates in various favorable homogeneous reactions [5].

Proline is the only amino acid that contains a secondary amine which categorizes it as an imino acid. Additionally, it is distinctive because the alpha-amino group is directly linked to the side chain, resulting in the alpha carbon being a direct component of the side chain. Proline may act as a potential endogenous excitotoxin [6-8]. Proline unique cyclic side chain confers a notable conformational rigidity that sets it apart from other amino acids. This structural characteristic also influences the speed at which peptide bonds form between proline and different amino acids. In a peptide bond where proline is incorporated as an amide, its nitrogen does not attach to a hydrogen atom, which prevents it from serving as a hydrogen bond donor, although it can still function as a hydrogen bond acceptor [9].

The electrochemical oxidation of catechols in the presence of various nucleophiles, including aspartic acid, glutamine, sulfanilic acid, ethanol, 2-thiobarbituric acid, b-diketones, 4-hydroxy-6-methyl-2-pyrone, 2-thiouracil, dimedone, 4,7-dihydroxycoumarin, 4,5,7-trihydroxycoumarin, 4-hydroxy-6-bromocoumarin, 3-hydroxycoumarin, 4-hydroxy-6-methyl-α-pyrone, 4-hydroxy-6-methyl-2-pyridone, and 4-hydroxycarbostyrile were studied [10-22]. To the best of our knowledge, there are no existing studies on the electrochemical oxidation of catechols involving proline. In this paper, we have studied the electrochemical properties of catechol in the presence of proline with three different electrodes, a wide range of concentrations of proline, and different pH levels.

Experimental

Catechol, proline, acetic acid, sodium acetate, potassium chloride, sodium dihydrogen phosphate, and disodium hydrogen phosphate were of analytical grade (E-Merck, Germany). Distilled water was used to prepare all solutions. Phosphate buffer (PB) and acetate buffer (AB) solutions were prepared in distilled water. Solutions of catechol and catechol with proline at different concentrations were prepared at various pH levels (5-11) using acetate or phosphate buffer solutions. The target pH values were calculated using the Henderson-Hasselbalch equation, and the buffer solutions were prepared accordingly.

Platinum and gold disks with a diameter of 1.6 mm (Bioanalytical Systems, Inc.) and glassy carbon (GC) disks with a diameter of 3 mm (Bioanalytical Systems, Inc.) were used as working electrodes for voltammetry. The working electrode used in controlled potential coulometry was an assembly of three carbon rods (6 mm diameter, 4 cm length). The electrode surface was polished with 0.05 μ m alumina before each run. The auxiliary electrode was a platinum coil (Bioanalytical Systems, Inc.), and the reference electrode was Ag|AgCl (3M KCl) (Bioanalytical Systems, Inc.). The working electrode was polished by gently pressing it against the polishing surface for 5-10 minutes and then thoroughly washed with deionized water. At this point, the electrode surface appeared as a shiny mirror. The potentio-stat/galvanostat was the μ Stat 8000 (Metrohm/Drop Sens). Nitrogen gas was bubbled through the one-compartment cell before the electrochemical run.

Results and discussion

Electrochemical behaviour of catechol with proline

The electrochemical characteristics of catechol in the absence and presence of proline were investigated using cyclic voltammetry (CV), differential pulse voltammetry (DPV), and controlled potential coulometry (CPC). Figure 1 (blue line) presents the cyclic voltammogram of 2 mM catechol on a 3 mm GC electrode in a phosphate buffer solution with pH 7 and a scan rate of 0.1 V s⁻¹. The

voltammogram reveals a single anodic peak at 0.44 V and a corresponding cathodic peak at 0.12 V, associated with the conversion of catechol to o-quinone and its reverse process.

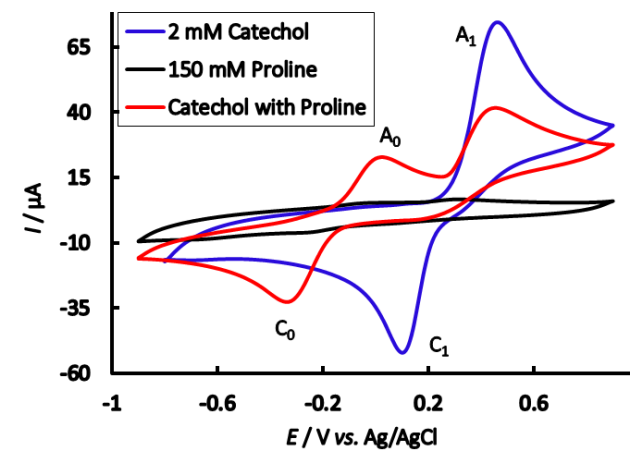


Figure 1. Cyclic voltammograms of catechol, proline, and 2 mM catechol with 150 mM proline on GC electrode in phosphate buffer solution of pH 7, at a scan rate of 0.1 V s⁻¹ (2^{nd} cycle). A_0 and A_1 are anodic peaks, and C_0 and C_1 are corresponding cathodic peaks

Pure proline exhibits no electrochemical activity within the potential range examined (Figure 1, black line). Figure 1 (red line) presents the cyclic voltammogram (CV) of catechol (2 mM) in the presence of proline (150 mM) during the second potential scan under the same conditions. In the second potential scan, catechol combined with proline displays two anodic peaks at 0.12 and 0.44 V, along with corresponding cathodic peaks at -0.32 and 0.20 V, respectively. The appearance of A_0 and C_0 peaks, along with the reduction of A_1 and C_1 peaks and the shifting of their peak positions upon the addition of proline, suggests that these alterations are likely due to a reaction between catechol and proline. This can be clarified by exploring the nucleophilic attack of proline on obenzoquinone. This phenomenon lowers the concentration of o-benzoquinone in the reaction layer, leading to a decrease in A_1 and C_1 peaks while simultaneously generating a catechol-proline adduct, which results in the appearance of peaks A_0 and C_0 . During the initial scan of the potential, the anodic peak of catechol with proline resembles that of pure catechol. However, in the subsequent potential scan, the peak current of A_1 and C_1 (depicted by the red line) shows a notable decrease compared to free catechol (shown by the blue line).

The peak current ratio for peaks A_1 and C_1 (I_{pa_1}/I_{pc_1}) showed a significant decrease with cycling, suggesting a chemical reaction between proline and the o-quinone generated on the electrode surface (step 1 in Scheme 1). This could point to the formation of (S)-1-(3,4-dihydroxyphenyl)pyrrolidine-2-carboxylic acid *via* a nucleophilic substitution reaction (step 2 in Scheme 1). This behaviour aligns with previous findings regarding the electrochemical oxidation of catechols when combined with aspartic acid, glutamine, and sulfanilic acid [23-25]. When the oxidation potential of the resulting product is relatively low, further oxidation tends to be reduced, which allows for additional oxidation and integration of other elements [26].

Specifically, in the case of catechol interacting with proline, the oxidation of the proline-substituted o-benzoquinone (step 3 in Scheme 1) occurs more readily than that of the original catechol. While this substitution product can be further attacked by proline, such reactions were not observed in the voltammetric studies due to the low reactivity of o-quinone 4 towards 2. Similar compounds generated electrochemically, like catechol and various nucleophiles, have also been documented [10-23,26]. When there are no other nucleophiles present, water or hydroxide ions typically react with o-benzoquinone [27].

Scheme 1. Reaction steps of catechol oxidation in presence of proline

In Figure 2a, the cyclic voltammograms (CV) of the second cycle for 2 mM catechol in the presence of 150 mM proline at the GC (3 mm) electrode in a buffer solution (pH 7) are presented at various scan rates. As the scan rate increases, the anodic and cathodic peak currents increase to 0.3 V $\rm s^{-1}$ for A₀ and C₀. Additionally, the cathodic peaks shift to the left, while the anodic peaks move to the right with the increasing scan rate. However, at scan rates of 0.4 to 0.5 V $\rm s^{-1}$, the anodic peak current for A₀ and C₀ decreased while the A₁ anodic peak current increased. At this point, the anodic peak potential continued to move to the right, whereas the cathodic peak potential shifted left. It was noted that the cathodic peak related to the catechol and o-benzoquinone redox reaction was quite small at the investigated scan rates, likely due to the rapid chemical reaction between proline and o-benzoquinone.

Figure 2b shows the plots of the net anodic and cathodic peak currents for 2 mM catechol with 150 mM proline during the second cycle, plotted against the square root of the scan rates. Here, the net current is calculated as the second peak minus the first one based on the scan-stopped method [28]. Although the peak current of A_1 and C_1 increases proportionally with the square root of scan rates, these lines do not pass through the origin. This indicates that the pure diffusion process does not fully control the peak current of the reactant at each redox reaction, suggesting that some surface-related chemical complications occur during the reaction.

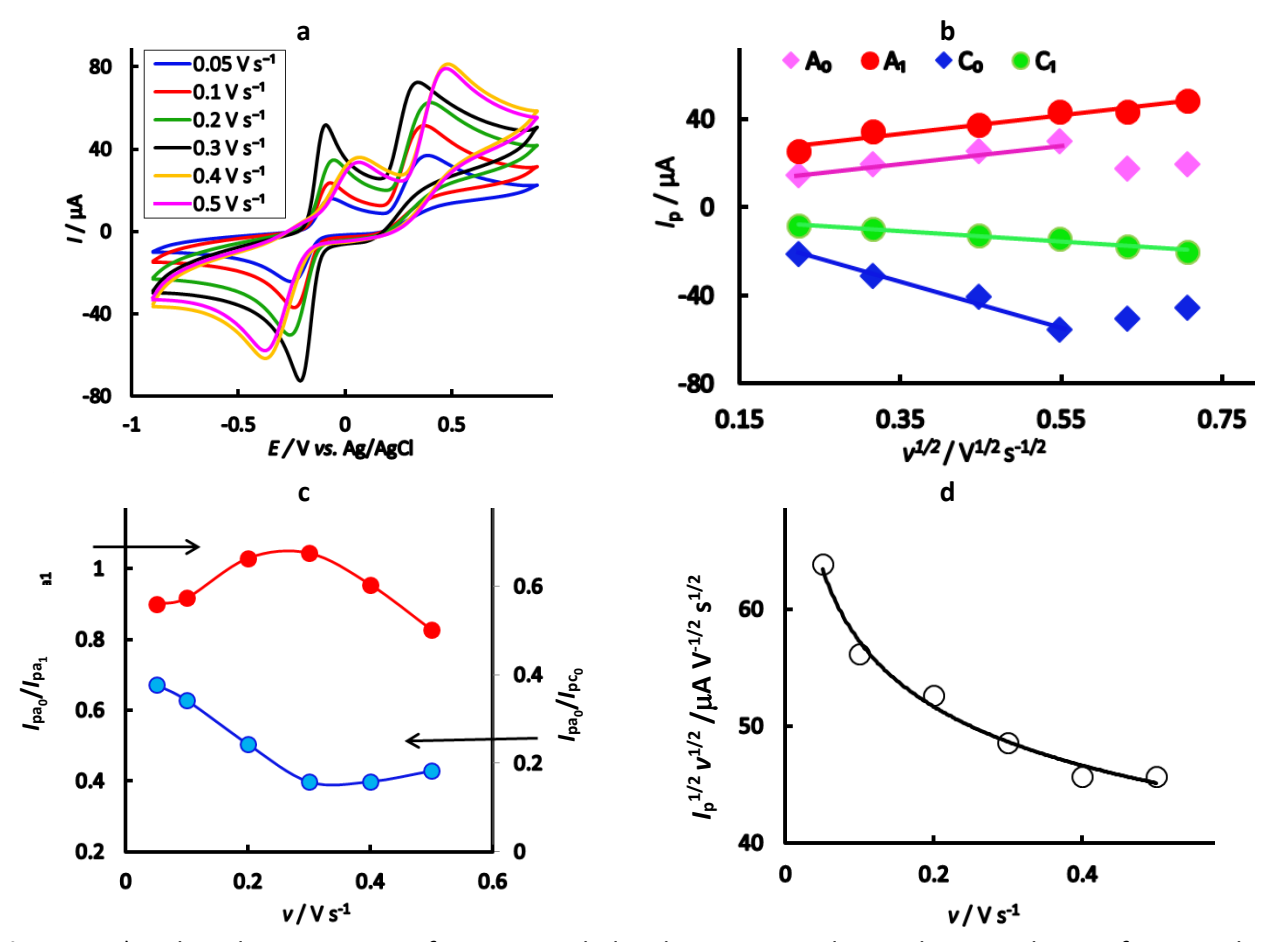


Figure 2. a) cyclic voltammograms of 2 mM catechol with 150 mM proline in the second scan of potential at the GC electrode in a buffer solution of pH 7 at different scan rate; b) plots of peak current vs. square root of scan rate in the same conditions. Legend shows the symbols of oxidation and reduction peaks; c) variation of peak current ratio of corresponding peak (l_{pa_0}/l_{pc_0}) and anodic peak (l_{pa_0}/l_{pa_1}) vs. scan rate in the same conditions; d) current function ($l_p/v^{1/2}$) vs. scan rate

For A_0 and C_0 , the peak current increases proportionally up to 0.3 V s^{-1} with increasing square root of scan rates. The anodic peak current ratio (I_{pa_0}/I_{pa_1}) for the catechol-proline mixture initially increased with rising scan rates up to 0.3 V s^{-1} and then decreased (Figure 2c). Correspondingly, the peak current ratio (I_{pa_0}/I_{pc_0}) also decreased with increasing scan rates initially but then increased after reaching 0.3 V s^{-1} (Figure 2c). Additionally, the current function value $(I_p/v^{1/2})$ was observed to decrease with rising scan rates (Figure 2d). The exponential trend observed in the current function versus scan rate graph suggests an ECE (electrochemical-chemical-electrochemical) mechanism for the electrode process [13,14,26]. This indicates that the reactivity of o-benzoquinone (1a in Scheme 1) with proline (2 in Scheme 1) firstly increases at lower scan rates but decreases at higher scan rates.

The evidence supporting a subsequent chemical reaction between o-benzoquinone **1a** and proline **2** (step 2 in Scheme 1) includes the following points:

- i. In the presence of proline, both the anodic peak current (I_{pa_1}) and cathodic peak current (I_{pc_1}) decrease during the second cycle (see Figure 1), suggesting that the electrochemically generated o-benzoquinone **1a** is partially consumed through a chemical reaction with proline **2**.
- ii. The ratio of the peak currents (I_{pa_0}/I_{pc_0}) decreases as the potential sweep rate increases up to 0.3 V s⁻¹, after which it begins to rise gradually. This suggests that at lower scan rates, a greater accumulation of cathodic species occurs, whereas at higher scan rates, anodic species are more prevalent.

- iii. The peak current ratio (I_{pa_0}/I_{pa_1}) shows an initial increase followed by stabilization. An increase in the scan rate leads to a reduction in the extent of the chemical reaction between **1a** and **2** while the cyclic voltammogram is being recorded [26].
- iv. The current function, represented as $I_p/v^{1/2}$, decreases exponentially with increasing scan rate. This finding suggests that the reaction mechanism involves a sequence of electron transfer, a chemical reaction, followed by another electron transfer type (see Scheme 1) [13,14].

Based on these results, it appears that the 1,4-Michael addition reaction of proline 2 to o-benzo-quinone **1a** produces compound **3**. The oxidation of this product **3** is facilitated compared to the oxidation of the parent molecule **1** due to the presence of the electron-donating amine group.

The cyclic voltammogram of pure catechol was also observed in a buffer solution of pH 7 by varying scan rates. The linear relationship between the anodic and cathodic peak currents versus the square root of the scan rates indicates that the peak current of the reactant during each redox reaction is influenced by the diffusion process.

Influence of pH

The electrochemical properties of catechol were investigated both in the presence and absence of proline by analysing the electrode response in buffer solutions with varying pH levels from 5 to 11. CV was conducted to examine the oxidation of 2 mM catechol at a scan rate of 0.1 V s⁻¹ across different pH values. In a buffer solution at pH 7, catechol produced a distinct reversible wave. The anodic peak potential for catechol shifted to the left as the pH increased. The electrochemical reaction involving catechol at pH 7 is characterized as a two-proton, two-electron transfer process (as illustrated in Scheme 1) [29,30].

The cyclic voltammogram of 2 mM catechol in the presence of 150 mM proline was analyzed using a 3 mm glassy carbon electrode in buffer solutions at pH levels ranging from 5 to 11 (see Figure 3a). At pH 5 to 7, the voltammetric behaviour of catechol indicates that new anodic and cathodic peaks developed upon second cycling, suggesting that the reaction between o-benzoquinone and proline occurred (Figure 3a). At pH 7, the peak currents for both the anodic peak (A₀) and the cathodic peak (C₀) are greater than those observed at pH 5. In contrast, at higher pH values (specifically between pH 9 and 11), the cyclic voltammograms of catechol exhibit irreversible characteristics. In the basic medium, OH⁻ acted as a stronger nucleophile than proline; it underwent a homogeneous chemical reaction with o-benzoquinone. This homogeneous reaction was too fast that it cannot be observed in the time scale of cyclic voltammetry. This suggests that in alkaline environments, the oxidation of catechol proceeds by undergoing an irreversible chemical reaction with hydroxide ions [30].

In neutral media, o-benzoquinone can react with the amine group *via* a nucleophilic substitution mechanism through a 1,4-Michael addition, resulting in the appearance of a new anodic peak in voltammetric cycling. The position of the redox couple peak varies with changes in pH.

Figure 3 b illustrates the relationship between oxidation peak potential (E_p) and pH. The slopes of the plot were determined graphically as the anodic peaks (39.0 and 32.0 mV/pH for anodic peaks A_1 and A_0) at 0.1 V s^{-1} , which aligned closely with the theoretical expectation for a process involving two electrons and two protons. This finding suggests that the oxidation processes of both catechol and the catechol-proline adduct proceed through the $2e^-/2H^+$ mechanism (refer to Scheme 1). It also implies that during the reaction, protons, as well as electrons, are released from the catechol-proline adduct. Other researchers have observed similar behaviours in studies of catechol and its derivatives [12-14,22,31]. In both acidic and basic mediums, the peak current ratio decreased.

The plot of oxidation peak (A_0) current (I_p) versus pH of the buffer solution is shown in Figure 3c. The data indicates that the peak current reaches its maximum at pH 7. At this pH level, the difference in the peak current ratio (I_{pa_0}/I_{pc_1}) between the presence and absence of proline was at its highest. This suggests that the electrochemical oxidation of catechol with proline is more effectively facilitated in neutral conditions, accelerating the rate of electron transfer. Therefore, this study adopts a buffer solution with a pH of 7 as the optimal medium for the electrochemical analysis of catechol in the presence of proline.

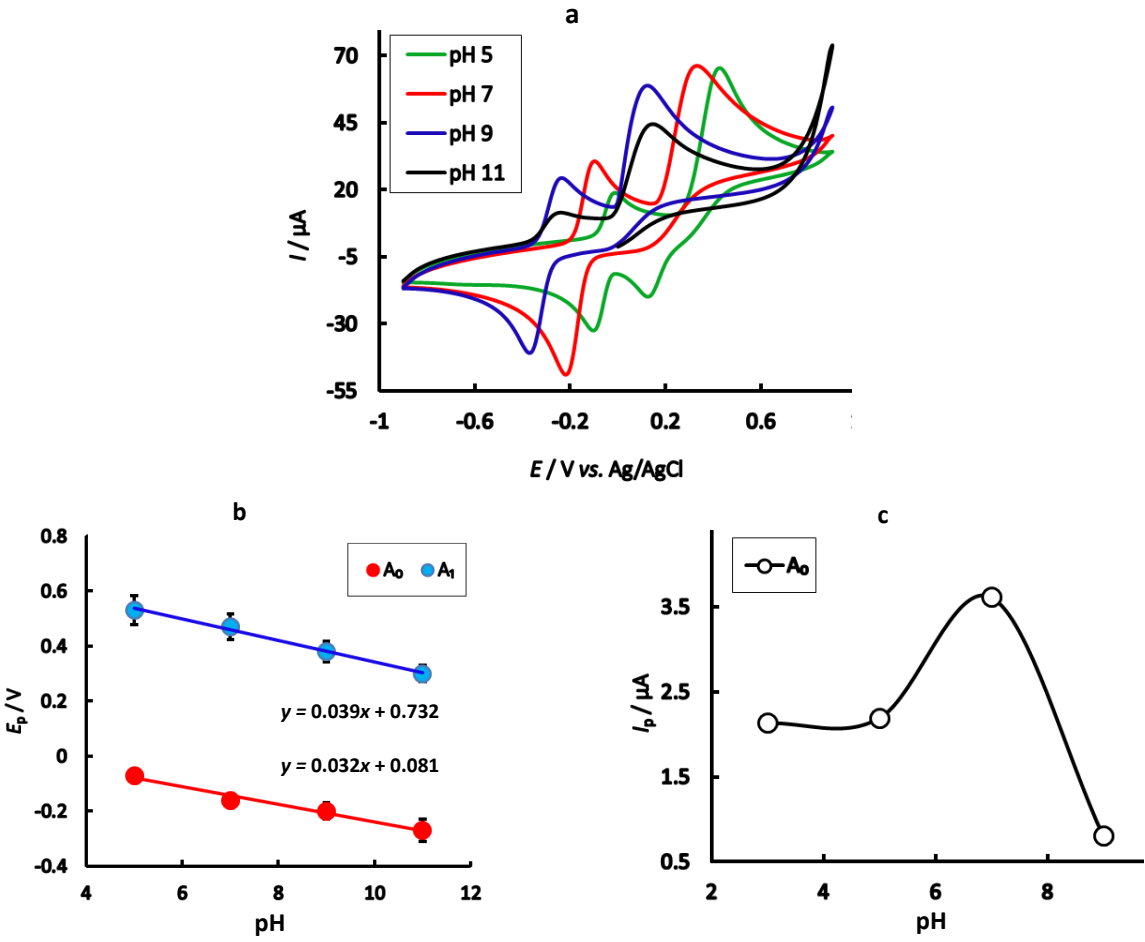


Figure 3. a) Cyclic voltammograms of 2 mM catechol with 150 mM proline of GC (3 mm) electrode in buffer solutions of different pH, at a scan rate 0.1 V s^{-1} ; b) plots of peak potential vs. pH in the same conditions; c) plots of peak current vs. pH in the same conditions. The meaning of symbols A_0 and A_1 is like in Figure 1

Concentration effect of proline

Figure 4a illustrates the changes in the voltammogram pattern by incorporating varying concentrations of proline (50, 100, 150, 200, and 250 mM) into a constant concentration of catechol (2 mM) of the glassy carbon electrode in a buffer solution of pH 7 and a scan rate 0.1 V s⁻¹. The net current intensity of the newly observed anodic and cathodic peaks increases as the proline concentration rises up to 150 mM. However, with further increases in proline concentration (beyond 150 mM), there is a decrease in the anodic and cathodic peak currents (see Figure 4b). At these higher proline concentrations (>150 mM), the excess amount of electro-inactive proline may accumulate on the electrode surface, leading to a reduction in peak current. This suggests that the nucleophilic substitution reaction of catechol in the presence of proline was most favourable at a concentration of up to 150 mM proline at pH 7.

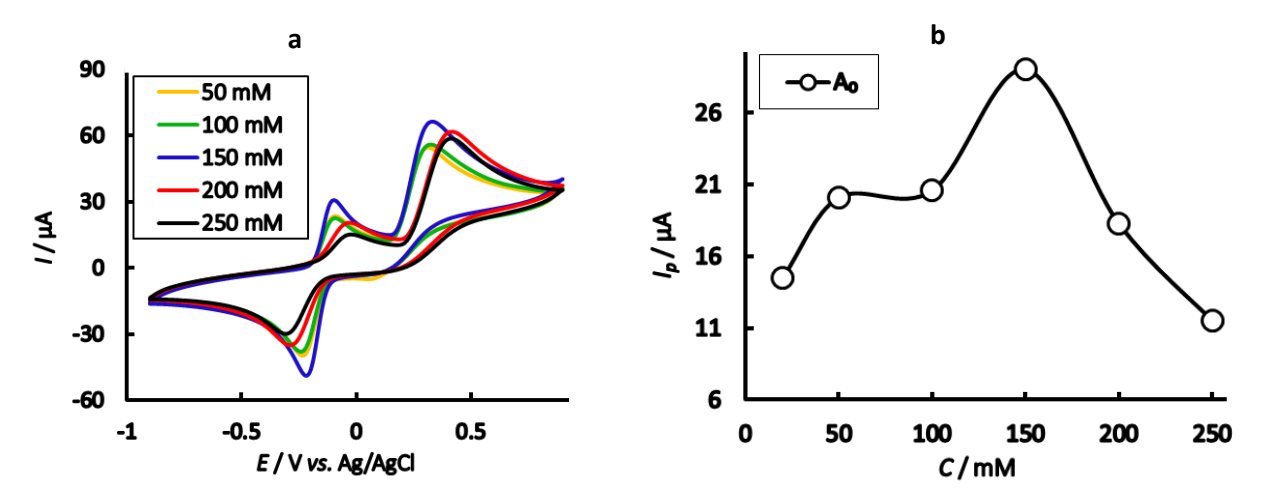


Figure 4. a) Cyclic voltammograms of composition changes of proline with fixed 2 mM catechol at GC electrode in buffer solution at pH 7, and scan rate 0.1 V s⁻¹; b) plots of anodic peak current vs. concentration of proline with fixed 2 mM catechol in the same conditions. The meaning of A_0 is like in Figure 1

Effect of electrode materials

The electrochemical characteristics of catechol were investigated both in the absence and presence of proline using various electrodes, including glassy carbon, gold, and platinum, under different pH conditions. The CV of 2 mM catechol in the presence of 150 mM proline at the GC, gold and platinum electrodes in buffer solution of pH 7 and a scan rate of 0.1 V s⁻¹ are presented in Figure 5a. The characteristics of the voltammograms, including peak positions and current intensities, vary across the different electrodes despite a larger diameter of the GC than gold and platinum electrodes.

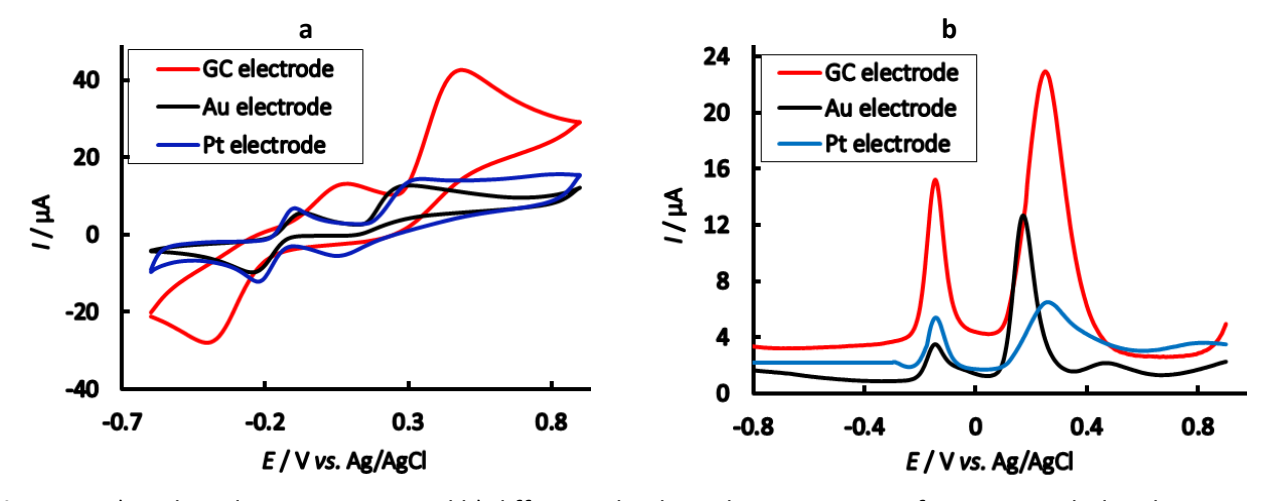


Figure 5. a) Cyclic voltammograms and b) differential pulse voltammograms of 2 mM catechol with 150 mM proline at GC electrode (3.0 mm) gold electrode (1.6 mm) and platinum electrode (1.6 mm) in buffer solution of pH 7 and scan rate 0.1 V s^{-1}

The electrochemical characteristics of catechol in the presence of proline, including variations in pH, concentration, and scan rate, have been extensively studied using platinum and gold electrodes. In the second potential cycle, all electrodes show a new oxidation and reduction peak at a lower oxidation potential. This phenomenon is likely due to the oxidation of the adduct formed between o-benzoquinone and proline. GC, Pt, and Au electrodes show two redox couples of adducts at 0.05/-0.38, -0.12/-0.21 and -0.08/-0.21 V, respectively. The DPV of 2 mM catechol in the presence of 150 mM proline at GC, gold, and platinum electrodes at pH 7 and a scan rate of 0.1 V s⁻¹ are also

presented in Figure 5b. The DPV response is similar to the CV response. However, the GC electrode demonstrated notably better voltammetric responses than other evaluated electrodes. As a result, this paper concentrates primarily on the properties of catechol with proline when utilizing the GC electrode.

Subsequent cycles of CV of catechol-proline derivative

Figure 6a illustrates the cyclic voltammogram of the initial 15 cycles of 2 mM catechol in the presence of 150 mM proline in a buffer solution of pH 7 buffer solution using a GC (3.0 mm) electrode, within a potential range from -0.9 to 0.9 V. The first cycle revealed an anodic peak at 0.38 V and a corresponding cathodic peak at -0.29 V, as marked by the red line, with a scan rate of 0.1 V s⁻¹. In the following cycles, a new anodic peak emerged around 0.02 V, while the current of the initial anodic peak steadily increased with cycling. In contrast, the current for the second anodic peak decreased and shifted positively. This behaviour is attributed to the formation of a catechol-proline adduct, which resulted in a gradual reduction in the redox couple height of catechol due to a nucleophilic substitution reaction occurring at the electrode surface (refer to Scheme 1). The gradual decline in the height of the peaks associated with the oxidation and reduction of catechol during cycling can be attributed to the increased formation of the catechol-proline adduct. This results in a reduced concentration of catechol or quinone available at the electrode surface. Over the first ten cycles, the first anodic peak current increases but is stabilized with subsequent cycles, likely due to the buildup of newly formed electro-inactive species blocking the electrode surface after extensive cycling.

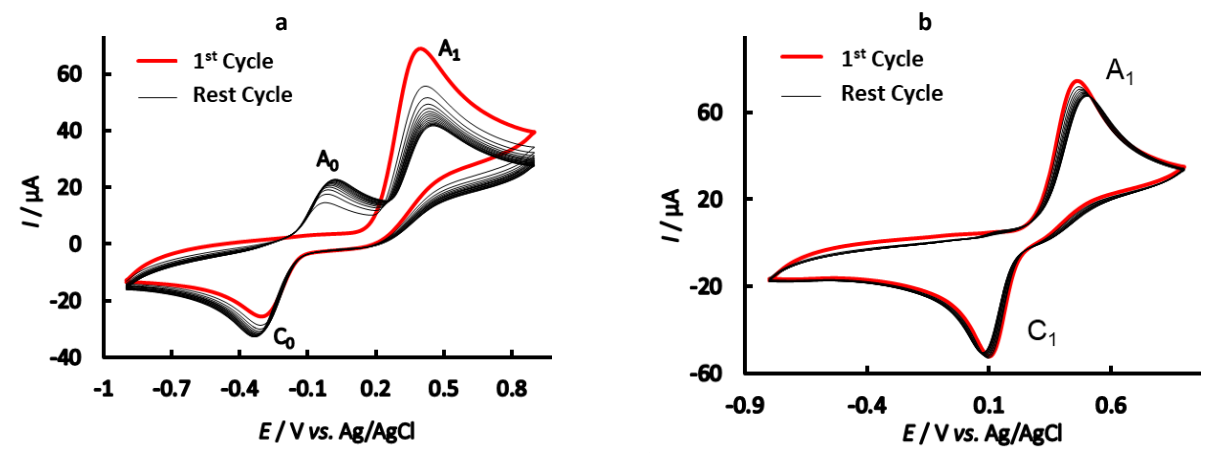


Figure 6. a) Cyclic voltammograms of 150 mM proline with 2mM catechol on GC (3 mm) electrode in the buffer solution of pH 7 at scan rate 0.1 V s^{-1} (15 cycles). The anodic peak current (A_0) and cathodic peak current (C_0) increased with the iteration scan from the first cycle; b) CV of 2mM catechol in the buffer solution of pH 7 at scan rate 0.1 V s^{-1} (15 cycles). The first cycle is denoted by red line and the rest of the cycles by black lines

In Figure 6b, the cyclic voltammograms of the first 15 cycles of 2 mM catechol on the GC (3 mm) electrode in a pH 7 buffer solution are displayed. At a scan rate of 0.1 v s⁻¹, one anodic peak appeared at 0.43 V, along with a cathodic peak at 0.11 V (red line), and no new anodic peak emerged in later cycles. This observation suggests that catechol primarily displayed one anodic and corresponding cathodic peak associated with its conversion to o-quinone (as shown in Scheme 1). Throughout the repetitive cycling of potential, the ratio of anodic to cathodic peak currents is nearly equal (illustrated in Figure 6b), which can be interpreted as an indicator of the stability of the o-quinone formed on the electrode surface [29]. This implies that reactions such as hydroxylation or dimerization [32,33] occur at a rate that is too slow to be detected within the time frame of cyclic voltammetry [29].

Following the addition of 150 mM proline during the first cycle (Figure 6a), no new reduction peak is evident; rather, the reduction peak shifted due to a decrease in catechol species caused by proline. In the second potential scan (Figure 6a), a new oxidation peak around -0.01 V appeared, likely corresponding to the oxidation of an adduct formed between o-benzoquinone and proline, as illustrated in Scheme 1.

Controlled-potential coulometry was conducted in an aqueous solution containing 1 mM catechol and 75 mM proline at 0.5 V in pH 7. The progression of the electrolysis was monitored using cyclic voltammetry and differential pulse voltammetry (Figure 7). As illustrated in Figure 7, during the coulometric process, peaks A_0 and C_0 appeared, but the height of peaks A_0 and C_0 did not increase in direct proportion to the progress of the coulometry, coinciding with a reduction in height for both the anodic peak A_1 and the cathodic peak C_1 (the meaning of symbols A_0 , C_0 , C_1 and C_2 is similar to Figure 1). Ultimately, all anodic and cathodic peaks disappeared after the consumption of 4 electrons per molecule.

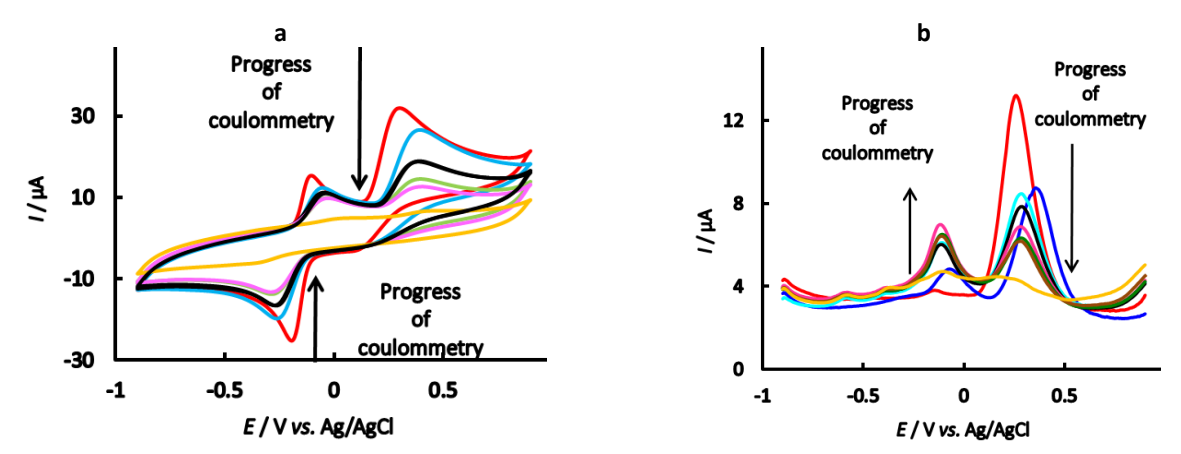


Figure 7. a) Cyclic voltammograms and b) differential pulse voltammograms (taken after a 30-minute interval) of 1 mM catechol in the presence of 75 mM proline of GC electrode in buffer solution, pH 7 during controlled potential coulometry at 0.5 V and scan rate 0.1 V s⁻¹

These observations enable us to suggest the pathway illustrated in Scheme 1 for the electro-oxidation of catechol 1 in the presence of proline 2. These findings indicate that the 1,4 addition reaction of proline 2 to o-quinone 1a occurs more rapidly than other secondary reactions, resulting in the formation of intermediate 3. The oxidation of this intermediate 3 is more favourable than that of the original starting molecule 1 due to the presence of an electron-donating group. Similarly, o-quinone 4 can also be attacked by proline 2 at the C-5 position. Nevertheless, no excessive reaction was detected during voltammetric experiments, likely due to the relatively low reactivity of o-quinone 4 towards the 1,4 (Michael) addition with proline 2.

Differential pulse voltammetry

In Figure 8, a DPV of 2 mM catechol in the presence of 150 mM proline in a second scan at different pHs (5 to 11) was exhibited. In a buffer solution with a pH of 7, catechol exhibited two distinct peaks when proline was present (Figure 8). In neutral media, the first and second anodic peaks were shown at -0.15 V and 0.24 V, respectively. In the second scan of potential, the anodic peak current intensity observed at pH 5, 9 and 11 is notably low. The DPV voltammogram is consistent with CV. From Figures 3 and 8, it was seen that two distinct anodic peaks exhibiting high current intensity were detected at pH 7 due to the oxidation of the o-benzoquinone-proline derivative. Product 3 can also be embattled by proline, but this reaction is not detected during the differential pulse voltammetry analysis.

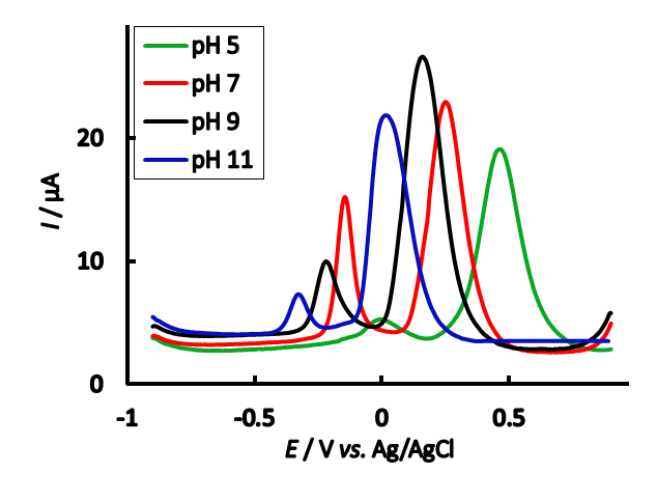


Figure 8. Differential pulse voltammograms in the second scan of 2 mM catechol with 150 mM proline of GC electrode at different pH levels of buffer solution and scan rate 0.1 V s^{-1}

Effect of deposition time in DPV

Figure 9 illustrates differential pulse voltammetry (DPV) responses for various deposition times (0, 10, 60, 120, 150 and 240 seconds) using a solution of 2 mM catechol and 150 mM proline in a buffer solution at pH 7.

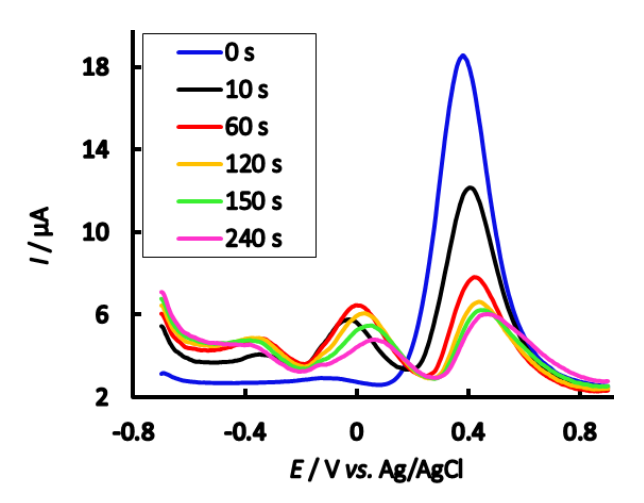


Figure 9. Differential pulse voltammograms of 2 mM catechol with 150 mM proline in buffer solution of pH 7 for various deposition time changes at E_{puls} 0.02 V, t_{puls} 20 ms and scan rate 0.1 V s^{-1}

It is shown that an increase in deposition time results in the appearance of a significant new peak at -0.02 V. A rise in deposition time by 10 seconds promotes nucleophilic attack, resulting in the formation of more catechol-proline adduct at the electrode surface. This leads to a decrease in the concentration of o-benzoquinone and an increase in the concentration of the catechol-proline adduct. Maximum peak intensity was achieved at a 60-second deposition time. However, when the deposition time extends beyond 60 to 240 seconds, both the first and second anodic peak currents diminish. It can be inferred that longer deposition times decrease the concentration of o-benzoquinone.

The effect of proline concentration on catechol was also examined using DPV (Figure 10). The study involved 2 mM catechol with proline concentrations ranging from 50 to 250 mM at pH 7. As shown in a previous CV shown in Figure 1, two distinct anodic peaks were observed with the addition of proline to catechol. Increasing the concentration of proline up to 150 mM resulted in a rise in the current of the first anodic peak. However, when the concentration was increased further, from 200 to 250 mM, a gradual decrease in all anodic peak currents was noted. At lower proline concentrations (<140 mM), the nucleophilic substitution reaction occurred to a similar extent, but as the concentration of proline

exceeded 140 mM, the nucleophilic attack on the o-benzoquinone generated at the electrode surface became more favorable. Further addition of proline beyond 150 mM led to an accumulation of excess electronactive proline on the electrode's surface, resulting in a reduction in peak current.

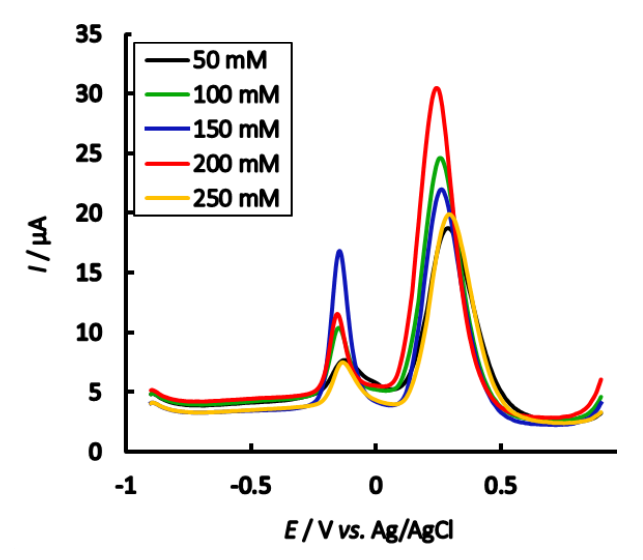


Figure 10. Differential pulse voltammograms of 2 mM catechol at different proline concentrations in the second scan of pH 7 at E_{puls} 0.02V, t_{puls} 20 ms of GC electrode and scan rate 0.1 V/s

Spectral analysis of catechol with proline

The FTIR spectra of the catechol-proline adduct were taken over the wavenumber range of 400 to 4000 cm⁻¹. The FTIR spectrum of the catechol-proline adduct has been shown in Figure 11.

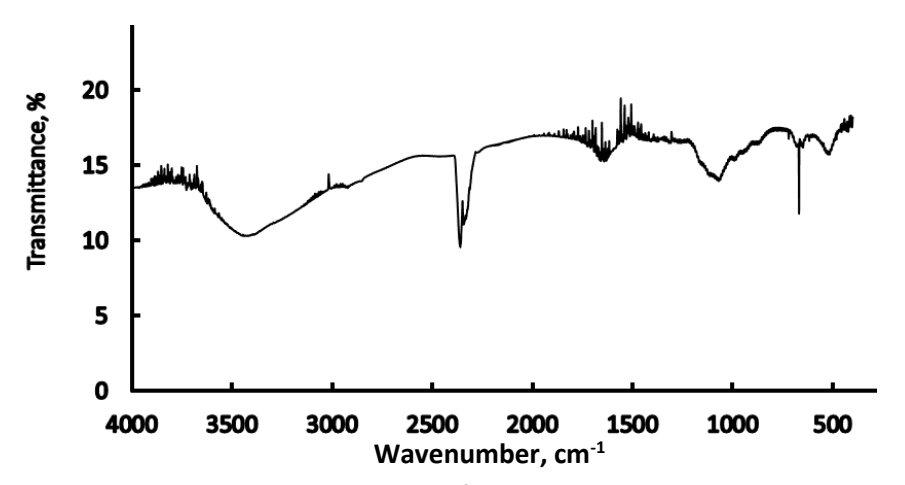


Figure 11. FTIR spectrum of catechol-proline adduct

Catechol displays an O-H stretching band at 3450 cm⁻¹, while proline exhibits a broad spectrum at 3380 cm⁻¹caused by the overlap of O-H and N-H stretching bands. In the catechol-proline adduct, the absorption peak corresponding to the broad O-H stretching vibration occurs at 3350 cm⁻¹. For the catechol-proline adduct, the peak intensity for N-H stretching decreases, and a significant change in fingerprint region is observed. Similar behaviours have been noted in studies of catechol and its derivatives [13]. This also verified the formation of a catechol-proline adduct.

Based on the preceding analysis, it is evident that the nucleophilic substitution reaction of catechol and proline is most favourable at a concentration of 150 mM proline and 2 mM of catechol and a pH of 7 at the GC electrode. This finding aligns with the results obtained from both cyclic voltammetry and differential pulse voltammetry.

Conclusions

The electrochemical behavior of catechol, both in the absence and presence of proline, was examined using cyclic voltammetry, differential pulse voltammetry, controlled potential coulometry, and FTIR spectroscopy. To determine the optimum reaction conditions of catechol and proline, an investigation was conducted to examine the effects of pH level, electrode materials, and solution concentration on the reaction. The oxidation of catechol leads to the formation of o-benzoquinone, which is subsequently attacked by proline. The products generated from the reaction are accomplished by transferring electrons at a more negative potential than catechol. The oxidation reaction of catechol-proline adducts is produced *via* the one-step 2e⁻/2H⁺ process. The voltammetric performance of the glassy carbon (GC) electrode is better than that of gold (Au) and platinum (Pt) electrodes. The peak current for the catechol-proline adduct during each redox reaction is governed by a diffusion process. The nucleophilic reaction involving of catechol in the presence of proline is most favourable at a concentration of 2 mM catechol and 150 mM proline and at pH 7 on a glassy carbon electrode. The catechol-proline adduct was electrochemically synthesized during coulometry, supported by FTIR spectrum. The nucleophilic addition reaction of proline with catechol occurs *via* an electron transfer, chemical reaction and electron transfer mechanism.

Conflict of interest: All authors declare no conflicts of interest

Acknowledgments: Thanks to Ministry of Science and Technology, Government of the People's Republic of Bangladesh and KUET for providing necessary facilities and financial support to this research work.

References

- [1] A. B. Barner, *Catechol, in Encyclopedia of Reagents for Organic Synthesis*, John Wiley & Sons, New York, USA, 2004. https://doi.org/10.1002/047084289
- [2] L. Khalafi, M. Rafiee, Kinetic study of the oxidation and nitration of catechols in the presence of nitrous acid ionization equilibria, *Journal of Hazardous Materials* **174** (2010) 801-806. https://doi.org/10.1016/j.jhazmat.2009.09.123
- [3] R.H. Bisby, R. Brooke, S. Navaratnam, Effect of antioxidant oxidation potential in the oxygen radical absorption capacity (ORAC) assay, *Food Chemistry* **108** (2008) 1002-1007. https://doi.org/10.1016/j.foodchem.2007.12.012
- [4] M. Rafiee, The Electron: The Simplest Chemical Reagent, *Synlett* **2007** (2007) 503–504. http://dx.doi.org/10.1055/s-2006-967938
- [5] D. Nematollahi, M. Rafiee, L. Fotouhi, Mechanistic study of homogeneous reactions coupled with electrochemical oxidation of catechols, *Journal of the Iranian Chemical Society* **6** (2009) 448-476. https://doi.org/10.1007/BF03246523
- [6] Edward C. Conley, Ion Channel Factsbook: Extracellular Ligand-Gated Channels. Academic Press, 1995, p. 126. ISBN 0-12-184450-1
- [7] V. Henzi, D. B. Reichling, S. W. Helm, A. B. MacDermott, Proline activates glutamate and glycine receptors in cultured rat dorsal horn neurons, *Molecular Pharmacology* **41** (1992) 793-801. https://pubmed.ncbi.nlm.nih.gov/1349155
- [8] O. E. Arslan, *Neuroanatomical basis of clinical neurology*. CRC Press, 2014, p. 522. ISBN 9780429105531
- [9] M. Y. Pavlov, R. E. Watts, Z. Tan, V. W. Cornish, M. Ehrenberg, A.C. Forster, Slow peptide bond formation by proline and other N-alkylamino acids in translation, Proceedings of the National Academy of Sciences of the United States of America 106 (2009) 50-54. https://doi.org/10.1073/pnas.0809211106

- [10] M. A. Motin, M. Nazim Uddin, P. K. Dhar, M. A. Hafiz Mia, M. A. Hashem, Voltammetric Electro-synthesis of Catechol-Aspartic Acid Adduct at Different pHs and Concentrations, *Analytical and Bioanalytical Electrochemistry* **8** (2016) 505-521. https://sid.ir/paper/346502/en
- [11] M. A. Motin, M. Alim Uddin, M. Nazim Uddin, P. K. Dhar, M. A. Hafiz Mia, M. A. Hashem, Electrochemical Oxidation of Catechol in the Presence of Sulfanilic Acid at Different pH, *Portugaliae Electrochimica Acta* **35** (2017) 103-116. http://dx.doi.org/10.4152/pea.201702103
- [12] M. A. Hafiz Mia, M. A. Motin, E.M. Huque, M. Nazim Uddin, P. K. Dhar, M. A. Hashem, Electrooxidation of catechol in the presence of L-glutamine at different pH and concentrations, *Analytical and Bioanalytical Electrochemistry* **9** (2017) 597-613. https://sid.ir/paper/346539/en
- [13] M. A. Hafiz Mia, M. A. Motin, E. M. Huque, Electrochemical Oxidation of Catechol in the Presence of L-Lysine at Different pH, *Russian Journal of Electrochemistry* **55** (2019) 370-380. http://dx.doi.org/10.1134/S1023193519050070
- [14] M. A. Hafiz Mia, M. A. Motin, E.M. Huque, Electrochemical Characterization of Catechol-Dimethylamine Adduct at Different pH Values, *Portugaliae Electrochimica Acta* **36** (2018) 437-454. http://dx.doi.org/10.4152/pea.201806437
- [15] M. A. Hafiz Mia M. A., Motin, E. M. Huque, Electrooxidation of catechol in the presence of l-histidine at different pH, Analytical and Bioanalytical Electrochemistry 10 (2018) 974-990. https://sid.ir/paper/346394/en
- [16] L. Khalafi, M. Rafiee, M. Shahbak, H. Shirmohammadi, Kinetic study of the oxidation of catechols in the presence of N-methylaniline, *Journal of Chemistry* 2013 (2013) 497515. https://doi.org/10.1155/2013%2F497515
- [17] S. Shahrokhian, A. Hamzehloei, Electrochemical oxidation of catechol in the presence of 2-thiouracil: application to electro-organic synthesis, *Electrochemistry Communications* 5 (2003) 706-710. https://doi.org/10.1016/S1388-2481(03)00170-X
- [18] D. Nematollahi, S. M. Golabi, Investigation of the Electromethoxylation Reaction Part 2: Electrochemical Study of 3-Methylcatechol and 2,3-Dihydroxybenzaldehyde in Methanol, Electroanalysis 13 (2001) 1008-1015. https://doi.org/10.1002/1521-4109(200108)13:12%3C1008::AID-ELAN1008%3E3.0.CO;2-1
- [19] D. Nematollahi, H. Goodarzi, Electrochemical study of catechol and some of 3-substituted catechols in the presence of 1,3-diethyl-2-thio-barbituric acid. Application to the electroorganic synthesis of new dispirothiopyrimidine derivatives, *Journal of Electroanalytical Chemistry* **510** (2001) 108-114. https://doi.org/10.1016/S0022-0728(01)00553-8
- [20] I. Tabaković, Z. Grujić, Z. Bejtović, Electrochemical synthesis of heterocyclic compounds. XII. Anodic oxidation of catechol in the presence of nucleophiles, *Journal of Heterocyclic Chemistry* **20** (1983) 635-638. https://doi.org/10.1002/jhet.5570200325
- [21] [21] D. Nematollahi, Z. Forooghi, Electrochemical oxidation of catechols in the presence of 4-hydroxy-6-methyl-2-pyrone, *Tetrahedron* **58** (2002) 4949-4953.https://doi.org/10.1016/S0040-4020(02)00422-2
- [22] F. Nourmohammadi, S.M. Golabi, A. Saadnia, Electrochemical synthesis of organic compounds: 1. Addition of sulfinic acids to electrochemically generated *o* and *p*-benzoquinones, *Journal of Electroanalytical Chemistry* **529** (2002) 12-19. https://doi.org/10.1016/S0022-0728(02)00906-3
- [23] A. Kiani, JB. Raoof, D. Nematollahi, R. Ojani, Electrochemical Study of Catechol in the Presence of Dibuthylamine and Diethylamine in Aqueous Media: Part 1. *Electroanalysis* **17** (2005) 1755-1760. https://doi.org/10.1002/elan.200503279
- [24] P. Janeiro, A. Maria, O. Brett, Catechin electrochemical oxidation mechanisms, *Analytica Chimica Acta* **518** (2004) 109-115. https://doi.org/10.1016/j.aca.2004.05.038



- [25] A. Masek, E. Chrzescijanska, M. Zaborski, Electrochemical Properties of Catechin in Non-Aqueous Media, *International Journal of Electrochemical Science* **10** (2015) 2504-2514. https://doi.org/10.1016/S1452-3981(23)04864-2
- [26] L. Papouchado, R. W. Sandford, G. R. Petrie, N. Adams, Anodic oxidation pathways of phenolic compounds Part 2. Stepwise electron transfers and coupled hydroxylations, *Journal of Electroanalytical Chemistry and Interfacial Electrochemistry* **65** (1975) 275-284. https://doi.org/10.1016/0368-1874(75)85123-9
- [27] P. A. Thibodeau, B. Paquette, DNA damage induced by catecholestrogens in the presence of copper (II): generation of reactive oxygen species and enhancement by NADH, *Free Radical Biology and Medicine* **27** (1999) 1367-1377. https://doi.org/10.1016/s0891-5849(99)00183-5
- [28] A.J. Bard, L. R. Faulkner, *Electrochemical Methods Fundamentals and Applications*, Second Edition, John Wiley & Sons, 2001, p. 226. ISBN 0-471-04372-9
- [29] D. Nematollahi, A. Afkhami, F. Mosaed, M. Rafiee, Investigation of the electrooxidation and oxidation of catechol in the presence of sulfanilic acid, *Research on Chemical Intermediates* **30** (2004) 299-309. https://doi.org/10.1163/1568567041257535
- [30] L. Papouchado, G. Petrie, R. N. Adams, Anodic oxidation pathways of phenolic compounds: Part I. Anodic hydroxylation reactions, *Journal of Electroanalytical Chemistry and Interfacial Electrochemistry* **38** (1972) 389-395. https://doi.org/10.1016/S0022-0728(72)80349-8
- [31] L. Papouchado, G. Petrie, J. H. Sharp, R. N. Adams, Anodic hydroxylation of aromatic compounds, *Journal of the American Chemical Society* **90** (1968) 5620-5621. https://doi.org/10.1021/ja01022a061
- [32] M.D. Rayn, A. Yueh, C. Wen-Yu, The electrochemical oxidation of substituted catechols, Journal of The Electrochemical Society **127** (1980) 1489. https://doi.org/10.1149/1.2129936
- [33] M. Pasta, F. L. Mantia, Y. Cui, Mechanism of glucose electrochemical oxidation on gold surface, *Electrochimica Acta* **55** (2010) 5561-5568. http://dx.doi.org/10.1016/j.electacta.2010.04.069



Open Access :: ISSN 1847-9286 www.jESE-online.org

Original scientific paper

Machinability studies on metal additive manufactured 316L stainless steel using electrochemical machine

Rajan Natarajan^{1,⊠}, Shanmugapriyan Kanagaraj¹, Thangavel Palaniappan² and Deepa Dhanaskodi³

¹Vinayaka Mission's Kirupananda Variyar Engineering College, Vinayaka Mission's Research Foundation, Deemed to be University, Salem-636308, India

²Erode Sengunthar Engineering College, Perundurai 638057, India

³Bannari Amman Institute of Technology, Sathyamangalam, 638401, India

Corresponding authors: [™]nrajaned@gmail.com

Received: November 12, 2024; Accepted: January 21, 2025; Published: January 30, 2025

Abstract

Metal additive manufactured 316L stainless steel is considered for machinability studies through electrochemical machining (ECM). This material is used in prototyping in the automotive, aerospace, jewellery and biomedical industries, where customized components for individual circumstances are required. In this study, ECM process parameters such as voltage, electrolyte concentration, duty cycle, and selection of an L16 orthogonal array sing four levels were considered for optimization. The multi-criteria decision machining method, namely entropy-based multi-objective optimization, is used for performance analysis based on the ratio analysis method. The study reveals that 14 V, 35 g l⁻¹ NaNO₃ electrolyte concentration, and 90 % duty cycle are recommended for optimal machining performance. According to the main effect table, the best combination is 16 V, 35 g l⁻¹ electrolyte concentration, and 60 % duty cycle. Analysis of variance result shows that the duty cycle accounts for approximately 27.06 1% of machining performance, voltage contributes by 24.015 % and electrolyte content contributes roughly 15.58 % to the machining performance. A scanning electron microscope was used to scan each micromachined hole, and different resolution images were taken in order to analyse the machined hole quality.

Keywords

Additively built austenitic steel; micromachined holes; electrochemical process parameters; multi-objective optimization (MOORA); entropy weighting; variance analysis

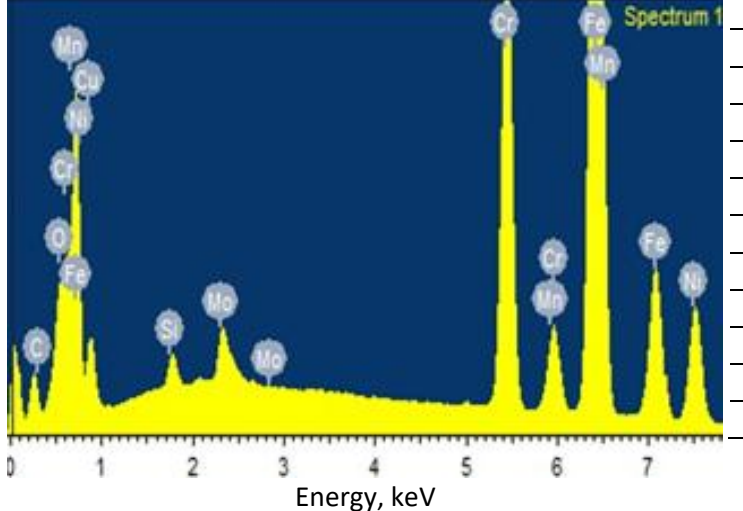
Introduction

Metal additive manufacturing (AM) has garnered widespread recognition on a limited range of elemental metals and alloys due to its capacity to produce small quantities at low cost, handle intricate part geometries and optimized topologies, attain moderate part density (>90 %), and demonstrate mechanical performance in uniaxial, biaxial, and torsion testing [1,2]. Masek *et al.* [3] have studied the

effect of milling parameters on the 3D-printed 316 stainless steel (SS). They stated that surface profiles and forces recorded during the machining of the additively built specimen indirectly revealed the variability of the mechanical characteristics. When low cutting conditions were used, the machinability of the additively created specimens improved. In the event of total force and surface roughness, increasing cutting circumstances deteriorate their relative machinability. The cutting reactions of Ti6Al4V alloy that was additively created using solid ceramic tools under dry high-speed milling procedures were investigated by Zhang et al. [4] in 2020. As a result of machining parameters, a number of issues were examined, including cutting forces and cutting temperature fields. The findings suggest that feed rate influences temperature fields and cutting force magnitudes more than cutting speed. The machinability of the Inconel 718 superalloy sintered using a direct laser was examined by Chen et al. [5] in 2021. The outcomes showed that the coated carbide instruments may be used to cut the LAM Inconel 718 superalloy. Using coated carbide tools, the LAM Inconel 718 superalloy produced cutting forces, temperatures, and vibrations that were approximately 9.63, 6.29, and 16.67 % lower than those of the wrought Inconel 718 superalloy, respectively. The study conducted by Karabulut and Kaynak [6] concentrated on the drilling process of Inconel 718 alloy, which was produced by selective laser melting AM. Using carbide drill bits and varying drilling parameters, such as feed values and cutting speeds, specimens created by selective laser melting (SLM) were drilled. This study demonstrated how surface roughness is decreased throughout the drilling process, improving the surface quality of Inconel 718, which is additively built. Additively manufactured Inconel 625 metal workpieces show significantly unique behaviour on the machinability aspect of the finish milling process. They experienced the tool wear of the inserts, such as edge chipping and coat peeling. They observed that the milling force increases with the cutting speed and feed rate [7]. Bai et al. [8] machined directed energy deposition ASTM A131 steel using a milling technique and found that the largest cutting forces were caused by interference between the cutting tool and a significant number of melt-pool barriers, which restrict material flow. Tool wear tends to increase during the machining of the samples. Li et al. [9] investigated the machinability of 3D-printed SS316L and reported that the cutting force components Fx and Fy are found to be 76.8 and 48.88 N, respectively. The impact of using a standard grinding procedure on surface roughness and residual stress has been investigated by Ramachandran et al. [10] in 2024. High-cycle fatigue mechanical testing was carried out to confirm improved output performance. The surface grinding process is responsible for the noticeable improvement. The aforementioned research makes it clear that machinability tests are conducted on additive manufactured (AMed) components with the goal of enhancing surface and dimension quality. These AMed components are typically surface-ground and machined using traditional production techniques. The inherent drawbacks of this method include high residual stress, excessive tool wear and damage, and increased heat generation at the tool-workpiece interface as a result of the higher mechanical properties of the integrated components. Electrochemical machining (ECM) is used to machine the AM components for holes to get around these issues. Process parameters such as voltage, electrolyte concentration, duty cycle, and selection of an L₁₆ orthogonal array (OA) were optimized using four levels of selection. The multi-criteria decision machining method, namely the entropy-based multi-objective optimization based on ratio analysis (MOORA) method, is used performance analysis. The MOORA method was used by Gadakh et al. [11] for welding factors optimization, Bhaskar and Khan [12] for dental material selection, Soundarrajan and Thanigaivelan [13] and Vempannan et al. [14] for ECM process optimization, and Thiraviam et al. [15] for wear parameters analysis. Literature data for the ECM process optimization using entropy and MOORA is generally sparse; hence, in this research, ECM parameters are optimized using this former method. A scanning electron microscope (SEM) was used to scan each micro-machined hole, and different resolution images were taken to analyse the machined hole quality.

Experimental

High-performance marine-grade austenitic stainless steel with molybdenum alloying for improved corrosion resistance in chloride conditions is called EOS stainless steel 316L. For many uses in the process, energy, paper, transportation, and other sectors, 316L is a standard material. A powdered stainless steel, called EOS stainless steel 316L, is designed to be used in the production of parts using direct metal laser sintering (DMLS) procedure using EOS metal systems. EOS stainless steel 316L is a high-performance metal powder commonly used in additive manufacturing, notably 3D printing procedures like DMLS. It is commonly used to create components that require great strength, corrosion resistance, and longevity. The energy dispersive X-ray spectroscopy (EDAX) tests were performed to check the composition of the specimen EOS stainless steel 316L and revealed that all the alloying materials were present in the expected composition. Figures 1 and 2 show the elements chart and machined as received components EOS stainless steel 316L, respectively. This component was subjected to ECM machinability studies for making micro-holes. Figure 3 shows the setup used for making micro-holes on the EOS stainless steel 316L.



Element	Content, wt.% Content, at	
0	5.74 21.56	
С	2.14	5.41
Si	0.63	0.99
Cr	16.23	13.77
Mn	1.10	0.88
Fe	61.65	48.69
Ni	9.69	7.28
Cu	0.52	0.36
Мо	2.31	1.06
Total	100.01	100.00
•		<u> </u>

Figure 1. Elements details of the EOS stainless steel 316L

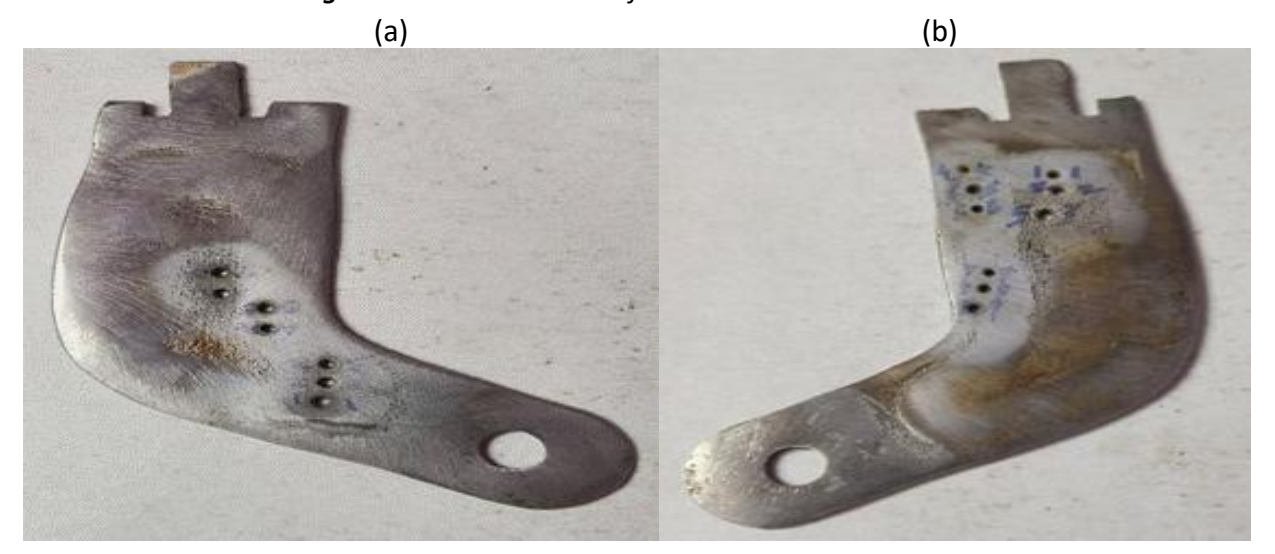


Figure 2. Machined EOS stainless steel 316L with (a) 7 holes and (b) 9 holes

The ECM setup consists of a machine structure, machining tank, filter with circulation pump, tool feeders with stepper motor and pulsed power supply [16]. In ECM, the tool electrode, the stitching needle of diameter 460 μ m, is connected with a negative power supply, while the workpiece EOS stainless steel 316L is connected with a positive power supply. The tool electrode circumference is insulated with bonding liquid to prevent the stray current. The electrolyte NaNO₃ is used to bridge two electrodes, and the pulse power supply initiates and sustains the electrochemical machining process as per Faraday's law of electrolysis [17]. The electrolyte is prepared by mixing different amounts of sodium nitrate salt in 1 l of distilled water. The brine solution is mixed thoroughly with the magnetic stirrer.

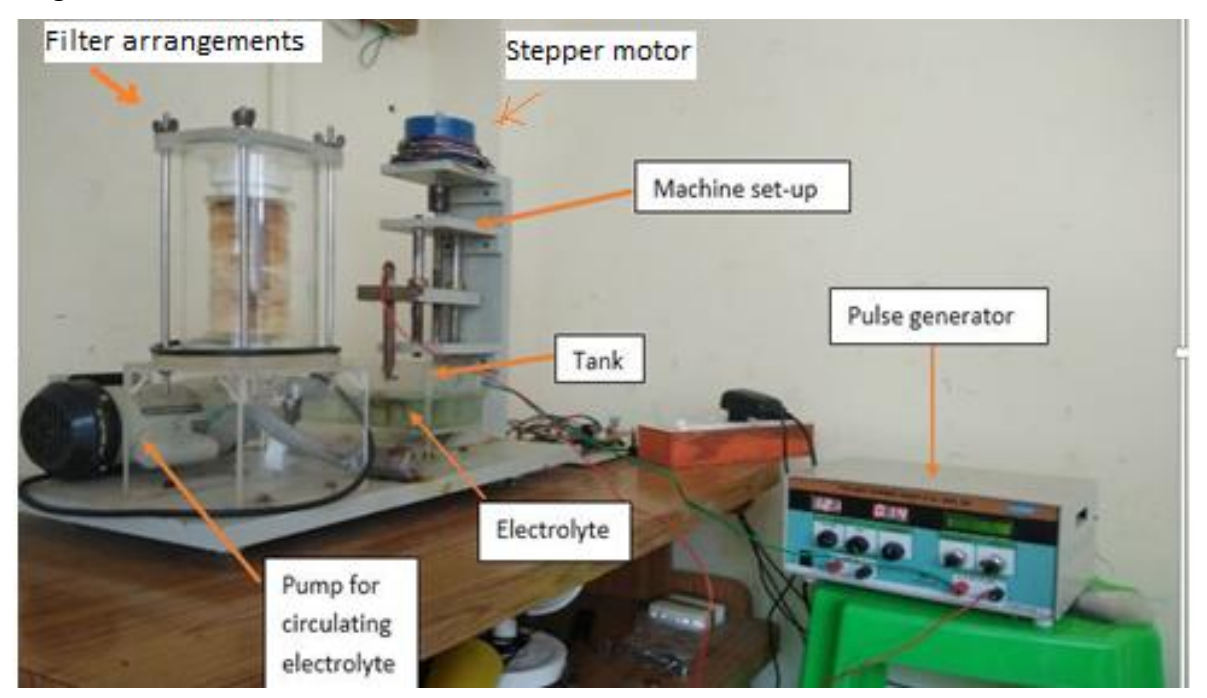


Figure 3. ECM setup with subsystems

In this experiment, the ECM process variables, namely voltage, electrolyte concentration and duty cycle, were varied and effects on the material removal rate (MRR) and overcut are followed. L_{16} OA is used for experiments, as presented in Table 1.

Table 1 . L ₁₆ OA experiment plan								
Exp. No	Voltage, V	NaNO ₃ electrolyte concentration, g l ⁻¹	Duty cycle, %	Material removal rate, mm min ⁻¹	Overcut, mm			
1	10	30	60	0.0291	0.625			
2	10	35	70	0.0306	0.580			
3	10	40	80	0.0521	0.349			
4	10	45	90	0.0312	0.568			
5	12	30	70	0.0320	0.604			
6	12	35	60	0.0308	0.567			
7	12	40	90	0.0412	0.340			
8	12	45	80	0.0317	0.581			
9	14	30	80	0.0430	0.478			
10	14	35	90	0.0605	0.330			
11	14	40	60	0.0648	0.320			
12	14	45	70	0.0719	0.121			
13	16	30	90	0.0711	1.018			
14	16	35	80	0.0769	0.430			
15	16	40	70	0.0798	0.525			
16	16	45	60	0.0839	0.591			

Table 1. L₁₆ OA experiment plan

The parameters and levels were selected as per the preliminary experiments, and OA is computed by considering the number of parameters and levels. The degrees of freedom were calculated using the formulae N(n-1), where N is the number of factors and n is the number of levels. The OA selection should be more than the calculated value of the degrees of freedom. MRR was calculated by dividing the thickness of the workpiece by machining time. The thickness of the specimen was 2 mm and machining time is measured in minutes. The overcut is a difference between the diameter of the tool electrode and the machined hole in millimetres [18].

Results and discussion

Entropy weighting method

The entropy approach is the best way to determine the significance of replies. The entropy method is important because it gives a quantitative framework for understanding and controlling uncertainty, complexity, and disorder in a variety of fields. Encapsulating fundamental concepts of variability and randomness allows for better decision-making, optimization, and analysis in both theoretical and practical applications. This method uses a number of steps to calculate the weight of responses. At first, a decision matrix D_{mxn} should be defined by Equation (1):

$$D_{\text{mxn}} = \begin{bmatrix} \alpha_{11} & \alpha_{12} & \alpha_{13} & \cdots & \cdots & \alpha_{1n} \\ \alpha_{21} & \alpha_{22} & \alpha_{23} & \cdots & \cdots & \alpha_{2n} \\ \alpha_{31} & \alpha_{32} & \alpha_{33} & \cdots & \cdots & \alpha_{3n} \\ \vdots & \vdots & \vdots & \ddots & \ddots & \vdots \\ \vdots & \vdots & \vdots & \ddots & \ddots & \vdots \\ \alpha_{m1} & \alpha_{m2} & \alpha_{m3} & \cdots & \cdots & \alpha_{mn} \end{bmatrix}$$

$$(1)$$

where α_{ij} represents the performance measure of the ith alternative (experiment number) on the jth attribute (output parameters), where m is the number of experiments and n refers to the number of output parameters (Gadakh *et al.* [11]).

Equation (2) normalizes the matrix responses:

$$\mu_{ij} = \frac{\alpha_{ij}}{\sum_{i=1}^{m} \alpha_{ij}^2}$$
 $j = 1, 2, ... n$ (2)

where, μ_{ij} is a dimensionless value belonging to the interval [0,1] for the ith alternative and jth attribute, which indicates the normalized performance.

Equation (3) calculates the entropy value V_i :

$$V_{j} = -\alpha \sum_{i=1}^{m} \mu_{ij} \ln (\mu_{ij})$$
 $j = 1, 2, ... n$ (3)

where $a = 1/\ln m$ is constant, and m is the number of alternatives.

Equation (4) calculates the degree of divergence:

$$F_{\rm j} = 1 - V_{\rm j} \tag{4}$$

Equation (5) could be used to calculate the weight of the jth criterion:

$$W_{j} = \frac{F_{j}}{\sum_{j=1}^{n} F_{j}}$$
 (5)

Multi-objective optimization based on ratio analysis

Multi-objective optimization based on ratio analysis (MOORA), called multi-criteria or multi-attribute optimization, involves optimizing multiple competing attributes while adhering to restrictions. The MOORA approach, developed by Brauers and Zavadskas [19], is a multi-objective optimization tool that can effectively address complicated manufacturing decision-making challenges. In comparison to other multi-criteria decision-making systems, the MOORA method is straightforward and easy to implement. Because this method is based solely on simple ratio analysis, it requires the fewest mathematical calculations, which may be useful and beneficial to decision-makers who do not have a strong foundation in mathematics. Additionally, the MOORA approach has a faster computing time. Unlike other multi-criteria decision-making procedures, the MOORA method can be performed using MS Excel. The MOORA approach is highly stable for a range of decision-making situations. The MOORA technique [19-22] begins with a decision matrix comparing the performance of options based on numerous criteria.

A ratio system is created to evaluate each alternative's performance on an attribute to a denominator that represents all alternatives for that attribute. Brauers and Zavadskas [19] analysed numerous ratio systems, including total ratio and Körth ratio. They found that the square root of the sum of squares of each alternative per attribute is the best choice for this denominator. This ratio is represented by Equation (6):

$$\alpha_{ij} = \frac{\alpha_{ij}}{\sqrt{\sum_{i=1}^{m} \alpha_{ij}^{2}}} \quad (j = 1, 2, 3, ... n)$$
(6)

The dimensionless number α_{ij} represents the normalized performance of the ith alternative on the jth attribute, falling within the interval [0,1]. In multi-objective optimization, normalized performances are added while maximizing helpful qualities and deducted when minimizing non-beneficial attributes. Thus, the optimization issue becomes as presented by Equation (7):

$$q_{i} = \sum_{i=1}^{g} \overset{\vee}{\alpha}_{ij} - \sum_{i=g+1}^{n} \overset{\vee}{\alpha}_{ij}$$
 (7)

In Equation (7), g represents the number of characteristics to maximize, (n-g) represent the number of attributes to minimize, and q_i represents the normalized evaluation value of the ith alternative across all attributes. Certain traits may be more significant than others. Prioritizing an attribute means multiplying it by its weight (significance coefficient) [18]. When the attribute weights are considered, Equation (3) becomes Equation (8):

$$q_{i} = \sum_{j=1}^{g} w_{j} \overset{\vee}{\alpha}_{ij} - \sum_{j=g+1}^{n} w_{j} \overset{\vee}{\alpha}_{ij} \quad (j = 1, 2, ... n)$$
 (8)

The weight of the j^{th} attribute (w_j) can be computed using the analytic hierarchy process or entropy approach.

The q_i value in the decision matrix might be positive or negative based on the sum of advantageous and non-beneficial features. An ordinal rating of q_i indicates final preference. The greatest option has the highest q_i value, while the poorest has the lowest.

The entropy-weighted MOORA approach was used to optimize MRR and overcut (OC). Equations (1) to (8) were used to calculate MOORA values and rankings, which are listed in Table 2. The attributes' weights were assigned using the entropy technique, with $w_j = 0.5406$ for MRR and $w_i = 0.4593$ for OC. The highest MOORA value is regarded as the best value and ranks first as the

optimal combination for best machining performance. As a result, the experimental run 10 has the highest MOORA value (0.1731). The 15^{th} (0.1731) and 14^{th} (0.1590) experimental runs are the next two best combinations. For optimal machining performance, 14 V, 35 g l⁻¹ electrolyte concentration, and 90 % duty cycle can be recommended.

Exp. No Square of output responses (α_{ij}^2) Normalized performance (α_{ij}^2) Highest Rank Material removal rate Overcut Material removal rate Overcut assessment a 1 0.3906 0.0759 0.0008 0.1403 0.2645 11 2 0.0009 0.3364 0.1440 0.2814 0.0778 9 3 0.0027 0.1215 0.1384 0.2642 0.0748 12 4 0.0010 0.3226 0.1584 0.0727 13 0.1853 5 0.0010 0.3652 0.1428 0.2704 0.0772 10 6 0.0009 6 0.3218 0.1933 0.2225 0.1022 7 0.0017 0.1156 0.2722 0.1538 0.0706 14 8 15 0.0010 0.2917 0.1490 0.0685 0.3371 9 0.2282 0.3235 0.0258 16 0.0018 0.0561 10 0.0037 0.1090 0.3201 0.4740 0.1731 1 0.1024 7 11 0.0042 0.3460 0.2003 0.0920 0.1122 12 0.0145 4 0.0052 0.3592 0.2443 13 0.3773 0.2751 0.1264 2 0.0051 1.0359 14 7 0.0059 0.1849 0.2003 0.0920 0.3460 15 0.0064 0.2752 0.3592 0.2443 0.1122 4 16 0.0070 0.3490 0.3773 0.2751 0.1264 2 4.3166 3.7340 $-a\sum_{i=1}\mu_{ij}\ln(\mu_{ij})$ -2.144 -1.67073 0.5406 0.4593

Table 2. MOORA based ranking

Analysis of variance table for multi-objective optimization

Analysis of variance (ANOVA) was used to statistically analyse the MOORA values in order to find relevant process parameters and their contributions to the machining performance [23]. As a result, the duty cycle accounts for approximately 27.06 % of machining performance. Voltage contributes 24.15 % and electrolyte content 15.58 % to machining performance, as shown in Table 3. According to the main effect Table 4, the best combination is 16 V, 35 g l^{-1} electrolyte concentration and 60 % duty cycle. The best combination is determined considering the highest-level values of machining factors superscripted with * in Table 4.

Degrees of Sequential sum of Adjusted Symbol *F*-value Contribution, % freedom squares mean square Voltage 1.454674 24.15 3 0.0040 0.001336 Electrolyte concentration 3 0.000862 0.938648 15.58 0.0026 **Duty cycle** 3 0.001497 1.630073 27.06 0.0045 Error 6 0.0055 0.000919 33.20 Total 15 0.016599 0.001107 100

Table 3. ANOVA table for MOORA

0.0596

0.0395

Figure 4 shows the main effect plot for MOORA values and the increasing voltage trend increases the output performance. The MRR and OC improve with the rise in voltage. The workpiece used for machining is a 3D-printed specimen with high toughness and strength. In order to electrochemically dissolve it, more voltage and electrolyte concentration are required [24]. The average density of the specimen is 7.9 g cm⁻³, and a higher electrolyte concentration is required for dissolution [25].

Machining factors	Signal to noise ratio for MOORA				
	LEVEL 1	LEVEL 2	LEVEL 3	LEVEL 4	Delta
Voltage	0.0753	0.0796	0.1008	0.1142*	0.0389
Electrolyte concentration	0.0763	0.1113*	0.0874	0.0826	0.0350

0.0949

0.0653

0.0991*

Table 4. Main effects table for MOORA

Duty cycle

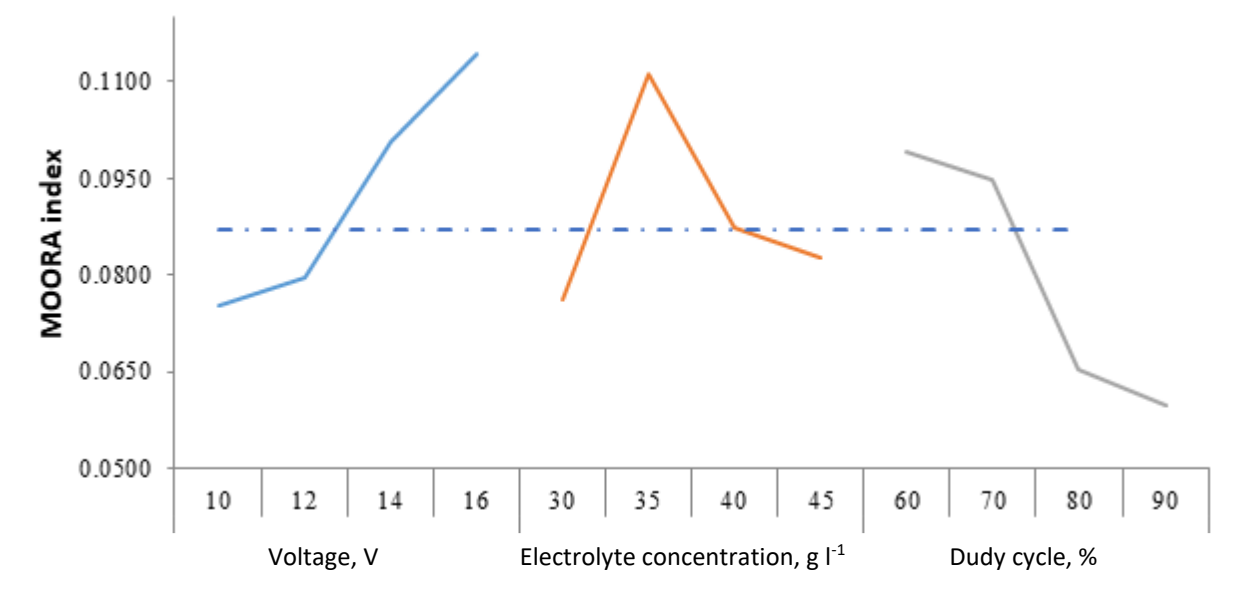


Figure 4. Main effect plot

Normally, in ECM, the electrolyte concentration in the 20 to 30 g l⁻¹ range is sufficient for efficient machining. In this MOORA, the optimal level and main effect plot show that 35 g l⁻¹ is required for machining EOS stainless steel 316L. Further increase in electrolyte concentration reduces the dissolution efficiency and accuracy. Many factors support this phenomenon, namely more hydrogen bubbles generation at the cathode, a huge mass of debris generation, and inadequate scavenging of electrolytes in the machining zone. An increase in the duty cycle has an insignificant effect on the ECM performance. The increase in duty cycle reduces the pulse-off time, which is essential for scavenging the machining zone. This short duration is insufficient for the evacuation of debris from the machining zone, leading to reduced performance.

Analysis of holes

It is evident from Figure 5 that for the hole machined at 16 V, 35 g I^{-1} of electrolyte concentration, and 60 % duty cycle, the over-etched region is witnessed around the circumference of the hole. It is due to the stray current effect on the electrode. It can be seen that the hole circumference is perfect and arresting the stray current lessens the over etched surfaces. Figure 6 shows the hole machined at ideal combinations, with no delaminated surfaces or micro-fractures observed. This phenomenon is due to the benefits of metal printing of components, which prevents future material deterioration.

^{*}Optimal parametric combination by MOORA

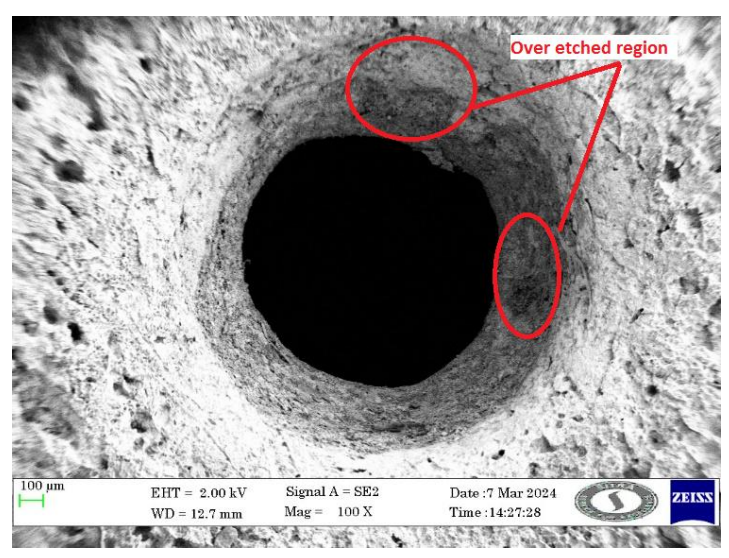


Figure 5. Hole machined at 16 V, 35 g l^{-1} of NaNO₃ electrolyte concentration, and 60 % duty cycle.

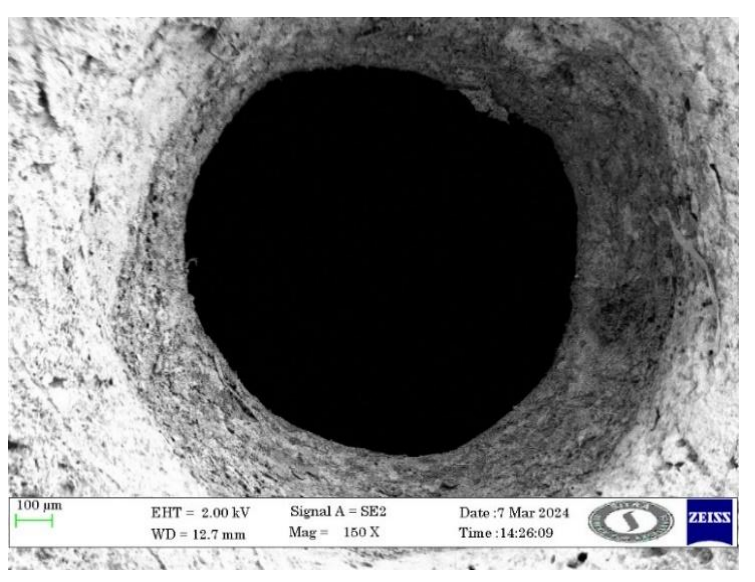


Figure 6. Hole machined at 14 V, 35 g l^1 NaNO₃ electrolyte concentrations, and 90 % duty cycle

Conclusions

In this experiment, the variation of ECM process variables, namely voltage, electrolyte concentration and duty cycle, are optimized with respect to material removal rate and overcut. L_{16} OA is used to conduct the experiments. The multi-criteria decision machining method, namely entropy-based multi-objective optimization based on ratio analysis (MOORA) method, is used for performance analysis. The attribute weights were assigned using the entropy technique, with $w_j = 0.5406$ for MRR and $w_j = 0.4593$ for OC. MOORA method recommends optimal machining performance as 14 V, 35 g l⁻¹ NaNO₃ electrolyte concentration, and a 90 % duty cycle. According to the main effect table, the best combination is 16 V, 35 g l⁻¹ NaNO₃, and 60 % duty cycle. ANOVA result shows that the duty cycle accounts for approximately 27.061 % of machining performance. Voltage contributes 24.015 %, and electrolyte content contributes roughly 15.58 % to machining performance. A scanning electron microscope was used to scan each machined hole, and different resolution images were taken in order to analyse the machined hole quality. The holes were machined at ideal combinations, with no delaminated surfaces or micro-fractures observed. This phenomenon is due to the benefits of metal printing of components, which prevents future material deterioration. Additive manufacturing technologies frequently result in materials having irregular microstructures,

porosity, and residual tensions. These irregularities can alter electrochemical reaction rates, resulting in unequal material removal. Different phases may dissolve at varying rates during ECM, resulting in localised overcutting or pitting. Microporosities and imperfections in 3D-printed materials can trap electrolytes and cause uneven dissolution. Layered structures and porosities cause non-uniform disintegration, resulting in uneven overcut profiles and low dimensional accuracy. These flaws can affect machining consistency and result in differences in MRR. Future studies can be planned to improve the hole dimensional quality.

References

- [1] P. Venugopal, R. Thanigaivelan, Performance of magnetized tool in electrochemical micromachining on scrapped alloy wheel matrix composite, *Journal of Electrochemical Science and Engineering* **13(3)** (2023) 553-561. http://dx.doi.org/10.5599/jese.1660
- [2] V. K. Sampath, P. Silori, P. Paradkar, S. Niauzorau, A. Sharstniou, A. Hasib, S. Villalobos, B. Azeredo, 3D printing of stainless steel 316L and its weldability for corrosive environments, *Materials Science and Engineering: A* 833 (2022) 142439. https://doi.org/10.1016/j.msea.2021.142439
- [3] P. Mašek, T. Fornůsek, P. Zeman, M. Bucko, J. Smolik, P. Heinrich, Machinability the AISI 316 stainless steel after processing by various methods of 3D printing, *MM Science Journal*November 2019 (2019) 3338-3346. http://dx.doi.org/10.17973/MMSJ.2019 11 2019091
- [4] H. Zhang, J. Dang, W. Ming, X. Xu, M. Chen, Q. An, Cutting responses of additive manufactured Ti6Al4V with solid ceramic tool under dry high-speed milling processes. *Ceramics International* **46** (2020) 14536-14547. https://doi.org/10.1016/j.ceramint.2020.02.253
- [5] L. Chen, Q. Xu, Y. Liu, G. Cai, J. Liu, Machinability of the laser additively manufactured Inconel 718 superalloy in turning, *International Journal of Advanced Manufacturing Technology* **114** (2021) 871-882. https://doi.org/10.1007/s00170-021-06940-8
- [6] Y. Karabulut, Y. Kaynak, Drilling process and resulting surface properties of Inconel 718 alloy fabricated by selective laser melting additive manufacturing, *Procedia CIRP* **87** (2020) 355-359. https://doi.org/10.1016/j.procir.2020.02.110
- [7] J. Fei, G. Liu, K. Patel, T. Özel, Effects of machining parameters on finishing additively manufactured nickel-based alloy Inconel 625, *Journal of Manufacturing and Materials Processing* **4(2)** (2020) 32. https://doi.org/10.3390/jmmp4020032
- [8] Y. Bai, A. Chaudhari, H. Wang, Investigation on the microstructure and machinability of ASTM A131 steel manufactured by directed energy deposition, *Journal of Materials Processing Technology* **276** (2020) 116410. https://doi.org/10.1016/j.jmatprotec.2019.116410
- [9] B. Li, R. Zhang, A. Malik, W. Li, Machinability of partition milling stainless steel/Inconel functionally gradient material printed with directed energy deposition. *The International Journal of Advanced Manufacturing Technology* **122(7)** (2022) 3009-3022. https://doi.org/10.1007/s00170-022-10111-8
- [10] M. K. Ramachandran, S. A. Sumaiya, M. Golvaskar, J. Wood, I. Sluder, C. S. Rakurty, M. Kannan, Improving the Fatigue Life of an Additively Manufactured Stainless-Steel Specimen Using a Secondary Grinding Process, *Turbo Expo: Power for Land, Sea, and Air* 88018 (2024) V009T17A011. https://doi.org/10.1115/GT2024-124342
- [11] V. S. Gadakh, V. B. Shinde, N. S. Khemnar, Optimization of welding process parameters using MOORA method, *The International Journal of Advanced Manufacturing Technology* **69** (2013) 2031-2039. https://doi.org/10.1007/s00170-013-5188-2
- [12] A. S. Bhaskar, A. Khan, Comparative analysis of hybrid MCDM methods in material selection for dental applications, *Expert Systems with Applications* **209** (2022) 118268. https://doi.org/10.1016/j.eswa.2022.118268



- [13] M. Soundarrajan, R. Thanigaivelan, Investigation of electrochemical micromachining process using ultrasonic heated electrolyte, in *Advances in Micro and Nano Manufacturing and Surface Engineering: Proceedings of AIMTDR 2018,* M. S. Shunmugam, M. Kanthababu, Eds., Springer Nature Singapore Pte LTD, 2019, 423-434. https://doi.org/10.1007/978-981-32-9425-7
- [14] C. Vempannan, T. C. Kanish, D. Thirumanikandan, B. Aswin, Electrochemical Micromachining Performance Optimization: Impact of Cathode Profile and Rotation on Machining Speed and Accuracy, in Advanced Manufacturing Techniques for Engineering and Engineered Materials, R. Thanigaivelan, N. Rajan, T.G. Argul, Eds., GI Global Scientific Publishing, 2022, 20-41. https://doi.org/10.4018/978-1-7998-9574-9.ch002
- [15] R. Thiraviam, V. Ravisankar, P. Kumar, R. Thanigaivelan, R. Arunachalam, A novel approach for the production and characterisation of aluminium—alumina hybrid metal matrix composites, *Materials Research Express* **7(4)** (2020) 046512. https://doi.org/10.1088/2053-1591/ab8657
- [16] S. Maniraj, R. Thanigaivelan, R. Viswanathan, P. Elumalai, Experimental investigation of MRR and ROC in aluminium metal matrix composites, *Materials Today: Proceedings* **45** (2021) 1102-1106. https://doi.org/10.1016/j.matpr.2020.03.190
- [17] S. Marichamy, S. Maniraj, R. Thanigaivelan, S. T. Kumaravel, K. V. Babu, P. Mallesham, Enhancement of material removal rate in EDM process using silicon carbide based strenx 900 steel, *Materials Today: Proceedings* **45** (2021) 780-782. https://doi.org/10.1016/j.matpr.2020.02.806
- [18] N. Sivashankar, R. Thanigaivelan, Electrochemical micromachining of magnesium AZ31 alloy using minimum quantity electrolyte, *Materials and Manufacturing Processes* **38(11)** (2023) 1406-1415. https://doi.org/10.1080/10426914.2022.2157429
- [19] W. K. M. Brauers, E. K. Zavadskas, The MOORA method and its application to privatization in a transition economy, *Control and Cybernetics* **35** (2006) 445-469. http://eudml.org/doc/209425
- [20] W. K. M. Brauers, E. K. Zavadskas, Z. Turskis, T. Vilutienè, Multi-objective contractor's ranking by applying the MOORA method, *Journal of Business Economics and Management* **4** (2008) 245-255. https://doi.org/10.3846/1611-1699.2008.9.245-255
- [21] D. Kalibatas, Z. Turskis, Multicriteria evaluation of inner climate by using MOORA method, *Information Technology and Control* **37** (2008) 79-83.
- [22] S. Chakraborty, Applications of the MOORA method for decision making in manufacturing environment, *International Journal of Advanced Manufacturing Technology* **54(9-12)** (2011) 1155-1166. https://doi.org/10.1007/s00170-010-2972-0
- [23] V.S. Gadakh, Application of MOORA method for parametric optimization of milling process, *International Journal of Applied Engineering Dindigul* **1(4)** (2011) 743-758.
- [24] R. Thanigaivelan, R. M. Arunachalam, A. Nithish, S. Venkatesh, P. Naveenkumar, S. Selvaganapathy, A. S. Aravind, Optimization of Laser and Electrochemical Process Parameters for Surface Modification of Hardness and Hydrophobicity on 316L Steel, *Lasers in Engineering (Old City Publishing)* **45** (2020) 69-84. https://www.oldcitypublishing.com/journals/lie-home/lie-issue-contents/lie-volume-45-number-1-3-2020/lie-45-1-3-p-69-84/
- [25] M. Shamsujjoha, S.R. Agnew, J.M. Fitz-Gerald, W.R. Moore, T.A. Newman, High strength and ductility of additively manufactured 316L stainless steel explained, *Metallurgical and Materials Transactions A* **49** (2018) 3011-3027. https://doi.org/10.1007/s11661-018-4607-2

© 2025 by the authors; licensee IAPC, Zagreb, Croatia. This article is an open-access article distributed under the terms and conditions of the Creative Commons Attribution license (https://creativecommons.org/licenses/by/4.0/)